ARISTOTLE UNIVERSITY OF THESSALONIKI
FACULTY OF SCIENCES
SCHOOL OF GEOLOGY
DEPARTMENT OF GEOPHYSICS

NIKOS A. SVIGKAS
MRes Geologist

A SEISMOLOGICAL AND REMOTE SENSING APPROACH OF GEODYNAMIC PHENOMENA

DISSERTATION THESIS

THESSALONIKI
2020

Στην Ειρήνη
στον Άγγελο και στην Αγγελική
ελάχιστο αντίδωρο για την υποστήριξη

ΝΙΚΟΣ Α. ΣΒΗΓΚΑΣ
MRes Γεωλόγος

ΤΗΛΕΠΙΣΚΟΠΙΚΗ ΚΑΙ ΣΕΙΣΜΟΛΟΓΙΚΗ ΠΡΟΣΕΓΓΙΣΗ ΓΕΩΔΥΝΑΜΙΚΩΝ ΦΑΙΝΟΜΕΝΩΝ

Υποβλήθηκε στο Τμήμα Γεωλογίας Α.Π.Θ.
Τομέας Γεωφυσικής

Ημερομηνία Προφορικής Εξέτασης: 09/04/2020

Αριθμός Παραρτήματος Επιστημονικής Επετηρίδας Τμήματος Γεωλογίας N°:198

<u>Τριμελής Συμβουλευτική Επιτροπή</u>

Καθηγήτρια................................Κυρατζή Αναστασία
Καθηγητής.................................Καρακώστας Βασίλειος
Διευθυντής Ερευνών...................Κοντοές Χαράλαμπος

<u>Εξεταστική Επιτροπή</u>

Ερευνητής..................................Atzori Simone
Διευθυντής Ερευνών...................Γκανάς Αθανάσιος
Καθηγητής .... Καρακώστας Βασίλειος
Διευθυντής Ερευνών.................. Κοντοές Χαράλαμπος
Καθηγήτρια................................ Κυρατζή Αναστασία
Αναπλ. Καθηγητής......................Λουπασάκης Κωνσταντίνος
Ερευνητής.................................. Παπουτσής Ιωάννης

Citation:

Svigkas N., 2020. – A seismological and remote sensing approach of geodynamic phenomena. Ph.D. Thesis, School of Geology, Aristotle University of Thessaloniki, Annex Number of Scientific Annals of the School of Geology No XXX, 267 pp.

Σβήγκας Ν.,2020. – Σεισμολογική και τηλεπισκοπική προσέγγιση γεωδυναμικών φαινομένων. Διδακτορική Διατριβή, Τμήμα Γεωλογίας Α.Π.Θ., Αριθμός Παραρτήματος Επιστημονικής Επετηρίδας Τμ. Γεωλογίας No XXX, 267 σελ.

TABLE OF CONTENTS

LIST OF FIGURES

LIST OF TABLES

PUBLICATIONS FROM THIS THESIS

Peer-Reviewed journals:

Svigkas N., Atzori S., Kiratzi A., Tolomei C., Antonioli A., Papoutsis I., Salvi S., Kontoes Ch. (2019). On the Segmentation of the Cephalonia–Lefkada Transform Fault Zone (Greece) from an InSAR Multi-Mode Dataset of the Lefkada 2015 Sequence, ***Remote Sensing***, 11(16), 1848; https://doi.org/10.3390/rs11161848

Svigkas N., Atzori S., Kiratzi A., Tolomei C., Salvi S. (2019). Isolating swarm sources using InSAR: the case of the February 2017 seismic swarm in Western Anatolia (Turkey), ***Geophysical Journal International***, Volume 217 (3), 1479–1495, https://doi.org/10.1093/gji/ggz093

Svigkas N., Papoutsis I., Loupasakis C., Tsangaratos P., Kiratzi A., Kontoes Ch. (2019). Radar space measurements of the deforming trends at northern Greece resulting from underground water activity*,* ***Advances in Remote Sensing and Geo Informatics Applications***, 309-313

Svigkas N., Papoutsis I., Loupasakis C., Tsangaratos P., Kiratzi A., Kontoes, Ch. (2017). InSAR time-series monitoring of ground displacement trends in an industrial area (Oreokastro — Thessaloniki, Greece): detection of natural surface rebound and new tectonic insights, ***Environmental Earth Sciences***, 76:195, DOI 10.1007/s12665-017-6517-9

Svigkas N., Papoutsis I., Loupasakis K., Tsangaratos P., Kiratzi A., Kontoes Ch. (2016). Rebound of land subsidence due to the natural recovery of the aquifers, monitored through multi-temporal interferometry: validation and interpretation by ground truth data in the case of Kalochori and Sindos regions, Northern Greece, ***Engineering Geology***, 209, 175-186, http://dx.doi.org/10.1016/j.enggeo.2016.05.017

Papers in Conference Proceedings:

Peer-Reviewed:

Tolomei C., Svigkas N., Fathian A., Atzori S., Pezzo G. (2018). Surface deformation and source modelling for the Mw 7.3 Iran earthquake (November 12, 2017) exploiting Sentinel-1 and Alos-2 Insar data. *Proceedings of International Geoscience and Remote Sensing Symposium (**IGARSS**),* Valencia 22-27 July, Spain

Loupasakis C., Raspini F., Svigkas N., Papoutsis I., Rozos D., Tsangaratos P., Moretti S., Kiratzi A., Kontoes Ch., Adam N. (2018). Advanced earth observation techniques applied for the study of land subsidence phenomena. The case of the Kalochori region, Thessaloniki Greece. *Proceedings of 1st conference of the **Remote Sensing and Space Applications Committee of the Geological Society of Greece**,* pp. 11-12.

Non Peer-Reviewed:

Svigkas N., Papoutsis I., Loupasakis K., Kontoes H., Kiratzi A. (2015). Geo-hazard Monitoring in Northern Greece Using InSAR techniques: the case Study of Thessaloniki, ***9th International Workshop FRINGE 2015*** *"Advances in the Science and Applications of SAR Interferometry and Sentinel-1 InSAR"*, ESA-ESRIN, Frascati, Italy

Abstracts at Conferences:

Svigkas N., Atzori S., Kiratzi A., Tolomei C., Salvi S. (2018). A source study of the February 2017 Biga Peninsula (Aegean Sea) earthquake swarm inferred from InSAR and seismic waveform measurements, The European Seismological Commission ***(ESC)*** 36th General Assembly, ***2018***, *Malta*

Svigkas N., Atzori S., Kiratzi A., Tolomei C., Salvi S. (2018). An InSAR study of the 2017 Biga peninsula swarm. European Geosciences Union ***(EGU)*** General Assembly, ***2018***, Vienna, *Austria*

Svigkas N., Atzori N., Kiratzi A., Tolomei C., Salvi, S. (2017). An Analysis of the 2017 Western Anatolia Earthquake Swarm in Biga Peninsula, Turkey, American Geophysical Union ***(AGU)*** Fall Meeting ***2017***, New Orleans, *USA*

Loupasakis C., Svigkas N., Papoutsis I., Rozos D., Adam N., Kiratzi A, Kontoes Ch, Raspini F., Moretti S. (2016). Advancements in the Research of the land subsidence phenomena at the wider coastal area of Thessaloniki, Greece. ***2nd International Workshop on Coastal Subsidence*** May 30 - June 1, **2016**, Venice, *Italy*

Svigkas N., Papoutsis, I., Loupasakis, K., Kontoes, H., Kiratzi, A. (2015). Land Deformation at the Thessaloniki - Giannitsa Plain (Greece) Deduced from 20-years Radar Observations using Persistent Scatterers Techniques. Abstract ID: 65112 American Geophysical Union ***(AGU)*** Fall Meeting ***2015***, San Francisco, *USA*

PREFACE

The work presented in this thesis was conducted in: the Aristotle University of Thessaloniki (AUTH) in Thessaloniki, the National Observatory of Athens (NOA) in Athens and in the Istituto Nazionale di Geofisica e Vulcanologia (INGV) in Rome.

I owe my deepest gratitude to my supervisor **Anastasia Kiratzi**. Her support and love, boosted me to go on through this period of my life. Her advice had a great impact on me, since the years of my undergraduate studies and she played a major role in my decision to follow the path I chose. I would like to thank her for the financial support and for giving me the chance to start this thesis with her. I thank her for our way of communication, for her teaching and for always being open to discussing ideas. Her support and mentoring helped me, when my self-doubts became toxic rather than constructive. Above all, I thank her for her trust and for allowing me totally free to make choices. My interaction with her, urged me to develop a more pragmatic attitude towards life, which is an essential factor to have through adulthood.

I am thankful to the other members of my PhD committee, **Vassilios Karakostas** for advising and the discussions, especially for the case of the Lefkada study. My director at NOA, **Haris Kontoes** is thanked for the financial support and for giving me the opportunity to work with his team at the Institute for Astronomy, Astrophysics, Space Applications and Remote Sensing, where I started collaborating with **Ioannis Papoutsis**, whom I also thank, since he was the first to introduce me to the deeper waters of remote sensing. During my stay in Athens, I also had a close collaboration with **Constatinos Loupasakis** from the National Technical University of Athens, who was always open to discuss and collaborate on several studies presented in this thesis.
The endless time that I had (and still have) together with **Simone Atzori** at INGV and his interest in my scientific development, are something that I can only be grateful for. Simone was always happy and available to answer to my questions, even though this could mean a bombardment of questions. I thank him for trusting me his codes, for being always willing to share his experience. His kindness and patience with me and the endless working hours we spent together, allowed me to feel comfortable enough, to express all my knowledge weaknesses, something that is a prerequisite for a teacher-student relationship. The support that I received for the current thesis by Simone was crucial and I sincerely thank him for this, but most of all for our friendship.
I would also like to express my gratitude to **Stefano Salvi**, my INGV director. I thank him for giving me the opportunity to work at INGV, allowing me to have at the same time as priority my thesis. I thank him for his generosity and the funding that I received for conferences, schools and scientific visits. The discussions we had together were rather enlightening, regarding the choices of my future scientific development. Most of all, I would like to thank him for his interest in my education, for his trust and for allowing me to enjoy a complete freedom, by creating a warm academic working environment.

Also I thank my current colleagues from INGV, **Cristiano Tolomei** and **Andrea Antonioli** for our collaboration. **Falk Amelung** is thanked for the period I spent at the University of Miami. **Cristiano Collettini** and **Marco Scuderi** from La Sapienza and **Sebastiano Lauro** from Roma Tre, for allowing me to sit in on their courses. I thank all the people of INGV in and out of the pollaio, for the great time that we have in Rome and also all my colleagues at NOA, where we had an everyday interaction while in Athens, enjoying the great view from our previous office at Penteli. I thank the colleagues that we were together during the first period of my thesis in AUTH and the Seismological station of AUTH, in particular **Harris Kkallas** and also **Konstantinos Leptokaropoulos** with whom we had fun and long discussions, while we were sharing for some time the same office.

I thank all my roommates and friends in Athens and Rome and my childhood friends in Thessaloniki.

My parents for their support, since day 0.

Special thanks to Ειρήνη of course, for the present and the future.

European Space Agency, Italian Space Agency, Canadian Space Agency, and Japan Aerospace Exploration Agency are thanked for the satellite data. Some of the hydrogeological data were from the Water Supply and Sewerage Company of Thessaloniki (EYATH), from ANATOLIKI S.A., Fikos Ilias and the project LIFE04/ENV/GR/000099 WATER AGENDA (lifewateragenda.org). Seismological data were from the national centres: the Geodynamic Institute of the National Observatory of Athens (http://bbnet.gein.noa.gr) and the Seismological Station of the Aristotle University of Thessaloniki (http://geophysics.geo.auth.gr). Jeff Freymueller and Cécile Lasserre are thanked for scientific discussions regarding the study of Oreoakstro. Christodoulos Kyriakopoulos is thanked for fruitful discussions on the Biga peninsula study. Antonio Avallone is thanked for discussions on the Lefkada 2015 sequence. Xanthos Papanikolaou and Demitris Anastasiou from Dionysos Satellite Observatory are also acknowledged.

During this thesis I received founding at first by: (a) by the European Union (European Social Fund—ESF) (MIS377335) and Greek national funds through the Operational Program "Education and Lifelong Learning" of the National Strategic Reference Framework (NSRF)—Research Funding Program: Thales - Investing in knowledge society through the European Social Fund (Coordinator Anastasia Kiratzi), then by (b) the European Union 7th Framework Programme (FP7-REGPOT-2012-2013-1), in the framework of the project BEYOND "Building a Centre of Excellence for EO-based monitoring of Natural Disasters", G. A. 316210 (Coordinator Haris Kontoes) and also by (c) Istituto Nazionale di Geofisica e Vulcanologia (INGV) (Coordinator Stefano Salvi).

Chapter.1 INTRODUCTION

The beginning of the history of Radar (Radio Detection And Ranging) Interferometry goes back to the ‘70s, where the US military applied the technique using airborne radar data to map topography (Graham, 1974). Later in the ‘80s, studies on estimating topographic maps based on InSAR Interferometric Synthetic Aperture Radar (InSAR) techniques were published (Gabriel and Goldstein, 1988). Very often, while estimating the topography for an area, there was a challenge because the estimated topographic signal, was not always cleared from deformation signals that might have occurred at the study area, during the monitoring period.

The first observation of surface movement caused by earthquake was from the 1892 Tapanuli earthquake, Sumatra from J.J.A. Müller, while a triangulation survey was taking place (Segall, 2010; Bonafede et al. 1992). Geodetic measurements from InSAR and GPS have offered a new way of looking into the tectonic processes from an additional approach. The first application of InSAR from the earth science community was presented to the classic paper of Massonnet et al. (1993), where it was shown that SAR interferometry can be used to monitor earthquake movements. Thanks to the open archive of European Space Agency’s (ESA) satellites together with the many other available radar sensors, an increasing amount of studies on various types of surface geophysical movements followed: earthquakes, volcanoes, glacial movements, delta subsidence, among others. During the last years, the major advancement was the launch of the Sentinel satellite family; the abilities of these sensors (and mainly the short revisit times) together with the free-data policy available to the scientific community, opened new research possibilities.

Conventional Differential Interferometry (DInSAR) exploits two radar images (the so-called “master” and “slave”) and the deformation that occurred during the time between the two satellite acquisitions can be measured. The Multi-Temporal InSAR (MT-InSAR) techniques use a series of radar images, and this enables the monitoring during large time-windows. This would not be feasible with DInSAR due to the temporal and spatial decorrelation of the SLC images (Zebker and Villasenor, 1992). Time-series deformation measurements are used to estimate the velocity of deformation. InSAR can be used to study natural phenomena, but sometimes also the consequences of anthropic activities that have an effect on the earth's surface. In many cases deforming signals, that were not previously known to exist, can be revealed. InSAR enables the urban monitoring, and of course, the monitoring of critical infrastructure.

In this thesis, both the conventional interferometry and multi-temporal techniques are exploited, depending on the goal and type of each study.

1.1 THESIS ROADMAP & CONTRIBUTIONS

The scope of the present thesis is to use geodesy to study the surface deformation occurring at specific areas of Greece and abroad. In all cases, the goal is the detection and measurement of the deformation and at a second stage the interpretation of it.

Overall, two different types of deformation are investigated:

- anthropogenic deformation
- tectonic deformation

In the following, the cases studied under these two general categories will be briefly introduced.

Chapter 2 describes the Earth Observation (EO) processing chains used and the SAR data exploited. Chapter 3 provides information on the geophysical modelling techniques adopted. Chapters 4 and 5 are the core of the thesis, presenting the different case studies. Summary and concluding remarks are presented in Chapter 6.

In Chapter 4, and in the first part of this thesis, a surface deformation study of northern Greece and more specifically Thessaloniki (the second largest city in Greece) and its vicinity, is conducted. The goal is the definition of the main driving mechanism by exploiting external data, together with the Earth Observation (EO) results. The ultimate question addressed in each case is whether the detected deformation signal is anthropogenic.

The focus is set at first at the area of Kalochori. The latter is located close to the city of Thessaloniki and is a main industrial centre of northern Greece. The area was known to be deforming since the '60s. The surface displacement is measured using MT-InSAR techniques (Persistent Scatterer Interferometry -PS and Small Baseline Subset – SBAS) exploiting the ESA imagery archive. Results of the ERS 1 and 2 satellites of this thesis are in accordance with previous studies indicating a subsiding trend. The new results presented here, derived from the ENVISAT satellite and shows that from 2003 to 2010, there was a reverse movement of the surface, indicating uplift. This was one of the first cases where this type of change in the deformation trend, had been recorded. Remote sensing results are taken into account together with external data and the analysis show that the main cause of the detected deformation is aquifer activity. The existing data give an insight on the surface's sensitivity to the temporal variability of the aquifers' trends.

Another area that was known to be under deformation is the Anthemountas graben. Time series techniques are used to detect and analyse the deformation pattern of the graben. Anthmountas is located at the east of the city of Thessaloniki and hosts the longest known tectonic structures close to the metropolitan area of the city. Inside the graben, lies also the International Airport of Thessaloniki. Previous studies have highlighted a subsiding surface during the years 1995 to 2001. Here, a complete SAR time-series monitoring from 1992 to 2010 is presented exploiting the ESA archive of: ERS1, ERS2 and ENVISAT imagery. The land use of the area makes Anthemountas a challenging case study. A steadily subsiding environment is revealed by InSAR that has been occurring during both decades. The detailed study of the deformation pattern together with the exploitation of in-situ data, define aquifer overpumping as the main cause of the detected subsidence. However, tectonic structures also play a role, as they appear to have a significant effect to the surface deformation rates. In addition, InSAR is applied for urban monitoring to locations of special interest in the broader study area like Thermi and Perea towns and the Thessaloniki International Airport. It is proved that the airport is under an increasing subsiding velocity during the two decades.

Oreokastro, is located NW of the city of Thessaloniki. Raucoules et al. (2008) identified for the first time a subsiding signal during the period 1992–1999. Different assumptions were proposed from various workers for this displacement signal; however, the driving mechanism had not been so far, solidly explained or proved and this was the motivation to study the specific area. Data from ERS 1, 2 and ENVISAT missions, acquired between 1992 and 2010, were analysed to enhance the understanding of this displacement signal. The analysis confirms a subsiding displacement pattern from 1992 to 1999, whereas the more recent results indicate that after 2003 the motion direction has changed to uplift. This subsidence and the subsequent uplift was not reflecting a natural process; on the contrary, the driver mechanism is anthropogenic, related to the regional aquifer activity. Focus is also set on the local fault network. The shape of the deformation pattern is spatially related with the network of faults dominating the area. Detailed analysis of the deformation pattern offer validations on previous assumptions regarding the length of the tectonic features of the area (like Asvestochori fault). This interaction with the aquifer activity shows that the specific fault acts as a groundwater barrier. Moreover, the surface deformation study conducted revealed a previously unknown structure, optimum oriented to the current stress regime.

Chapter 5, the second part of the thesis, is focused on seismotectonic studies in Greece, and abroad. More specifically, the tectonics of the areas of interest are studied by exploiting satellite data from seismic events. At first, the displacement pattern caused by the events was measured and then, the consequent step was the modelling of the source that caused this deformation. Except the tectonic interpretations, there is a focus to test the ability of the new satellite advancements to be furtherly exploited in areas of earthquake seismology that currently are geodetically less studied.

The *first case study* is the 2017 Iran-Iraq, Mw 7.3 earthquake. This is based on a multi-frequency (C and L band) surface deformation study. 500 casualties and building failures were in the aftermath of the earthquake that occurred close to the Iran-Iraq borders. The event is located at a plate boundary where two plates (Arabian and Eurasian) collide and create the Zagros Mountains. A dataset of ascending and descending satellite passes of Sentinel-1 and ALOS-2 (Wide Swath) satellites were processed to estimate the static surface displacement caused by the tectonic activity of the area. The use of the rich InSAR dataset enabled to obtain a complete overview of the crustal displacements field caused from the mainshock. The land use of the area allowed to have a displacement maps with a high-coherence signal that were furtherly exploited for the seismic source definition.

The *second case study* is from the Ionian Islands region. Cephalonia-Lefkada Transform Fault Zone (CTF) is the most active area in the eastern Mediterranean. It is an active boundary, located in the Ionian Sea (Greece), which separates continental subduction to the north from oceanic subduction to the south. The area is an open field of study since CTF geometry has not yet being defined. A rich multi-modal dataset of the most recent earthquake of the region, the 17 November 2015 Mw 6.4 event was exploited and new surface displacement InSAR results are presented, that offer additional constraints on the fault segmentation of the area. Based on this dataset and by exploiting available information of earthquake relocation and seafloor bathymetry, a different source definition of the 2015 sequence is proposed compared, to those published already. The modelling proposed includes an additional southern fault segment, oblique to the segment related with the mainshock, which indicates that the CTF structure is more complex than previously believed.

The *third case study* is from the cross-border region of Greece and Turkey. Earthquake swarms are sequences, which are not characterized by a distinct mainschok, thus they are considered a specific type of seismic sequence. Swarms do not leave a significant deformation signal on the earth's surface and in many cases there is a complete absence of it, since the seismic events occurring, are minor to moderate in magnitude. This absence of surface deformation is the reason why an InSAR swarm study is not straightforward. Moreover, another obstacle is that when using InSAR, the time of the satellite passes do not always allow the temporal isolation of the seismic events. That is why there are only few InSAR swarm studies. In early 2017, at western Anatolia, a moderate size M5+ earthquake swarm-type activity burst at the tip of the Biga peninsula (western Turkey). Biga peninsula is a location where important tectonic structures meet. The area is an actively deforming region whose deformation is taken up predominantly by normal faulting, sometimes combined with a strike-slip component. Displacement patterns based on selected radar image pairs of Sentinel-1 and ALOS-2 and source modelling results are presented in an attempt to study the swarm activity. Overall, it is shown that the Sentinel-1 family, together with the other available radar satellite installations, could potentially provide additional opportunities to study these type of phenomena. It is demonstrated that InSAR can nowadays start being an additional tool for studying seismic swarms in a systematic manner.

Chapter.2 METHODS AND DATA

2.1 SYNTHETIC APERTURE RADAR (SAR)

Synthetic Aperture Radar (SAR) has been in use for more than 30 years for Earth Observation (Moreira et al. 2013). The SAR sensor is an active remote sensing system that acts as both transmitter and receiver of electromagnetic waves within the microwave frequencies. One of its main advantages is that it is an “all-weather” sensor since the radiated waves can penetrate the cloud cover. In addition, it is not dependent on existence or absence of daylight (Tomiyasu, 1978; Woodhouse, 2006; Franceschetti and Lanari, 2009). The SAR sensor moves along the orbit (ascending or descending) in the direction of azimuth and is a side-looking system that transmits microwave pulses whose backscattering from the Earth’s surface is received in the range direction (Fig. 2.1). The transmitted narrow beam scans a strip of the Earth’s surface (strip-map SAR) and has a specific incidence angle; different satellites can have different incidence angles.

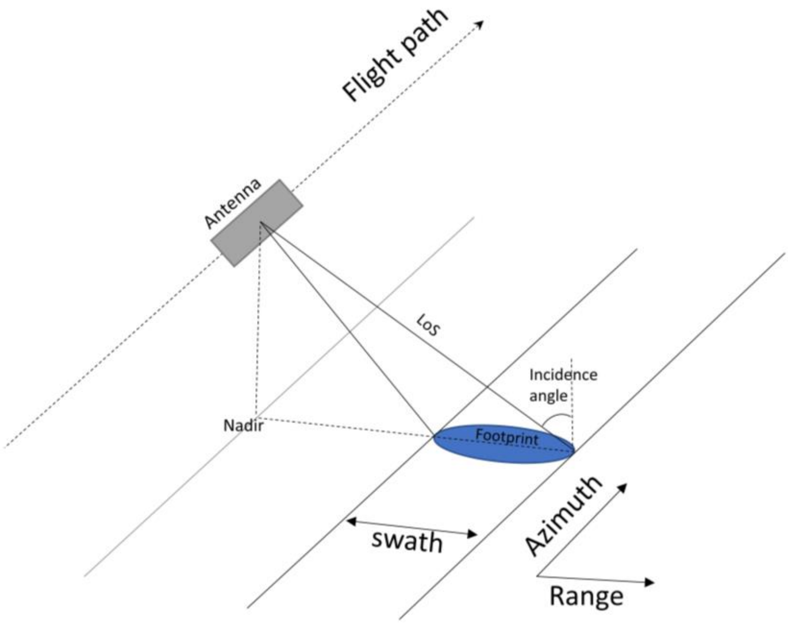

Figure 2.1 Synthetic Aperture Radar geometry.

A two-dimensional array is created from the time-delay and the amplitude of the backscattering (Chan and Koo, 2008). This array is a SAR image containing information on both the amplitude and phase of the received wave. The minimum distance between two targets on the ground in order to be distinguished, is called resolution. The range resolution (Rr) of the transmitted pulse (τ) is:

$$\mathrm{R_r} = \frac{c\tau}{2} \tag{2.1}$$

where c is the speed of light. The azimuth (A_r) resolution is:

$$\mathrm{A_r} = \frac{L}{2} \tag{2.2}$$

where L is the length of the antenna. A very long antenna can be synthesized (focusing) by the motion of the platform (Curlander and McDonough, 1991). The focused images are the Single Look Complex (SLC). Each pixel of latter is a complex number containing the magnitude and the phase information of the wave.

After the transition of the pulse, a portion of the energy returns back to the satellite (backscattering). Thus, the SLC image formed depends highly on the characteristics of the Earth's surface and especially the slope and the roughness (Fig. 2.2). This can be seen at the amplitude image where there is the intensity of the signal that returned back to the satellite.

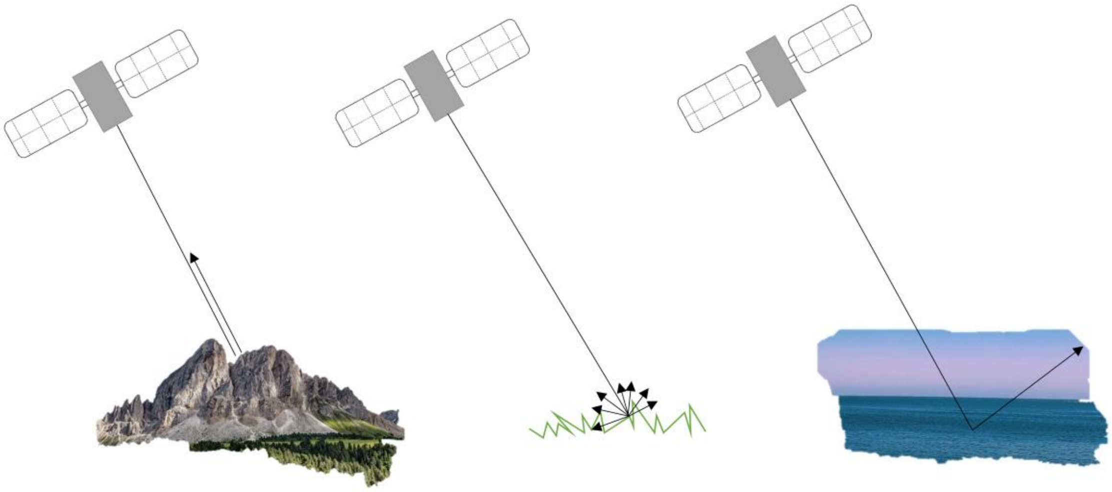

Figure 2.2 The amount of backscattering depends on the earth's surface. The far left sketch shows a surface which is perpendicular to the incidence angle of the satellite. This is the case of the maximum backscattering. Middle sketch is depicting a rough surface where there is less backscattering. A smooth surface is depicted in the last sketch to the right, where there is no return signal to the satellite.

Urban fabrics and other man-made objects are likely to produce more backscattering (they appear brighter in the amplitude images). On the other hand, densely vegetated areas have lower backscattering. Areas with no backscattering appear dark, like for example the sea in Figure 2.3.

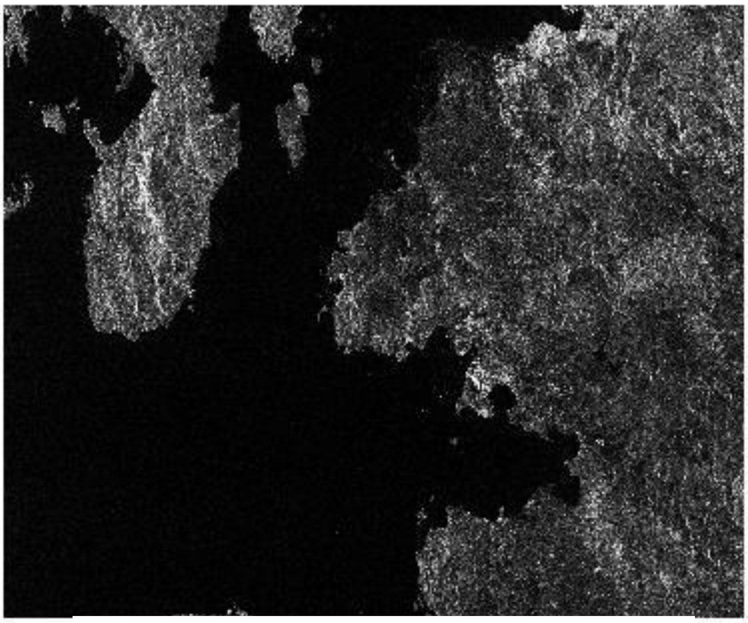

Figure 2.3 Example of an SLC amplitude image.

Regarding the phase of the backscattered signal, it is a measurement of the distance between the on-earth target and the satellite. Different targets on the earth that are distant, are having different delays between the transmitted and the received signal. The signal is almost sinusoidal, thus these delays can be approximated with the phase-shift between the transmitted and the received signal. This phase shift when the electromagnetic wave travels a distance R is equal:

$$\vartheta = 2\pi f t = \omega t = \frac{\omega R}{c} = \frac{2\pi R}{\lambda} \tag{2.3}$$

where ϑ is the phase, f is the wave frequency, t is the travel time, ω is the angular frequency, c is the speed of light and λ is the wavelength. Since the wave travels twice, (2.3) becomes:

$$\vartheta = \frac{4\pi R}{\lambda} \quad (2.4)$$

This is of course only the last fraction of the wave's travel distance, since the signal has a periodic nature (Ferretti et al. 2007).

2.2 INTERFEROMETRIC SYNTHETIC APERTURE RADAR (INSAR)

The goal of spaceborn InSAR is to measure the change in distance between the surface and the satellite. This is achieved by defining the phase change between two SLC images acquired in different time over the same area with the same viewing geometry. In this way the surface displacement that occurred during the two acquisitions can be found (Fig. 2.4).

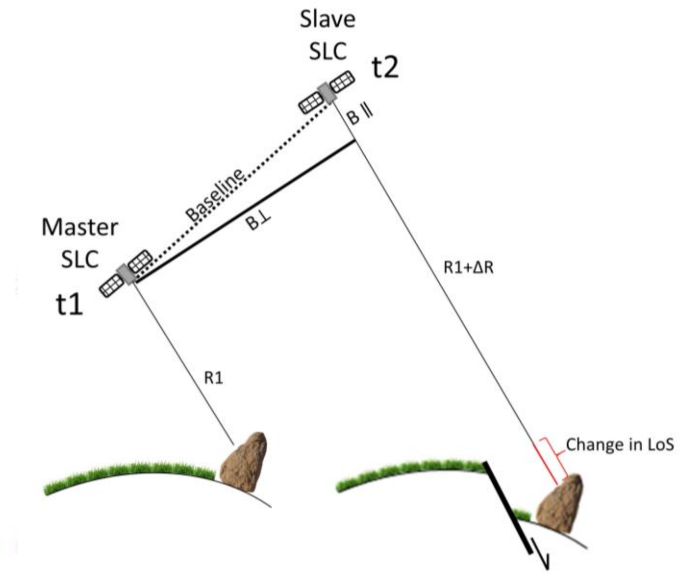

Figure 2.4 Two-pass differential interferometry. One SLC image acquired before (at time t1) the deformation case under study, and one after (at t2) is required. B⊥ and B|| are the normal and paralel baselines. The change in range ΔR due to the fault movement is measured via the estimation of the phase changes Δϑ between the two considered acquisitions (based on Osmanoğlu et al. 2016).

At first, the two SLC images need to be coregistered. During this procedure there is the alignment between the first image (master) and second one (slave). Assume two SAR signals where R is the Line-Of-Sight (LoS) range, χ is the azimuth and ϑ is the phase (Hanssen, 2001):

$$U_1(R,\chi)=|U_1(R,\chi)|e^{j\vartheta_1(R,\chi)} \quad \text{and} \quad U_2(R,\chi)=|U_2(R,\chi)|e^{j\vartheta_2(R,\chi)} \tag{2.5}$$

To form an interferogram, the "master" image (U_1) is multiplied by the complex conjugate of the "slave" image (U_2).

$$\mathrm{Intf}(R,\chi)= U_1(R,\chi)\, U_2(R,\chi)*=|U_1(R,\chi)||U_2(R,\chi)|e^{j\Delta\vartheta(R,\chi)} \tag{2.6}$$

where $\Delta\vartheta(R,\chi)=\vartheta_1(R,\chi)-\vartheta_2(R,\chi)$.

$$\Delta\vartheta(R,\chi)=\frac{4\pi\Delta R}{\lambda} \tag{2.7}$$

where ΔR is the path difference between the two acquisitions (Fig. 2.4).

The estimated interferogram, which expresses the differences in LOS direction, contain signal contributions from various components:

$$\vartheta_{\mathrm{int}} = \vartheta_{\mathrm{topo}} + \vartheta_{\mathrm{def}} + \vartheta_{\mathrm{atm}} + \vartheta_{\mathrm{flat}} + \vartheta_{\mathrm{noise}} \tag{2.8}$$

$\vartheta_{\mathrm{topo}}$ is the phase difference from topography (iso-height contours), ϑ_{def} is the phase component that derived from the surface's motion (i.e. deformation), ϑ_{atm} is the phase delay between the transmition and reception of the signal due to the atmosphere, the phase with respect to a flat surface is $\vartheta_{\mathrm{flat}}$, $\vartheta_{\mathrm{noise}}$ is phase due to noise. Since in our case we are interested in the deformation occurred on the Earth's surface, all the other factors are considered as noise and they are subtracted from the calculated intereferograms. The topographic contribution can be subtracted by using information from a Digital Elevation Model –DEM, as for example from the Shuttle Radar Topography Mission SRTM (Farr et al. 2007). Atmospheric contributions can be eliminated or decreased using external information (e.g. Yu et al. 2017; 2018a; 2018b), the flat earth phase is related to the parallel baseline (B||) and the orbital parameters are used to perform the flattening. Precise orbital data (e.g. from TU Delft in case of the ENVISAT satellite) can offer a better estimate on the position of the satellite. After all the corrections, a wrapped phase map is generated showing the surface deformation that occurred in-between the two satellite acquisitions (e.g. Fig. 2.5a). This technique is called Differential Interferometric Synthetic Aperture Radar (DInSAR).

Very often there might be signal decorrelation. A way to measure this is to estimate the complex correlation coefficient (coherence) of the two radar images:

$$\gamma = \frac{\Sigma\left|U_1 U_2^{*}\right|}{\sqrt{\Sigma|U_1|^2 \Sigma|U_2|^2}} \tag{2.9}$$

Coherence values range from 0 to 1, indicating total decorrelation or full coherence, respectively. To perform a differential interferogram there needs to be an amount of coherence. Low coherence areas are not used in the procedure and usually are masked. This can happen for example at areas with vegetation or due to the near-fault motions (e.g. Fig. 2.5b).

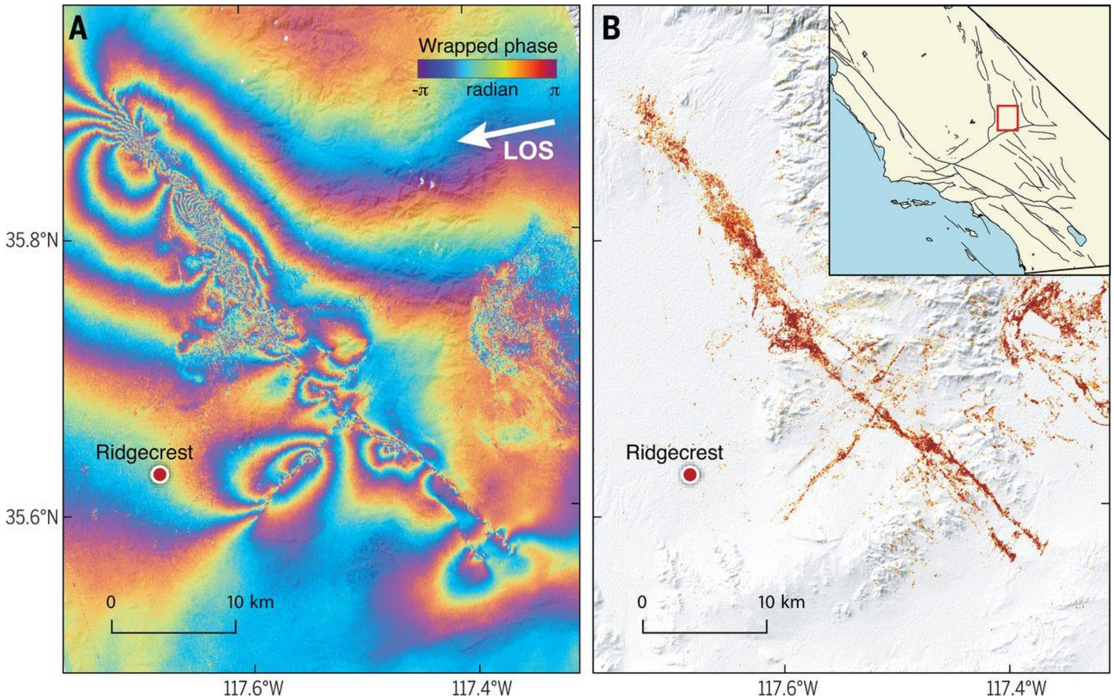

Figure 2.5 a) Wrapped interferogram of the Ridgecrest 2019 earthquakes. b) Loss of coherence in the near fault area (Ross et al. 2019).

The created wrapped interferogram is subjected to filtering (e.g. Goldstein & Werner, 1998) to reduce the noise. One fringe is a full color cycle (e.g. here yellow-blue-red) indicates a surface displacement of λ/2 (where λ : sensor's wavelength). The phase of an interferogram is ambiguous. This is because only the non-integer part is measured; thus the interferometric phase is referred as wrapped modulo 2π; the created interferogram has a non-continuous phase. In order to retrieve the ambiguous integer multiplies of 2π phase, a procedure called "unwrapping" is performed (Fig. 2.6). To perform unwrapping, a satisfying level of coherence is required. With unwrapping, the numbers of full phase cycle can be retrieved. Finally, a continuous geocoded displacement map is created (in LoS), showing the satellite-ground displacement.

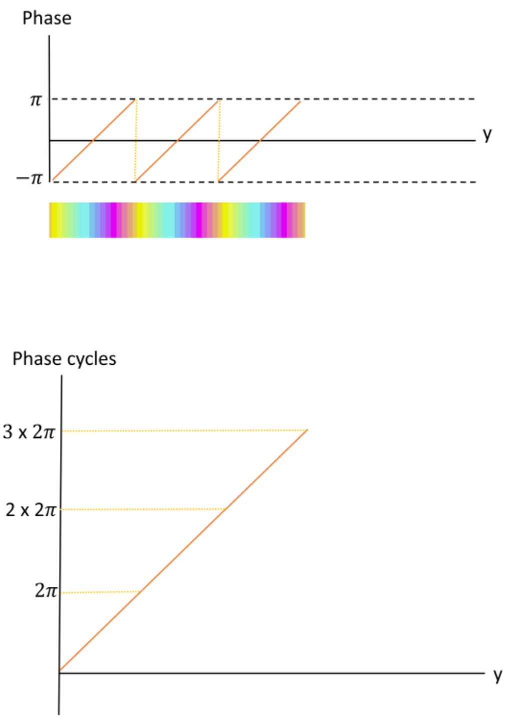

Figure 2.6 The ambiguous phase differences (upper graph) is represented as modulo 2π. The absolute phase (bottom graph) is obtained through the phase unwrapping step.

There are small differences in the processing steps depending the processor adopted, however the basic concepts are common to all codes and softwares. The graph of Figure 2.7, shows the usual steps followed. In this thesis, the following softwares were used for DInSAR processing: ROI-PAC (Repeat Orbit Interferometry PACkage) code

(Rosen et al. 2004) by the Jet Propulsion Laboratory division of NASA and Caltech, DORIS (Delft object-oriented radar interferometric software) code (Kampes et al. 2003) by the Delft Institute of Earth Observation and Space Systems, SNAP (Sentinel Application Platform) software from European Space Agency (ESA) (and previously Sentinel Toolbox) and SARscape software by Sarmap ©.

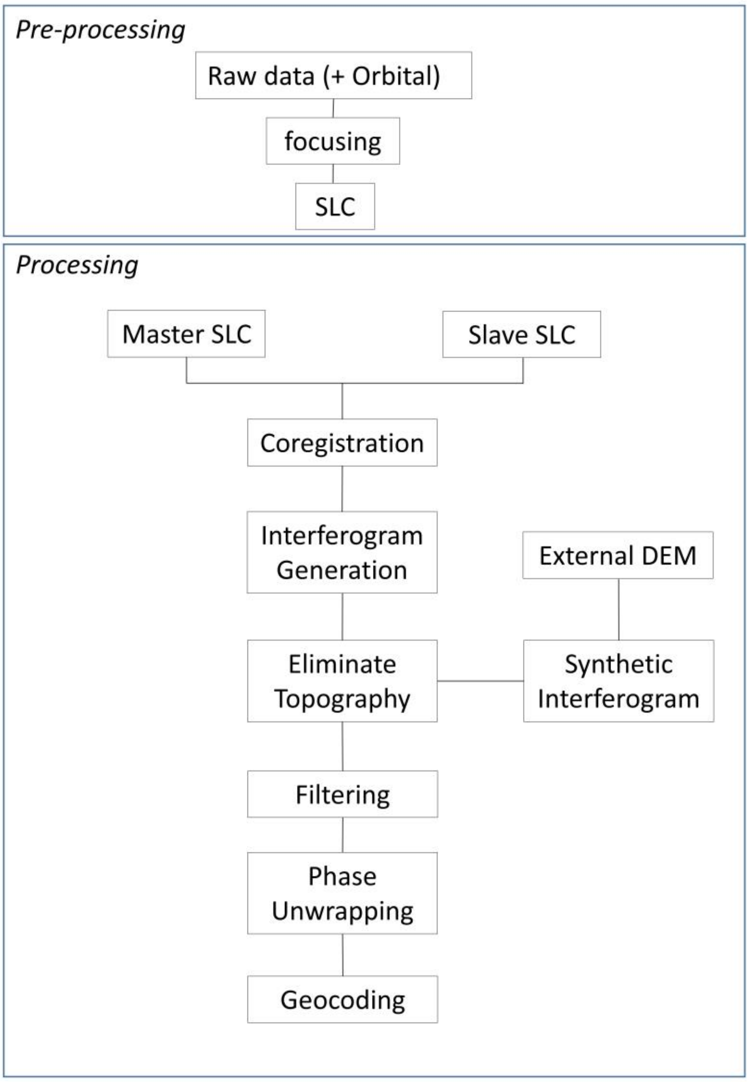

Figure 2.7 Chart showing the standard Differential InSAR processing chain for measuring surface deformation.

An example of the steps of the processing procedure, is presented below (Fig. 2.8). The presented deformation pattern is from the Philippines earthquake, that struck the Island of Leyte on the 6th of July 2017 (Mw 6.5).

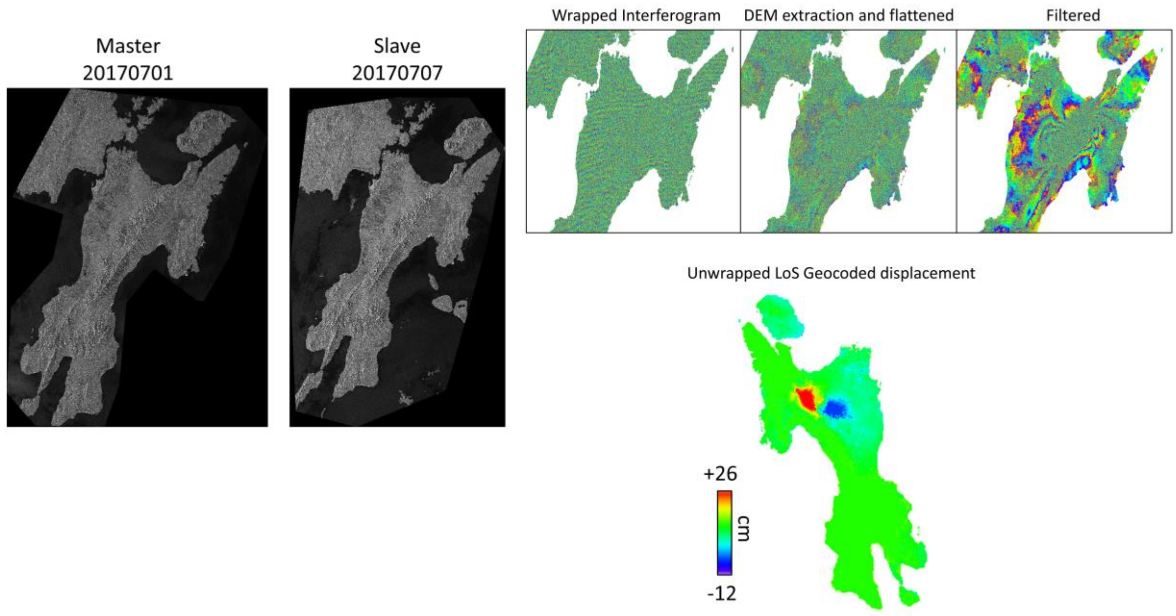

Figure 2.8 Interferometric processing steps of the Philippines 2017 earthquake.

Among the limitations of conventional interferometry is sometimes the existence of atmospheric signal that affects the result of the displacement pattern. There are methods as previously mentioned for estimating and eliminating the atmospheric delays but this task is not always easy. In addition, another potential problem that might arise, are problems in the unwrapping procedure. Among the most important limitations is a potential low coherence of the interferometric pair. It should be mentioned that for the estimation of surface deformation, it is desired ideally to have a small normal baseline. A large normal baseline, would result in low coherence (e.g. Fig. 2.9). The same is when there is a long temporal baseline. Moreover, the lack of backscattered signal in areas covered with water is the reason why we cannot have satellite deformation studies over seas or lakes, which is one of the main limitations of InSAR that also can diminish the signal's ability to be further exploited for post-processing (geophysical modelling). The need for the reduction of the temporal decorrelation has led to the invention of the advanced InSAR techniques known as Multi-Temporal InSAR (MT-InsAR).

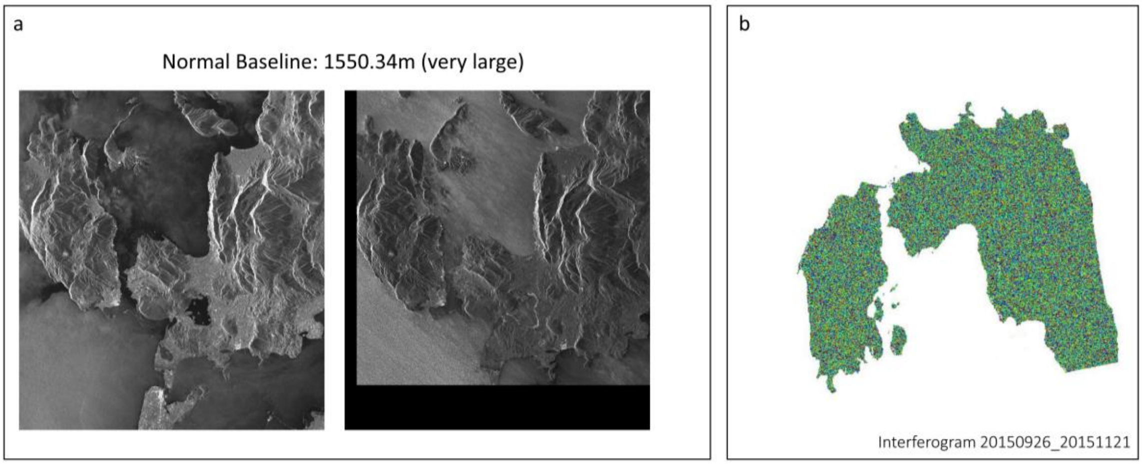

Figure 2.9 Example of a low coherence interferometric result, a) SLC images (in radar coordinates) having a high value of normal baseline (~ 1.5km), b) Differential Interferogram of the two images where, as expected, there is major loss of coherence.

2.3 MULTI-TEMPORAL INSAR

Conventional DInSAR is a powerful tool to measure ground deformation between two satellite acquisitions. Permanent Scatter Interferometry (PS) and Small Baseline Subset (SBAS), are advanced time-series techniques in the family of Multitemporal InSAR (MT-InSAR). MT-InSAR uses a series of SAR images that enables the surface monitoring during large time-windows. This would not be feasible with classical DInSAR mainly due to the decorrelation of the SLC images (Zebker and Villasenor, 1992). The result of SAR time-series is a velocity map of surface deformation and the relative displacement time series. These techniques have significantly contributed to the study of slow deforming areas.

The PS technique is ideal for infrastructure monitoring. The basic idea is the identification of scattering elements of the ground that do not change a lot over time (i.e. they have stable radiometric characteristics). There are algorithms that use the amplitude variation as a criterion to identify these scatterers (the Persistent Scatterers Candidates – PSC). In case the same amount of noise is put on a scatterer with high amplitude and on a scatterer with low amplitude, the first one will have a smaller phase change (Fig. 2.10). There are approaches estimate the amplitude dispersion value (Ferretti et al. 2001):

$$D = \frac{\sigma}{\mu} \tag{2.10}$$

where σ is the standard deviation and μ is the mean of amplitude values (Ferretti et al. 2001).

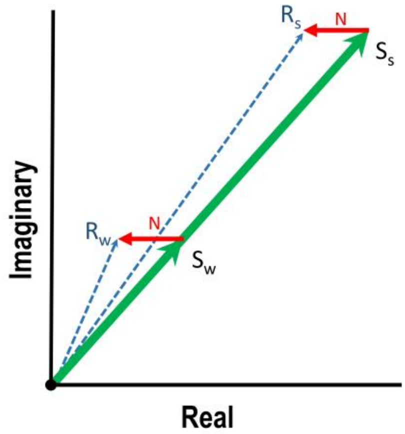

Figure 2.10 When the same noise N is applied to a strong Ss and a weak Sw signal the phase angle of the resulting vector Rw of the latter, has a larger change (reproduced from Osmanoğlu et al. 2016).

In the PS technique, among the entire radar dataset one image is chosen as the master; all the other images are considered as slaves. The optimum master image is the one that maximizes the expected coherence regarding Doppler, Perpendicular, Temporal baselines (Hooper et al. 2007). The master-slave combinations are the interferograms to be formed (Fig. 2.11).

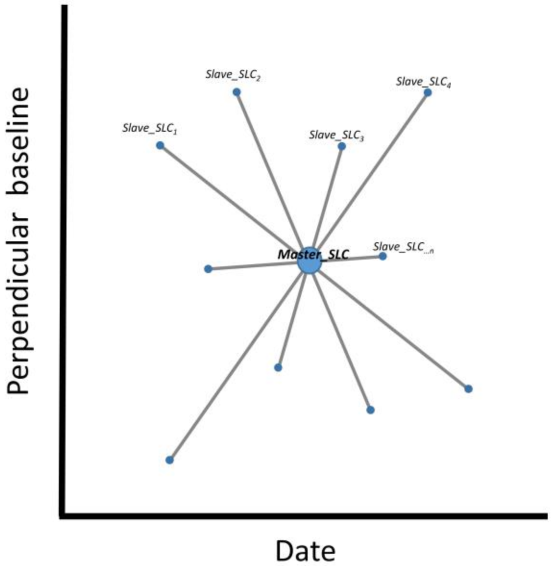

Figure 2.11 Sketch of an SLC network during PS processing. One image is defined as master and all the rest as slaves.

The definition of the Persistent Scatterers Candidates (PSC) is an important step and thus after the creation of the interferograms, the points that have a dispersion value below a specific threshold (e.g. 0.25, Osmanoğlu et al. 2016) are chosen as PSCs. Then there is a DEM subtraction and an estimation of the residual DEM and the removal of the atmospheric phase screen (APS). Methods like these are ideal for finding the deformation velocities of urban areas because structures like fences, buildings, infrastructure etc. have stable scattering characteristics and can be easily considered as PSC.

In case there is an absence of anthropogenic structures, the criterion of an amplitude dispersion alone could lead to have a restricted number of velocity data points. Another approach was proposed by Hooper et al. 2004, 2007 (implemented in the StaMPS code) where the identification of PSC is achieved considering mainly the stable phase characteristics in time and space rather than a strict amplitude dispersion criterion alone (Osmanoğlu et al. 2016). The values of a specific pixel is the sum of the returns from the different scatterers located on the earth's surface. In case there is a change at the position of these scatterers, the return phase of the specific pixel will be changed. This is the case in low signal-to-noise scatterers (e.g. in cultivated vegetated areas for example).

However, if within a pixel there is a dominant scatterer (persistened scatterer pixel), the returns of the phases are going to cause a smaller variability to the overall phase value in a way that the decorrelation can be avoided and thus information on the displacement can be found (Hooper et al. 2007) (Fig. 2.12).

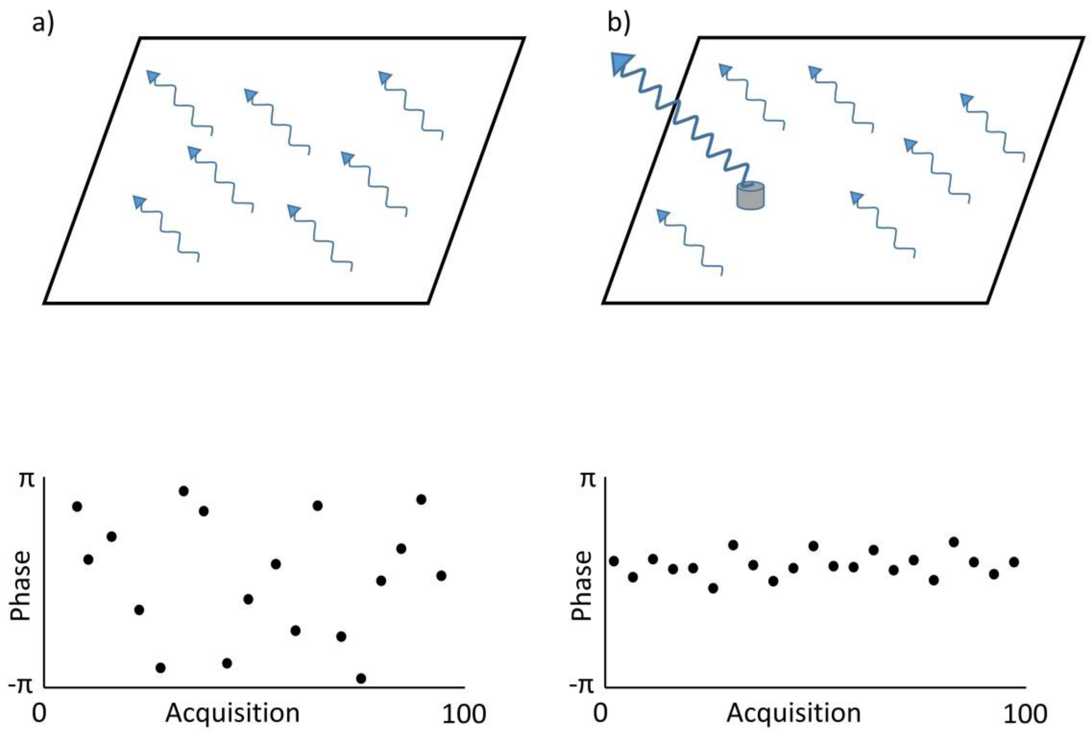

Figure 2.12 Sketch depicting a simulation of the InSAR phase for multiple iterations over: a) a distributed scatterer pixel, where there is a phase dispersion and b) a pixel where there is a dominant scatterer that contributes to a more stable backscattered phase signal. The latter case is a persistent scatterer pixel (reproduced from Hooper et al. 2007).

A potential dominant scatterer could be a tree trunk or a large rock. Thus, in the case of Persistent Scatterers at first, there is the investigation of the amplitude characteristics and then the phase characteristics are taken into account. Hence, the residual phase ϑ in the *ith* differential interferogram of the x-th pixel is:

$$\vartheta_{x,i} = \vartheta_{topo\ x,i} + \vartheta_{def\ x,i} + \vartheta_{atm,\ x,i} + \vartheta_{orb\ x,i} + \vartheta_{noise\ x,i} \qquad (2.11)$$

where $\vartheta_{\text{topo x,i}}$ is the residual topographic phase resulting from DEM errors, $\vartheta_{\text{def x,i}}$ is the movement of the pixel in LoS, ϑatm, x,i is the phase resulting from the differences of the two atmospheric delays between two passes, $\vartheta_{\text{orb x,i}}$ is phase due to inaccurate orbits and finally $\vartheta_{\text{noise x,i}}$ is the noise which is a result of the variability in scattering, thermal noise, and errors in coregistration. In equation (2.11) it is assumed that $\vartheta_{\text{def x,i}}$, $\vartheta_{\text{atm, x,i}}$ and $\vartheta_{\text{orb x,i}}$ are spatially correlated over an area of a specific length (L) whereas ϑtopo x,i and ϑnoise x,i are spatially uncorrelated with a mean of zero.

A pixel is considered as PS in case when ϑnoise is small enough that it does not obscure the signal (Hooper et al. 2007). The variation of the first four terms of (2.11) dominates the signal imposing a difficulty to understand whether a pixel is a PS directly from the wrapped phase. For this reason, these terms are estimated and subtracted from (2.11). The phase error due to DEM is proportional to the perpendicular component $B\perp$ of the baseline:

$$\vartheta_{\text{topo x,i}} = B_{\perp,\text{ x, i}}\ \mathrm{K} \tag{2.12}$$

where K is the proportionality constant.

As already stated, initially for the PS selection, the amplitude criterion is applied by estimating the amplitude dispersion index where a relatively high threshold value can be adopted (e.g. 0.4). In this way most of the selected pixel candidates are not actual PSs. However, the initial reduction of the candidates is still useful since the final choice is made later based on the phase characteristics.

The average of the phase of the last four norms of equation (2.11) from all the PS candidates within a circular patch with radius L (and having as centre the pixel x) is:

$$\overline{\vartheta_{\text{x,i}}} = \overline{\vartheta_{\text{def x,i}}} + \overline{\vartheta_{\text{atm, x,i}}} + \overline{\vartheta_{\text{orb x,i}}} + \overline{\vartheta_{\text{noise x,i}}} \tag{2.13}$$

where the bar denotes the mean. By subtracting (2.13) from (2.11) it is:

$$\vartheta_{\text{x,i}} - \overline{\vartheta_{\text{x,i}}} = \vartheta_{\text{topo x,i}} + \vartheta_{\text{noise x,i}} - \overline{\vartheta_{\text{noise x,i}}} \tag{2.14}$$

the term ϑtopo x,i is estimated (via the estimation of the proportionality constant K) and subtracted from (2.14), at the same time, the term $\overline{\vartheta_{\text{noise x,i}}}$ is assumed to be small, thus if N is the number of interferograms, the phase stability indicator γx is:

$$\gamma_{\text{x}} = \frac{1}{N}\left|\sum_{i=1}^{N} \vartheta_{\text{x,i}} - \overline{\vartheta_{\text{x,i}}} - \vartheta_{\text{topo x,i}}\right| \tag{2.15}$$

Thus overall, for the phase stability analysis: from each PS candidate the mean of the other local candidates is subtracted, the factor K is estimated and then γ_{x}.

It should be noted that at the beginning of the procedure $\overline{\vartheta_{\text{noise x,i}}}$ is probably not going to be small. This is because most of the PS candidates at this point are dominated by noise. For this reason, at the beginning, the candidates with low γ_{x} are discarded and the mean of every circular patch is re-estimated leading to a smaller $\overline{\vartheta_{\text{noise x,i}}}$ .This iterative procedure ends when $\overline{\vartheta_{\text{noise x,i}}}$ actually becomes negligible which means that γ_{x} is dominated by $\vartheta_{\text{noise x,i}}$. Then based on a threshold value of γ_{x} the PS pixels are selected (Hooper et al. 2004, 2007; Agram, 2010).

Then the phase is unwrapped (Hooper, 2009; Hooper and Zebker, 2007). During this procedure, it is important that the phase difference between neighbouring pixels is less than π. For this reason, a high PS density is desired. The displacement rate is estimated based on the LoS displacement using least squares. The result of the PS time series are velocities in mm/yr.

The decorrelation can also be minimized in case the interferograms to be formed have a small temporal and normal baseline. Thus, another SAR time-series technique is Small Baseline Subset - SBAS (Berardino et al. 2002; Lanari et al. 2004). In this case an SLC network is created considering the minimization of the temporal, perpendicular, Doppler baselines. Instead of a unique master image, a network of master and slave SLC images is generated based on the prementioned criteria (Fig. 2.13). After the definition of the SLC connections, the interferograms are generated. The interferograms are then unwrapped (only for the pixels, showing a coherence value greater than a fixed threshold) and via singular value decomposition method, the time-series results can be estimated (Crosetto et al. 2005). Finally, an atmospheric filtering is applied, which is the extraction of the signal with high spatial and low temporal correlation (Ferretti et al. 2000, 2001).

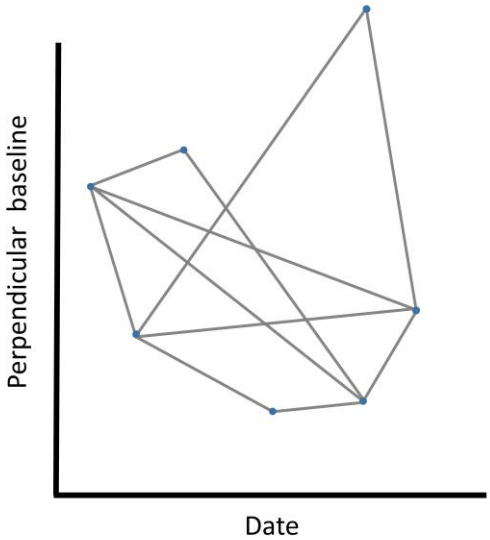

Figure 2.13 Sketch of an SLC network of SBAS processing. During SBAS analysis, there are multiple master and slave images.

In SBAS, multi-looking of the images can potentially takes place (Berardino et al. 2002) because this would increase the Signal-to-Noise ratio. However, there is also the approach of processing all the images in full resolution (Hooper, 2008). In Hooper, 2008 there is the definition of slowly-decorrelating filtered phase pixels (SDFP) which are defined by their phase characteristics. This is achieved by investigating first the amplitude difference dispersion $D_{\Delta A}$:

$$D_{\Delta A}=\sigma_{\Delta A}/\mu_A \tag{2.17}$$

where $\sigma_{\Delta A}$ is the standard deviation of the difference in amplitude between master and slave and μ_A is the mean amplitude. In this way some of the pixels are discarded and then again here (like in the case of PS that was previously mentioned) the phase stability is analised to conclude to the pixels that are SDFPs (Hooper et al. 2007). It is important to note that, even if the method to estimate PSs and SDFPs is the same, potentially different pixels are chosen in each case since in the former case there is no spectral filtering and only a single master image, whereas in SBAS, there are multiple master images together and spectral filtering (Hooper, 2008). After defining the SDFPs the unwrapping of the phases takes place the time-series are estimated using least-squares approach (e.g. Schmidt and Bürgmann, 2003).

Both the techniques of PS and SBAS are computationally more demanding than conventional InSAR. In the StaMPS code, there is also the ability to combine the PS and SBAS results (Hooper et al. 2008), creating a denser spatial coverage that potentially is easier to unwrap. There are differences between the two approaches but of course, these also depend on the codes and software adopted. In general, PS can be used for estimating the velocity of point targets and is an approach that can be efficiently applied for in urban areas (e.g. the city of Thessaloniki in this thesis) or for infrastructure monitoring. On the other hand, SBAS can be used for the analysis of the distributed targets and spatially smooth phenomena; in this thesis, both approaches are used.

Part of the time-series processing was conducted with the StaMPS (Stanford Method for Persistent Scatterers) algorithm (Hooper 2006; Hooper et al. 2007). Prior to the time-series processing with the StaMPS code, the focusing was accomplished with ROI-PAC (Repeat Orbit Interferometry Package) (Rosen et al. 2004), developed by California Institute of Technology and Jet Propulsion Laboratory (NASA), and the interferograms were generated with DORIS (Delft Object-Oriented Radar Interferometric Software) (Kampes et al. 2003). Additionally, SAR time-series were generated also using the commercial software SARscape developed by Sarmap, CH.

2.4 RADAR SATELLITES

2.4.1 Frequency bands of the radar sensors

Radar satellites emit pulses within the microwave region of the spectrum. Currently, the predominant wavelengths for InSAR are the L-band, the C-band and the X-band (Table 2.1).

Table 2-1 Frequencies currently used for radar interferometry.

Band	Frequency (GHz)	Wavelength (cm)
L	1-2	15-30
C	4-8	3.75-7.5
X	8-12.5	2.4-3.75

The frequency heavily affects the information that can be extracted in each case. In general, the longer the wavelength, the longer the penetration (Fig. 2.14).

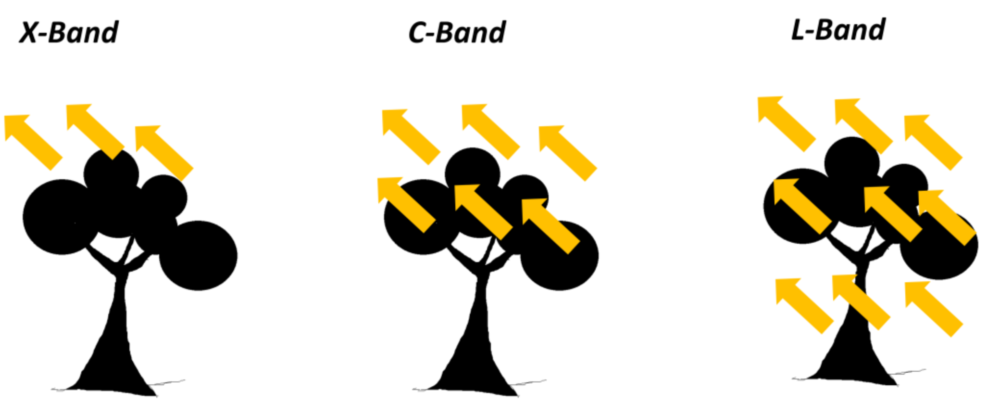

Figure 2.14 Penetration through vegetation when using different frequencies. Except the band adopted, penetration depends also on the moisture of the target.

Several satellites from the different space agencies have been developed over the years and new ones are planned in the future (Fig. 2.15)

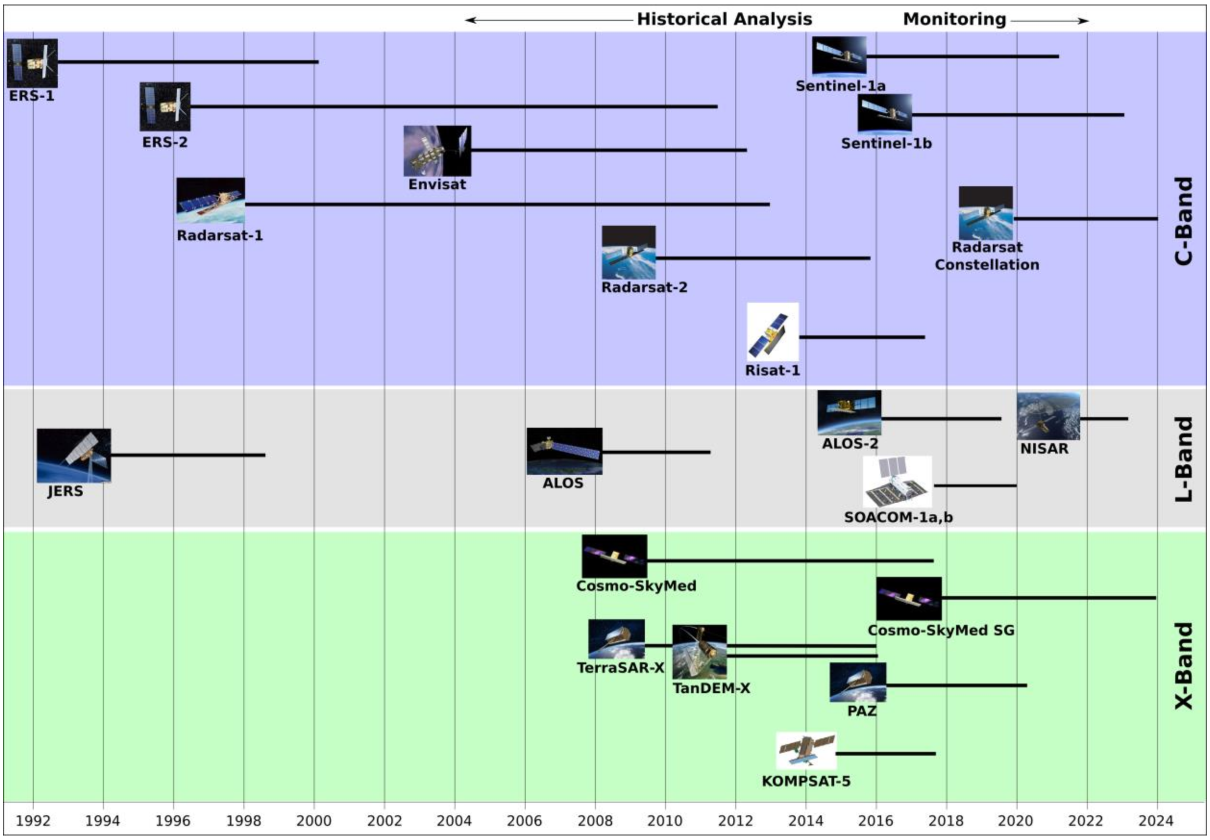

Figure 2.15 Previous, current and planned satellite missions.
European Space Agency (ESA): ERS-1, ERS-2, Envisat, Sentinel-1
Japan Aerospace Exploration Agency (JAXA): JERS-1, ALOS-1, ALOS-2
Canadian Space Agency (CSA): Radarsat-1, Radarsat-2, Radarsat constellation
Deutsches Zentrum für Luft- und Raumfahrt e.V. (DLR): TerraSAR-X, TanDEM-X
Indian Space Research Organization (ISRO): RISAT-1, NISAR (w/ NASA)
Comision Nacional de Actividades Espaciales: SAOCOM
Italian Space Agency (ASI): COSMO-Skymed
Instituto National de Técnica Aeroespacial (INTA): PAZ
Korea Areospace Research Institute (KARI): KOMPSat-5
National Aeronautics and Space Administration (NASA): NISAR (w/ ISRO)
(https://www.unavco.org/instrumentation/geophysical/imaging/sar-satellites/sar-satellites.html).

2.4.2 SAR satellite data exploited

For this thesis, various datasets from different sensors were exploited; below there is a brief description of the satellites.

ERS

In 1991, European Space Agency (ESA) launched the first of the two European Remote Sensing Satellites (ERS) (Fig. 2.16). The project was continued with a second satellite launched in 1995. Both ERS-1 and ERS-2 share similar characteristics both emitting radar pulses in the C-band with a temporal sampling acquisition of 35 days. ERS-2 was designed to have some improvements and additional sensing abilities.

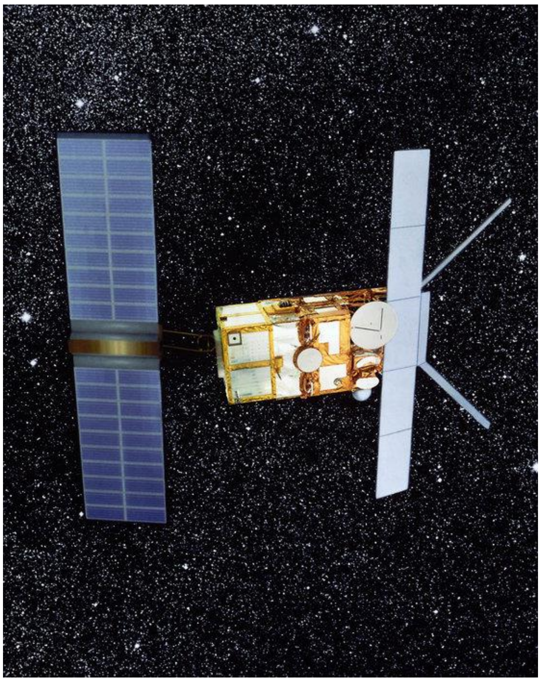

Figure 2.16 The ERS satellite (source: http://www.esa.int/spaceinimages/Images/2000/10/ERS_satellite)

ENVISAT

The continuation of the ERS 1 and 2 monitoring, was achieved with ENVISAT (Fig. 2.17). This ESA mission (C-band) was created to have improved instruments compared to its ancestors. It was launched in 2002 and it was the world's largest civilian satellite. Even though it was expected to last for a longer period, the mission ended in 2012 when there was an unexpected loss of the contact with the satellite. The mission was planned to have the same acquisition time sampling and orbit tracks of the ERS1-2 sensors so to get a near-continuous acquisition temporal span from 1992 to 2010.

Figure 2.17 Representation of the ENVISAT satellite (source: https://earth.esa.int/web/eoportal/satellite-missions/e/envisat)

Hence, regarding SAR interferometry, the ERS-1, ERS-2 and ENVISAT archives is a precious dataset offering about two decades of monitoring; also today part of it is still unexploited. Currently the imagery are free via ESA On-the-fly service.

SENTINEL

The successor of ERS-1, 2 and ENVISAT is ESA's Sentinel 1 constellation, which consists of two satellites (Sentinel-1 A & B). The activity of Sentinel 1 is within the European Union's Earth Observation program, named Copernicus. Both of the sensors use the C-band; the first of the two satellites (Sentinel 1A) was launched in 2014 and the second (Sentinel 1-B) in 2016 (Fig. 2.18). Among its novelties (like the Terrain Observation with Progressive Scans -TOPS acquisition mode) a great improvement is the short revisit time that the two satellites together can offer. The two-satellite constellation offers a revisit time of ~6 days.

Figure 2.18 The Sentinel 1B satellite (source: https://sentinel.esa.int/web/sentinel/missions/sentinel-1/overview)

The short revisit time are crucial for example in the case of studying seismic events. Moreover, the rich dataset with the high frequency sampling provides opportunities for InSAR products that potentially have higher coherence. Sentinel mission is ideal for operational services and it has changed the practises of data distribution since the imagery is open, free and very easily accessible for everyone. The Sentinel era boosted the scientific research in Earth sciences and some of the new possibilities are investigated in the current thesis.

COSMO-SkyMed

COSMO-SkyMed (COnstellation of small Satellites for Mediterranean basin Observation) is an earth observation system operated by the Italian Space Agency (ASI) and funded by the Italian Ministry of Defence (MoD) and the Italian Ministry of Research (MUR). The first satellite was launched in 2007. The constellation is consisted by 4 satellites and frequency of the sensors is 9.6 GHz (X –band) and both a right and left direction. The 4 days revisiting time of InSAR mode makes the COSMO-skyMed family an important tool for emergency operations that Civil Protection authorities can benefit from.

Radarsat

Radarsat-1 was a commercial satellite launched in 1995 from the Canadian Space Agency (CSA) and was operational until 2013. The satellite was equipped with a C-band system. Radarsat-2 was launched in 2007 and is still being operational for more than 10 years and it has 24 days repeat cycle.

Figure 2.19 Radarsat-2 (source: http://www.asc-csa.gc.ca/eng/satellites/radarsat2/Default.asp)

ALOS

The Japanese Aerospace Exploitation Agency (JAXA) launched in 2006 the Advanced Land Observing Satellite (ALOS) that remained operational for 5 years and had a revisit time of 46 days. Its successor is ALOS-2 (Fig. 2.20) that was launched in 2014 has a revisit time of 14 days and both left and right side capability. The satellite is having on-board L-band sensors, an important feature since L-band is affected less by temporal decorrelation; this is an asset especially in vegetated areas. Moreover, it has the capability to acquired SAR image in the Wide-Swath mode (Scansar) with a footprint of ~350x350 km. This acquisition mode is very useful when studying the ground displacement occurring after large earthquakes (e.g. at subduction zones).

Figure 2.20 ALOS-2 (source: https://directory.eoportal.org/web/eoportal/satellite-missions/a/alos-2)

Chapter.3 GEODETIC MODELLING

3.1 INTRODUCTION

The 1892 earthquake in Tapanuli was the first seismic event to be observed geodetically (Segall, 2010; Bonafede et al. 1992) and this was achieved from triangulation measurements from J. J. A. Müller. This observation showed that the earth deforms in response to seismic events. Since then, the advent of GPS stations and the first publication of InSAR-captured earthquake deformation pattern (Massonnet et al. 1993) led to an increase of interest within the scientific community for the field of earthquake geodesy.

While the measurement of the surface deformation caused by a seismic event is important itself and can offer various geological insights, geophysics focuses more on the interpretation of this measurement and attempts to define the reason that caused it. In the case of an earthquake, by benefiting from static surface displacement data offered by GPS and InSAR, a source that describes the cause of the tectonic activity can be defined.

The new technologies and especially SAR interferometry offered new capabilities for earthquake geodesy. In the past, ground-based methods had to be employed before the occurrence of a seismic activity. This meant that most of this activity globally, would not be feasible to be monitored and studied. No mater its limitations, the high ground resolution and the spatial coverage and the low-cost (compared to GPS), led radar interferometry to be an important tool to look into tectonic processes. Of course, even better results are expected in the future with the combination of the global coverage offered by radar satellites with denser GPS networks that can also offer submarine measurements.

Since a straight observation of the seismic source is not feasible, specific techniques - geophysical inverse theory- are used to find which would be the source that "best" predicts the detected deformation. The source is represented by a model. The latter, is a major simplification of the natural complex processes, that take place in the Earth and it is a-priori assumed to have generated the deformation up to the surface. More specifically, the model describes the connection of the source's (in our case the seismic fault) motions to the surface's motions. The choice of the model is pre-defined. Thus during inversion, the unknown is not the model itself, but its parameters. The comparison of the observed and predicted displacement can lead us to estimate the optimum model parameters to be adopted. Bellow the general approach followed and the applied solving technique are described.

3.2 GENERAL APPROACH

The basic assumption for the geodetic modelling adopted here is that earth has an elastic behaviour, which enables the use of elastic dislocation theory for modelling crustal deformation, caused by earthquakes. Steketee (1958) simplified the elastic equations of the Italian mathematician Volterra to be the first to apply it for modelling deformation due to faulting. It was in 1985 when Yoshimitsu Okada gave explicit solutions of the Steketee's formulas that model surface deformation due to shear and tensile faults in an elastic, homogeneous and isotropic half-space.

The surface displacement data are point measurements derived from the processing of the raw data of either GPS or InSAR. In this thesis, the input used for modelling are the unwrapped interferograms. Since InSAR has a high spatial resolution, the unwrapped interferograms should be downsampled in order to reduce the computational load. There are different ways to sample the InSAR displacement, like quadtree decomposition (e.g. Jónsson et al. 2002), application of algorithms based on resolution (e.g. Lohman et al. 2005) or the creation of a 2D grid (e.g. Atzori et al. 2009). Here, the latter approach was chosen in order to have a control over the total amount of data points that are participating each time in the inversion and also to have a control over the location of the samples; this is an important factor regarding the detail level of the source that can be obtained in the case of slip distribution models (Atzori and Antonioli, 2011). Thus, a dense grid of samples can be established at the area of the displacement and a coarser one at the other parts of the unwrapped interferogram.

The modelling procedure adopted here is consisted of two optimisation problems that are solved in order to define the optimum fault parameters that best describe the detected surface deformation. The first optimisation problem is based on the assumption of a rectangular finite fault model with shear dislocation assuming a uniform slip on it. The second optimisation problem solves for the slip distribution on the fault plane. In the first case, the geometry of the fault is estimated (e.g. the parameters of: strike, dip, rake, slip, fault location, length, depth, width) (Fig. 3.1); this is a non-linear problem since these parameters are non-linearly related to surface displacement. On the contrary, the slip distribution is linearly related with the surface deformation thus for the slip distribution modelling, a linear inversion is applied. In the next section, there is a description of these two types of modelling.

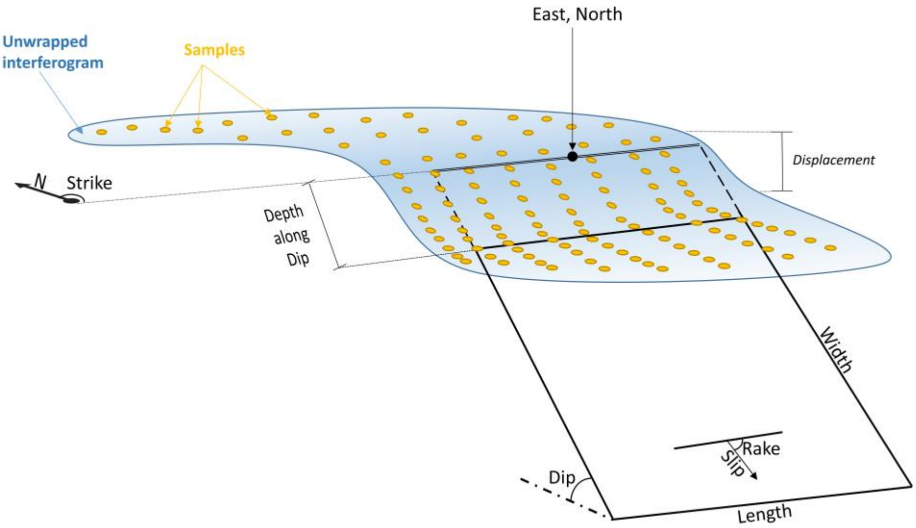

Figure 3.1 Parameters of the fault shown here are the unknowns to be estimated. The input of the modelling are sample points derived from the unwrapped interferograms. The data points d= [d_1 , d_2 , d_3 ,..., d_N]^T are the surface measurements from which we would like to obtain the model parameters m = [m_1 , m_2, m_3 ,...., m_M]^T where d and m are N and M dimensional vectors respectively.

3.3 Non-Linear Inversion

3.3.1 Setting the problem

As stated, the modelling of the geodetic data for the seismic source definition is an optimization procedure. These type of problems might not have a unique answer. Practically the problem to be solved is a system of equations that might not have an exact root. This means that by making updates on an initial guess the parameter values (initial model), we can only obtain the optimum solution.

In order to find the optimum geophysical source model that predicts the observed displacement, Gaussian statistics are assumed for the data themselves and the solution is the one that minimises the cost function between the observed and modelled surface data points. To achieve this, an algorithm is adopted where the values of the fault parameters (the unknowns) are adjusted based on a specific update rule in order to define the global minimum of the cost function.

Here, the algorithm of Levenberg (1944) and Marquardt (1963) is used which is creating at first a random configuration, within predefined value limits, of the source's parameters (initial guess). Then, based on the Okada formulation, a forward model is created and then the misfit between the observed and modelled deformation is checked. During the procedure, parameters are iteratively updated in an attempt to minimise the cost function Φ (i.e. minimise the weighted mean sum of the squares of the errors between observed and modelled data):

$$\Phi = \frac{1}{N}\sum_{i}^{N}\frac{(\mathrm{d_{i,obs}} - \mathrm{d_{i,mod}})^2}{\sigma_i} \tag{3.1}$$

where $\mathrm{d_{i,obs}}$ and $\mathrm{d_{i,mod}}$ the observed and modelled displacements of the i-th data point and σ_i the standard deviation of the N points. To escape from local minima of the cost-function, once a minimum is found, the procedure is repeated again from a random configuration and a solution is considered acceptable (optimum estimate), only in case the same minimum value is found multiple times.

3.3.2 The Levenberg - Marquardt algorithm

Levenberg – Marquardt method is widely used in the scientific community and it is considered a standard tool for solving least squares problems. It is an optimisation method used to find the minimum of a cost function. The actual algorithm is consisted of the separate work of Kenneth Levenberg published in 1944 and an update of it from Donald Marquardt, published in 1963.

The essence of the algorithm is actually a combination of the Gradient descent and the Gauss-Newton methods. The method exploits the contribution that each of the two-optimisation methods have to offer and it choses autonomously to adopt the most appropriate one in each step during the optimisation procedure. The main goal is to have a fast and stable convergence. In the case of Gradient descent, the cost function is minimised by adjusting the model parameters in the direction where there is the greatest reduction. In the case of Gauss-Newton method, there is the assumption that the cost function is locally a parabola. In order to overcome the drawbacks that each of the two techniques has, the Levenberg – Marquardt method acts as a Gradient descent method when during the optimisation we are far from a minimum and when we are close to the optimal value, it acts as the Gauss-Newton method.

Below, a more detailed description of the algorithm is provided. Since, Levenberg – Marquardt is a combination of previously established methods, Gradient descent and Gauss-Newton are also discussed separately.

3.3.3 The Gradient Descent method

As stated, the methods of finding a minimum described here are iterative. Gradient descent algorithm is a first order algorithm, which means that it uses the first order derivative of the cost unction to conclude to a minimum. In general, the most critical difference between the different optimisation methods that are going to be described here, are the criteria with which the parameter values are adjusted to continue to the next iteration and in consequence to the next quality control of the fitting. These changes derive from the update rule that needs to be followed in each iteration. In gradient descent, the general update rule is:

$$m_{i+1} = m_i - \theta \nabla \Phi \tag{3.2}$$

where m_i are the initial parameters, m_{i+1} is the updated parameter configuration, θ is the learning constant, and $\nabla\Phi$ is the gradient of the total error function. Regarding the latter term, it is the 1st–order derivative with respect to all parameters:

$$\nabla\Phi = \frac{\partial\Phi}{\partial Par} = \left[\frac{\partial\Phi}{\partial Par_1} \quad \frac{\partial\Phi}{\partial Par_2} \quad . \quad . \quad \frac{\partial\Phi}{\partial Par_M}\right]^T \tag{3.3}$$

In general, this method can be applied to simple cost functions (Lourakis, 2005). The main issue of this update rule is that when we have a large gradient, we make large steps towards the minimum and when we have a small gradient (gentle slope), we make small steps towards the minimum. Ideally, we would like the opposite for a better convergence.

3.3.4 The Gauss-Newton method

To have an improvement of the predescribed disadvantages, second order information can also be exploited. The Gauss-Newton method approximates the cost function as quadratic at the neighbourhood of the optimal solution (Björk, 1996). If the the cost function would be a parabola, there would be no need to use the Gradient decent method. However, here the cost function potentially has a much more complex form than a simple parabola. Still, close to a minimum, we can linearize the function and approximate it as a Taylor series expansion locally, around m_0 where we can neglect the higher order terms. This will contribute to converge quicker than using Gradient descent.

Around m_0, the function is:

$$\Phi = \nabla\Phi(m_0) + (m - m_0)^T \nabla^2\Phi(m_0) + \dots \text{ higher order terms} \tag{3.4}$$

The update rule is:

$$m_{i+1} = m_i - (\nabla^2\Phi(m_i))^{-1} \nabla\Phi(m_i) \tag{3.5}$$

$\nabla^2\Phi(m_i)$ is the Hessian matrix (H), in order to simplify the calculated process, since we neglected the higher order terms of the Taylor series, we can estimate an approximation of the Hessian (an approximation of the second order derivatives) by exploiting the Jacobian matrix. Thus, in this case the Hessian can be expressed as:

$$\nabla^2\Phi(m_i)=J(m_i)^T J(m_i) \tag{3.6}$$

In this way, the estimation of the second-order derivatives is avoided and a more rapid convergence can be achieved. This can be done only where a linear (or near-linear) approximation of Φ is reasonable and when the residuals are small.

3.3.5 The Levenberg method

As already stated, the quadratic rule assumes a linear approximation and this could be realistic only at the neighbourhood of the minimum. The proposal of Kenneth Levenberg was based on the observation that if the Gradient descent and the Gauss-Newton methods would act complementary, they would offer a better convergence. More specifically, when we are far from the minimum, the Gradient descent method can be used and when we approach the minimum, the quadratic rule of Gauss-Newton comes in handy. Levenberg method actually offers a way to mix the two approaches based each time on an error check that defines the “blending” of the two methods in order to obtain better performance. The update rule here is:

$$m_{i+1} = m_i - (H + \mu I)^{-1} \nabla\Phi(m_i) \tag{3.7}$$

where H is the (approximated) Hessian, μ is the "blending" factor and I is the identity matrix. It can be seen from equation (3.7) that when μ is small (close to zero), we follow a quadratic approximation, whereas when μ is large, the Gradient descent method is applied. The adjustment of the μ factor is dependent of the result of the error check. When the error is increased (from the previous error estimation), we are away from the minimum, thus we increase the μ factor to follow the Gradient descent approach. On the contrary, when the error is decreased, then the quadratic rule is working (we are close to minimum), so the μ factor needs to be decreased (Fig. 3.2). This blending of the two techniques helps to have a rapid convergence to the local minimum (Lourakis, 2005; Madsen et al. 2004; Gavin, 2011).

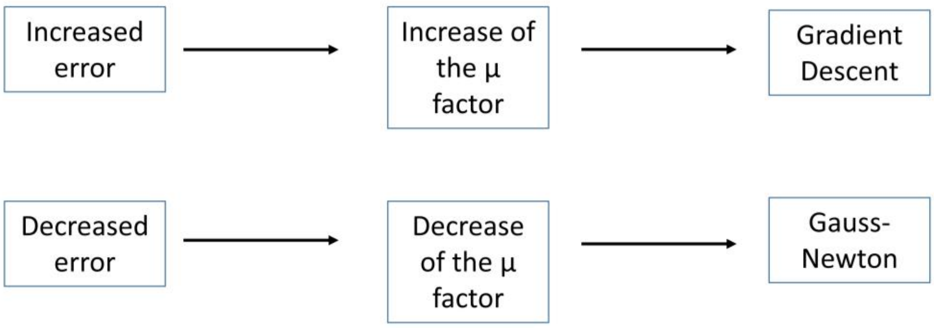

Figure 3.2 Schematic summary of the adjustment criteria followed for the definition of the blending factor, when using the Levenberg method.

3.3.6 Marquardt's modification

In Levenberg's method if μ is large (Gradient descent), then the Hessian is not calculated. Marquardt noticed that there is still a benefit from the Hessian matrix, even in the case the algorithm works in the Gradient descent manner. This would lead to have a larger movement towards the directions that have a smaller gradient. Practically, to do this, Marquardt replaced the identity matrix in the update rule of Levenberg's method with the diagonal of the Hessian:

$$m_{i+1} = m_i - (H + \mu Z)^{-1} \nabla\Phi(m_i) \tag{3.8}$$

where Z is the diagonal of the Hessian. Moreover, this latter update rule is the one adopted in Levenberg-Marquardt algorithm.

Overall, the algorithm's main steps are the following:

1. Estimation of an initial guess of the parameters (random choice within specific value window)

2. Forward modelling using Okada's equations

3. Estimation of Error

4. Application of the Levenberg-Marquardt update rule and definition of a new set of parameters

5. Forward modelling using Okada's equations and estimation of Error

6. If the Error of step 5 is smaller than that of step 3, then the estimated parameter values (from step 4) are accepted and the μ factor is decreased. Then go to step 4 again.

Else

7. If the Error of step 5 is higher than that of step 3, then the estimated parameter values (from step 4) are not adopted and the values are reset to the previous configuration and the μ factor is increased. Then go to step 4 again.

8. Finish the procedure when a maximum of iterations is reached or when the Error becomes smaller than the required value.

One of the issues when training the algorithm is the need to perform matrix inversion while applying the update rule. However, this is no problem for medium sized networks, which perform very well in practise. Additionally, the non-linear least squares might have cost functions with many local minima and falling into one of those (resulting in missing the global one) depends upon the initial guess. Levenberg-Marquardt algorithm itself does not protect us from falling into one of those, however, as previously stated, an implementation of the method with multiple restarts, offers a safe way of defining the global minimum (Fig. 3.3).

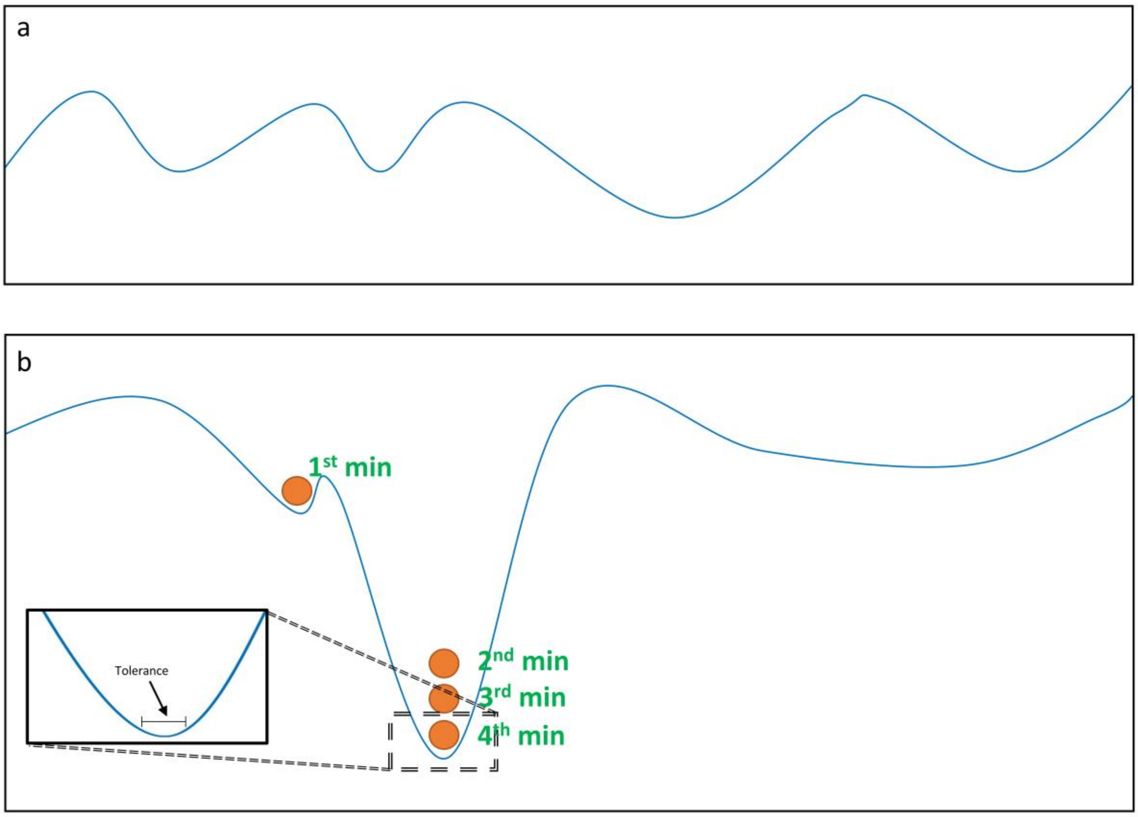

Figure 3.3 Schematic graph that represents two examples of cost functions. a) A non-linear case. Here, the estimation of the extrema is a challenging task. b) In this case the estimation of the minimums is easier. The algorithm is implemented in a way to accept a value as the optimal, when there are multiple equal results for the minimum. The definition of different minimum values as equal is defined based on a tolerance value.

3.4 Linear Inversion

After the definition of the fault's geometric parameters, the on-fault dislocation can be estimated. The uniform slip solution is extended to let the slip vanish to zero and it is divided to subpatches. Now the unknowns are the slip values of each subpatch. As stated, the slip is depended linearly to the surface displacement. The relation of the model parameters (the unknowns) with the surface data point d can be expressed analytically with the following system of equations:

$$\begin{bmatrix} d_1 \\ d_2 \\ d_3 \\ . \\ . \\ . \\ . \\ . \\ . \\ d_N \end{bmatrix} = \begin{bmatrix} G_{11} & G_{12} & G_{13} & \cdots & G_{1M} \\ G_{21} & . & . & \cdots & . \\ G_{31} & . & . & \cdots & . \\ . & . & . & \cdots & . \\ . & . & . & \cdots & . \\ . & . & . & \cdots & . \\ . & . & . & \cdots & . \\ . & . & . & \cdots & . \\ . & . & . & \cdots & . \\ G_{N1} & G_{N2} & G_{N3} & \cdots & G_{NM} \end{bmatrix} \begin{bmatrix} m_1 \\ m_2 \\ m_3 \\ m_4 \\ m_5 \\ . \\ . \\ . \\ m_M \end{bmatrix} \tag{3.9}$$

or

$$d_{\text{obs}} = Gm \tag{3.10}$$

where $d$obs are the observed data, G are the Green's functions and m are the parameters to be found (unknowns). Since the observations are usually much more than the number of unknowns, the system is over-determined and its solution in a least-squares sense is:

$$m = [G^{T}G]^{-1}G^{T}d \tag{3.11}$$

However, the patches located at larger depths are less constrained. This is because InSAR is a surface measurement and therefore have a weak control over deep parameters. The use of (3.10) and (3.11) as if they are, would cause a high scattering among the slip values (Atzori and Salvi, 2014). The result might be mathematically correct and a good fit might be achievable, but it would lack the physical meaning. For this reason, a modification of (3.11) would be useful. An extension of the system by adding in the Green's functions matrix an underdetermined part allows the estimation of a more reliable solution:

$$\begin{bmatrix} d_{\mathrm{obs}} \\ 0 \end{bmatrix} = \begin{bmatrix} G \\ \varepsilon\, \nabla^2 \end{bmatrix} m \tag{3.12}$$

In the above equation, ∇^2 is a Laplacian operator and ε is the damping factor. The slip on the fault varies along strike (x) and down-dip (y) thus in our case, the Laplacian operator is defined as:

$$\nabla^2 = \frac{\partial}{\partial x^2} + \frac{\partial}{\partial y^2} \tag{3.13}$$

More specifically, for each patch i, the Laplacian operator is the scalar (Jónsson et al. 2002):

$$l_{\mathrm{i}} = \frac{S_{\mathrm{i-1,j}} - 2S_{\mathrm{i,j}} + S_{\mathrm{i+1,j}}}{(\Delta l_1)^2} + \frac{S_{\mathrm{i,j-1}} - 2S_{\mathrm{i,j}} + S_{\mathrm{i,j+1}}}{(\Delta l_2)^2} \tag{3.14}$$

Where $S_{\mathrm{i,j}}$ is the value of slip of the patch in the ith row and jth column of the fault (Fig. 3.4) and Δl_1 and Δl_2 are distances between adjacent patches.

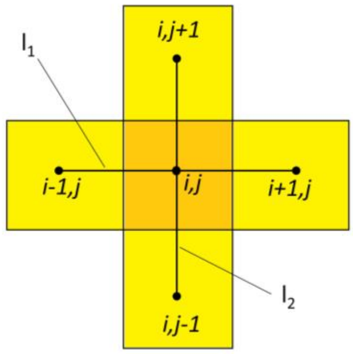

Figure 3.4 The finite-different sum method as presented in equation (3.14). The central patch is smoothed over the side patches.

The damping factor ε in equation (3.12), practically tunes the smoothing. In the case of the earthquake slip distributions, the higher the damping, the more gently the slip values vary over the fault's surface. At the same time, the fitting decreases as damping increases. The best possible fit of a fault model could be achieved using a zero damping; but the results, though mathematically correct, would be geologically non-realistic. Thus, an optimum damping value needs to be adopted. There is a wide literature about the ways to choose the damping factor (fit/roughness curves, minimum seismic moment, etc.), the practise adopted here is via trial-and-error in order to select the damping value with the criterion of obtaining the best compromise between best data fit and fault reliability according to the resulting slip distribution and peak slip values. The estimation of an optimum-damping factor allows avoiding the overfitting of noisy data (Maerten et al. 2005). Additionally, during the procedure of linear inversion, a non-negative condition is added to avoid backslip.

3.5 UNCERTAINTY

Various sources of uncertainty can affect the InSAR data (e.g. Hanssen, 2001; Goldstein, 1995). Important sources of error are for example the atmospheric signals that vary smoothly and create spatially correlated errors (Sudhaus and Jónsson, 2008). Knowing the quality of the input data helps to the estimation of the seismic model parameters.

In the case of non-linear inversion, the uncertainty propagation is a not a straightforward task, thus an empirical approach can be used. At first, the variance/covariance matrix [cov d] of data can be created. This can be achieved by analysing the autocorrelation function of part of the interferogram that contains only noise (and no displacement) and fitting a function like (3.15) (e.g. Parsons et al. 2006) to a covariance vs distance scatter plot.

$$C(r) = \sigma^2 e^{-ar} \tag{3.15}$$

where $\sigma^2$is the variance the distance r is the distance of the observations and α expresses how fast the correlation decreases with distance.

After the estimation of the variance/covariance of the data [cov d], synthetic noise datasets can be generated with the following formula:

$$d_{\text{noise}} = Ld_{\text{Gauss}} \tag{3.16}$$

where L is the matrix derived from the Cholesky decomposition of $[\text{cov d}] = LL^{\text{T}}$.

Thus, the estimation of the source model uncertainties can be achieved by adding this realistic noise (e.g. Funning et al. 2005 among others) to the observed interferograms and then the non-linear inversion is again performed starting this time from the optimum parameter configuration, previously estimated. In this way, we can "propagate" the uncertainties of the input data, to the model uncertainties (Wright et al. 2003; Sudhaus and Jónsson, 2009)

This procedure should be repeated tens or hundreds of times in order to collect enough amount of results that can represent the uncertainties and the trade-offs of the parameters. Obviously in the case of a strong signal, we expect low uncertainties, on the contrary very low-signal interferograms might not enable a well-constrained solution (Fig. 3.5). It often happens to have trade-offs between coupled parameters (i.e. the parameters cannot be, independently, estimated) (Fig. 3.6). Representations of the uncertainties of each parameter can be shown with histograms and scattered plots.

In the case of linear inversion, normal rules of the error propagation can be applied. Thus after estimating the [cov d], the equation (3.17) can be applied, to obtain [cov m] which is the variance-covariance matrix of the model parameters (in this case the slip).

$$[cov\ m] = G^{-g}[covd]G^{-gT} \tag{3.17}$$

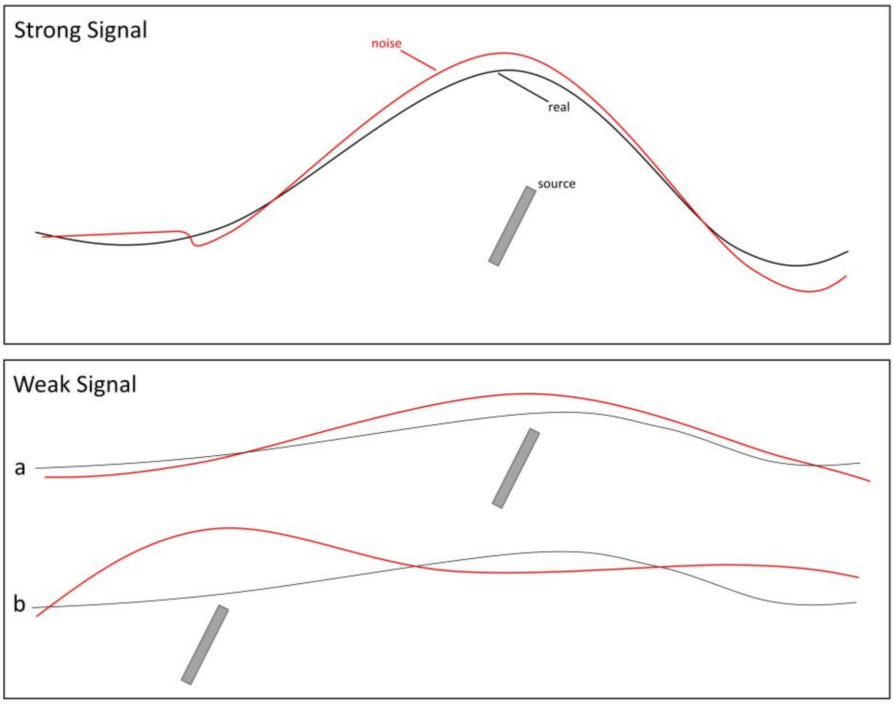

Figure 3.5 Behaviour of source parameters with respect to the quality of the signal. Black lines note the "real" signal and the red lines, the noisy. In the upper panel, where the signal is strong, the addition of noise has a small impact on the definition of the source providing a solution with low uncertainty. In the lower panel, the deformation signal is low enough that each time the noise changes, there is also a consequent change in the source's parameters (e.g. here the source's position, in cases a) and b). The signal of the lower panel, will provide a source solution with a higher uncertainty.

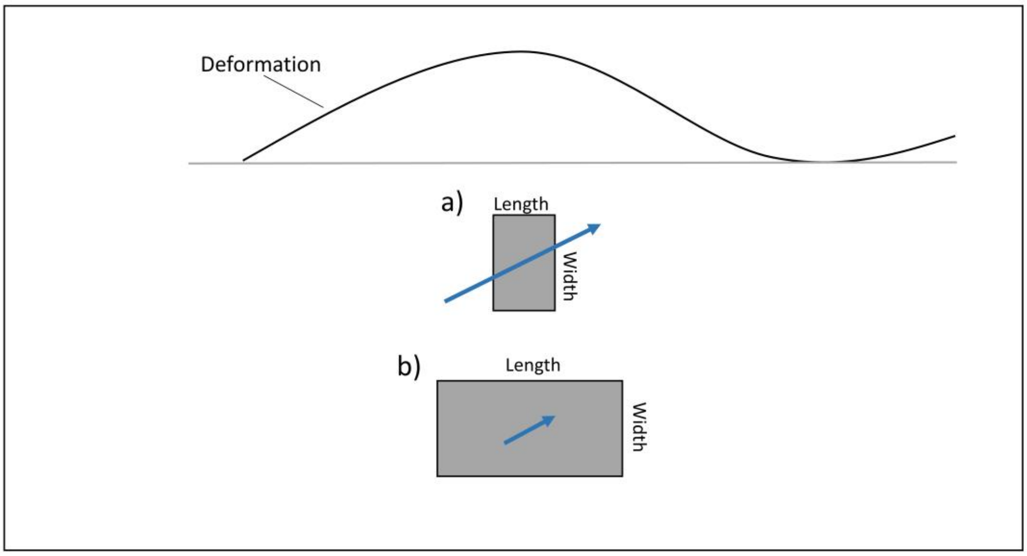

Figure 3.6 Figure representing a case where the length of the source is having a trade-off with the slip. Grey rectangles represent a slip source. The length of the blue arrows indicate the amount of slip. The observed deformation signal (black line) can be equally predicted by both the two models.

Chapter.4 ANTHROPOGENIC DRIVEN DEFORMATION

4.1 THE EXAMPLE OF KALOCHORI

4.1.1 Introduction

Groundwater level variation can have an impact on the surface deformation (e.g. Galloway et al. 1998; Ikehara and Phillips, 1994) and InSAR techniques have been among the tools successfully applied for the study of deformation, due to the activity of aquifer systems (e.g. Amelung et al. 1999; Bell et al. 2008; Galloway and Hoffmann, 2007; Galloway et al. 1998; Zhong and Danskin, 2001). Worldwide, numerous studies have highlighted the occurrence of subsidence due to groundwater overpumping (e.g. Phien-wej et al. 2006; Raspini et al. 2013; Taniguchi et al. 2009). Uplifting deformation due to natural rebound has been reported for example in the work of Chen et al. (2007) in Metropolitan Taipei Basin or Ishitsuka et al. (2014) at the Bangkok plain, who reported the phenomenon at a previously subsided site.

The urban expansion and the economic activities related with everyday life, affect the natural evolution of the landscape and the physical processes. In Greece, this interaction is pronounced in Kalochori and Sindos, two sites that are strongly related to industrial activities, which are in turn related to the metropolitan city of Thessaloniki (Fig. 4.1). At these sites, a subsiding trend was first detected in the 1960s and was highlighted from studies using ground truth techniques (Andronopoulos et al. 1990; Doukas et al. 2004; Hatzinakos et al. 1990; Loupasakis and Rozos, 2009; Rozos and Hatzinakos, 1993; Stiros, 2001). It was after 2000 and the advent of satellite technology that boosted more detailed studies (Costantini et al. 2016; Mouratidis et al. 2009; Psimoulis et al. 2007; Raspini et al. 2014; Raucoules et al. 2008). ERS 1, 2 data from the '90s successfully verified the subsidence phenomena adding new information on their distribution and deformation rate. A change in the sense of motion, was first identified by Svigkas et al. (2015) where a preliminary ENVISAT SAR data analysis showed that, for the post 2000 period up to 2010, the area was being under an uplifting trend. GNSS studies performed by Ganas et al. (2016), spanning 2013-2015, shown a mixed uplift and subsidence pattern for Kalochori.

4.1.2 Deformation History at the Area of Study

Kalochori and Sindos are located at Thessaloniki plain, which extends at the western part of Thessaloniki city. The Thessaloniki plain, the largest deltaic plain in Greece (~2000 km2), is surrounded by mount Vermio (~2,100 m) and Pieria hill from the south and mount Paiko (1600m) from the north (Fig. 4.1). The plain is crossed by the rivers Axios, Loudias and Aliakmon, which constitute an important geomorphological factor that formed the site as it is today. The area of Kalochori and Sindos used to be a delta, some thousands years ago (Psimoulis et al. 2007). Numerous archaeological discoveries, like the remains of the ancient port of Pella (Petsas, 1978), which was a harbour at the times of Alexander the Great, give insights about the continuously changing geomorphology. During the years, the human factor had the key-role for the evolution of morphology at this particular plain (Sivignon, 1987). Indicative examples of human intervention at the plain, since the ancient times, would include: diversion and alignment of rivers, the development of an irrigation network, construction of dams, overpumping of the underwater aquifers (Kapsimalis et al. 2005). The formation of the basin bearing the present morphological features was the result of the intense active tectonics of the Upper Pleistocene (Syrides, 1990).

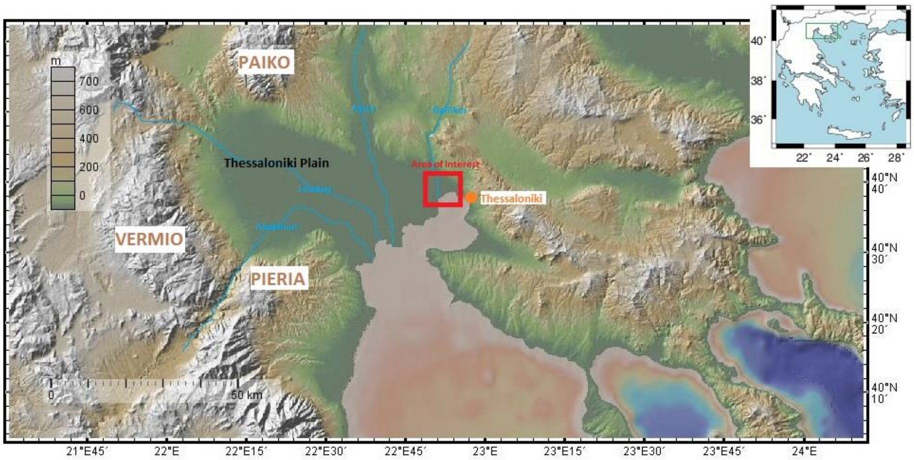

Figure 4.1 The areas of Kalochori and Sindos is denoted with the red rectangle. The upper right inset is the area shown at the main map with respect to Greece (Svigkas et al. 2016).

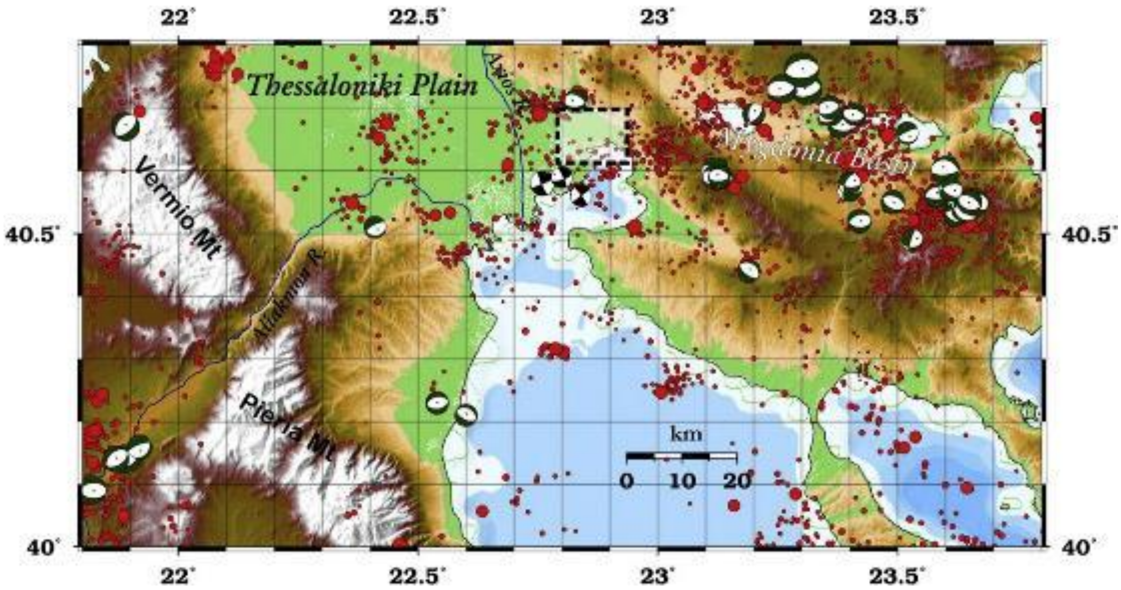

Figure 4.2 Seismicity (1980-2016). Most of the modern seismicity is occurring within the Mygdonia Basin. Events with Mw>4 are depicted with beachballs. The current stress regime indicates a ~N-S extension. Dashed rectangle denotes the area of study (Svigkas et al. 2016).

The broader area is seismologically active (Paradisopoulou et al. 2006, 2016; Gkarlaouni et al. 2015). The modern seismicity and the tectonic activity in the broader region is summarized in Figure 4.2. The focal mechanisms (beach-balls) of the stronger earthquakes (Mw> 4), depicted in the figure, show that they are mainly located in the Mygdonian basin, and are all connected with normal faulting. The present day stress field in the broader region suggests approximately N-S extension, in accordance with the E-W strike of major active structures (Kiratzi, 2014 and references therein). The region under study (dashed rectangle) is related with sparse microseismicity and the available focal mechanisms for a moderate sequence, which occurred in 2012 close to region, indicate strike-slip motions along NE-SW trending planes.

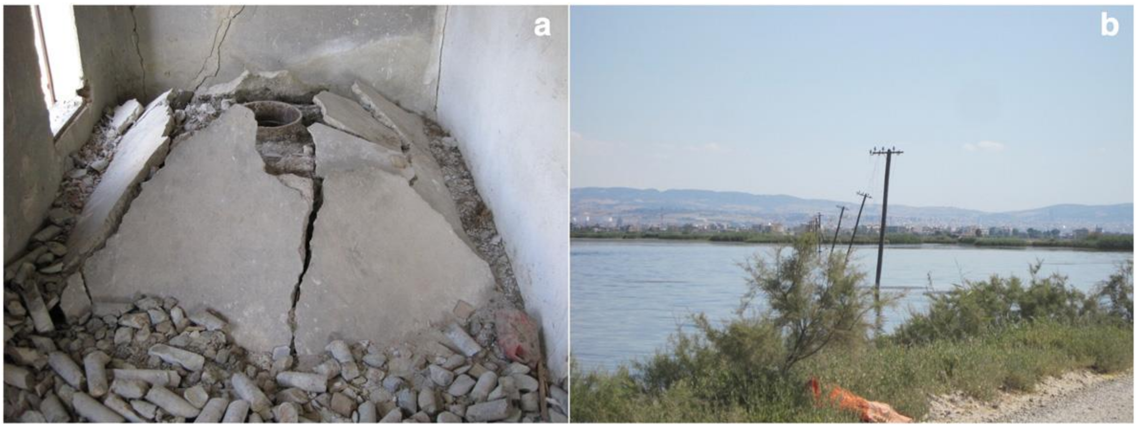

Figure 4.3 Failures at the areas of Kalochori. a) Pipe upheaval and b) damage at the electricity network.

At coastal areas, the phenomenon of subsidence can remarkably raise the risk of flooding. Delta municipality (where Kalochori and Sindos belong to) is just a few meters above the sea level and the coastal front of Kalochori lies below it. In 1964, there was the first detection of subsidence in the form of seawater invasion. In 1965, an intensive rainfall took place, causing seawater inundation threatening the houses located at the southern part of Kalochori. As a countermeasure, in 1969 the government built the first embankment to protect the area from the sea. Unfortunately, this construction had frequently suffered severe failures.

All the efforts aiming to reinforce the embankment were in vein. The first collapse occurred four years after its construction and a new construction was built in 1976. However, before the end of the 1970s, it was destroyed. The need for the protection of the coastal area, led the government to take more measures against the hazard and thus in 1980 a larger embankment (the one that still stands today) was constructed that was considered to be more suitable to face the wave loadings and the subsidence deformations. This manmade sea-barrier isolated an area of land, turning it into a lagoon. In order to avoid new flood phenomena, pumping stations were widely used during wet seasons. The continuous subsidence has caused significant damage, as for example water well pipe protrusion, farmland flooding and loss of infrastructures (Fig. 4.3).

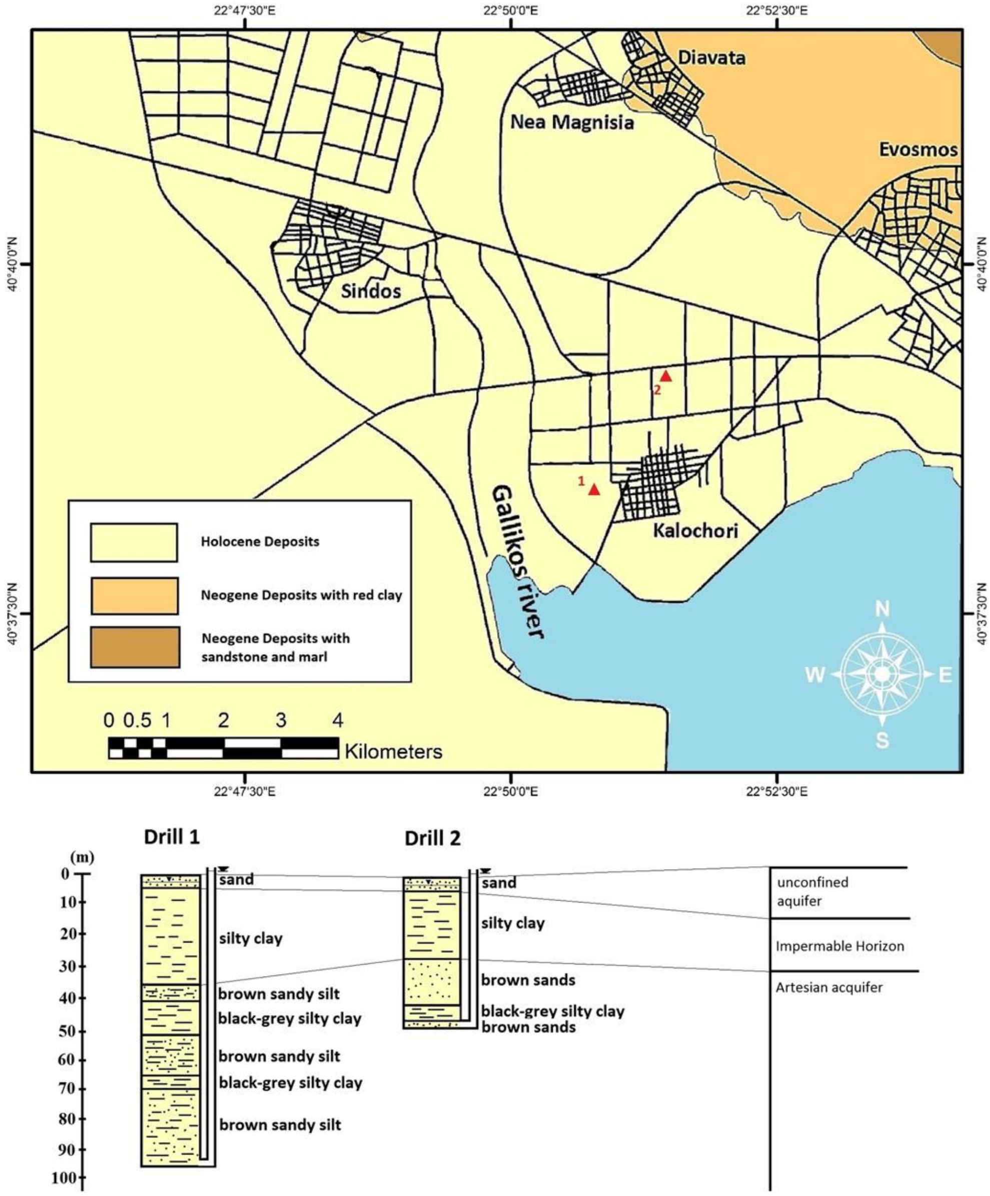

Figure 4.4 Geological map of the area (modified after IGME, 1978 and Raspini et al. 2014). With red triangles, two drills are denoted. Bellow the map the Drills` logs and the aquifers succession are presented Drill loggings are from Andronopoulos et al. (1990). (From Svigkas et al. 2016).

At this point, it should be noted that at the entire study area neither surface ruptures nor strong differential displacements have been reported, despite the intensity of the land subsidence phenomena. This phenomenon is unique, at least in Greece, and it can only be attributed to the absence of faults intersecting the top layers within the narrow limits of the study area. It is a fact that the faults' offset create intense variations at the thickness of the compressible formations leading to the manifestation of differential displacements in case of ground water drawdown (Loupasakis et al. 2014). The aforementioned hazardous facts have invoked a rising interest among the scientists to elucidate the driver mechanism, and various ideas were discussed about the nature of the subsidence.

The Kalochori and Sindos sites have been studied using ground truth, levelling, GPS and InSAR techniques (e.g. Costantini et al. 2016; Doukas et al. 2004; Mouratidis et al. 2009; Psimoulis et al., 2007; Raspini et al. 2014; Raucoules et al. 2008; Stiros, 2001). The consensus amongst scientists was that the detected subsidence is mainly attributed to the excessive ground water pumping (Andronopoulos et al. 1990; Hatzinakos et al. 1990; Loupasakis and Rozos, 2009; Raspini et al. 2014; Rozos and Hatzinakos, 1993) while additional deformations due to natural compaction of loose Quaternary deposits cannot be excluded (Psimoulis et al. 2007). Several other scenarios have also been proposed. For example, Doukakis (2005) linked the deformation to the effects of the caused coastal erosion and sea level rise due to climate change. A more geotechnical approach included coastal flowing sand phenomenon and the consolidation of the loose silty-clay deposits (Dimopoulos, 2005). Stiros (2001), attributed the detected subsidence to the cumulative effect of a piezometric surface decline, the oxidation of peat soils in the vadose zone, the synsedimentary deformation of the delta, the consolidation of the deeper sediments (as a result of the upper strata loading) and the consolidation of near surface sediments.

4.1.3 Geological and hydrogeological setting

The wider, Sindos and Kalochori areas founded over Quaternary deposits. Sands, clays and silty clays are the main contents of these deposits (Hatzinakos et al. 1990; Rozos et al. 2000) (Fig. 4.4). North and northeastern of the study area there are sandstones, and red clays, contents of the Neogene basement outcrop. Their depth underneath Kalochori is known to be at 700 m (Demiris, 1988). The upper strata of the Quaternary formations, down to a depth of at least 200 m, can be divided in three horizons. According to Rozos et al. (2000) the order is: a) a sandy horizon, b) an impermeable silty clay layer and c) alternating layers of coarse and fine sediments. The upper horizon consists of yellow-brown fine to medium grain sands with silty bands intercalations. At a depth of 25 to 35 m, at the Kalochori region, and a few meters shallower at the wider Sindos area, lies the underlying impermeable silty clays horizon. Finally, the deeper horizon consists of alternating brown sands and black-grey silty sands (Loupasakis and Rozos, 2010). The uppermost sandy horizon hosts a shallow unconfined aquifer. This shallow aquifer contains very poor quality water, has an upper level of 1.3 m and a lower level of 3 m. The thickness of this underground water body is 10 to 15m. Below the silty clay impermeable horizon, lies an artesian aquifers system with good water quality, hosted inside the alternating layers.

4.1.4 History of the water level changes

Back in the 1950s at the study area, the lower aquifer system was artesian. On the contrary, that was not the case for the next decades, which were characterized by a continuous lowering of the piezometric surface of the deeper aquifer (Raspini et al. 2014). At the wider area of Kalochori and Sindos more than 400 deep wells were extracted (Soulios, 1999) and except those of the Water Supply Company, the vast majority of the rest were unauthorized high consumption industrial drills. The lowering of the piezometric surface was more intense since the early 1980s where many deep drills had already been active and the decrease of the confined aquifer's level was lowered down to 40 m (Andronopoulos et al. 1990).

On the contrary, piezometry of the upper unconfined aquifer has not been subjected to any change. This is because the water quality of the upper aquifer is low leading to its light exploitation. Furthermore, the intense cultivation of rice at the majority of the farmlands of the area kept this aquifer to a continuous recharge.

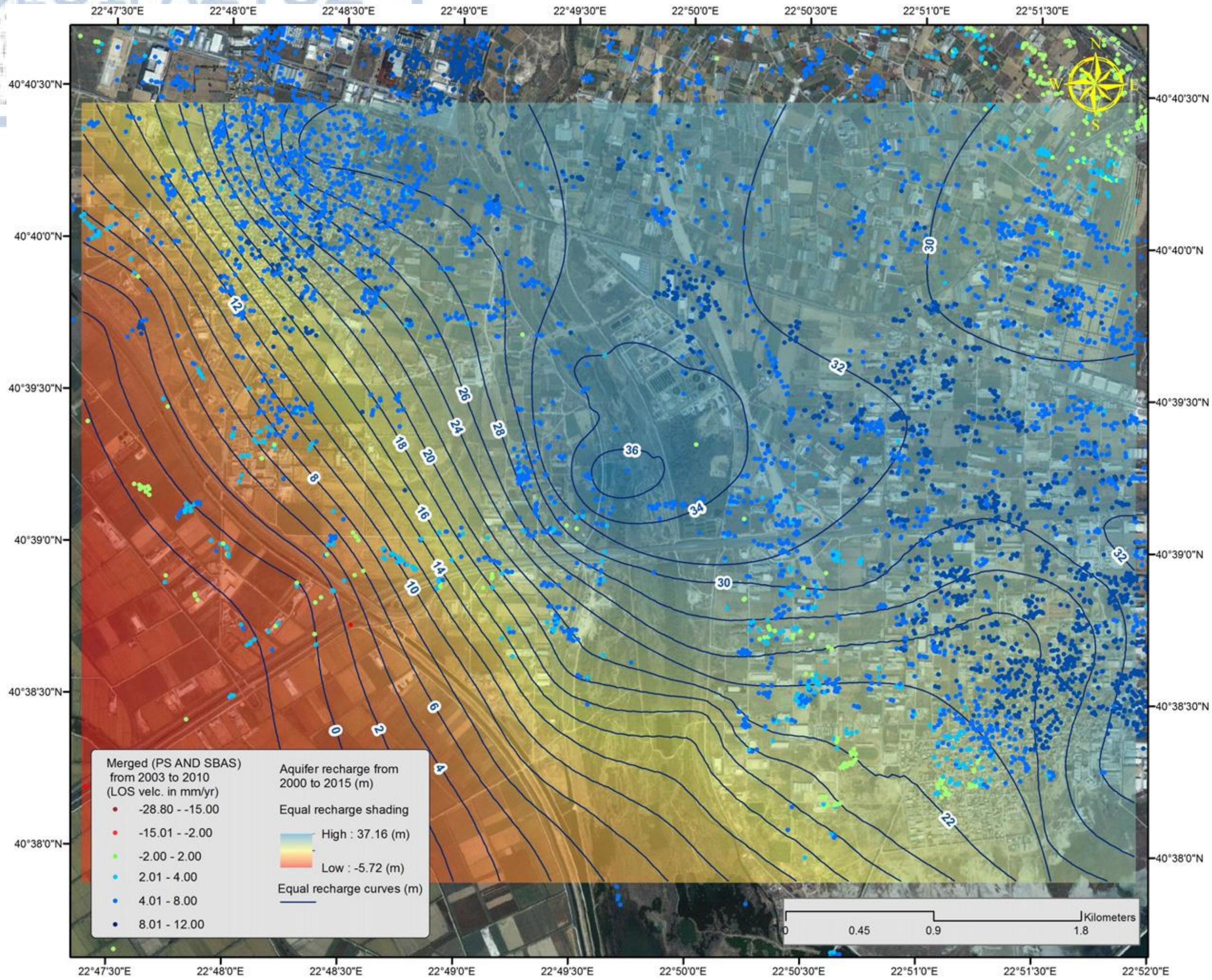

Figure 4.5 Image presenting the groundwater recharge between June 2000 and June 2015. The dots are SAR data indicating displacements along LOS in mm/year (2003–2010). Positive values of the aquifers recharge contour indicate uplifting of the ground water level (Svigkas et al. 2016).

In the mid-1980s a temporary groundwater level recovery of 5 to 15 m occurred since the Water Company had stopped pumping, aiming to control land subsidence phenomena. In late 1990s, the increasing water consumption, by the industries, led the underground water level to be at its maximum depth of 35–40 m below ground level (Raspini et al. 2014, Soulios, 1999). Interestingly enough, in 2012, the aquifer appeared to be partially recovered and the water level was located from +1 above to 8 m below ground level. The spatial distribution of the groundwater level recovery between 2000 and 2015 is presented in the form of equal recharge contour lines in Figure 4.5. It is clear that at 2015 the water level appears to be recovering; throughout the entire study area. The aforementioned recovery is highly connected with the economic crisis that has led many of the industries to shut down, reducing radically the water consumption.

4.1.5 Data

ERS 1/2 & Envisat satellites were exploited for the time spans 1992 to 2000 and 2003 to 2010 respectively. The dataset, ordered by the European space agency (ESA), consisted of 46 Images (level_0) for ERS missions and 37 (level_0) for ENVISAT, from track 279, descending mode. The images that initially participated in the processing are in Tables 4.1 and 4.2. The Shuttle Radar Topography Mission SRTM Digital Elevation Model (Farr and Kobrick, 2000) was used for the topographic correction. For Orbital corrections the information from the Department of Earth Observation and space systems (DEOS) of the Delft University of Technology and VOR data from ESA were adopted. Moreover, ground truth data from field surveys and hydrogeological data from the water supply and Sewerage Company of Thessaloniki are taken into account for the validation and interpretation of the detected signal.

Table 4-1 The ERS dataset.

Dates	Perpendicular Baseline	Δt (days)
12-Nov-92	127	-933
19-Aug-93	-318	-653
28-Oct-93	593	-583
03-Jun-95	0	0
13-Aug-95	100	71
30-Dec-95	445	210
31-Dec-95	199	211
09-Mar-96	527	280
14-Apr-96	201	316
18-May-96	157	350
19-May-96	82	351
01-Sep-96	-67	456
06-Oct-96	-506	491
15-Dec-96	-369	561
04-May-97	-310	701
08-Jun-97	-15	736
13-Jul-97	-361	771
17-Aug-97	-158	806
21-Sep-97	-110	841
30-Nov-97	129	911
04-Jan-98	-261	946
19-Apr-98	206	1051
28-Jun-98	116	1121
02-Aug-98	221	1156
06-Sep-98	-831	1191
28-Feb-99	47	1366
13-Jun-99	48	1471
18-Jul-99	340	1506
22-Aug-99	-525	1541
26-Sep-99	481	1576

Table 4-2 The ENVISAT dataset.

Dates	Perpendicular Baseline	Δt (days)
9-Mar-03	-404	-2065
22-Jun-03	-232	-1960
11-Jul-04	-231	-1575
24-Oct-04	394	-1470
6-Feb-05	-474	-1365
13-Mar-05	366	-1330
17-Apr-05	156	-1295
22-May-05	-126	-1260
4-Sep-05	639	-1155
26-Feb-06	-317	-980
11-Jun-06	-314	-875
16-Jul-06	793	-840
11-Feb-07	-298	-630
5-Aug-07	-158	-455
6-Apr-08	221	-210
20-Jul-08	48	-105
2-Nov-08	0	0
11-Jan-09	-49	70
15-Feb-09	-79	105
26-Apr-09	-155	175
31-May-09	31	210
13-Sep-09	342	315
22-Nov-09	209	385
27-Dec-09	-379	420
7-Mar-10	-213	490
11-Apr-10	136	525
20-Jun-10	-2	595

4.1.6 SAR Processing steps

At the beginning of the processing, within linux, the level_0 products (raw satellite data) are focused using the ROI-PAC (Rosen et al. 2004) code for the creation of a Single Look Complex Image (SLC). The orbit information was obtained using the getorb software (http://www.deos.tudelft.nl/). The final choice of the master image was based on the script “master_select” of the StaMPS code package (Hooper et al. 2007). In addition, the area of interest was chosen and cropped. That area had to be included in all the slave images. In order to have an accurate estimation of the phase differences, the ground area contained in the master image had to be identified in all the images. Cross-correlation techniques was used to co-register the SLC pairs, using the DORIS code (Kampes et al. 2003), within linux.

Firstly, an orbital coregistration was performed based on the satellite orbits. Offsets of all the slave images, relative to the master, were estimated. Then, a coarse correlation took place to achieve a pixel level accuracy. The magnitude of the signal was used to estimate a correlation function for each SLC pair. Finally, a fine coregistration took place that created links of the master and all the slaves, at a sub-pixel level. There is a possibility the direction and magnitude of some offset vectors to deviate from those of the majority of the other vectors. If there are many of these cases, there is the whole process could fail and eventually lead to a coregistration error. This can happen if for example the area of interest is not contained in all the slave images. After the co-registration, the phases of the two SLC images are subtracted and the interferograms are formed. Then the interferograms’ flattening took place where the contribution from the earth’s curvature (whose estimation was based on a reference ellipsoid), was subtracted from the wrapped phase. Finally, before the PS processing, the phase contribution of the topography was subtracted. For this step, external topographic information was used (SRTM DEM). The result is a wrapped Differential interferogram (DInSAR) that depicts the crustal deformation, which occurred between the two passes of the satellite (Fig. 4.6).

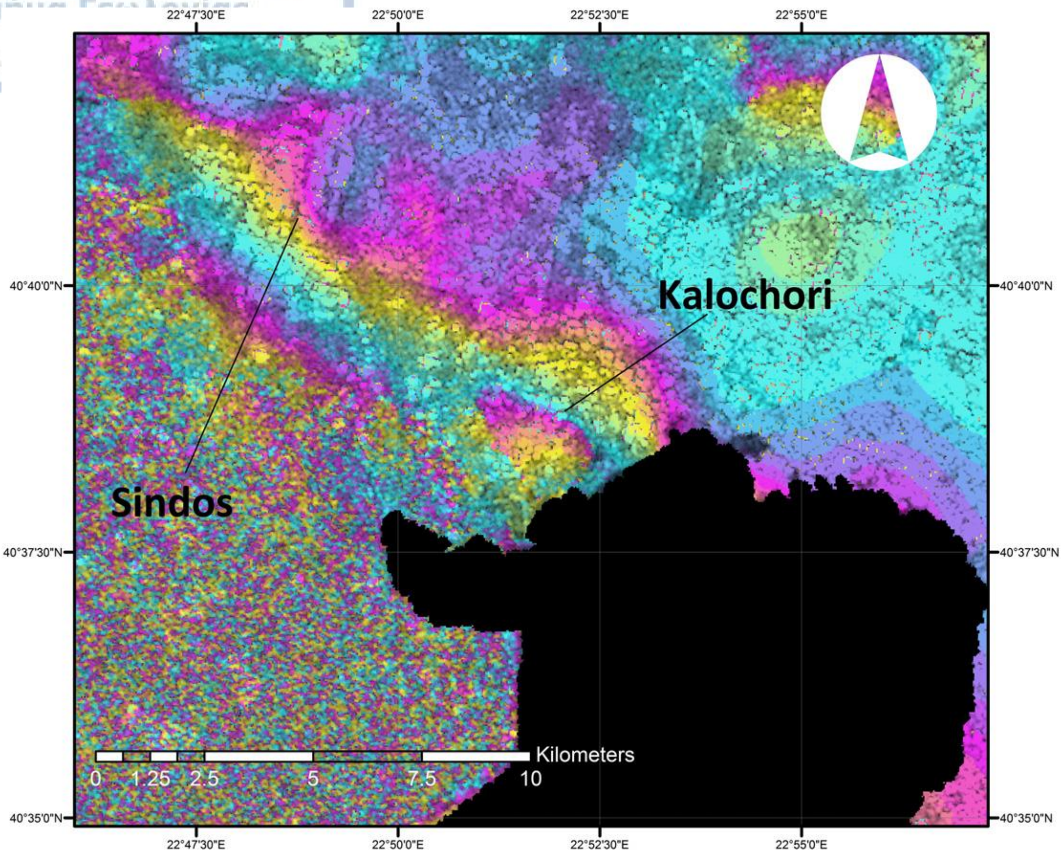

Figure 4.6 Differential Interferogram of the pair of the acquisitions: 17 September 1995 and 1 September 1996. Areas with random colours (at the south western part) are areas of low coherence. This is due to the agricultural lands of the Thessaloniki Plain. The areas of Kalochori and Sindos are located in detected deforming areas (which are locations with non-random colours that form the "fringes") as it can be seen on this phase map (Svigkas et al. 2016).

For the PS technique, a network of SLC pairs was created in which all of the SLC slaves are connected with a unique SLC image (master). In the case of Kalochori, the StaMPS (Stanford Method for Persistent Scatterers) code (Hooper 2006; Hooper et al. 2007) was used which is consisted by scripts written in Matlab. The procedure initially searches in the stack of the interferograms for PS candidates. The latter are specific points in the study area, that pass the criteria of stable radiometric characteristics throughout time. These points, strongly correlated in time and space, are the points on the surface at which ground velocities are going to be estimated. Most of the times, PS can be urban constructions, metallic fences, corner reflectors etc. Thus, within Matlab the wrapped interferograms were subdivided to patches. This step protects the processing from RAM memory problems in case the area of interest is large. The number of patches were divided in a way to obtain 5 million pixels per patch. Also at this stage, an amplitude dispersion index threshold is set. Unlike other MT-InSAR algorithms, in StaMPS at first a loose criterion is initially set (in the kalochori case, the value 0.4 was adopted). Not all the initially selected points are going to be PSs. The final definition of the PS pixels are going to be based on their phase stability. Then, a grid size of 50m was assumed for the estimation of spatially correlated phase. The latter was achieved via iterations and the phase stability indicator γ was estimated for each pixel. The value 0.005 was adopted for the threshold for change in the mean value of γ. The final selection of the PS pixels was based on the phase characteristics. In the next step, the weeding of the PS candidates took place. During this procedure at the beginning, there is a check on whether there are candidates with duplicate coordinates and then the pixels that have a contribution from neighbouring ground resolution elements are discarded. The PS weeding is achieved by dropping the PS candidates that have a phase noise standard deviation > 1. The phase of the selected PS pixels was corrected for the spatially uncorrelated look angle error (DEM) and then all the patches of the wrapped interferograms were merged back. A filtering (Goldstein and Werner, 1998) of the wrapped interferograms was applied, adopting an alpha value of 0.8. A critical subsequent step is the unwrapping of the interferograms. The unwrapping was performed with respect to a reference point (a stable area in the city centre of Thessaloniki) and a 3D phase unwrapping algorithm was exploited (Hooper, 2009; Hooper and Zebker, 2007). Finally, in StaMPS there was the choice for the estimation of the spatially correlated look angle error (SCLA). This error is subtracted from the wrapped phase and then the interferograms are again unwrapped. The result are the velocities of every PS point, in mm/yr. The method of Small Baseline Subset (SBAS) is also implemented in the StaMPS code (Hooper, 2008). The technique minimizes the effect of limited coherency. In StaMPS the slowly-decorrelating filtered phase pixels (SDFP) are analysed following similar steps with the previous approach. However in SBAS, a connection graph of SLC pairs (DInSARs) was created based this time on the choice of the maximum allowed baselines and the maximum allowed temporal separation. StaMPS offers also the possibility to merge the PS and SDFP results. This can help during the processing, since it can offer a richer spatial data coverage than can potentially lead to an easier and more reliable unwrapping. Below the merged time-series results are presented.

4.1.7 Results and Discussion

Figures 4.7 and 4.8 show the deformation velocities for the period 1992–2000 and 2003 to 2010, respectively. As it can be seen the deformation patterns of the two periods present opposite trends. From 1992 to 2000, a subsiding surface was revealed (more than 20mm/year) and from 2003 to 2010, there is uplift (up to 12 mm/year). When it comes to the spatial amount of the uplifting pattern, Kalochori is having larger values of uplift, when compared to Sindos. A technical validation of the results stems from the fact that these very interesting ground velocity estimations were measured by all the three techniques applied (PS, SBAS, Merged result). For a further processing validation of the intriguing uplifting pattern of ENVISAT, the same dataset was processed, this time using the SARscape© software. The SARscape results are shown in Figure 4.9 and indicate a great similarity (max. uplift 11 mm/yr), with those of the StaMPS code.

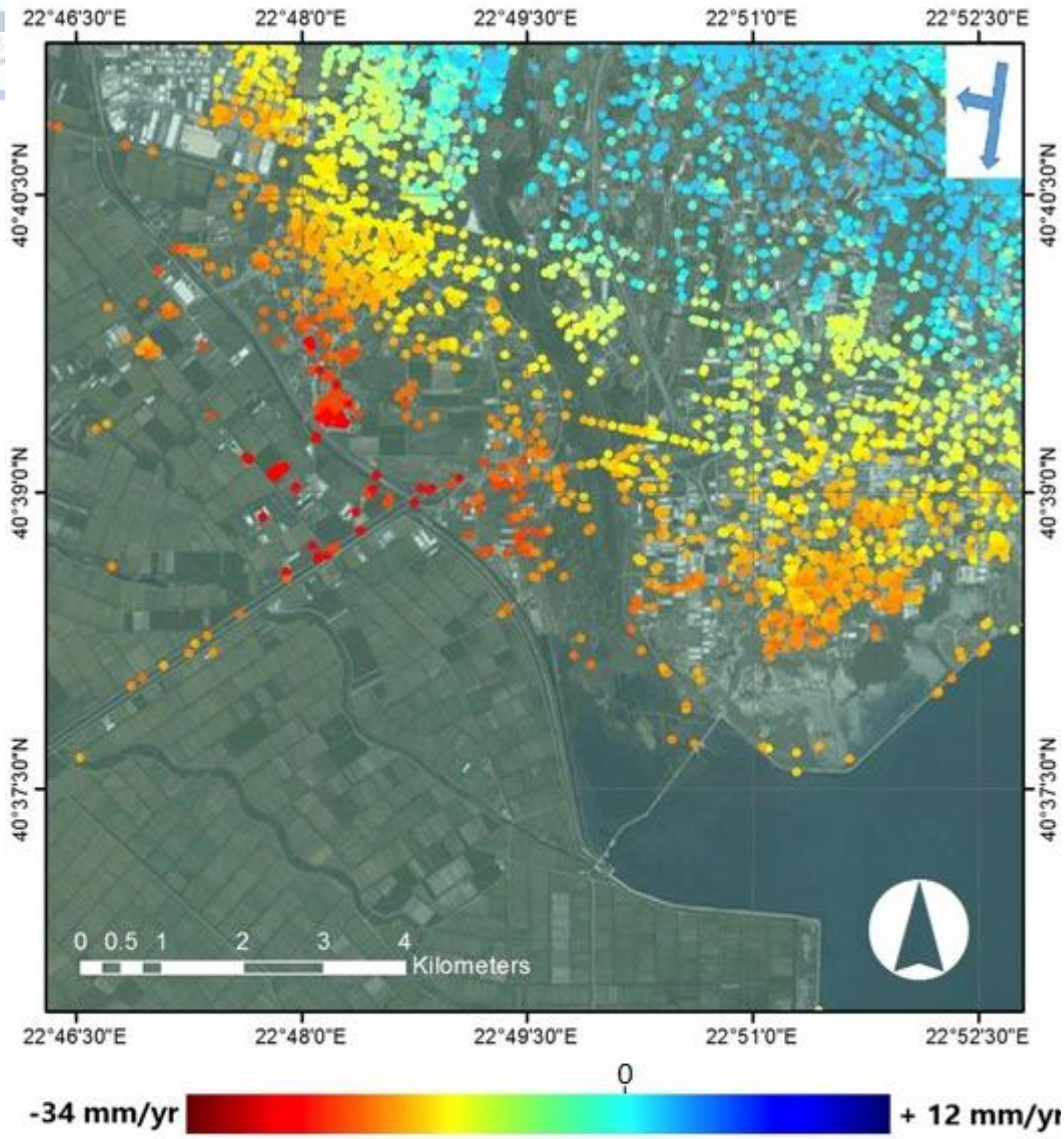

Figure 4.7 StaMPS velocities from1993 to 2000 as derived by the analysis of ERS 1 & 2 data. During this time, the study area was subsiding with a rate of more than 20mm/year. The large arrow depicted in the inset in the upper right, shows the direction of the descending path and vertical smaller arrow shows the line of sight direction of the satellite (Svigkas et al. 2016).

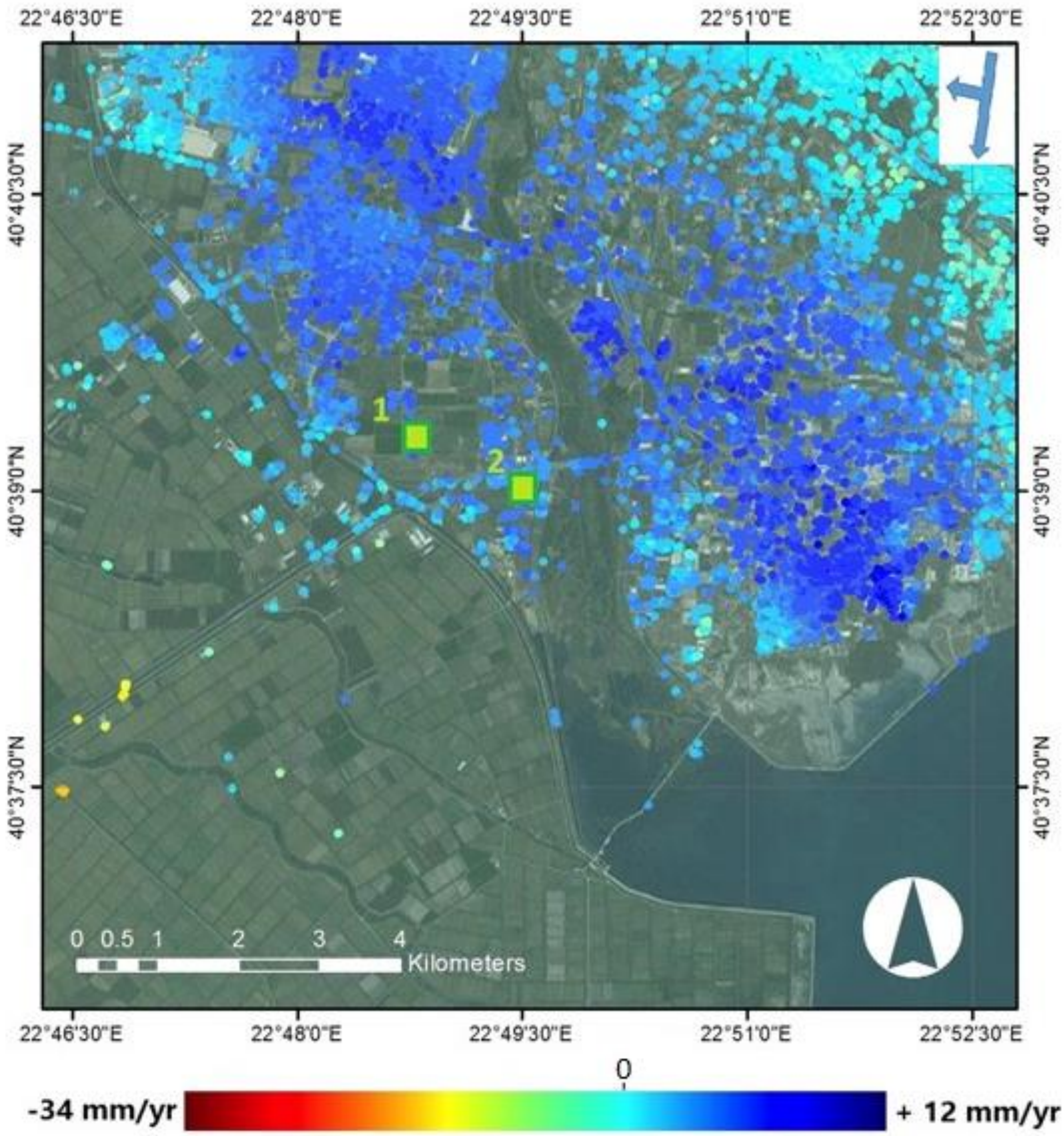

Figure 4.8 StaMPS velocities from2003 to 2010 from the analysis of ENVISAT data. The area is subjected to uplift. The uplifting rates are up to 12mm/year. The green rectangles (1 and 2) denote the location of the drills whose data were used for designing the curves of Fig. 4.10. The large arrow depicted in the inset in the upper right, shows the direction of the descending path and the smaller arrow shows the line of sight direction of the satellite (Svigkas et al. 2016).

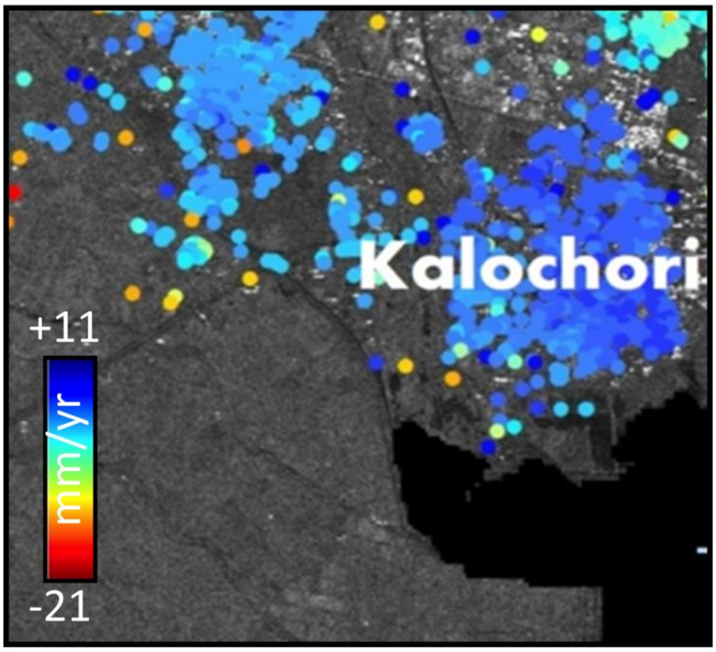

Figure 4.9 Surface velocities from 2003 to 2010 (ENVISAT data) using SARscape software (Svigkas et al. 2016).

In order to further validate and interpret these results, ground truth data were exploited. In Figure 4.5 the velocities derived from the SAR analysis are compared with the groundwater level recovery between 2000 and 2015, presented in the form of equal recharge contour lines. Positive contour values indicate recharge and, there is a clear relation of the uplifting trend detected by the SAR analysis with the spatial distribution of the aquifers recovery. There is not a straight correlation between the maximum water level recharge values and the maximum amount of uplift throughout the whole area. That is because except the ground water level, the different geotechnical characteristics and the stratigraphy variations affect the uplift ratio. In the same context, a more in-depth analysis was conducted by designing the graphs of Figure 4.10. The two-decade deformation history was plotted together with the ground water level measurements. The velocity points (time series) and drills are from the same neighbourhood (green rectangles in Fig. 4.8). When looking at the general trend of both graphs (Fig. 4.10), the surface deformation is presenting three distinctive trends. The first one (negative slope) is expressing the first period where subsidence was occurring. The second one (positive slope) after 2000 presents the uplifting trend. Finally the third one (positive slope) after 2007 denotes a smoother uplifting trend.

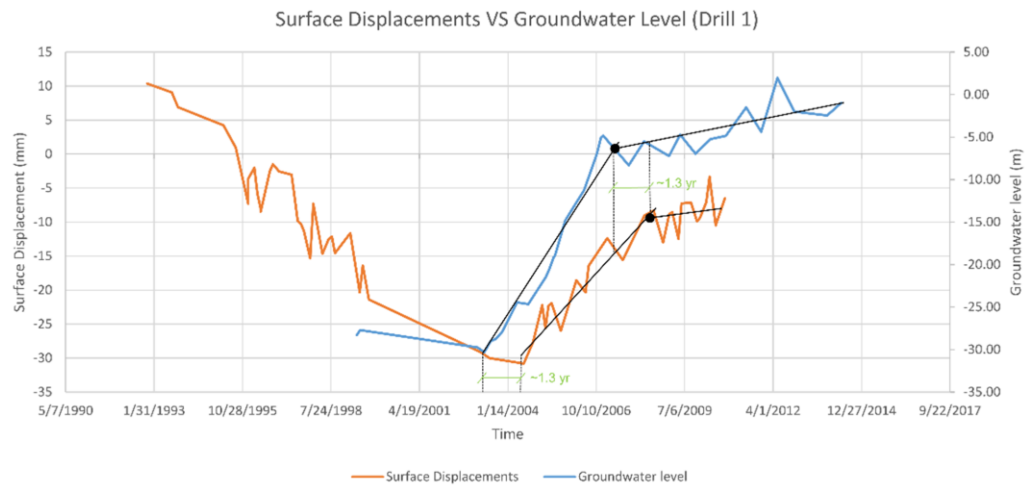

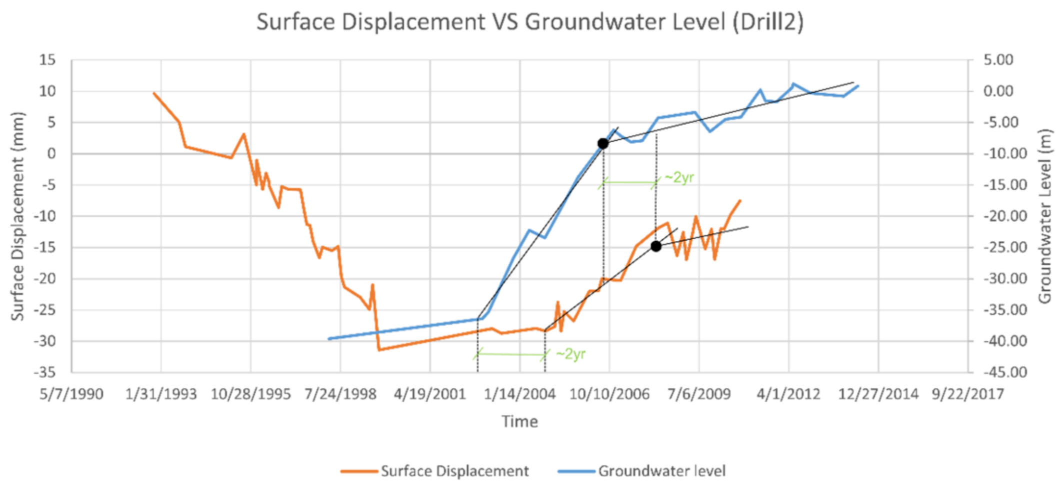

Figure 4.10 Upper panel: Graph comparing the ground water level variations at Drill 1 with the surface deformation time series at a nearby data point produced by the SAR analysis. Lower panel: Graph comparing the ground water level variations at Drill 2 with the surface deformation time series at a nearby data point produced by the SAR analysis (Svigkas et al. 2016).

The comparison of the subsiding trend with the aquifer water level measurements makes clear that the changes of the aquifer level is followed by a response detected at the surface. It is important to point that there is a sufficient time lag between the recharge initiation and the responding uplift at the ground surface. As presented in Figure 4.10 this time-lag is approximately 1.3 to 2 years and it can be completely justified by the consolidation theory (Terzaghi, 1943). Specifically, the swelling index, Cs, representing the increase of the void ratio, e, as a function of the reduction of effective stress, σ_{ef}, is 5 to 10 times smaller than the compression index, C_c, representing the reduction of the void ratio, e, as a function of the increment of effective stress. Thus, soil formations swell 5 to 10 times less when a load is removed, than compress when the same amount of load is applied. That means that in order to get measurable swelling indications the reduction of the effective loads has to be intensive. This is why, at the typical oedometer test, maximum loading is gradually applied in more than five stages and unloading in just one stage, by removing all loads at once.

In the case of aquifer recharge, the unloading is applied by the increment of the pore pressure, decreasing proportionally the effective stresses.

4.1.8 Conclusions

Time-series surface deformation analysis is carried out for the areas of Sindos and Kalochori. For the interpretation and validation, groundtruth-based data were used. Sindos and Kalochori (parts of the Delta municipality) are both industrial suburbs of the city of Thessaloniki. ERS and ENVISAT images covering the study area, from 1993 to 2010, have been analysed by generating more than 250 Interferograms. For the wider study area, various studies have already highlighted a subsiding trend, attributed by most of the researchers to the overexploitation of the aquifers. SAR Interferometry is one of the tools widely used up to now for the detection and investigation of subsidence phenomena occurring from 1993 to 2000. In this study, the previously detected subsidence is validated, whereas now an uplifting trend is highlighted for the same area from 2003 to 2010. The detected deformation rebound of 2003 to 2010, occurring in agreement to the recharge of the aquifers, proves that the ground water overexploitation was the driving mechanism of the subsidence phenomena. Even though the parallel activity of other phenomena, such as natural compaction and soil oxidation cannot be excluded, the detected rebound leaves no room for other speculations concerning the dominant driving mechanism. It is clear that even though other deformation mechanisms might be occurring, their contribution was neglectable and unable to restrain the surface rebound that took place the last decade. The most intriguing result of the validation procedure was the detected 1.3 to 2 years long time lag between the recharge initiation and the responding uplift of the ground surface. This fact is recorded and reported for the first time and it is clearly justified by the consolidation theory. The interpretation of the observed uplift phenomenon is linked to the fact that at the beginning of the 21st century the financial status at the industrial areas of Kalochori and Sindos changed. Several water consuming industries of the secondary economic sector, such as textiles, clothing and skin processing industries, shut down and their place was taken by companies of the tertiary economic sector, such as logistics and import–export companies. This change on the economic status of the area together with the national economic collapse led to the gradual reduction of the ground water consumption and as a result to the aquifers recharge.

4.2 The Case of Anthemountas Basin

4.2.1 Introduction

Anthemountas region was subjected to a population increase over the last years. The lower cost of living (house renting etc.), compared to the city centre, established the area as an attractive location for the locals to live or set up their companies. The region hosts a number of critical facilities, including the Thessaloniki International Airport "Makedonia", alongside agricultural and industrial settlements (WaterinCore, 2009).

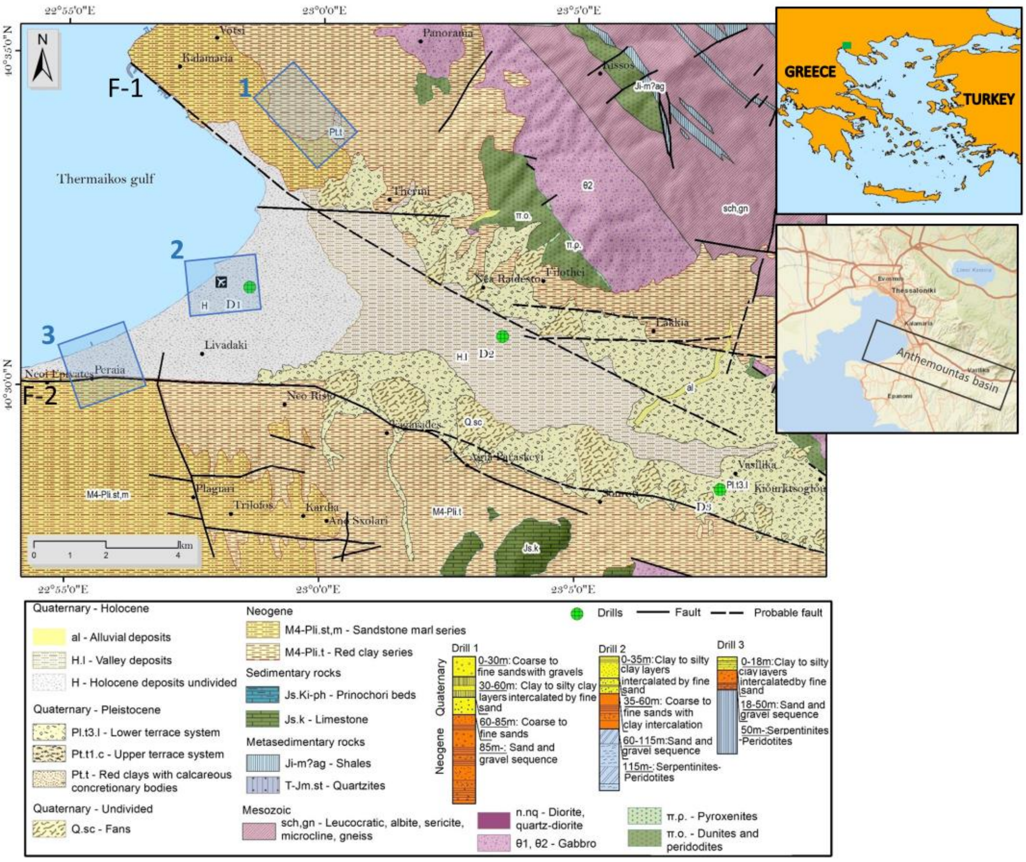

Figure 4.11 Geological map depicting the area of interest. Blue rectangles outline areas this study focuses on: 1) Area close to Thermi village, 2) International Airport of Thessaloniki, 3) Town of Perea. Upper inset map: area of interest (green rectangle) with respect to the Greek territory. Lower inset map: Broader area of Anthemountas basin. The geological map is modified from IGME Geological Map Sheets, Epanomi (1969), Thessaloniki (1978), Thermi (1978) and Vasilika (1978).

The development trends in Anthemountas had already started before the beginning of the '90s, and caused a drop of the underground water level (Fikos et al. 2005). Raucoules et al. (2008) firstly detected a subsidence signal at the graben based on ERS satellite imagery using repeat-pass space borne SAR (Synthetic Aperture Radar) interferometry. Raspini et al. (2013) used the ERS imagery to focus at the deformation of the basin as a whole and attributed the subsidence phenomena to aquifer overpumping. The region drew the attention of the geo-engineers back in 2005, when extensive fractures occurred at Perea (Fig. 4.11, rectangle 3). Perea and other suburbs in Anthemountas undergo a rapid development and the groundwater demand is significant since it is the main supply of water for domestic, irrigation, industrial and livestock uses (Kazakis et al. 2013). The population is ~56,000 people, growing fast; the water demands are mainly fulfilled by the exploitation of the porous aquifers, which are developed in the Neogene and quaternary deposits of the lowlands. More than 1,000 boreholes have been drilled (Kazakis et al. 2013). In this context, a revisit of the on-going deformation pattern, within this socially and economically critical area, was worthwhile.

In this thesis, new radar time-series results are presented to study the displacement that occurred during the post 2000 period, not being examined so far, seeking to define whether the previously detected subsidence had stopped or is still on going during the '00s. We build upon the results of previous studies (Raspini et al. 2013), but we augment the observation period and process both the ERS and ENVISAT datasets to study the phenomenon during the two monitoring decades. The main tool for this study is Interferometric Synthetic Aperture Radar (InSAR) and more specifically the Multi-temporal InSAR (MT-InSAR) techniques of Persistent Scatterer Interferometry (PSI) and Small Baseline Subset (SBAS) methods that enable the small-scale surface deformation monitoring over large time spans. SAR interferometry is a tool of research to many disciplines: earthquakes, aquifer activity, glaciers, landslides, volcanoes (e.g. Parsons et al. 2006; Amelung et al. 2000; Galloway et al. 1999).

Remote sensing results are examined together with other data sources including: geology, faulting, seismology and hydrogeological in-situ data. Focus is given on specific sites to study their deformation in more detail (Thermi, Perea, and Thessaloniki International Airport) (see Fig. 4.11, rectangles 1, 2, 3). Finally, the relation of the detected deformation with two of the longest known tectonic structures close to the metropolitan area of Thessaloniki city is discussed.

4.2.2 Geologic and Seismotectonic setting

The Anthemountas basin covers an area of ~370 km² with high hills and semi-mountainous relief (mean altitude 259 m). It was formed during a phase of extensional stresses since the Miocene, which created NW-SE and E-W basins (Tranos et al. 2003 and references therein). Figure 4.11 depicts the geological context of the area. The basin has a Mesozoic bedrock, consisting mainly of phillites, gneiss and granites. Above the bedrock, the Neogene deposits consist a top sand and gravel layer and a bottom clay-marl layer (Anastasiadis et al. 2001; Rozos et al. 1998). At the top, the Quaternary formations are located constituting of alterations of clastic and fine sediment (Zervopoulou 2010; Rozos et al. 1998; Thanasoulas 1983). The borehole data (Fig. 4.11) indicate that the Quaternary deposits close to the coastal area, consist of three main horizons: The top layer is coarse to fine sand. Bellow there is a clay to silty clay horizon and in the third horizon are the Neogene deposits characterized by coarse to fine sands. Moving towards the East, the thickness of the sediments is decreasing.

The broader region is seismically very active with a prevailing normal faulting (Fig. 4.12) responding in an approximately N-S extensional stress field. Within the basin itself, the morphology is dominated by two long tectonic structures (F-1, F-2) with normal faulting, bounding its north and south edge (Figs 4.11 and 4.12). The north branch (F-1), has a length of about 21km and is considered as inactive (e.g. Zervopoulou, 2010). The south branch (F-2) strikes E-W and has a length of about 30km. This structure hosts a historical strong event, (asterisk in Fig. 4.12), and is related with more intense microseismicity. This microseismicity alongside morphotectonic studies define it as an active fault structure (Zervopoulou, 2010) that crosses through the suburbs of the metropolitan area of Thessaloniki, as for example Perea. In the following sections, we will also investigate any interaction between these tectonic features with the displacement pattern derived from the InSAR time-series.

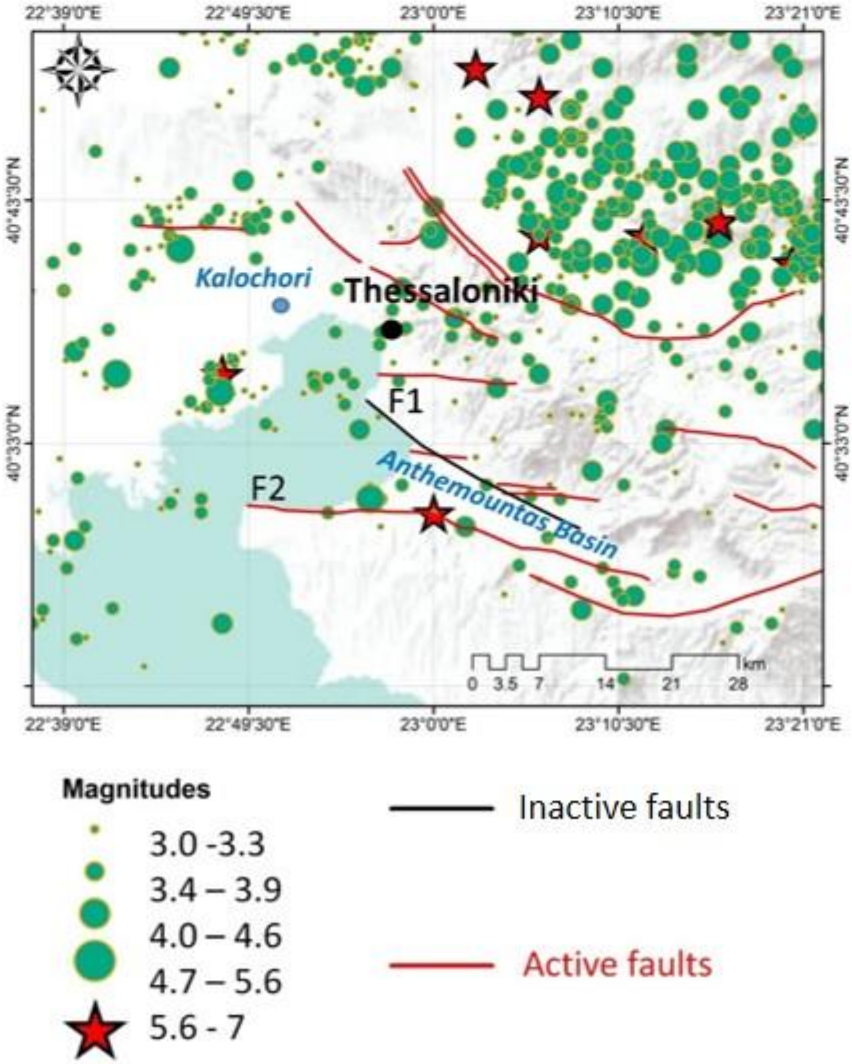

Figure 4.12 Seismicity (green circles) in the broader area and active faults (red lines). The red asterisks denote strong (M.6) earthquakes. The faults are from Zervopoulou (2010) and the NOA fault database (Ganas et al. 2013). F-1: Northern fault branch, F- 2: Southern fault branch bounding the Anthemountas basin.

4.2.1 Hydrogeologic setting

Three aquifer systems are hosted at the plain of the Anthemountas basin (Nagoulis and Loupasakis, 2001): a shallow phreatic aquifer system, developed within the upper coarse-grained Quaternary deposits, a semi-confined alternating aquifer, which extends down to depths of 200m, within the lower Quaternary and the upper sand and gravel sequence of the Neogene deposits, and the deep confined aquifer system which could be further separated into two very deep isolated aquifers. The first extends south of the Anthemountas fault, occupying the lower Neogene deposits and the Mesozoic limestone and the second-deep confined aquifer characterized as a low enthalpy thermal aquifer which extends along the normal fault bordering the basin to the north (close to the Thermi village). According to Nagoulis and Loupasakis (2001), these systems do not seem to be affected by the variations of the ground water level of the two shallower aquifer systems. The area, which has undergone in the '90s an extensive development, is under an increased demand for water. This fact has left affected the deep semi-confined aquifer, which suffered an excessive lowering (Fig. 4.13).

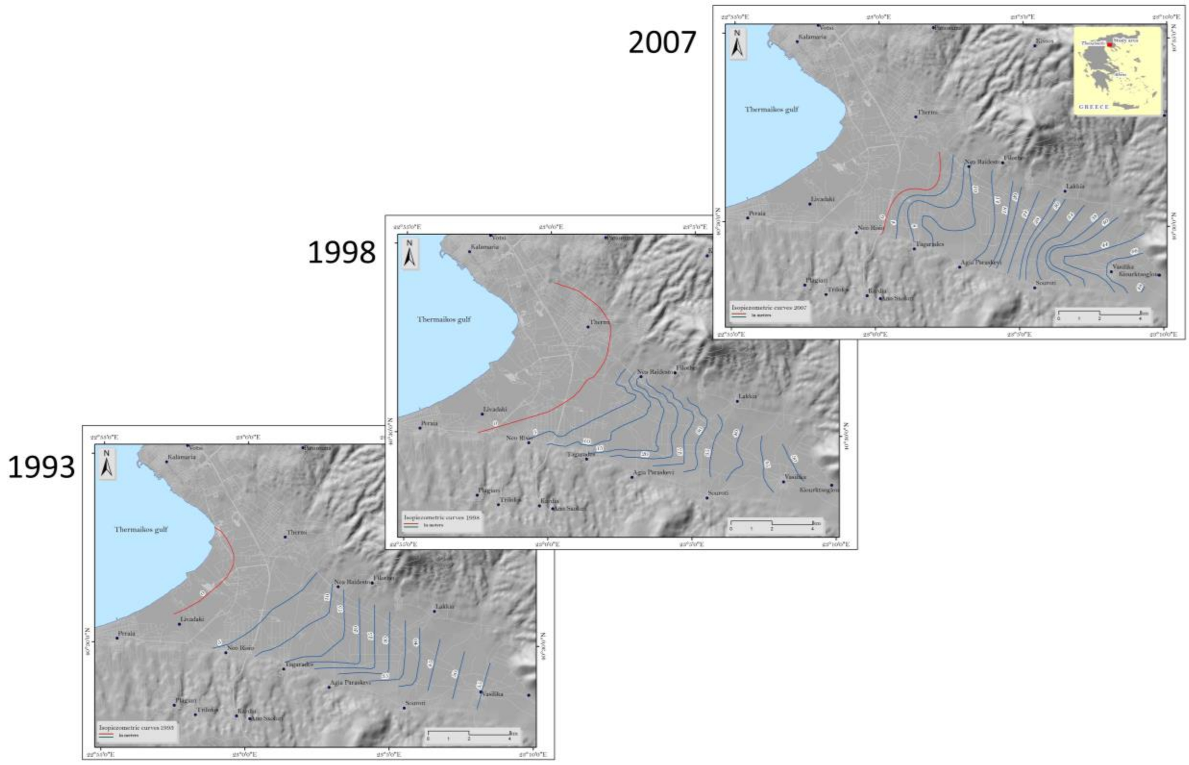

Figure 4.13 Isopiezometric curves at the area of Anthemountas indicate a continuous lowering of the underground water level. Data of 1993 and 1998 are from (Nagoulis and Loupasakis, 2001), data of 2007 are from the Lifewateragenda project.

4.2.2 InSAR Analysis - Data and Methods

For the study, the same initial dataset of Tables 4.1 and 4.2 was exploited. Two radar datasets covering the period 1992-2010 were used: descending raw (Level 0) data from the European Space Agency (ESA) of ERS 1, ERS 2 and ENVISAT satellites were the basis of this analysis. Orbital data from Delft University of Technology and ESA were used. The topography correction in the interferometric process was achieved using the Shuttle Radar Topography Mission (SRTM) Digital Elevation Model (Farr et al. 2007). For the pre-processing the ROI_PAC code was used (Rosen et al. 2004), for the interferogram generation the DORIS code (Kampes et al. 2003) and for time-series interferometric processing the StaMPS PS and SBAS implementation was used (Hooper, 2006; Hooper et al. 2007; Hooper and Zebker, 2007) and also the SARscape software.

Initial pre-processing included the focusing of the raw ERS1, 2 and ENVISAT data in order to create Single Look Complex (SLC) images. Each pixel of each SLC image contains information about the amplitude (measure of the backscattering of the electromagnetic signal) and the phase. SLC image pairs are created to generate the wrapped interferograms by subtracting their phases. Then, corrections for the orbits and topography are applied and finally the wrapped interferograms are filtered (Goldstein and Werner, 1998) for an increase of a Signal-to-Noise ratio. The result is a differential interferogram that shows the displacements in the Line-of-Sight (LoS) of the sensor. During the PS technique, the SLC network is created by using specific criteria (see chapter 2) defining one "master" image and all the rest were the "slaves". For the SBAS technique, an SLC network is created considering the minimization of the temporal, perpendicular and Doppler baselines. During the processing, any corrupted or poor quality interferogram was excluded from the procedure.

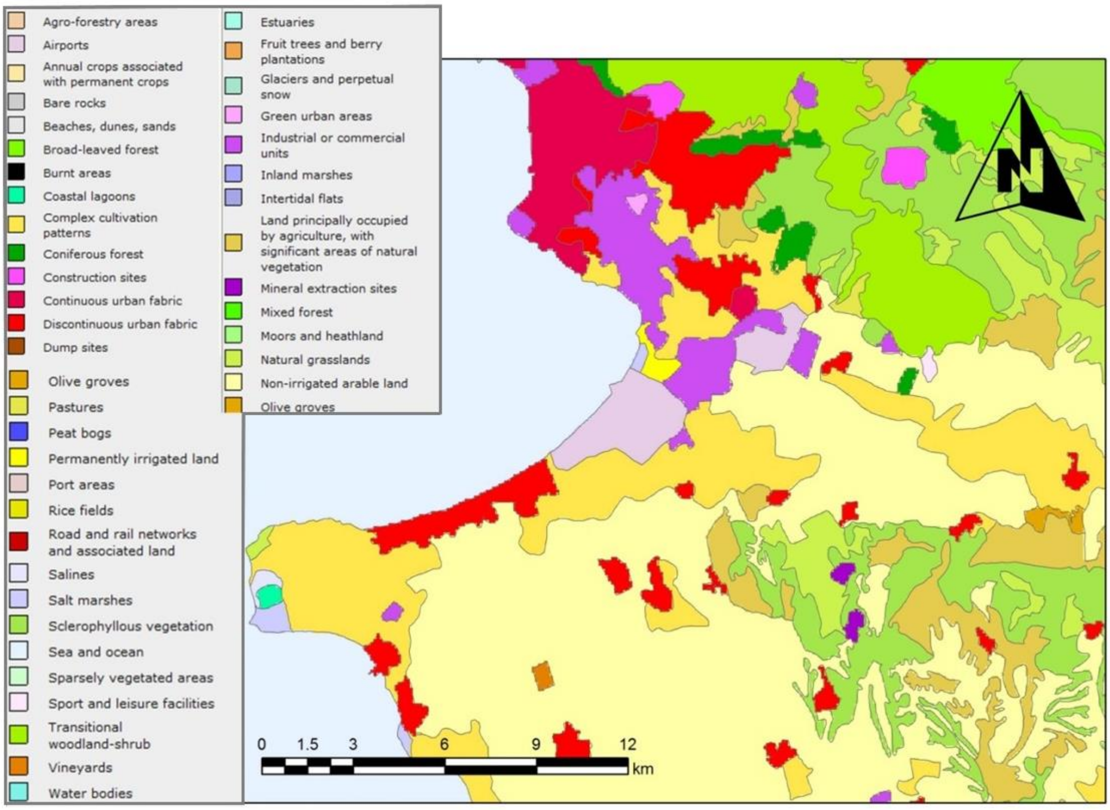

Figure 4.14 Land use at the area of Anthemountas is creating a challenging environment to apply SAR time-series techniques (Land use source: Corine land cover).

The unwrapping reference point was set at the city of Thessaloniki in accordance with previous InSAR studies (e.g. Svigkas et al. 2015, 2017; Raspini et al. 2013, 2014; Raucoules et al. 2008) which is relatively stable in both decades.

As previously stated, when applying MT-InSAR, urban areas are easier to monitor because manmade structures like fences, buildings, infrastructure etc. have stable scattering characteristics and can be easily considered as PSC. Using this approach, the PSC identification in areas outside the urban areas, in pixels that do not have any dominating scatterers (e.g. in agricultural lands), is challenging and in some cases even not feasible. The land use area of Anthemountas basin contains a few urban areas (Fig. 4.14), but to its main part is not urban.

4.2.3 Results

The calculated surface deformation from 1992 to 2010, presented at two time slots (one for the ERS and one for the ENVISAT satellite). In Figures 4.15 there is the SBAS processing of ERS dataset, using SARscape and in Figure 4.16 the ERS and ENVISAT StaMPS processing results are presented. During the entire period of analysis, significant deformation signal has been identified. It is noticeable that the deformation rate increased during 2003-2010. Despite the land use cover, which renders difficult the application of SAR time-series, we were able to detect deforming data points, also at the eastern part of the basin. From 1992 to 1999, the StaMPS results (Figure 4.16) show that the maximum deformation was -18 mm/yr, in accordance with the results of Raucoules et al. (2008) and also those deriving from SARscape shown in Figure 4.15.

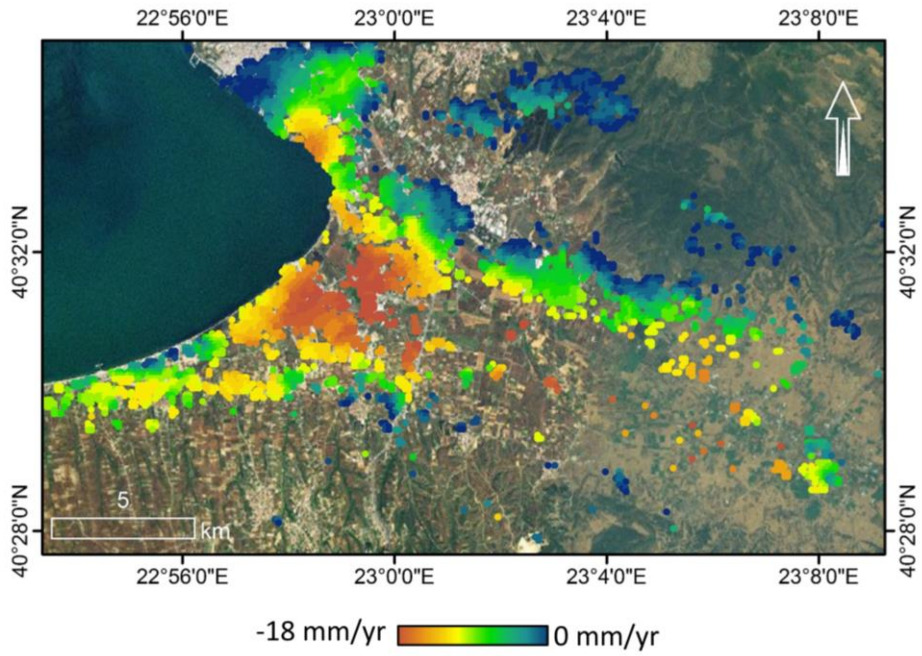

Figure 4.15 SBAS velocity result from SARscape software using the ERS satellites for Anthemountas basin (Svigkas et al. 2019a).

The results presented, derived from the ENVISAT (Fig. 4.16b) analysis, clearly show that deformation was taking place also during the '00s and most importantly there was an increase of the maximum surface deformation during the years 2003-2010, to reach values up to -30mm/yr. The maximum values of displacement in the entire Anthemountas basin are observed eastern of the airport during both decades.

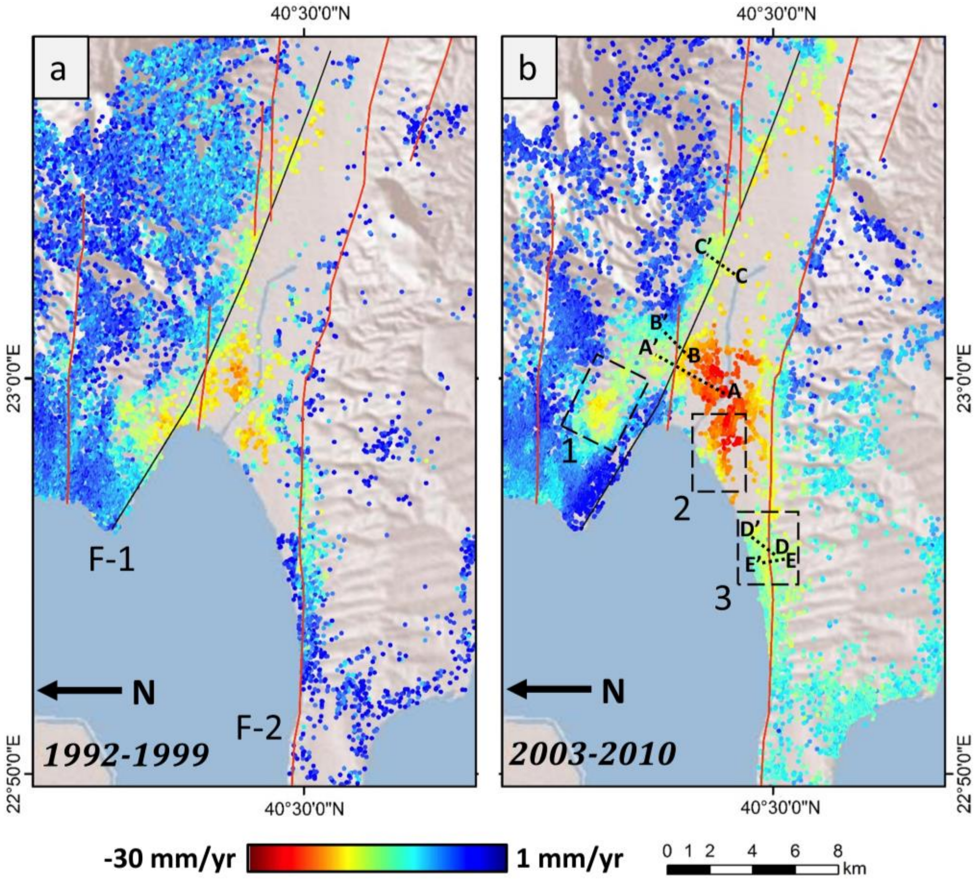

Figure 4.16 StaMPS time-series results of Anthemountas basin. a) velocities for the period 1992-1999 b) velocities for the period 2003-2010. Red and black lines are the faults of the area. Black dashed rectangles are areas of focus in this study: 1) Area close to Thermi village, 2) Makedonia Airport, 3) Town of Perea. Black dotted lines are the velocity profiles presented in Figures 4.17, 4.18.

4.2.4 Interpretation of detected signal

The aim of this study is two-fold: to not only detect and measure the deformation in Anthemountas basin, but also interpret the main mechanism that caused these ~2decade deformation signals. Of course, the case of natural compaction can be expected at the recent alluvial deposits, but additional phenomena should also be considered.

It could be inferred that there is a spatial relation between the detected deformation and the faults. However, a careful screening of the velocities around the areas where the faults lie, reveal that the spatial distribution of deforming signals is not affected by the existence or non-existence of the faults: deformation is present along the fault and also south and in some cases north of F-1 (Fig. 4.16), during both monitoring decades. For a detailed analysis, surface velocity profiles (Fig. 4.17, 4.18) were created in selected areas aiming to investigate the relation of the faults with the surface displacement. Focusing at different locations of the north and southern branches of Anthemountas, the profiles do not show any change in the velocities that would clearly define tectonic activity as the main driving mechanism. However, there is a very clear interaction between the fault and the surface velocities: each time that a profile meets a fault, there is a significant change in the rate of deformation. The detected deformations are strongly affected by the existence of the faults.

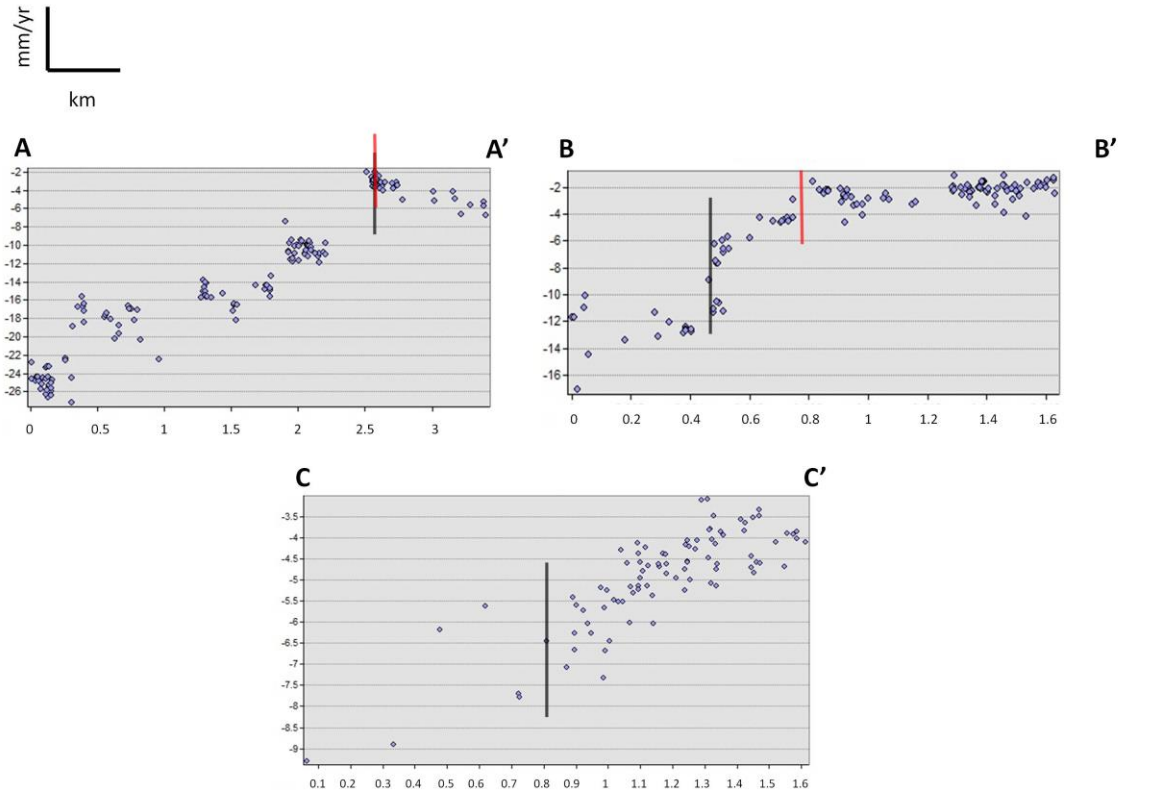

Figure 4.17 Velocity profile results from the map of Figure 4.16b. The vertical black or red lines on the graph indicate the location of the faults intersecting the profile. The profiles show an interaction of the displacement trends with the faulting of F-1.

For the validation of the remote sensing results, the hydrogeological data should also considered. As shown in Figure 4.13, there is a further reduction of ground water level in the '00s with respect to the underground water level of the '90s. Thus, when looking at the hydrogeological data and the remote sensing results of both decades, it is clear that the isopiezometric curves of the deep semi-confined aquifers for the years 1993, 1998 and 2007 were continuously lowering, leading to the occurrence of the detected land subsidence phenomena.

In the following, we will focus our discussion to a number of critical infrastructure of interest located in the region.

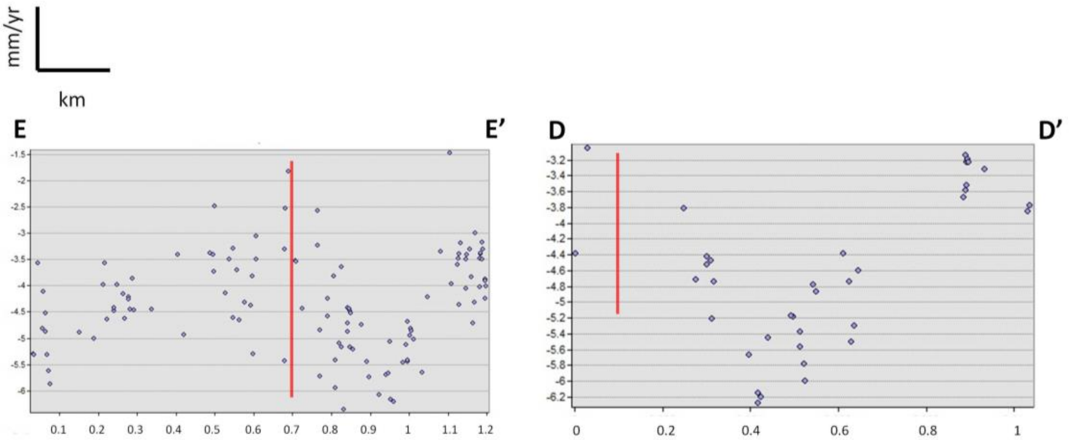

Figure 4.18 Velocity profiles at the area of Perea. The surface lines of the profiles can be seen in Figure 4.16b and (enlarged) in Figure 4.23. Red vertical lines indicate the location of the fault along the profile.

4.2.5 Farm school and NOESIS cultural centre

At the NE of Thermi an isolated deforming area is detected during the ENVISAT dataset (rectangle 1 in Fig. 4.16b). Here the velocities are -10mm/yr. This area hosts a farm school and the Thessaloniki Science Centre and Technology Museum “NOESIS”, a cultural and educational infrastructure. In Figure 4.19 the ENVISAT results reveal, at the southern sector of the building of “NOESIS”, a maximum deformation of -6 mm/yr.

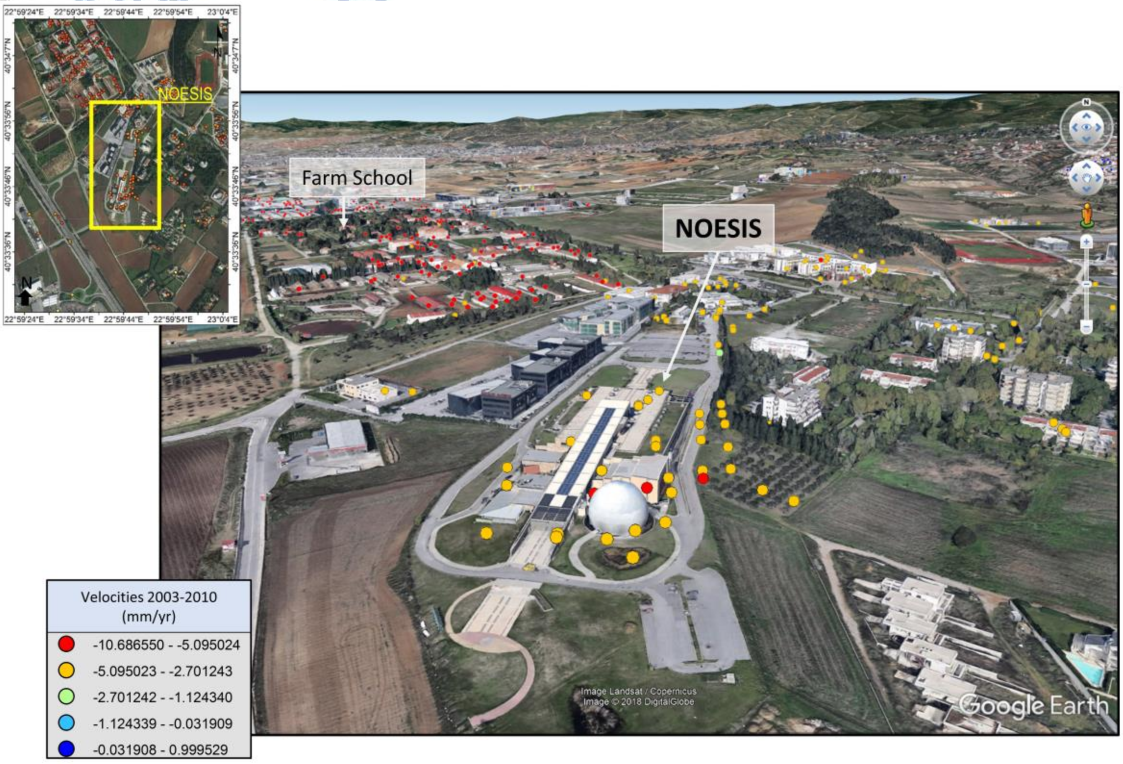

Figure 4.19 Displacement pattern detected during the second decade of monitoring for the Thessaloniki Science Center and Technology Museum "NOESIS". The yellow rectangle of the upper left inset map defines the NOESIS building. The maximum deformation is located at the southern part of the facility and is -6 mm/yr. The farm school is located at the northwest of "NOESIS" where larger deformation values are detected.

4.2.6 International Airport of Thessaloniki

The Thessaloniki International Airport lies 14km to the southeast of the city (Fig. 4.11) and is the second largest airport in Greece. It acts as a connection center when it comes to trade transportations but also for international and domestic flights. The airport area is noted in rectangle 2 of Figure 4.11 and 4.16b. Figure 4.20 summarizes the velocity results for the airport. The latter has two main runways: one with the code name "10-28" and the other "16-34. Numerous velocity points have been located to critical areas of the airport like the runways and the Terminal building. The lack of data points on the extension of runway "10-28" to the sea was expected and justified from the fact that its construction begun in ~2003 leading to a loss of coherence at the specific site. Construction phases of the runway are shown in Figure 4.21. During 2003-2010, the results indicate an increase of the deformation. The analysis of the ENVISAT results detected maximum deforming values of about -27mm/yr. The distribution of displacement along runways "10-28" and "10-34" is better shown in the velocity profiles (Fig. 4.22). Overall, for the airport, the results indicate that: a) an increasing deformation rate to the nowadays Terminal of the airport. Maximum values are -11 mm/yr in the first monitoring decade and -16 mm/yr during the second. Northwestern of the current Terminal, the maximum displacement value of the broader area changed from -12 mm/yr to -17 mm/yr (white circular notation in Figure 4.20b). It is worth noting, that this specific deforming area is located exactly at the place where a new Terminal and a new apron are currently under construction.

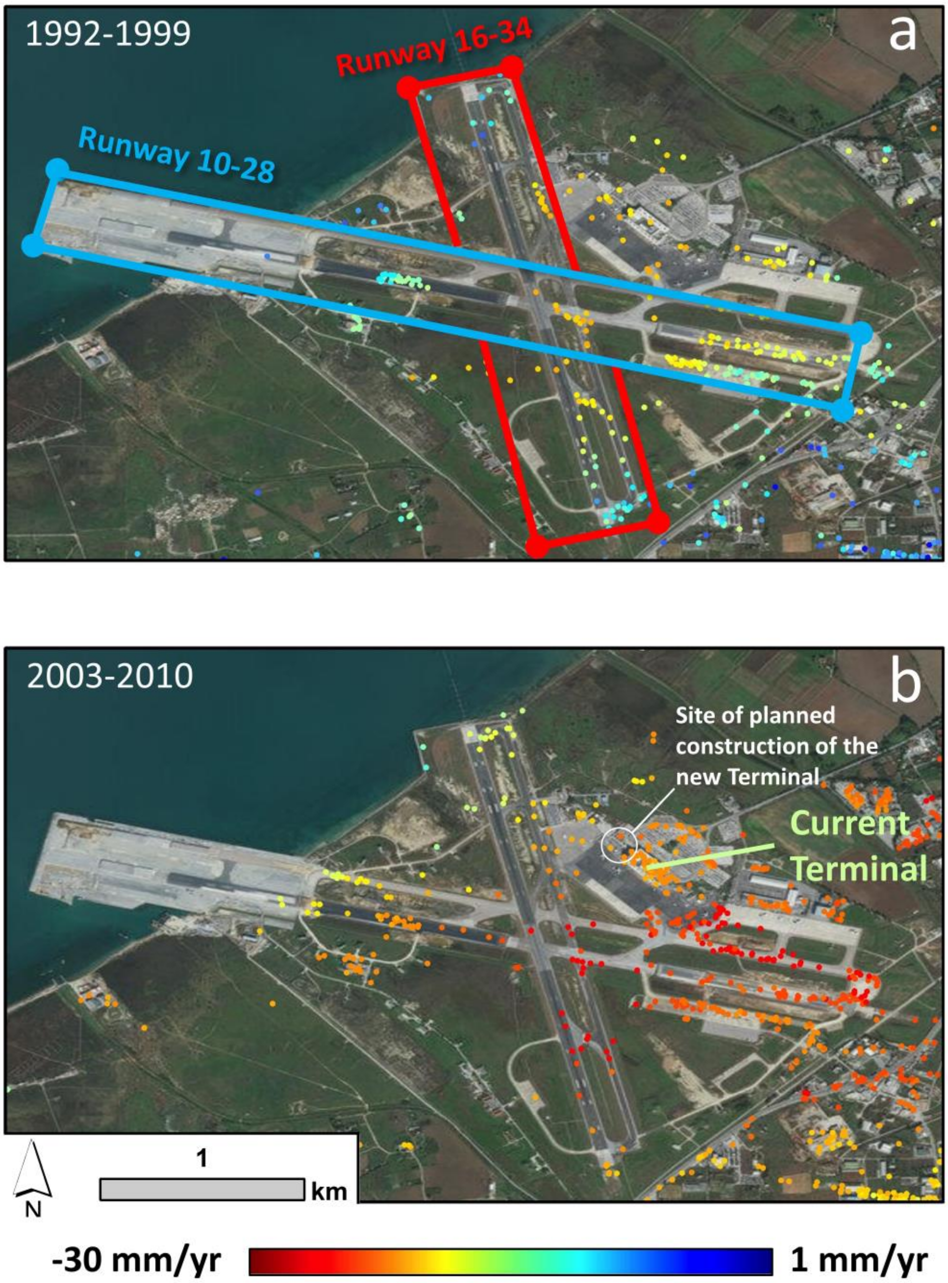

Figure 4.20 Displacement pattern of ERS (upper panel) and ENVISAT (lower panel) at the area of the International Airport of Thessaloniki. Subsidence is occurring during both periods and the maximum values are observed at cross point of the two runways. The current terminal is subject to deformation, while subsidence is also detected at the area where a new Terminal is planned to be constructed. The blue and red rectangle encompassing the runways denote the slices of the velocity profiles presented in Figure 4.22.

Figure 4.21 Evolution of the construction phases of the extension of runway 10-28 to the northwest. The existence of water and the frequent changes of the land pattern have created a loss of coherence on the part of the runway that is extending over the sea (images from google Earth).

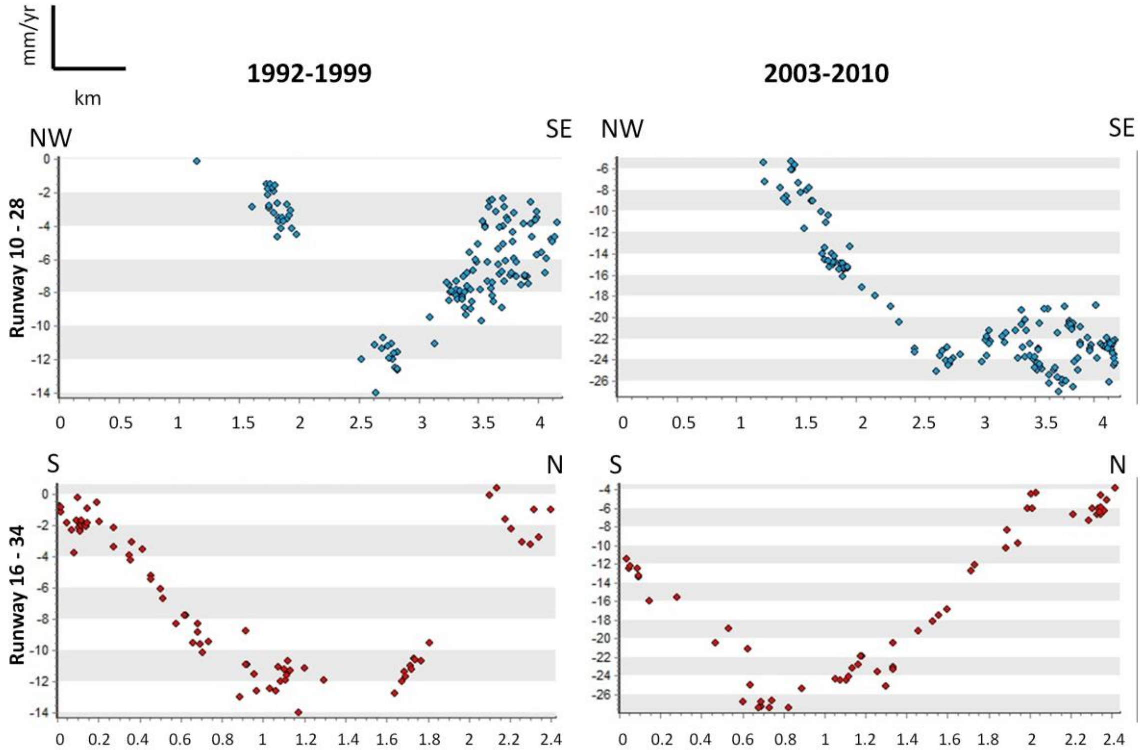

Figure 4.22 Velocity profiles across the runways of Thessaloniki International Airport. The upper panels show the velocity points for the profile along runway 10-28 (blue polygon in Fig. 4.20a) while the lower panels are for the profile along runway 16-34 (red polygon in Fig. 4.20b).

4.2.7 Town of Perea

Perea (rectangle 3 in Figures 4.1 and 4.16b) was among the most popular summer holiday destination for Thessalonians during the '60s and '70s. The rapid and fictitious Greek economic growth of the '80s enabled more and more locals to choose more distant summer destinations. However, the area was kept growing very fast all these years and after 2000 there was an increase in the number of permanent residences.

One of the most crucial issues about Perea is that the southern branch of Anthemountas fault passes through its urban fabric, as it can be seen in Figure 4.23. During 2003-2010, displacement is present to both the footwall and the hanging wall of the north-dipping normal fault (F-2). A closer look at the deforming areas shows that the SAR results, enabled us to detect buildings that have construction failures which were identified during a field survey at the area (Fig. 4.23, 4.24).

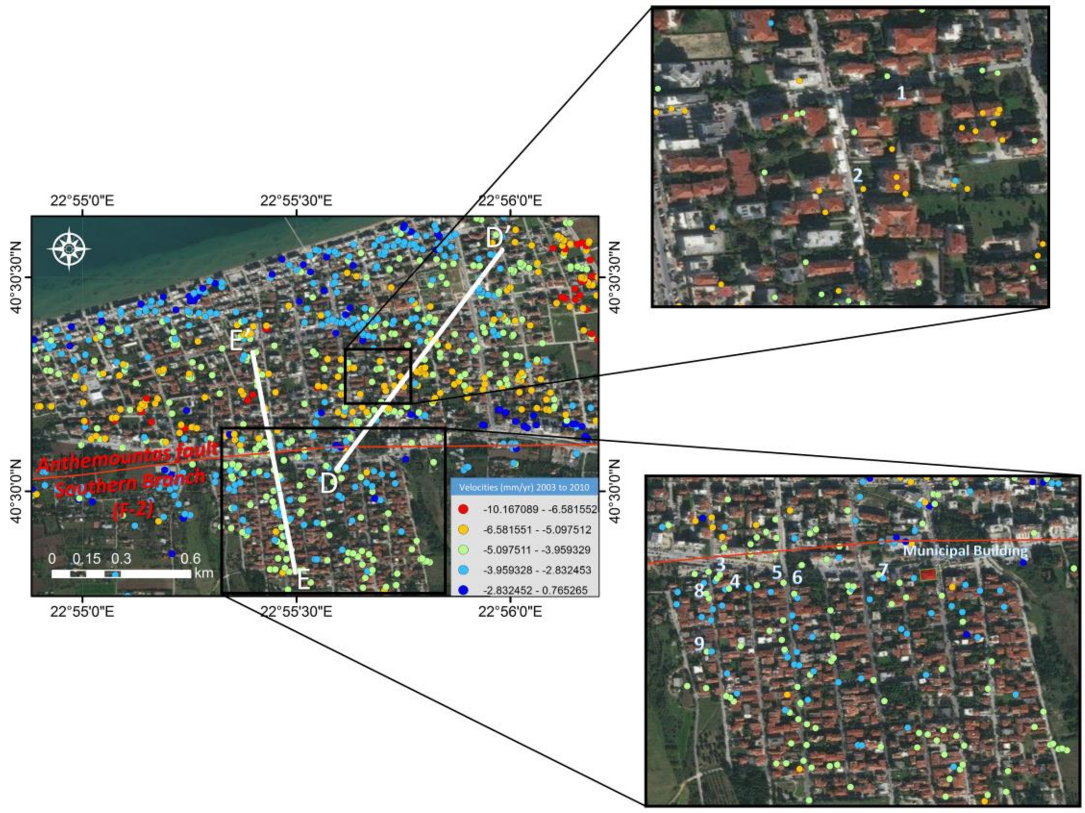

Figure 4.23 Close-up of the area of Perea (rectangle 3 in Fig. 4.11 and rectangle 3 in Fig. 4.16b) showing the displacement of the second monitoring decade (ENVISAT). Velocities in the area show that some locations are stable and others are deforming (with maximum velocity -10 mm/yr). The red line is the southern branch of Anthemountas fault (F-2 in Fig. 4.16b). The white lines in the map are the velocity profiles (E'-E, D'-D) presented in Figure 4.18. Numbers in the two smaller inset maps to the right, are showing in detail the surface velocities occurring at the area together with numbering that represents the failures detected during the field investigation. A picture for each failure number is shown in Figure 4.24.

Figure 4.24 Failures detected at Perea at the areas where there are deformation point results during the ENVISAT monitoring. Red arrows in each image highlight the failures. Numbers of these images can be found also at the two inset maps of Figure 4.23.

Zervopoulou (2010) discusses as potential causes of the Perea failures the aquifer overpumping or the movement of the fault. In Perea from 1992 to 1999, the hanging wall of F-2 appears to be almost stable (Fig. 4.16a). In contrast, during the same period, the footwall is the one deforming. This displacement pattern is not in accordance with the extensional stresses that act at the area thus for the first decade, the tectonic displacement is not the preferred candidate as the main driving mechanism of the detected deformation. During the second decade, the ENVISAT results show that the footwall continues to subside but additionally there is also subsidence to the hanging wall (Fig. 4.23 and rectangle 3 in Fig 4.16b).

4.2.8 Conclusions

The surface deformation of Anthemountas basin is studied via SAR time-series. New SAR results are presented here that show increasing displacement values with the passing of time. Even though the dielectric characteristics of the land enhance difficulties to the time-series monitoring in Anthemountas, from this study a rich number of data revealed new areas that appear to be under deformation. Subsidence is not restricted only close to the faults of Anthemountas and at the proximity of the coastline but also at the far eastern part of the basin.

Additionally, another intriguing result is the existence of subsidence at areas occupied by Neogene deposits.

In the area of study, tectonic movements cannot be ruled out; however, their magnitude should be smaller compared to the maximum values of displacement detected. Hence, the main driving mechanism of the deformation is aquifer overpumping. Nevertheless, the faults are found to directly affect the velocity tendencies. This is reasonable as the footwall consists of stiff Neogene deposits while at the hanging wall, the Neogene deposits are covered by a thick layer of compressible quaternary formations, presenting stronger deformation values.

In conclusion, the detected subsidence in Anthemountas has mainly an anthropogenic cause that lasted continuously at least for 20 years. An area of interest that is subsiding is detected to the north-west of Thermi. At this site, an infrastructure under subsidence was the Thessaloniki Science Center and Technology Museum "NOESIS". Perea is also another location under a subsiding regime in both decades. This comes in accordance with the fact that during the '00s there was an increasing development at the area together with the increase in the number of permanent residences; these increased the water demands at the area.

Overall, a continuation of subsidence now or in the future could cause additional severities and additional building failures. This is crucial both for the various residential areas but also for the Makedonia Airport. Specifically, for the airport, the study presented here shows that there was an increasing subsidence rate at the area where the two runways of the Airport intersect. Moreover, increasing subsiding velocity was detected at the locus of both the current Terminal but also at the site where a new Terminal building is planned to be constructed.

4.3 THE OREOKASTRO CASE

4.3.1 Introduction

A significant number of important industries were established around Thessaloniki over the years. Nowadays, many of these industries no longer exist, reflecting in part the aftermath of the recent fiscal crisis.

The focus of the present study is the industrial area southern of Oreokastro (Fig. 4.25), which is a suburb, north of Thessaloniki. Previous studies, covering the period 1992–1999, indicated that the broader region of Oreokastro (e.g. the area of Galini) (Fig. 4.25) was subsiding. However, sufficient interpretation of the mechanism was not provided. Synthetic aperture radar (SAR) satellites had been used in the past for various applications (e.g. Battazza et al. 2009; Sonobe et al. 2014). In this study, the interferometric synthetic aperture radar (InSAR) technology is used to study in detail the deformation pattern, deformation history and also interpret the mechanism causing it. Here, the deformation history from 1992 to 2010, exploiting ERS 1, 2 and ENVISAT satellites, is presented. Also, an interpretation of the deformation mechanisms and the ambiguous deforming signals, of the industrial area of Oreokastro is attempted.

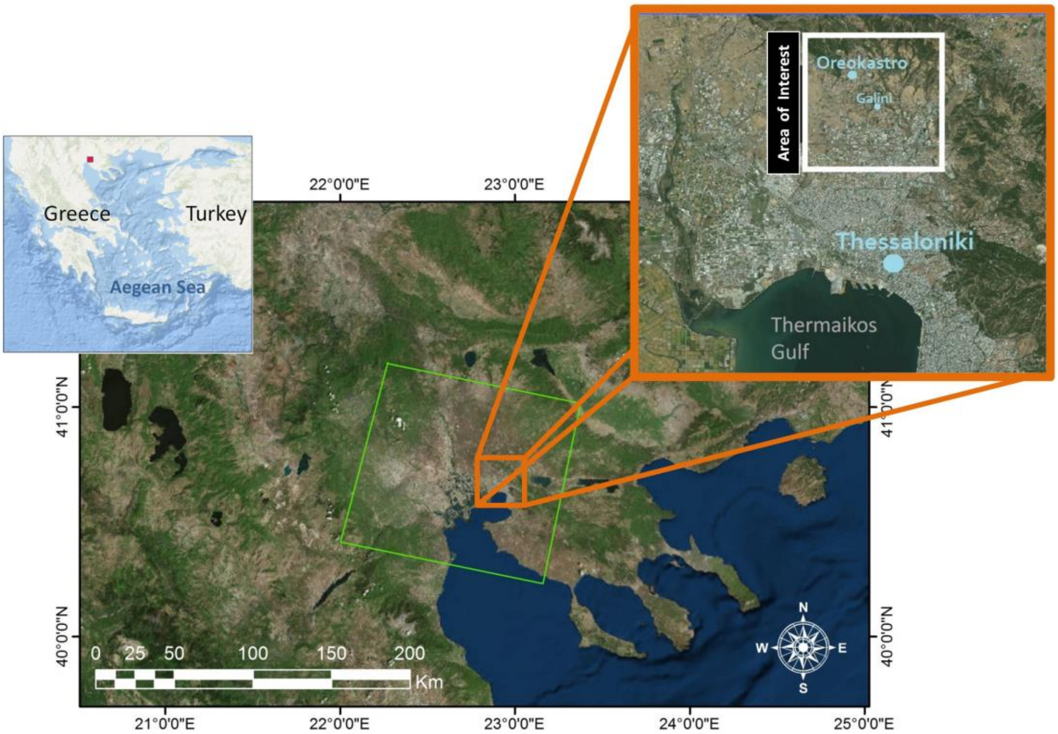

Figure 4.25 Broader region, and the focus region of study, where Oreokastro and Galini are shown in the inset, north of the metropolitan area of Thessaloniki. The green rectangle shows the ERS and ENVISAT satellite frame. In the inset map of Greece to the upper left, the broader study area is denoted with the red rectangle (Svigkas et al. 2017).

4.3.2 Geology and seismicity of the area

The broader area of Oreokastro lies mainly on Neogene formations. The urban fabric of the town is located on Pliocene lake and fluvial deposits, consisting of red clays intercalated by sands, pebble gravels and marls, and at a lesser extent of Pre-Alpine carbonate rocks and schists (Fig. 4.26). Two available drill profiles show Pliocene clays intercalated by sand, lying above the Pre-Alpine bedrock. The previously described stratigraphy contains a system of successive confined aquifers, which prior to the installation of the industries, were artesian. The faults of the area are part of the broader tectonic regime of the Mygdonian graben.

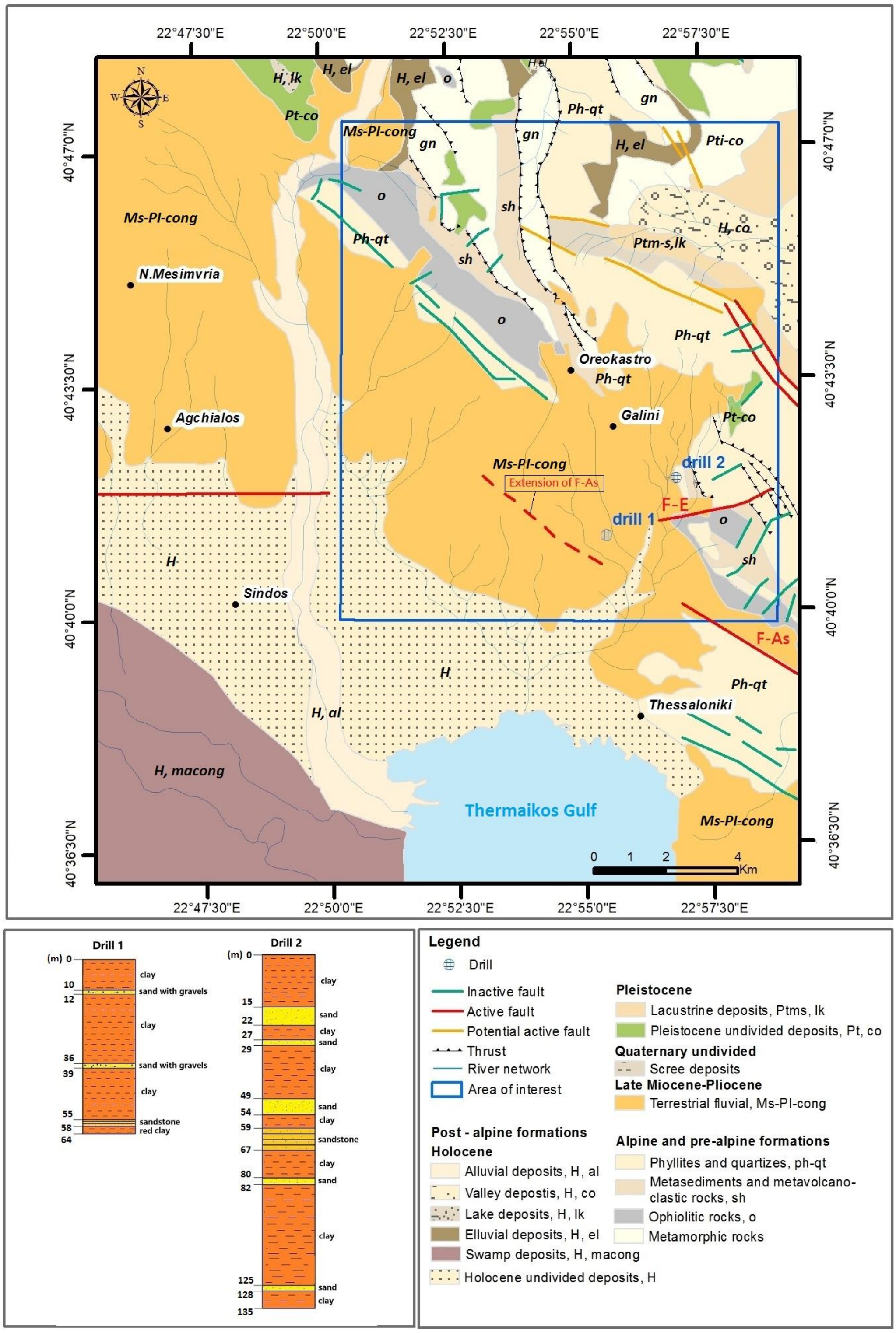

Figure 4.26 Geology of Oreokastro and the surrounding area. The location of the two geotechnical drills located at the bottom left of the figure, is noted on the map. Borehole data are archives of the Directory of Environment, Thessaloniki Prefecture. Map is from EPPO (1996), Neotectonic Map of Greece, Thessaloniki sheet (image from Svigkas et al. 2017).

The governing extensional stresses are expressed with normal faulting and seismicity all over the area most of which is localized within the graben (Fig. 4.27). Two main tectonic structures cross south of Oreokastro (Fig. 4.27), the extension of Asvestochori fault (fault F-As) and the Efkarpia fault (fault F–E) (Zervopoulou, 2010; Zervopoulou and Pavlides, 2005). The Asvestochori fault, at the northern side of the city of Thessaloniki, follows the Exochi–Asvestochori axis and crosses south of the study area. This is a normal fault, considered by structural geologists as potentially active (Zervopoulou, 2010). The Efkarpia fault is located at the northern part of the city close to the Efkarpia suburb, at a distance of 6 km from the city centre. This structure is also considered as potentially active (Zervopoulou, 2010). No strong earthquakes have been recorded during the instrumental period; however, the abundant microseismicity (e.g. Papazachos et al. 2000; Paradisopoulou et al. 2006; Garlaouni et al. 2015) renders these structures, from a seismological point of view, to be considered as active.

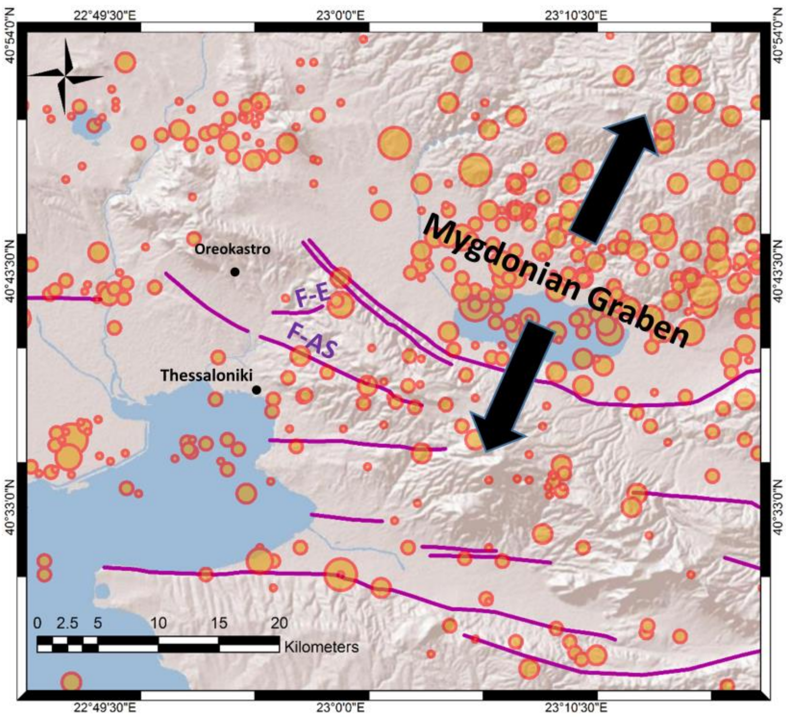

Figure 4.27 Location of Thessaloniki and Oreokastro, alongside the two main tectonic features of F–As and F–E, in terms of the broader regional tectonic pattern. Most of the seismicity is located in Mygdonian Graben which is under an extensional stress regime (Svigkas et al. 2017).

4.3.3 Previous studies for the area of Oreokastro

The deforming pattern detected in the region south of Oreokastro attracted the attention of many researchers (Raucoules et al. 2008; Mouratidis, 2010; Zervopoulou, 2010; Mouratidis et al. 2011; Svigkas et al. 2015; Costantini et al. 2016). Raucoules et al. (2008) were the first to find a deforming signal during the period 1992–1999 (-10 to -20 mm/year) using radar interferometry. Prior to the InSAR studies, the area was not known to deform. Previous hypotheses regarding the nature of the deformation were mainly related to the tectonic activity and the microseismicity (Raucoules et al. 2008; Mouratidis 2010; Mouratidis et al. 2011). Zervopoulou (2010) mentions that in 2006 there were cracks reported on the buildings of the area that can be attributed either to aseismic slip or to overpumping. The aforementioned studies had a significant contribution to the investigation of the phenomenon, although only the work of Zervopoulou (2010) had a considerable focus on Oreokastro. In most cases, the reference to this area was a subpart of a more general study. That is why, even though these studies were complete, when it comes to the interpretation of the driving mechanism of the detected deformation pattern, there is a lack of proof and of a clear and systematic answer. Raucoules et al. (2008) were the first to detect subsidence in the region and in their preliminary study Svigkas et al. (2015) were the first to detect an uplifting pattern for the period of 2003–2010. This change in the deformation pattern is the motivation of the present work, which seeks a more in depth and detailed analysis of the deformation pattern observed at the industrial area of Oreokastro, spanning two decades, alongside a plausible interpretation of the driving mechanism.

4.3.4 Methods, data and software

InSAR has been previously used effectively to monitor the aquifer activity (e.g. Ikehara and Phillips 1994; Amelung et al. 1999; Galloway et al. 1999; Bell et al. 2008; Taniguchi et al. 2009; Lu and Danskin 2001; Chen et al. 2007; Raspini et al. 2013, 2014; Ishitsuka et al. 2014; Svigkas et al. 2016) and is considered as an important input for hydrogeological research. In SAR time-series techniques, radar images that spread in time are processed in pairs and these form the differential interferograms. Each point of a differential interferogram represents a phase difference between the two satellite acquisitions. This phase difference is contaminated with noisy signals, present due to temporal and geometric decorrelation effects and because of atmosphere perturbations between successive image acquisitions. Following a number of corrections (orbits, digital elevation model, and changes in atmosphere) and filtering, the phase difference of each point is translated to surface displacements. Over the years, many time-series techniques have been developed (e.g. Kampes and Usai 1999; Berardino et al. 2002; Arnaud et al. 2003; Mora et al. 2003; Lanari et al. 2004; Hooper et al. 2004, 2007; Duro et al. 2005; van der Kooij et al. 2006; Costantini et al. 2008; Ketelaar 2009). The implemented techniques herein are the small baseline subset (SBAS) (Berardino et al. 2002), the permanent scatterers (PS) interferometry (Ferretti et al. 2000, 2001) and a hybrid approach merging both estimation worlds (Hooper 2006; Hooper et al. 2007). PS and SBAS methods exploit stacks of the differential interferograms that are formed based on connections of the satellite acquisitions, as described in the previous sections of this thesis.

ERS 1,2 (46 level_0 Images) and ENVISAT (37 level_0 images) data both from track 279, covering the period 1992–1999 and 2003–2010, respectively, courtesy of the European Space Agency (ESA) were exploited. For the analysis, orbital data were used from Delft University of Technology and VOR data were offered by ESA. The datasets used and the SBAS connection graphs created in the SAR analysis procedure, are presented in Figure 4.28. Topographic corrections were based on the SRTM Digital Elevation Model V3, 90-m spatial resolution (e.g. Farr and Kobrick, 2000), and the mass processing was conducted with the StaMPS (Stanford Method for Persistent Scatterers) algorithm (Hooper 2006; Hooper et al. 2007) and also with the SARscape© software (from Sarmap, CH). Prior to the time-series processing with StaMPS, the focusing was accomplished with ROI-PAC (Repeat Orbit Interferometry Package), developed by California Institute of Technology and Jet Propulsion Laboratory (NASA), and the interferograms were generated with DORIS (Delft Object-Oriented Radar Interferometric Software).

ERS

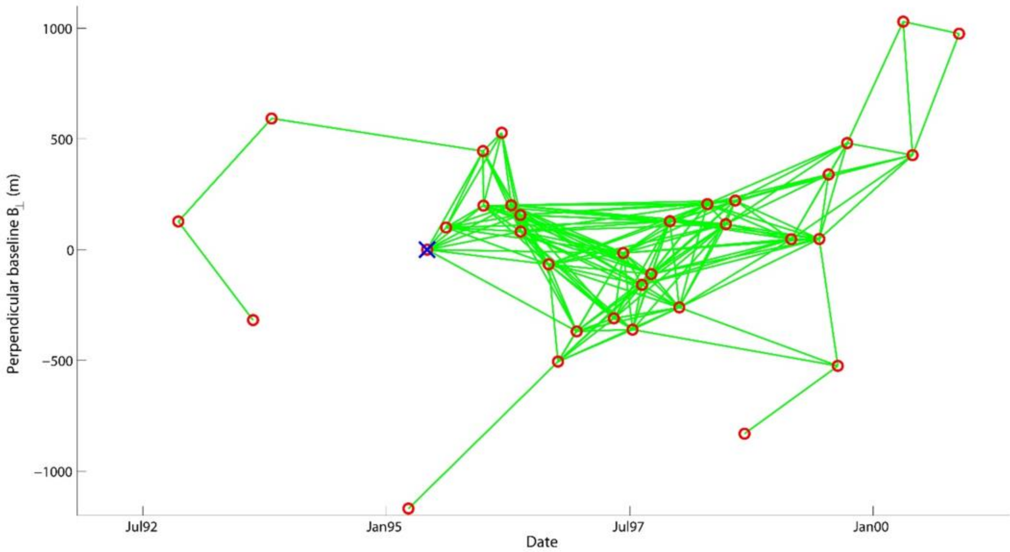

ENVISAT

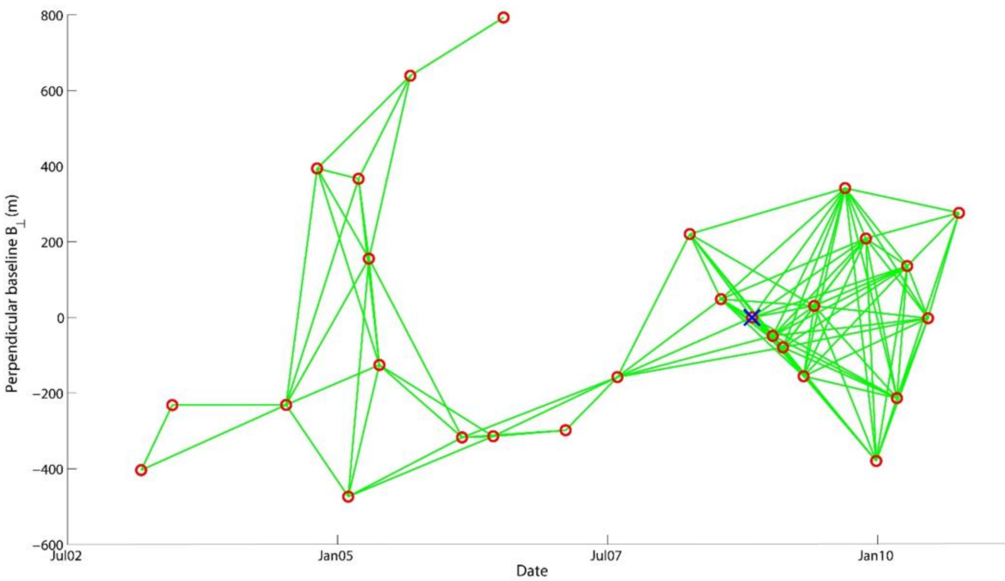

Figure 4.28 Graphs showing the radar data used in the study and the SBAS SLC connections for ERS and ENVISAT datasets.

4.3.5 Displacement results for Oreokastro

Time-series analysis results are presented in Figures 4.29 and 4.30, as derived by both PS and SBAS using the StaMPS algorithm. The analysis shows that the metropolitan area of Thessaloniki is relatively stable. When it comes to the area southern of Oreokastro, close to Galini, subsidence is the main deformation feature during 1992–1999, according to both PS and SBAS (Fig. 4.29).

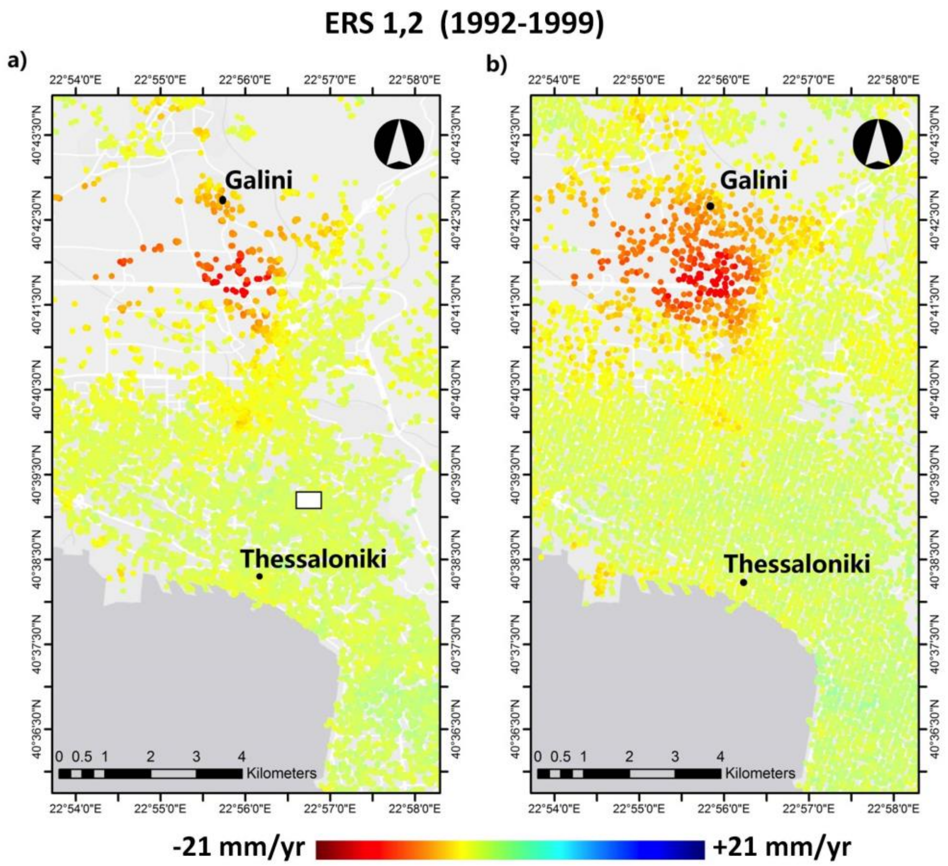

Figure 4.29 Results of the a) PS and b) SBAS analysis for the period 1992–1999. The metropolitan area of Thessaloniki is stable. The largest deformation signal is detected southern of Oreokastro close to Galini (up to -21 mm/year). The white rectangle in (a) shows the reference area used for the SAR processing. As it can be seen, the results of the PS and SBAS techniques are in agreement (Svigkas et al. 2017).

However, during the second decade (Fig. 4.30) there is a different pattern of deformation at the same area that indicates an uplifting surface. In Figure 4.31, the combined velocity result of the PS and SBAS (from StaMPS) for both decades at the broader area of Oreokastro is presented. Unwrapped interferograms are shown in Figure 4.32. For a further validation of the detected uplifting signal during the second decade and in order to cross-check the StaMPS results, the SARscape software was also used for the ENVISAT dataset. All results from all implemented techniques, from both software, are in accordance; the uplifting pattern during 2003–2010 is fully confirmed. The SARscape results are shown in Figure 4.33.

Repeated field inspections were performed at the area in order to chart the potential building failures that the deformation pattern might had created. The detected deforming points, which were estimated from the SAR processing analysis, have an great spatial relation with failures detected at the industrial buildings during the field survey.

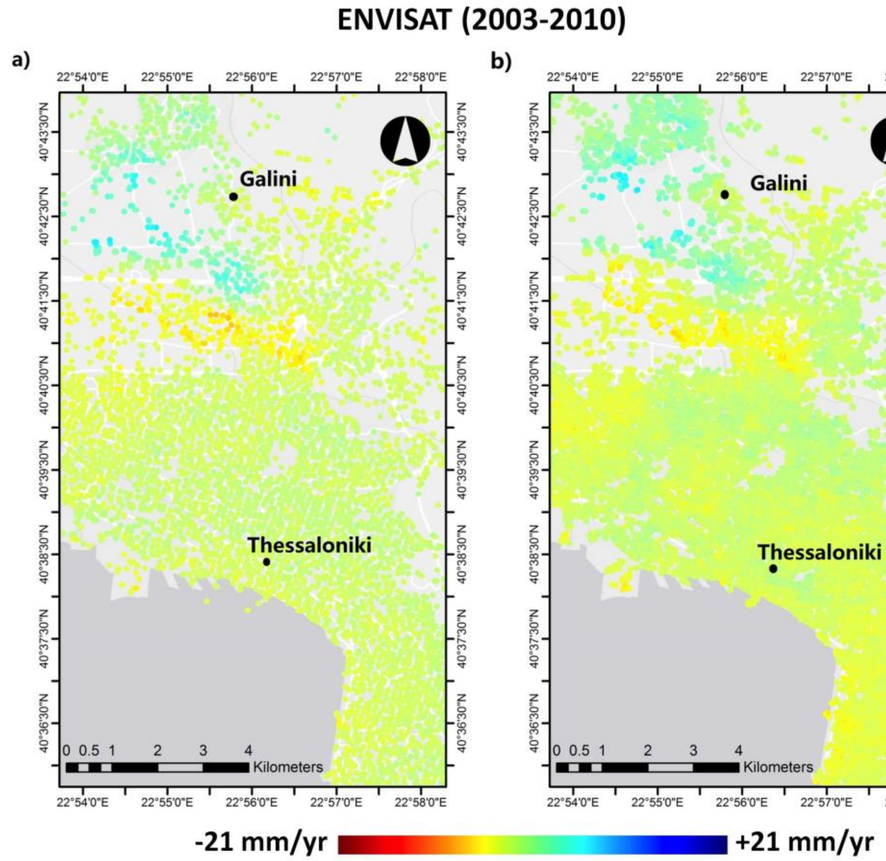

Figure 4.30 Results of the SAR time-series analysis for the period 2003–2010. a) PS results, b) SBAS results. Again, the results of the two techniques are in agreement. The interesting fact is that in the study area close to Galini, during the second decade, there is an uplifting trend that is opposed to the deformation pattern of the 1990s. The maximum detected uplifting value is about +9 mm/yr (Svigkas et al. 2017).

In Figure 4.34, the detected building failures are shown, together with the detected deforming points from 1992 to 1999 and in Figure 4.35 the PS time-series graph of a point located at the same area is presented. In all cases, the failures were attributed to the differential settlements of the building due to the subsidence.

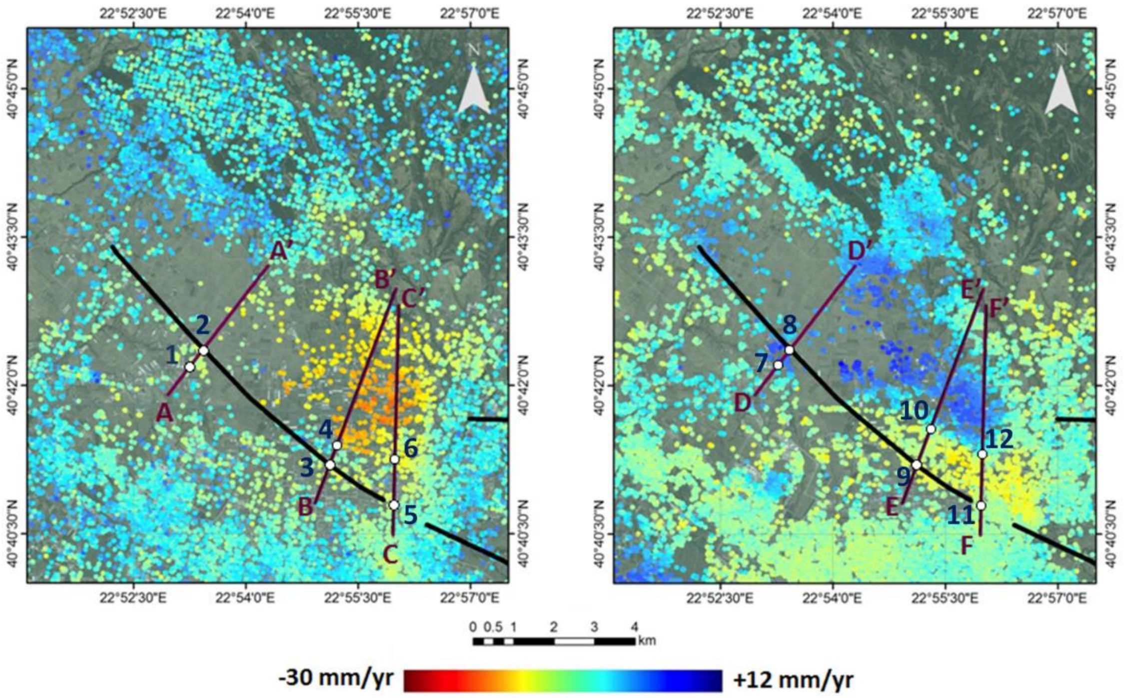

Figure 4.31 Combined results of the PS and SBAS techniques of the broader area of Oreokastro. Known faults (black continuous lines) from NOA fault database. During 1992–1999 (left) the maximum subsidence value is 21 mm/year, and during the second decade (right) the maximum uplifting value is 9 mm/year. The faults appear to interact with the deformation pattern; they act as groundwater barriers. Traces A–A', B–B', C–C', D–D', E–E', F–F' on the two maps, are the velocity and topographic profiles presented in Figs 4.40-45. Points 1–12 are ad hoc selected locations (Svigkas et al. 2017).

ERS unwrapped

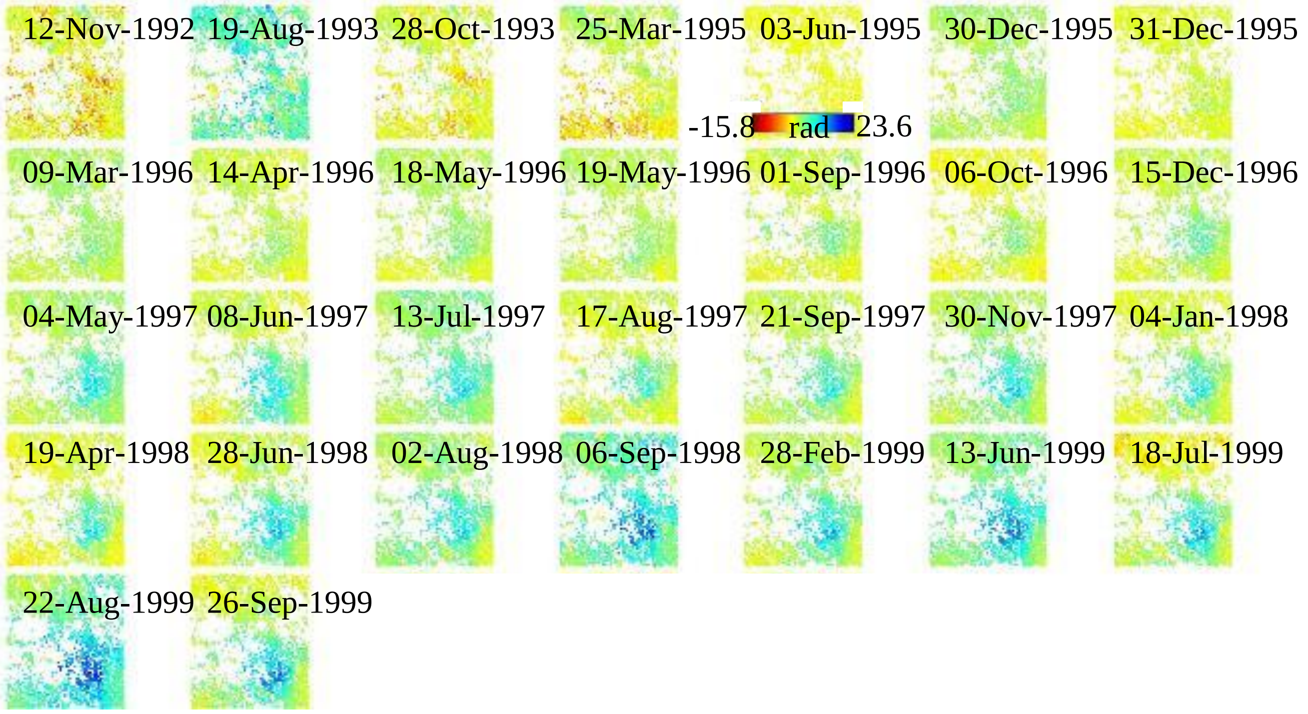

ENVISAT unwrapped

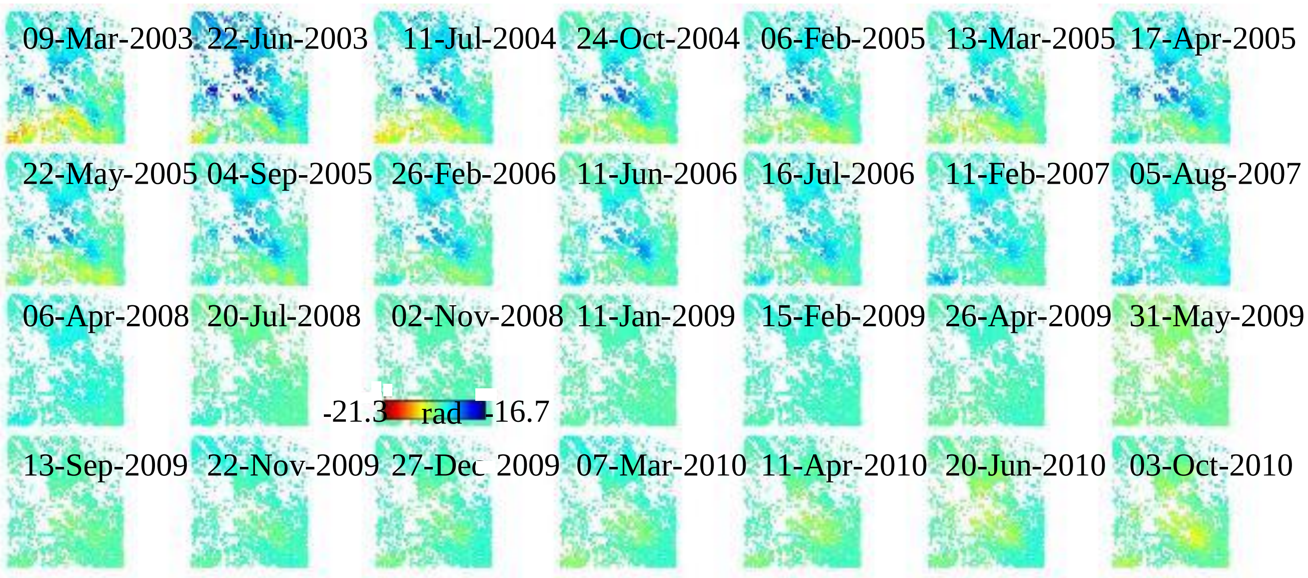

Figure 4.32 StaMPS unwrapped Interferograms of ERS 1,2 & ENVISAT.

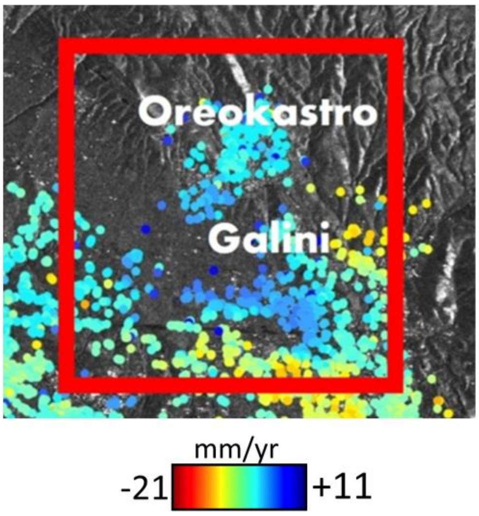

Figure 4.33 ENVISAT surface velocities of the study area using the SARscape software (Svigkas et al. 2017).

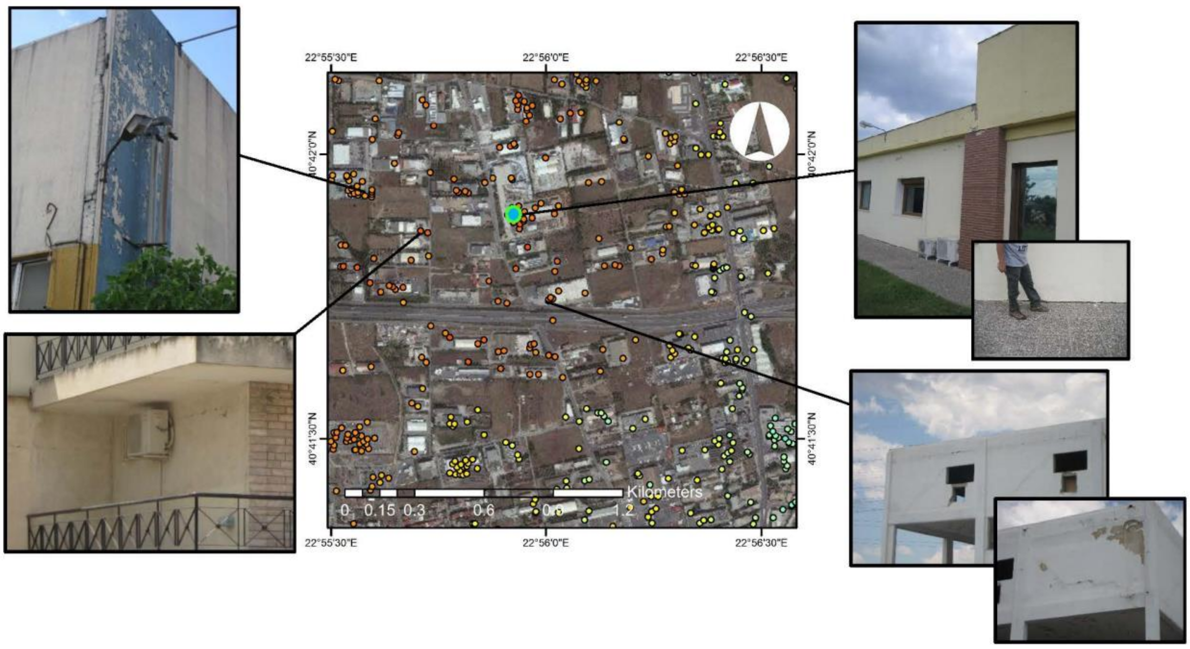

Figure 4.34 Map showing the correlation of the time-series measurements of the first decade (subsidence) with failures detected in the field (left and right). The light blue-light green dot is a point whose time-series is presented in Figure 4.35 (Svigkas et al. 2017).

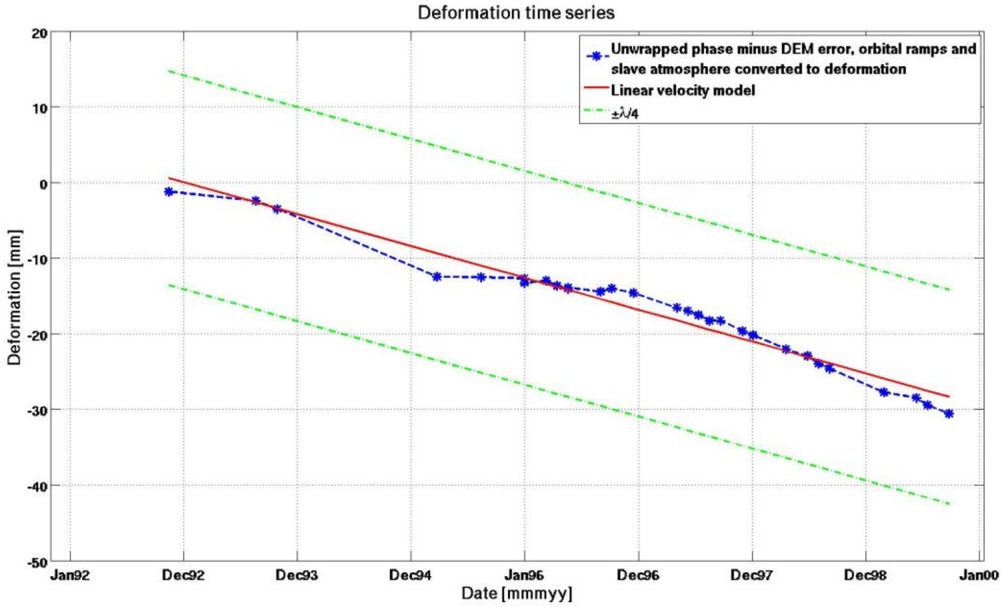

Figure 4.35 Deformation time-series of the point in map of Figure 4.34 (Svigkas et al. 2017).

4.3.6 Investigation of driving mechanisms

For the broader industrial area of Oreokastro, one of the scenarios that previous studies have proposed as a mechanism is a connection of the deforming signal with seismicity and fault activity. This interpretation is not supported by the magnitude of the detected deforming signal in the 90s (-21 mm/year) which is far too large for this small area to be solely due to tectonic activity. The contribution of tectonic activity in the deforming signal is either zero or negligible, and for the latter case it is valid only for the period 1992–1999. The deformation history over the two decades provides interesting insights; there are extensional tectonics in the area that cannot be expressed by an uplifting surface. Thus, the scenario of tectonic activity and aseismic slip as the main driver mechanism that caused the deformation pattern at Oreokastro is rejected. Another plausible scenario for the detected deformation could be the natural compaction of the sediments. However, this phenomenon cannot take place in already consolidated or even over-consolidated Neogene formations, like the formations that occupy the narrow study area. Furthermore, this scenario is not in accordance with the change in the trend of the deforming pattern that took place during the second decade, because, fundamentally, the subsidence due to natural compaction is irreversible. As a result, natural compaction cannot be considered as the main driving mechanism of the deformation phenomena. Interesting conclusions can be extracted from the correlation of the land use with the deformation pattern. The focus area is one of the industrial zones of Thessaloniki. This area hosts numerous water-consuming industries such as textile and fabric production units, mineral oil and lubricant production units, paint factories among others. For decades, the need for water was covered by municipality drills and by private drills, in the latter case most of them illegal. This status changed in 2008 when the Thessaloniki Water Supply and Sewerage Co. SA (trading as EYATH SA) connected Oreokastro to the water supply network of Thessaloniki. Despite this fact, some private drills are still in operation, nowadays. As presented in Figure 4.36, the areas with the largest amount of deformation are confined within the limits of the industrial zone and as previously stated, within an area with overexploited aquifers, at least before 2008.

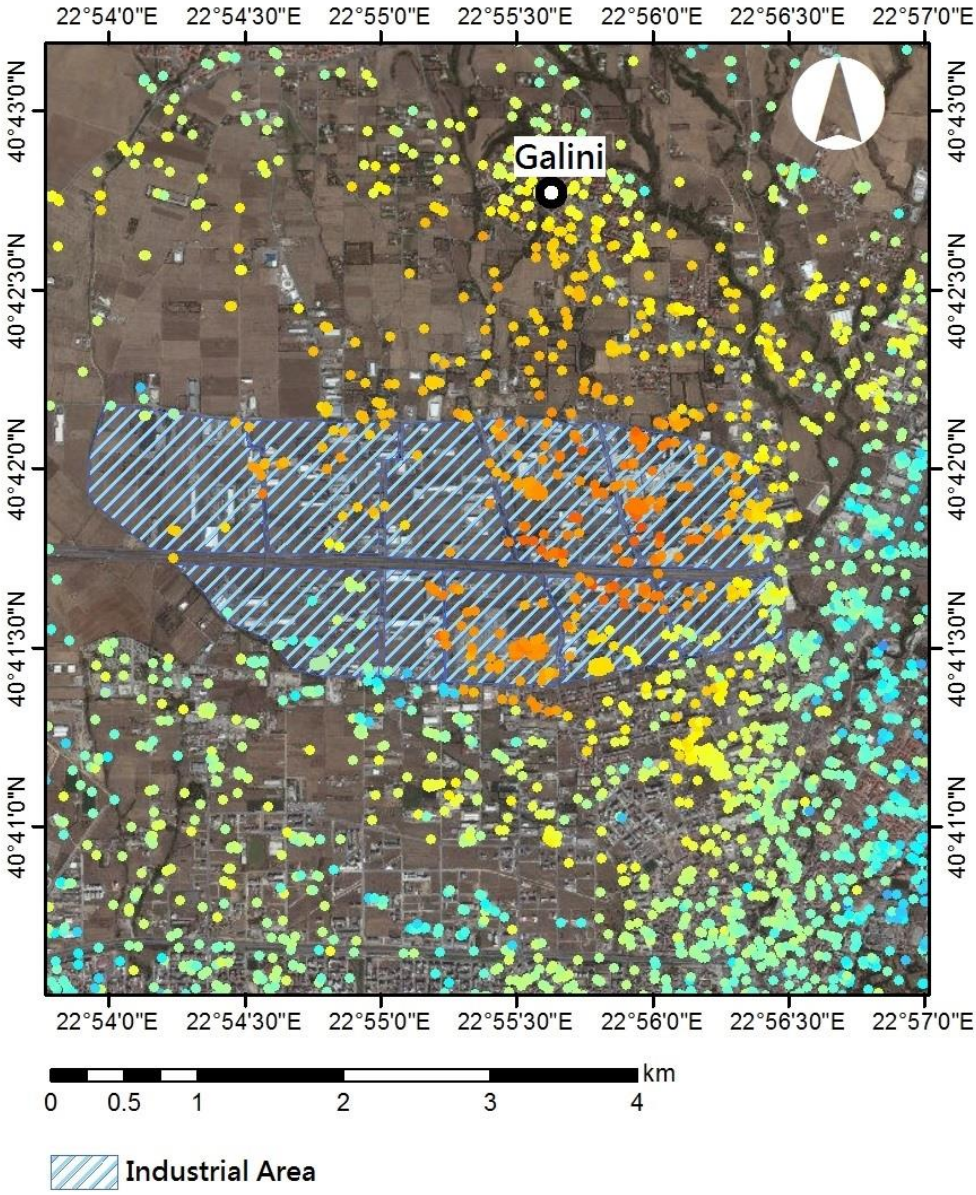

Figure 4.36 Industrial areas of Oreokastro are highlighted within the hatched polyline. The spatial relation of the SAR point measurements indicating the subsidence distribution (ERS dataset) with the high water demand industrial land use, is in agreement with the scenario assigning the phenomena to the aquifer overpumping (Svigkas et al. 2017).

To exploit these options, the hydrogeological regime of the confined aquifers of the study area was examined by evaluating measurements of the ground-water level, conducted by the authors. Unfortunately, the measurements refer to random campaigns conducted since 1995 up to the present. According to these data, the aquifers, which during the 1960s were artesian, ended up at the winter of 1995 with a drawdown from -60 to the maximum value of -200 m. On the contrary, based on the data of the winter of 2016, the falling trend was reversed and the aquifer recovered sufficiently presenting groundwater level values from -10 to -55 and in some cases with artesianism. The recharge of the aquifer system is presented in Figure 4.37. In order to construct the contour curves that express the spatial distribution of the groundwater recharge, Kriging techniques were utilized at the groundwater level differences (between 1995 and 2016). Kriging is a technique for making optimal, unbiased estimates of regionalized variables at non-sampled locations, using the structural properties of the semivariogram and the initial set of data values (David, 1977). The main advantage of Kriging is that it takes into consideration the spatial structure of the parameter that is investigated an approach that is not followed in other methods like arithmetic mean method, nearest neighbour method, distance weighted method and polynomial interpolation (Ly et al. 2013). In addition, Kriging provides the estimation variance at every estimated point, which is an indicator of the accuracy of the estimated value (Kumar, 2007).

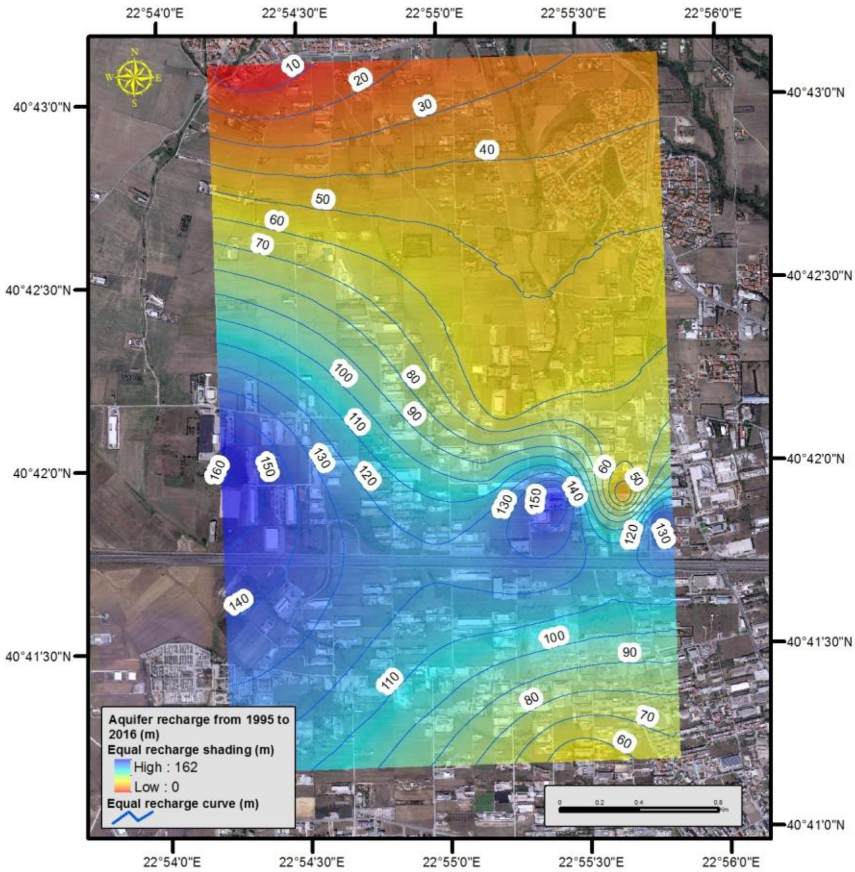

Figure 4.37 Image presenting the groundwater recharge (in m) between winter 1995 and winter 2016. Positive values of the aquifers recharge contour indicate recharge of the groundwater level (Svigkas et al. 2017).

The artesianism in the area was also expressed with inundation phenomena with limited extent (Fig. 4.38). This recharge could be attributed to two factors: firstly, to the establishment of a water network at the industrial area, connected with the water supply network of EYATH S.A., and secondly to the financial crisis that led numerous industries to shutdown, reducing the overall water consumption at the entire industrial zone. To sum up, the detected deformation pattern as well as the trend eversion can be clearly combined with the hydrogeological regime of the study area and as a result, the groundwater variations can be considered as the main driver mechanism of the land subsidence-uplift phenomena.

Figure 4.38 Inundation phenomena due to the recovery of the underground water level (Svigkas et al. 2017).

4.3.7 Investigation for new tectonic insights

A thorough look at Figure 4.31 indicates that there is a possible relation of the faulting regime of the wider area with the deformation pattern. The deformation pattern of the 2003–2010 dataset appears to be bordered to the west by the extension of the Asvestochori fault. This can also be seen clearly from the differential interferogram presented in Figure 4.39. Thus at first, the existence of the fault that was presented by structural geologists in the past is also detected via satellite-based observations. Secondly, the fact that the deformation pattern related with aquifer activity is affected by tectonic structures gives valuable information regarding the effect of the fault to the extent of the aquifers.

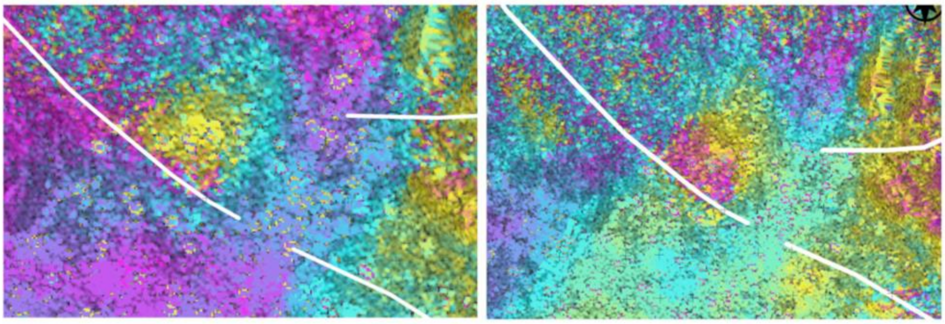

Figure 4.39 Differential interferogram presenting the interaction of the fault with the deformation pattern of Oreokastro.

Previous satellite remote sensing studies using SAR Interferometry in Las Vegas Valley, Los Angeles, Bakersfield and other areas (Amelung et al. 1999; Galloway et al. 1999; Bawden et al. 2001; Lu and Danskin 2001) indicate that the existence of faults may play an important role in the surface deformation caused by aquifer activity. In our case, the pattern detected at the industrial area of Oreokastro appears to be a spatially fault-controlled and confined deformation. The extension of Asvestochori fault, south-west of Oreokastro, appears to affect radically the stratigraphy of the Neogene sediments controlling the extent and the continuity of the aquifers, practically acting as a groundwater barrier. Moreover, the careful screening of the deformation pattern reveals a feature that is not supported by any known structure. More specifically, the localized uplifting deformation pattern of 2003–2010 appears to have an abrupt ending to the southeast, creating a linear feature.

In order to better investigate this, but also define better the aforementioned interaction with the extension of the Asvestochori fault, a series of velocity profiles were created (Figs. 4.40-45) at crucial locations together with the topographic profiles for the same traces. The profiles' surface traces (A–A', B–B', C–C', D–D', E–E', F–F') are depicted in Figure 4.31. Points 1–12 of Figure 4.31 are located at areas where the profile trace cuts either the unknown linear feature or the Asvestochori fault. The points are also notated in every velocity profile. Indeed, in the velocity profiles it can be clearly seen that there is a disturbance or change of the velocity trend each time that it meets either the

Asvestochori fault (these areas are notated with black vertical lines in the velocity profiles) or the proposed linear feature (these areas are notated with red vertical lines in every velocity profile). The linear feature is an unknown fault or structure that restricts the deformation pattern, which is either subsiding (Figs. 4.40-42) or uplifting (Figs. 4.43-45). This previously unidentified structure appears to lie at the area acting, as a groundwater barrier. The proposed structure is presented in Figure 4.46. A drilling or a geophysical survey campaign can be conducted at the area that would offer further insights.

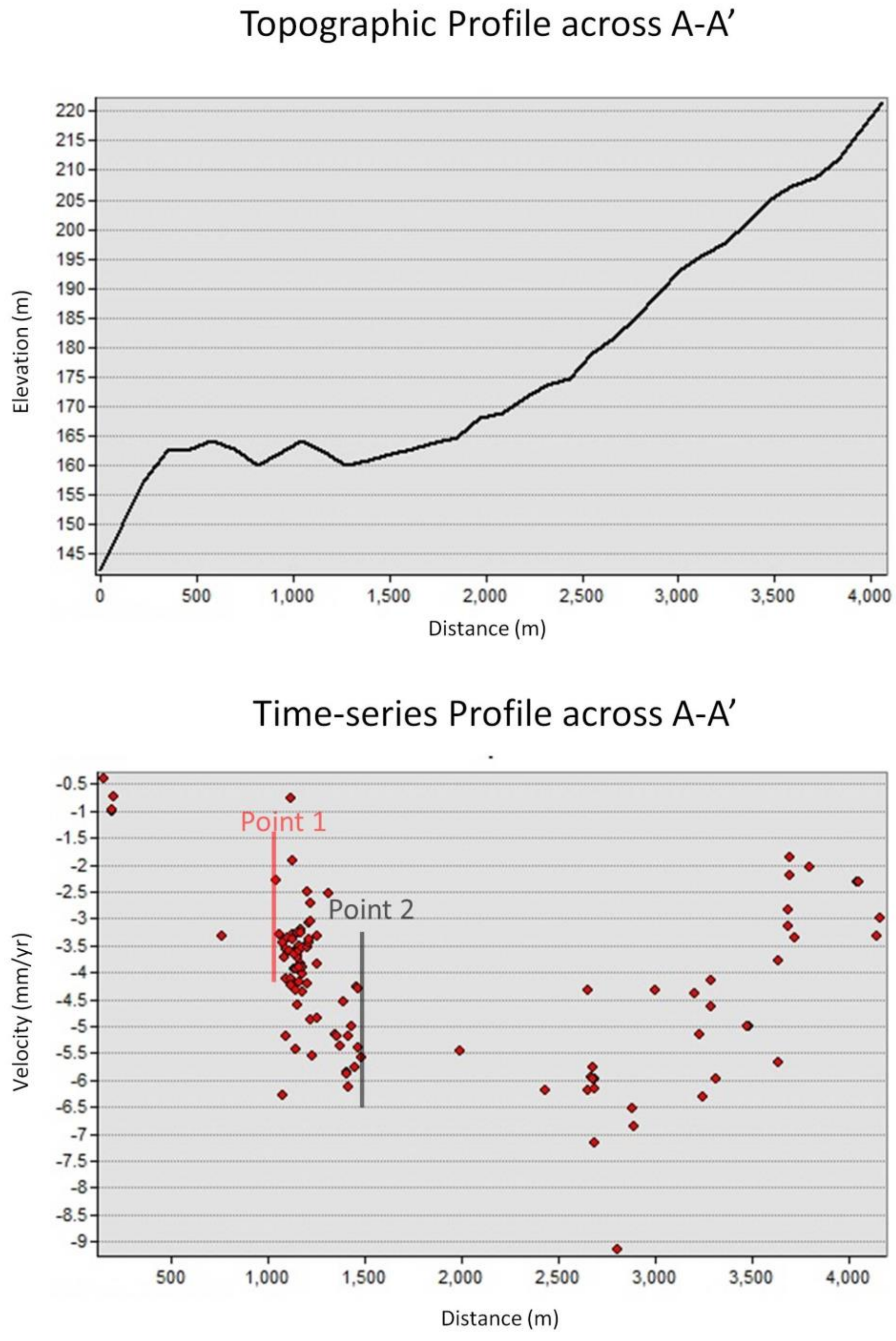

Figure 4.40 Velocity and topographic profiles for the trace A–A’. The intersection of each trace’s profile with the Asvestochori fault (Fig. 4.31) is denoted with a black vertical line. The intersection of each trace’s profile with the previously unknown structure is denoted with a red vertical line. Notice that in either cases there is a low or sharp disturbance in the velocities (Svigkas et al. 2017).

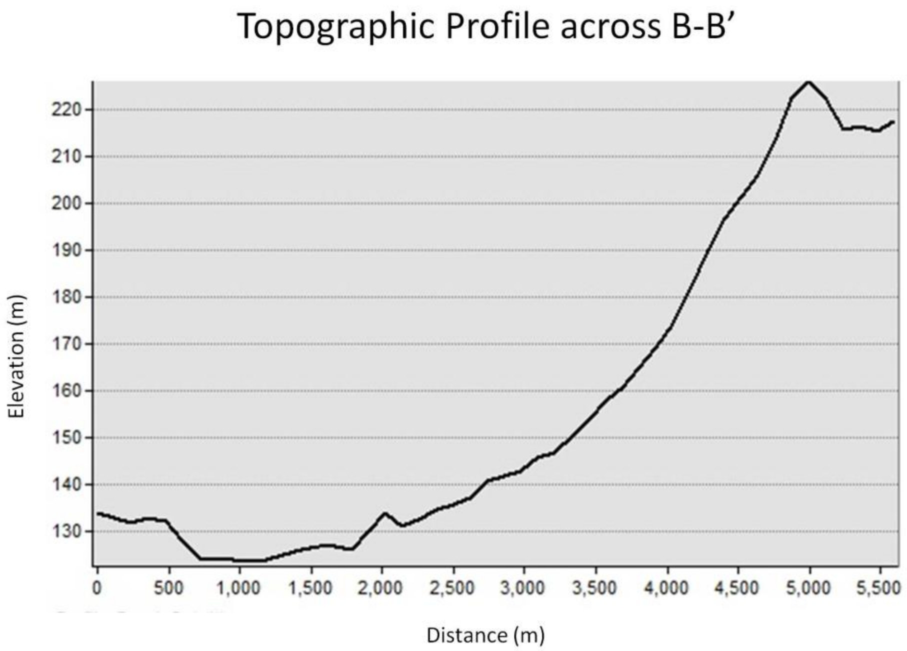

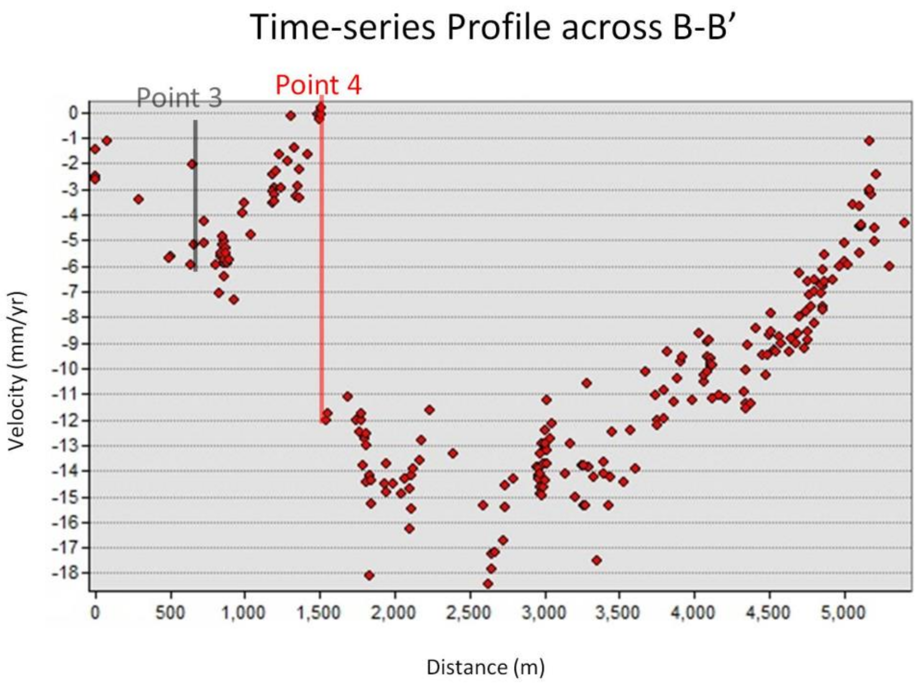

Figure 4.41 Velocity and topographic profiles for the trace B– B'. The intersection of each trace's profile with the Asvestochori fault (Fig. 4.31) is denoted with a black vertical line. The intersection of each trace's profile with the previously unknown structure is denoted with a red vertical line. Notice that in either cases there is a low or sharp disturbance in the velocities (Svigkas et al. 2017).

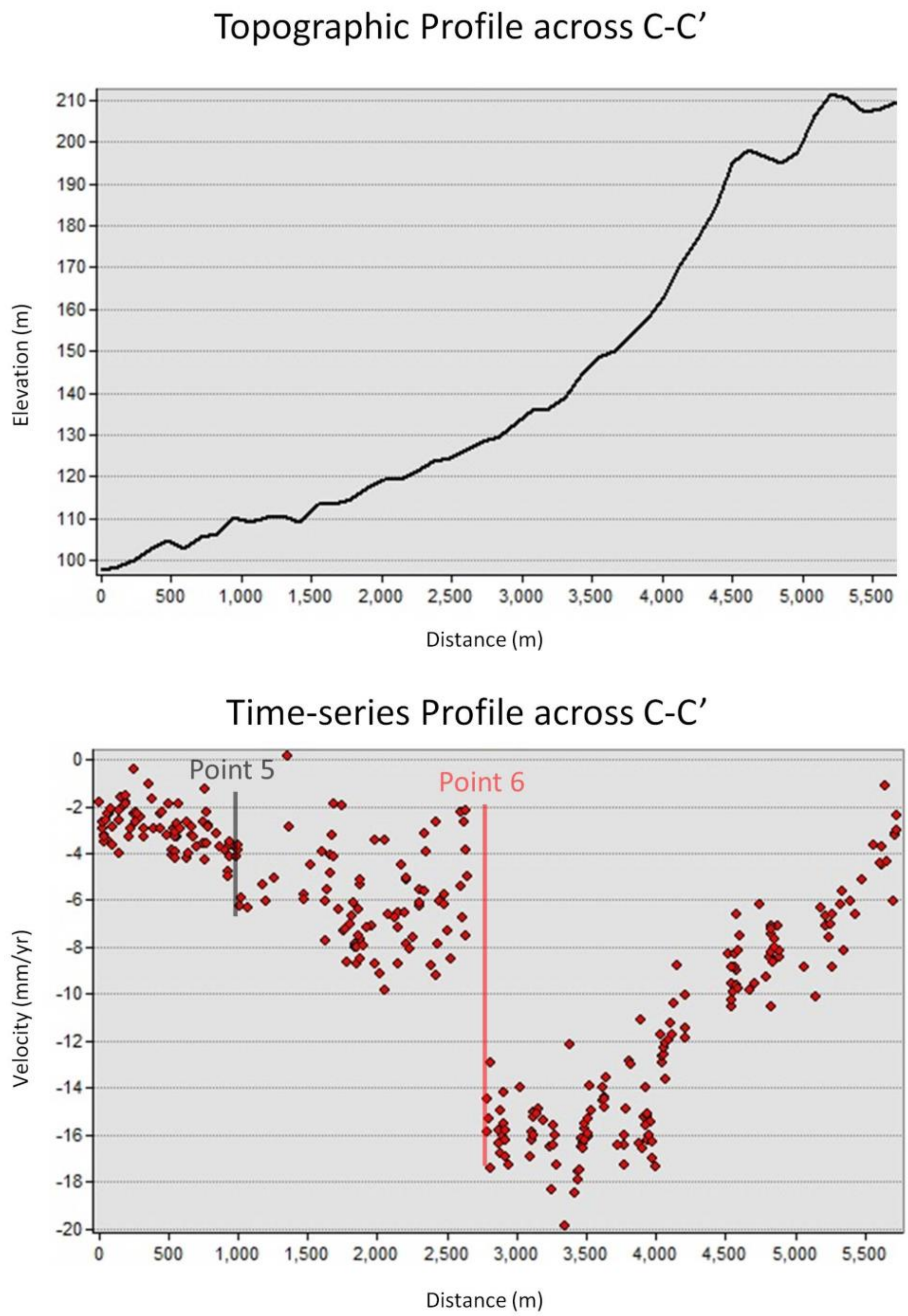

Figure 4.42 Velocity and topographic profiles for the trace C– C’. The intersection of each trace’s profile with the Asvestochori fault (Fig. 4.31) is denoted with a black vertical line. The intersection of each trace’s profile with the previously unknown structure is denoted with a red vertical line. Notice that in either cases there is a low or sharp disturbance in the velocities (Svigkas et al. 2017).

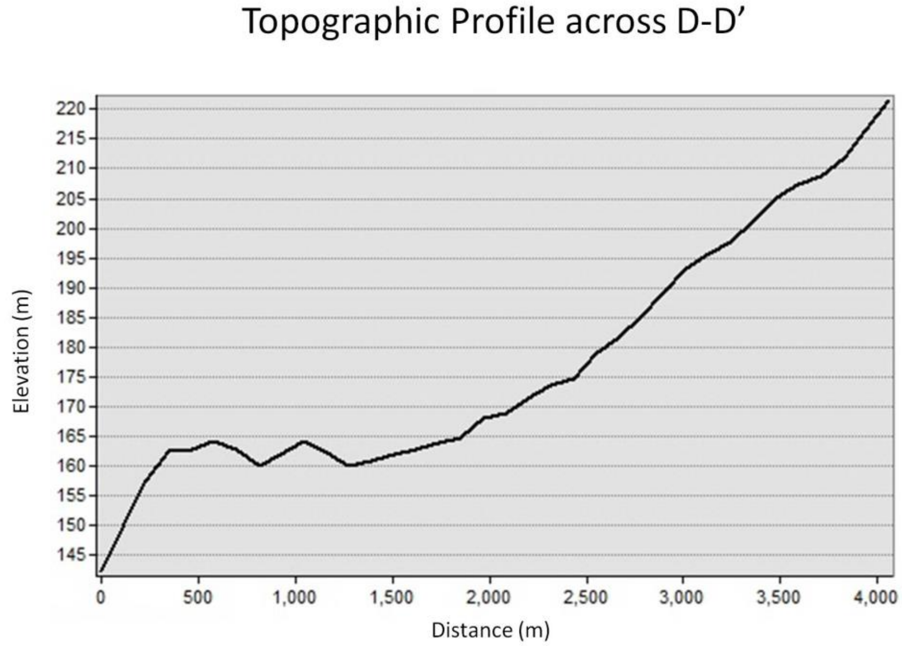

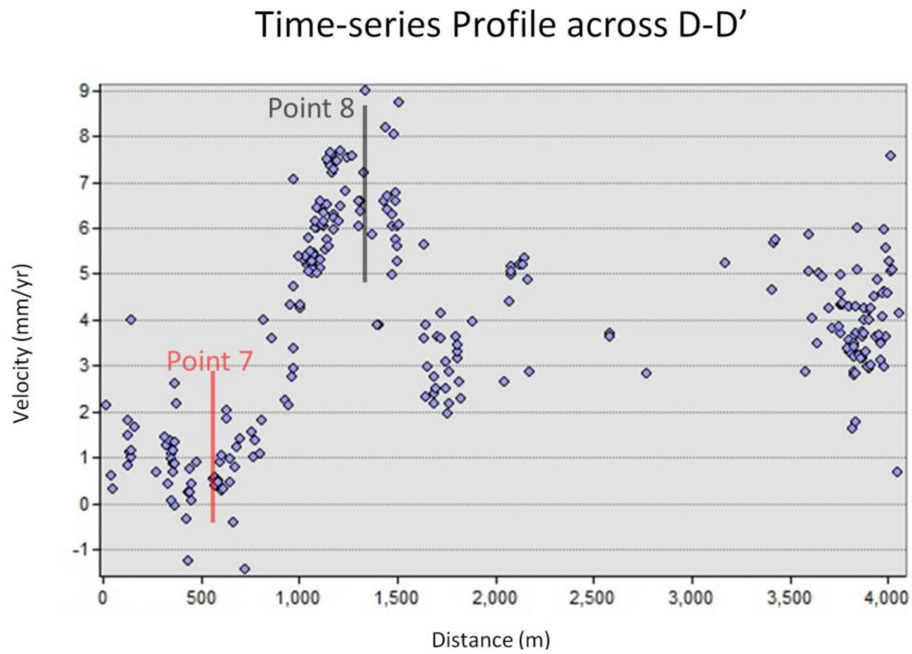

Figure 4.43 Velocity and topographic profiles for the trace D– D’. The intersection of each trace’s profile with the Asvestochori fault (Fig. 4.31) is denoted with a black vertical line. The intersection of each trace’s profile with the previously unknown structure is denoted with a red vertical line. Notice that in either cases there is a low or sharp disturbance in the velocities (Svigkas et al. 2017).

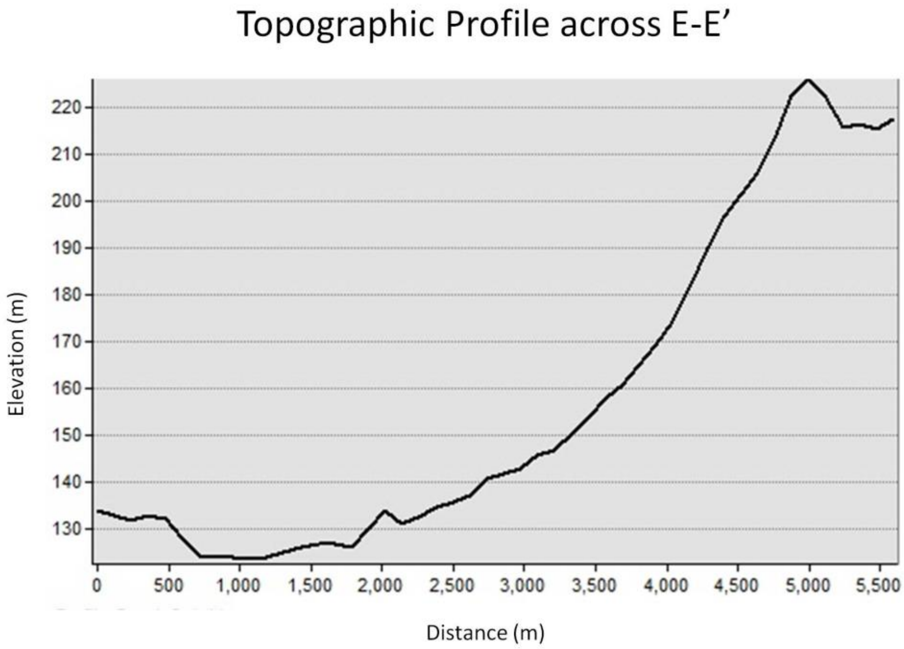

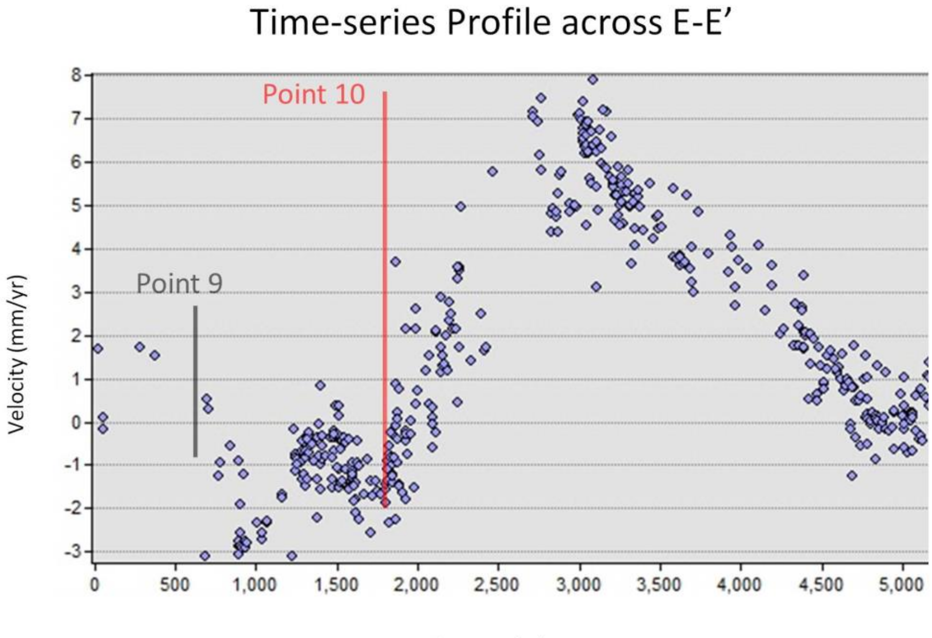

Figure 4.44 Velocity and topographic profiles for the trace E– E'. The intersection of each trace's profile with the Asvestochori fault (Fig. 4.31) is denoted with a black vertical line. The intersection of each trace's profile with the previously unknown structure is denoted with a red vertical line. Notice that in either cases there is a low or sharp disturbance in the velocities (Svigkas et al. 2017).

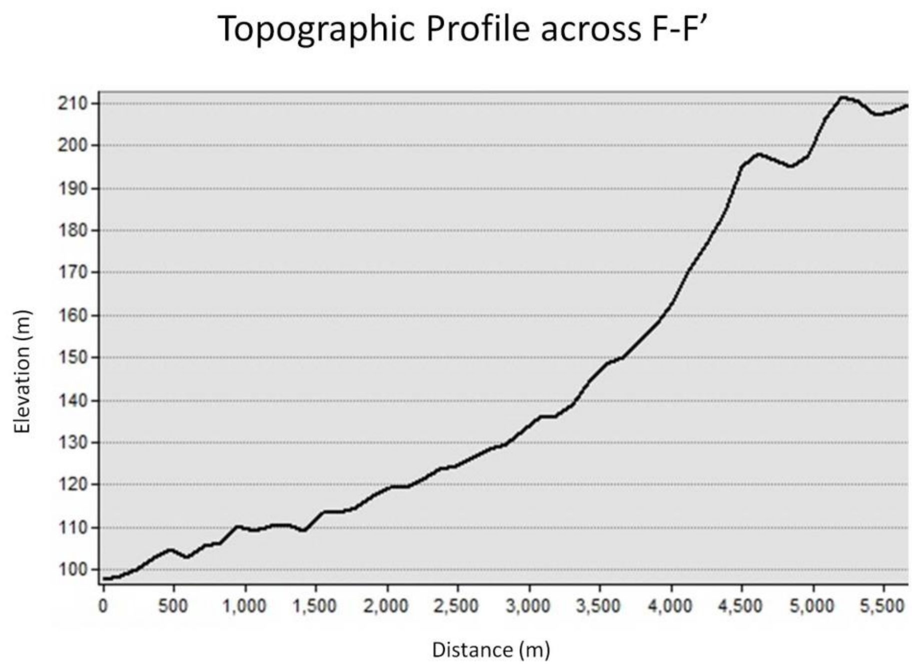

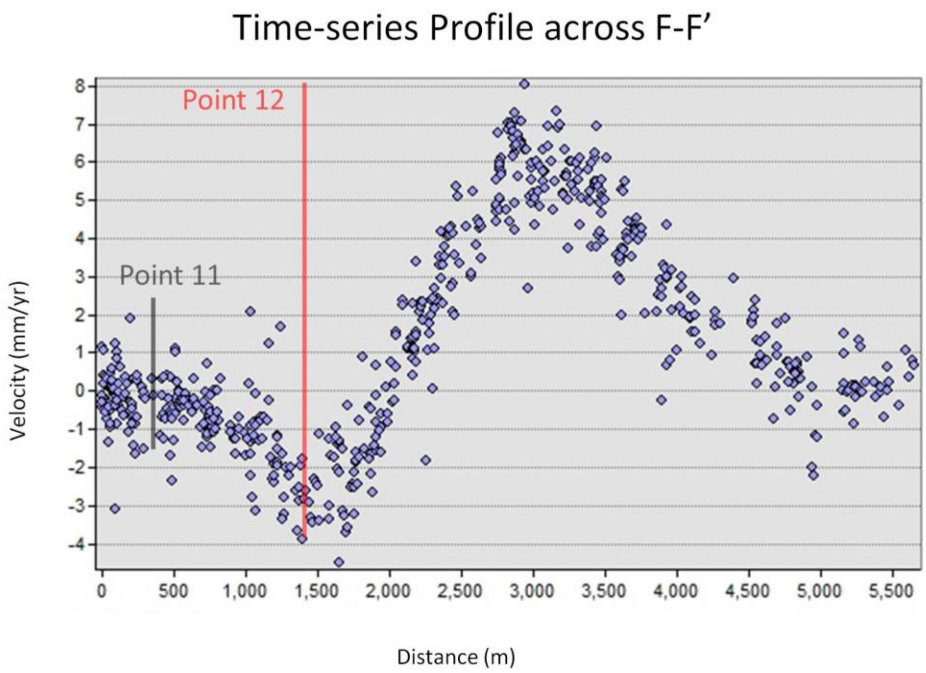

Figure 4.45 Velocity and topographic profiles for the trace F– F'. The intersection of each trace's profile with the Asvestochori fault (Fig. 4.31) is denoted with a black vertical line. The intersection of each trace's profile with the previously unknown structure is denoted with a red vertical line. Notice that in either cases there is a low or sharp disturbance in the velocities (Svigkas et al. 2017).

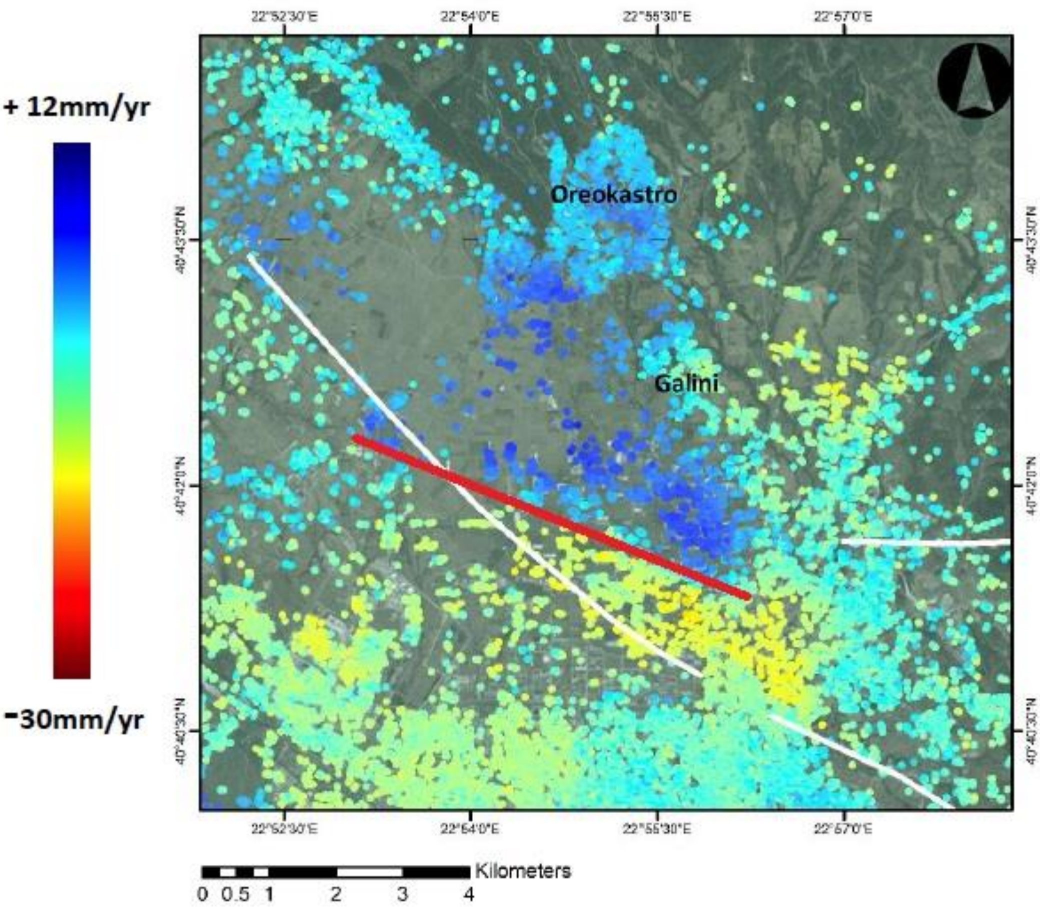

Figure 4.46 Localized deformation pattern of the second decade stops abruptly at its southern side, along a WNW–ESE linear feature, marked with the red line, oblique to the known fault of the region. A previously unknown structure, optimum oriented to the active stress field, appears to exist (Svigkas et al. 2017).

4.3.8 Conclusions

The 1992–2010 datasets from ERS and ENVISAT are exploited to monitor the surface deformation at the wider area of Thessaloniki using a multi-technique and a multisoftware approach. The focus of our study is the industrial area of Oreokastro, to the north of the city of Thessaloniki. Previous studies have captured the deformation pattern of the '90s, when studying the broader region; however they did not focused solely to this area, to seek for a clear interpretation. During the first decade, the deformation signal indicates a clear subsidence related to the industrial activities at the broader area of Oreokastro, causing numerous failures to buildings. On the contrary, after 2000 the deforming trend has changed to uplift, a fact that made the area an intriguing case study. Seeking for the driving mechanism, the scenario of tectonics was excluded due to the excessive deformation rates that cannot be attributed to the tectonic activity. Furthermore, the eversion of the deformation trend from subsidence to uplift excludes the hypothesis of the natural sediment compaction, since this mechanism is irreversible. The fact that the subsiding deformation has been confined within the limits of the industrial area with the overexploited aquifers, as well as the fact that the deformation trend changed radically to uplift when the consumption of the groundwater was reduced, sets the overexploitation of the aquifers as the main driving mechanism of the phenomena. From a tectonic point of view, the shape of the deformation pattern is well correlated with the network of faults dominating the area. The satellite monitoring supports the fact that the Asvestochori fault extends towards the NW. It is this extension that acts as a boundary to the aquifer, rendering the detected signal as a fault-controlled deformation. Moreover, this fault-controlled deformation revealed a new, previously unknown geologic structure and further studies are proposed for this specific site. The above findings provide substantial information for the geological regime of the industrial area and its future development.

Chapter.5 DEFORMATION DUE TO TECTONIC ACTIVITY

5.1 THE IRAN-IRAQ 2017 EARTHQUAKE

5.1.1 Introduction

On 12 November 2017, an earthquake occurred at the Iran-Iraq borders with magnitude Mw 7.3 (Fig. 5.1). The event took place at the Zagros Mountains (the Zagros fault thrust) at a collision zone between the Arabian and Eurasian plate. Zagros orogen is experiencing a convergence of a rate of 18-25 mm/yr (Reilinger et al. 2006). The event occurred at a site where no surface rupture was known to exist (Kobayashi et al. 2018; Wang et al. 2018) and caused a lot of damages (Fig. 5.2) and loss of lives mostly at the city Sarpol-e Zahab (Vajedian et al. 2018). It was in fact the strongest earthquake recorded in the area (Feng et al. 2018).

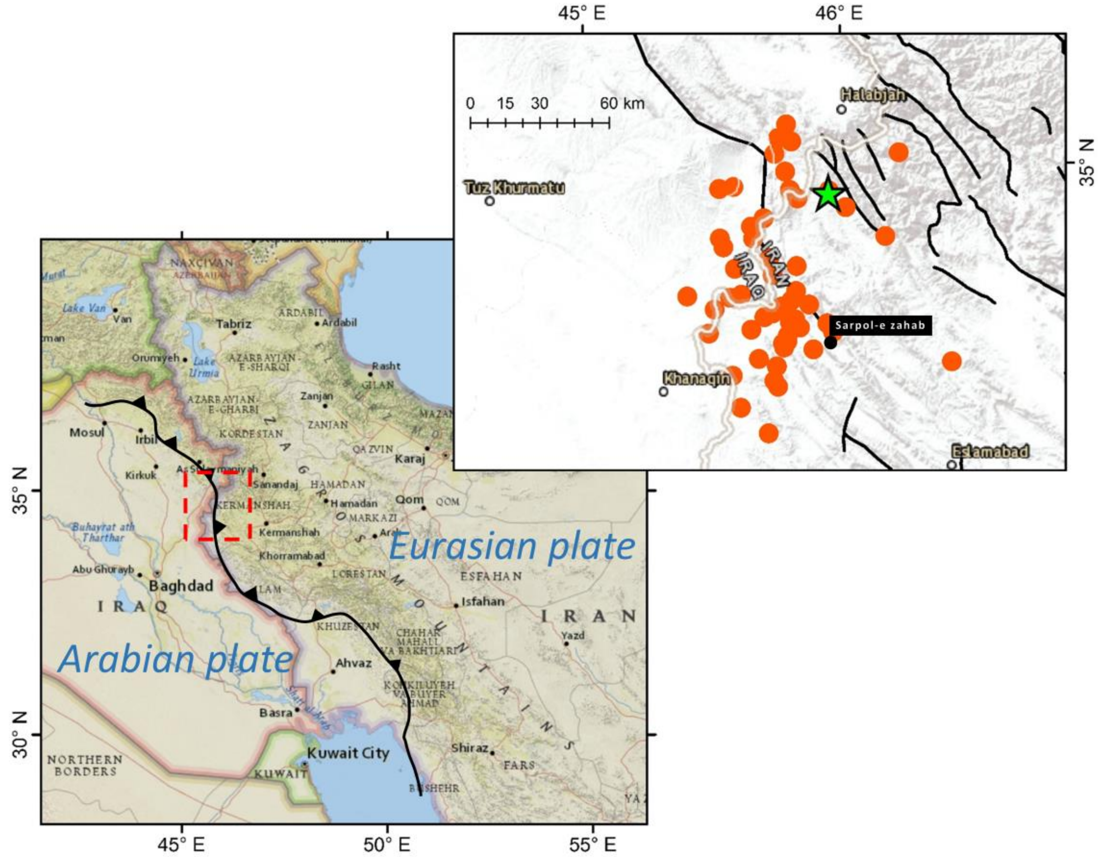

Figure 5.1 Map showing the larger scale tectonics acting at the area. Black line notes the collision between Arabian plate and Eurasian plate. The red dashed rectangle is the locus of this study. In the upper right inset map the location of the November 2017 seismic event is shown (green star). Also aftershocks (M ≥ 4) are shown in orange. The city with the highest number of deaths (Sarpol-e Zahab), is located southern of the epicentre. Seismicity is from the USGS catalogue.

Figure 5.2 Building failures in Sarpol-e Zahab city. Images are from Zare et al. (2017) earthquake report.

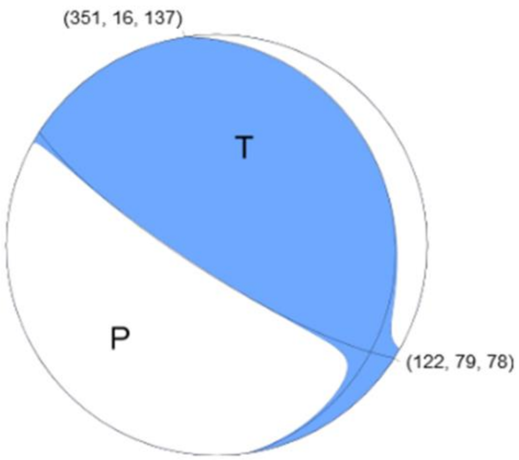

Nodal Planes

Plane	Strike	Dip	Rake
NP1	351°	16°	137°
NP2	122°	79°	78°

Principal Axes

Axis	Value	Plunge	Azimuth
T	1.110e+20 N-m	54°	18°
N	0.028e+20 N-m	12°	125°
P	-1.137e+20 N-m	33°	223°

Figure 5.3 USGS solution from: https://earthquake.usgs.gov/earthquakes/eventpage/us2000bmcg/moment-tensor.

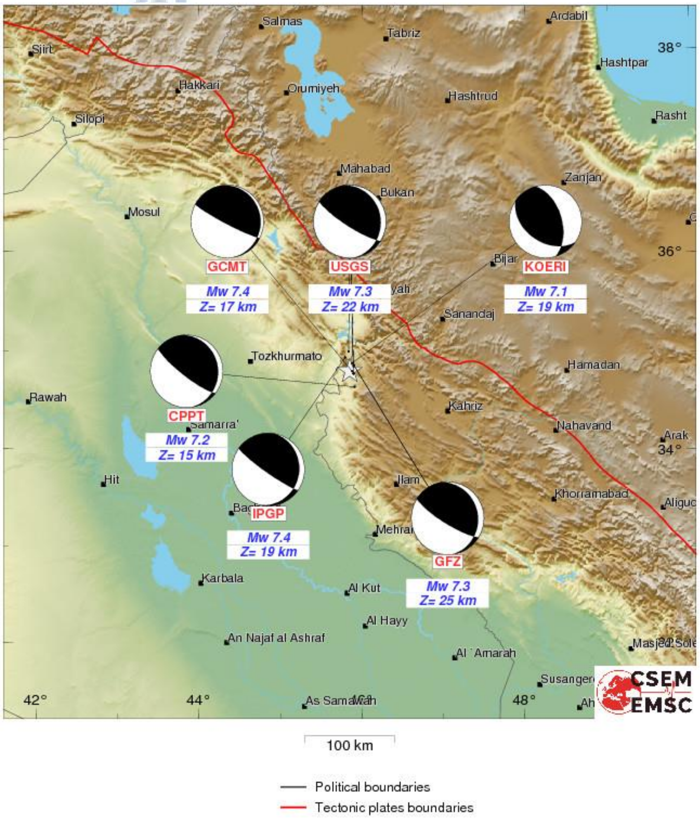

Figure 5.4 Solutions from different agencies. Map is from https://www.emsc-csem.org/Earthquake/260/M7-3-IRAN-IRAQ-BORDER-REGION-on-November-12th-2017-at-18-18-UTC.

SAR interferometry is exploited here to measure the surface deformation and present the seismic source that caused it. As shown below, two types of models are performed one for uniform slip and one estimating the slip distribution on the fault plane.

5.1.2 Data and Methods

The Sentinel-1 satellite family is exploited here together with the ALOS-2 wide swath imagery. Five SLC pairs were created consisting of images before and after the earthquake (Table 5.1). For the remote sensing analysis the SARscape software was used and the topographic corrections were achieved by exploiting the Shuttle Radar topography Mission (SRTM). The SAR images were multilooked by the factors if 14 × 13 for Sentinel-1 and 6 × 45 for ALOS-2. The wrapped interferograms were filtered using the

Goldstein approach (Goldstein & Werner, 1998) and unwrapping was performed using the Minimum Cost Flow algorithm (Costantini, 1998).

Table 5-1 SAR dataset used.

Mission	Pre event_ Post event (yyyymmdd)	λ (cm)	Acq. Mode	Orbit
ALOS-2	20160809_20171114	24	WD	Asc.
ALOS-2	20171004_20171115	24	WD	Desc.
Sentinel-1	20171111-20171117	5.6	IW	Asc.
Sentinel-1	20171107-20171119	5.6	IW	Desc.
Sentinel-1	20171112-20171118	5.6	IW	Desc.

Regarding the source definition, two types of source models were performed. A homogenous and isotropic elastic half-space equation from Okada (1985) was assumed and at first, a uniform slip model is presented. The second model shown is the estimated slip distribution on the fault plane (e.g. Atzori et al. 2009). Prior the geodetic modelling the unwrapped interferograms were undersampled to decrease the computational load. The uniform slip model was based on a non-linear inversion by applying the Levenberg-Marquardt algorithm (Levenberg, 1944; Marquardt, 1963). Slip distribution was estimated by non-linear least squares. To get a reliable result a damping factor was adopted by trial-and-error (Menke, 1989).

5.1.3 Co- Seismic Displacement results

To have a good sense of the surface movement, various interferograms capturing the event, were generated. Figures 5.5-5.7 present the measured displacements by the different sensors and line of sights.

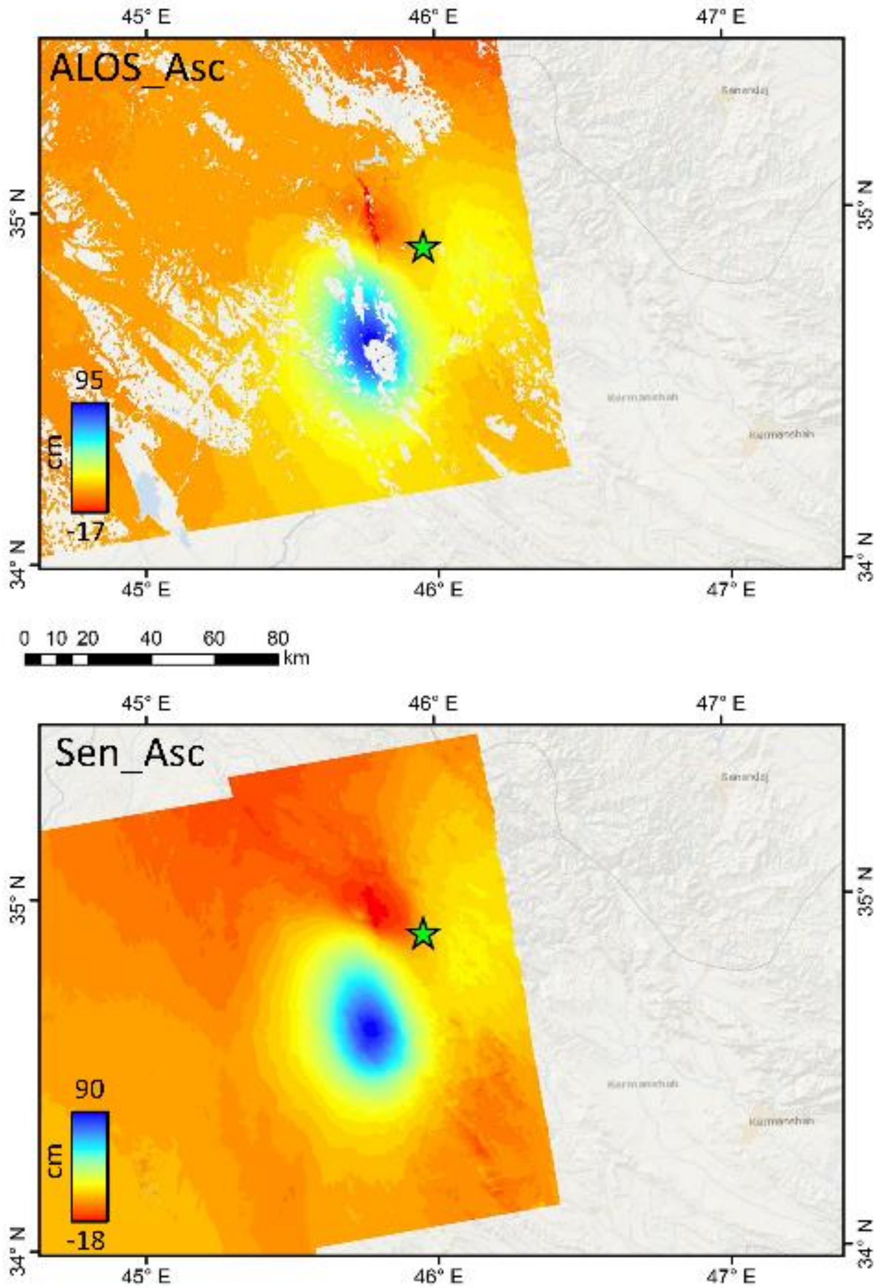

Figure 5.5 Displacement results of the ascending passes of ALOS (up) and Sentinel (down).

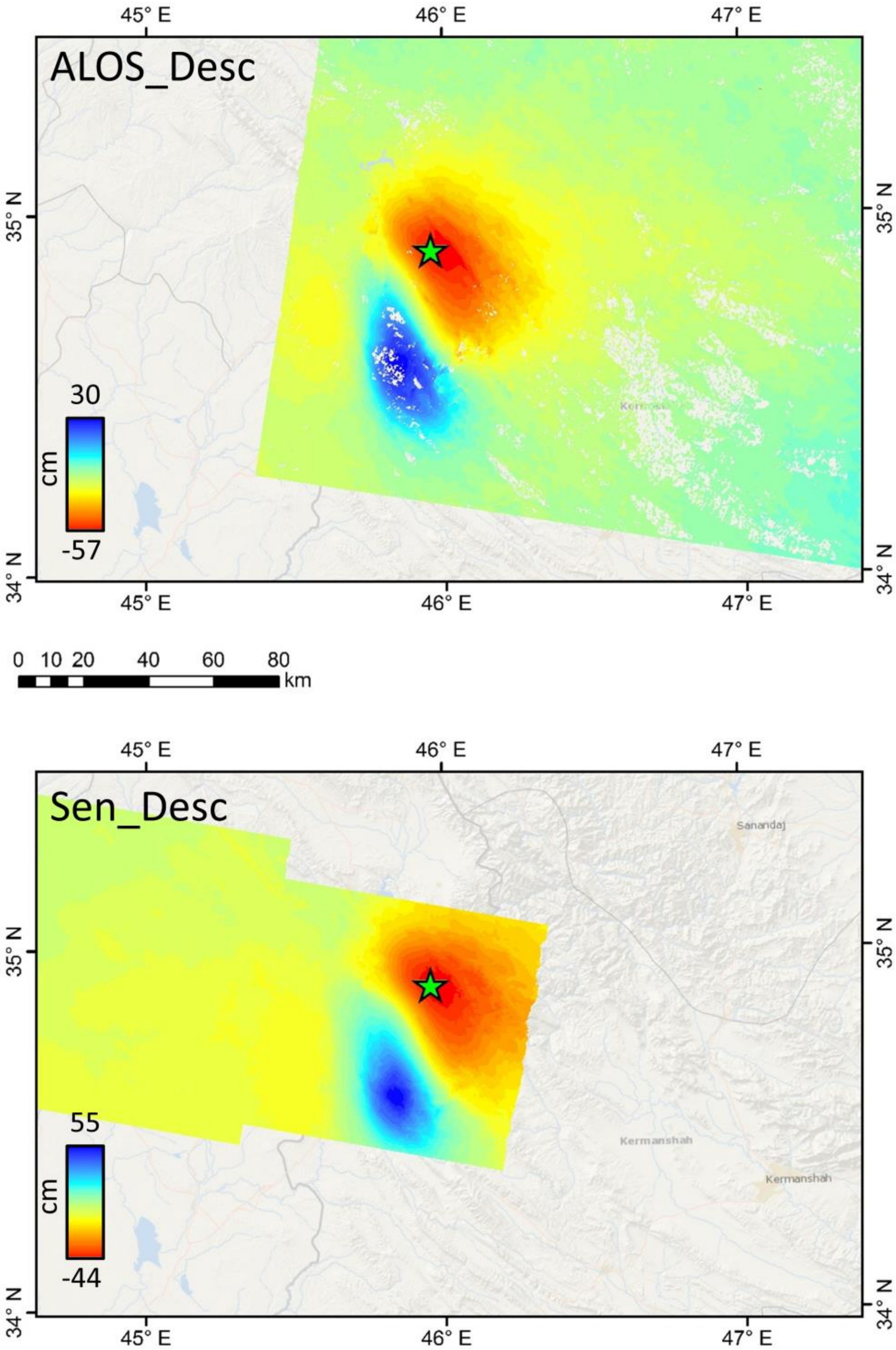

Figure 5.6 Displacement results of the descending passes of ALOS (up) and Sentinel (down).

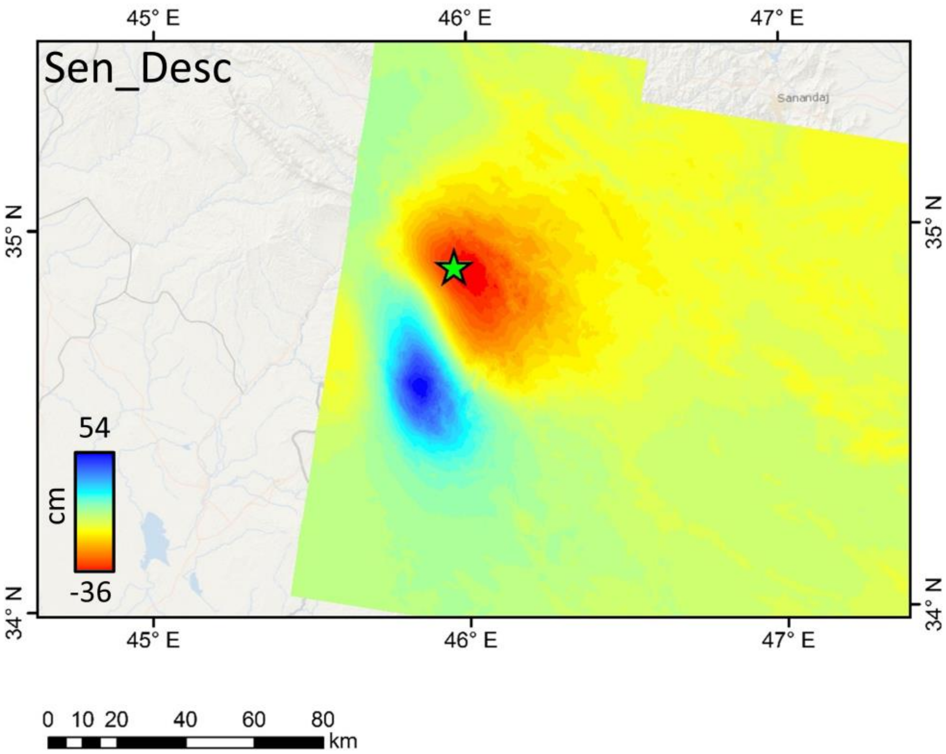

Figure 5.7 Sentinel Descending displacement result.

In the ascending pass, by taking into account both interferograms, the overall displacement is from -18 to +90 cm. Maximum detected values in the descending pass is -57 and +54 cm. Overall, the dielectric characteristics of the surface allowed to obtain a high quality signal. To this contributed even more the magnitude of the event.

5.1.4 Seismic source results

The displacement samples were the input for the source modelling. All the parameters were left free and the adopted algorithm converged quickly –a result of the high quality input signal. The proposed source (Fig. 5.8) is striking ~354° and has a shallow dip of about 16°. The estimated magnitude is Mw 7.2, in accordance with that of USGS (Mw 7.3). The strong signal allowed having a good fitting between the observed and modelled displacements (Fig. 5.9) and a well-constrained source. Uncertainties are presented in Table 5.2 and in Figure 5.10.

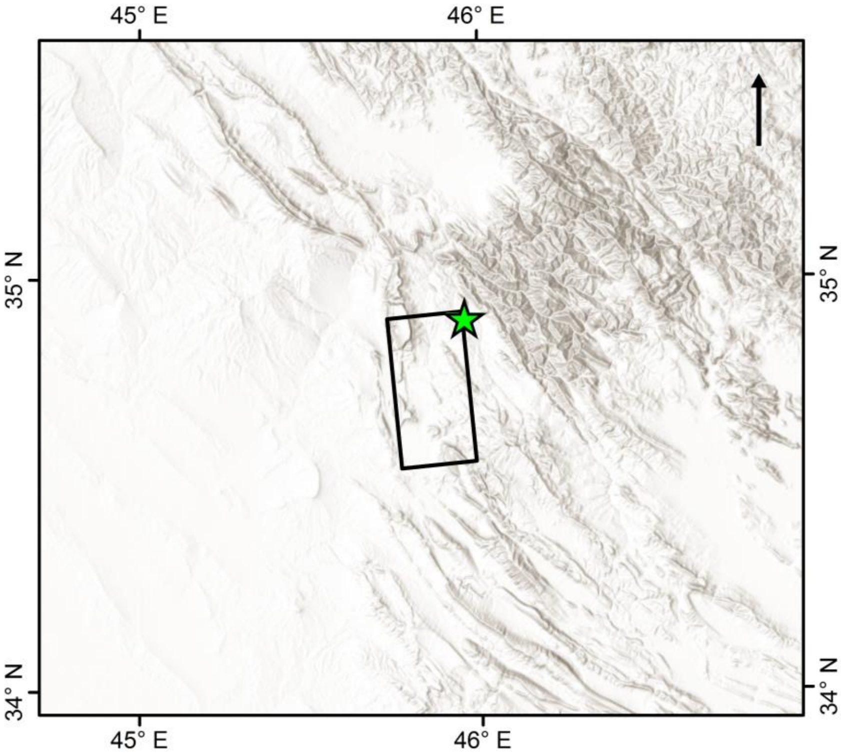

Figure 5.8 Uniform slip seismic source as derived from non-linear inversion. Parameters are presented in Table 5.2. Green star denotes the epicentre.

Table 5-2 Non-linear inversion results and uncertainties.

Parameters	Best fit	Uncertainty
Length	40400.4 m	264.3 m
Width	21040.4 m	229 m
Depth	11394.5 m	138 m
Dip	16.39 deg	0.22 deg
Strike	354.18 deg	0.45 deg
East	568596.3 m	103.3 m
North	3842523.8 m	136.2 m
Rake	137.50 deg	0.53 deg
Slip	3.1614 m	0.0422 m

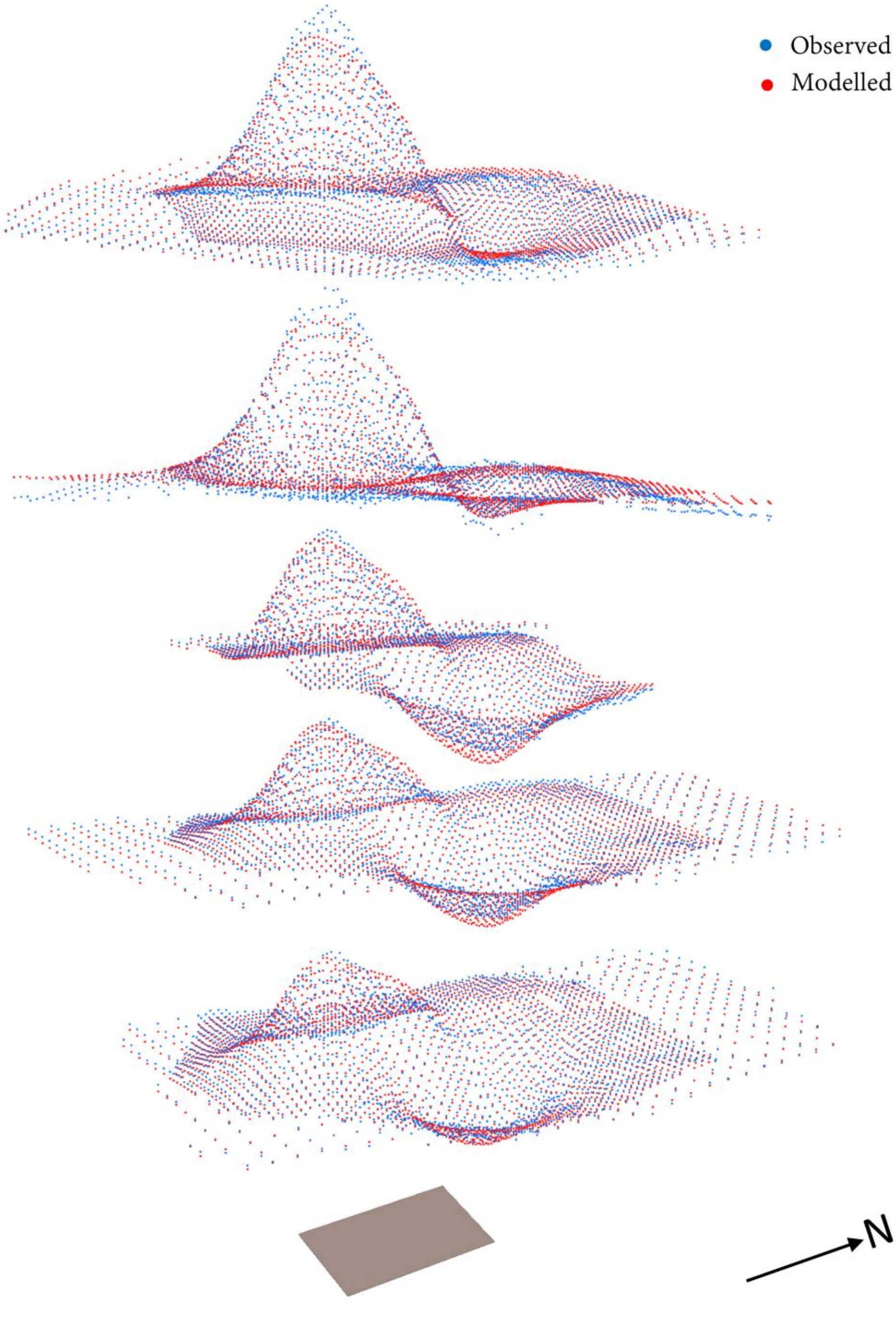

Figure 5.9 Comparison between the observed (blue) and modelled displacements (red) shown in 3D. The grey rectangle is the uniform slip source.

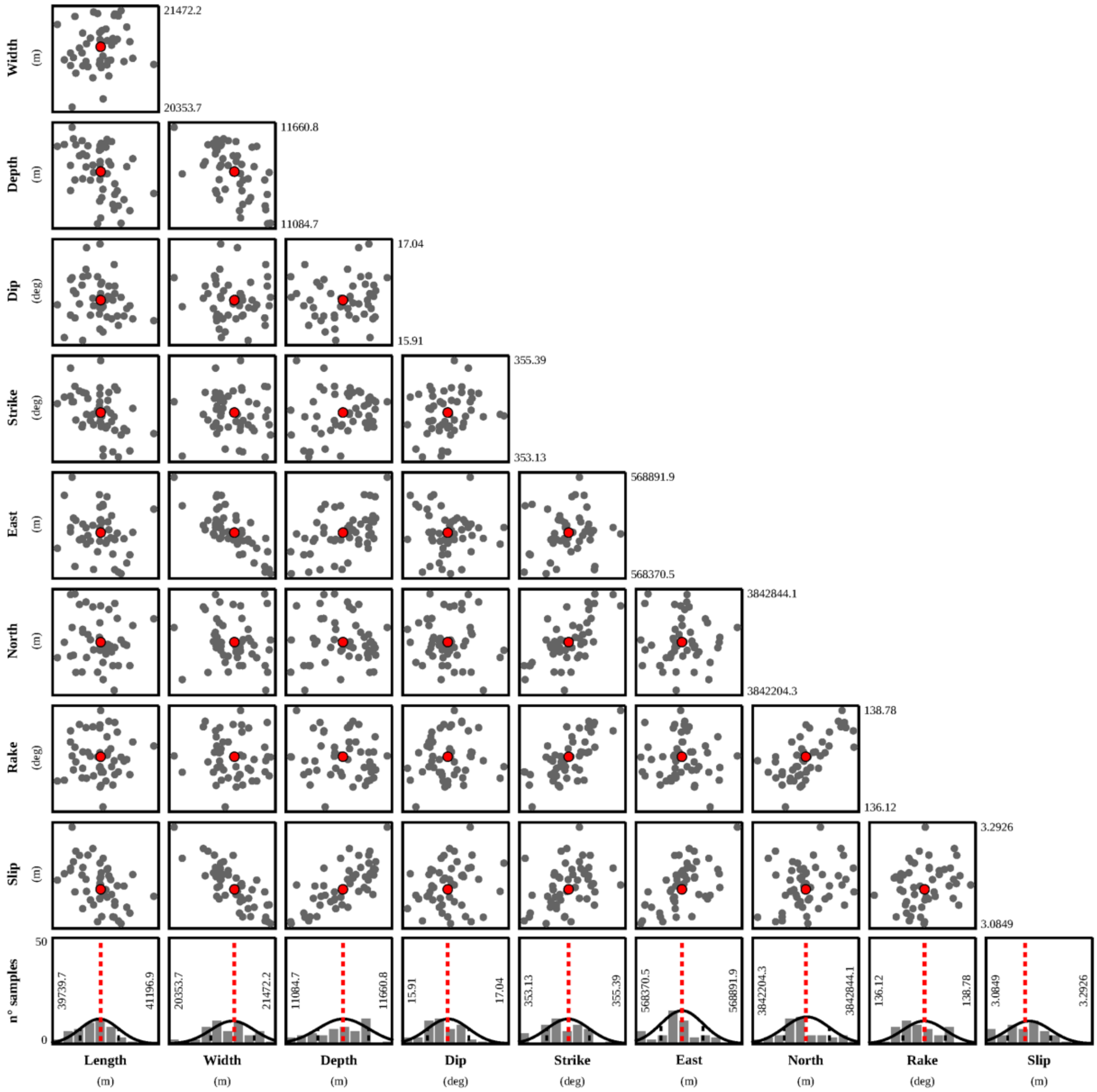

Figure 5.10 Uncertainties and trade-offs of the non-linear solution.

Table 5-3 RMS values of non-linear inversion.

SLC pairs	RMS value (m)
20160809_20171114	0.03
20171004_20171115	0.027
20171111-20171117	0.029
20171107-20171119	0.025
20171112-20171118	0.024

For the slip distribution model, the dip, strike and rake were fixed, the length and width of the uniform slip solution were extended and the fault was subdivided in patches of 5 × 5 km and the adopted damping factor was 0.03. The proposed model is a 90 × 80 km structure with a maximum slip of 4.4m located at the depth of 14 km (Fig. 5.11). The estimated moment magnitude is Mw 7.3 in accordance with the seismic waveform results. The resolution of the slip distribution is presented in Figure 5.12. RMS values are shown in Table 5.4 and comparison between the observed and modelled interferograms are in Figure 5.13.

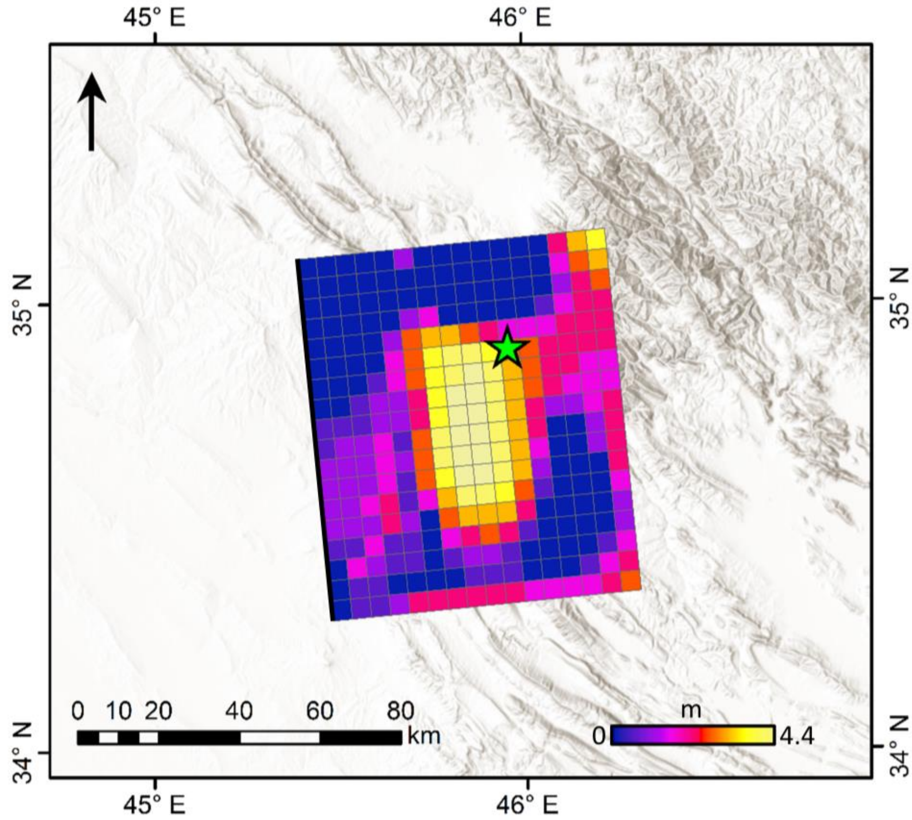

Figure 5.11 Slip distribution model of the November 2017 event. Green star denotes the epicentre.

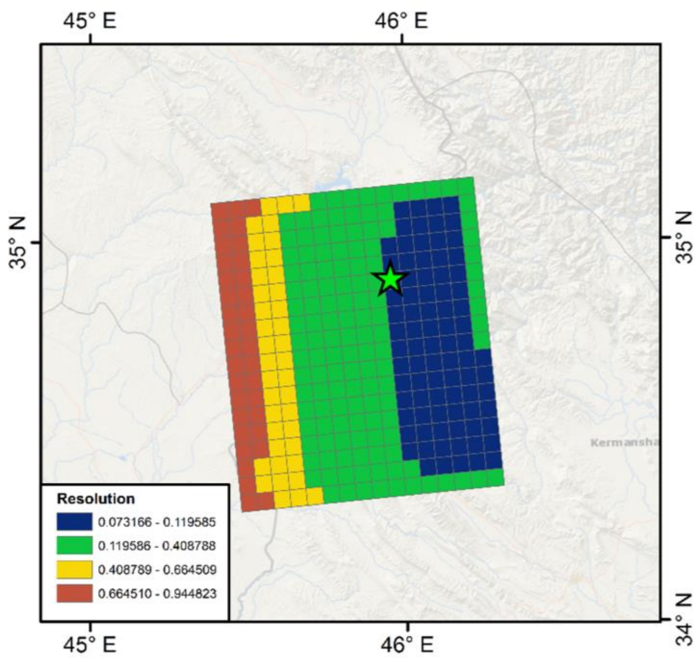

Figure 5.12 Resolution of the slip distribution model.

Table 5-4 RMS values of linear inversion.

SLC pairs	RMS value (m)
20160809_20171114	0.025
20171004_20171115	0.022
20171111-20171117	0.022
20171107-20171119	0.02
20171112-20171118	0.019

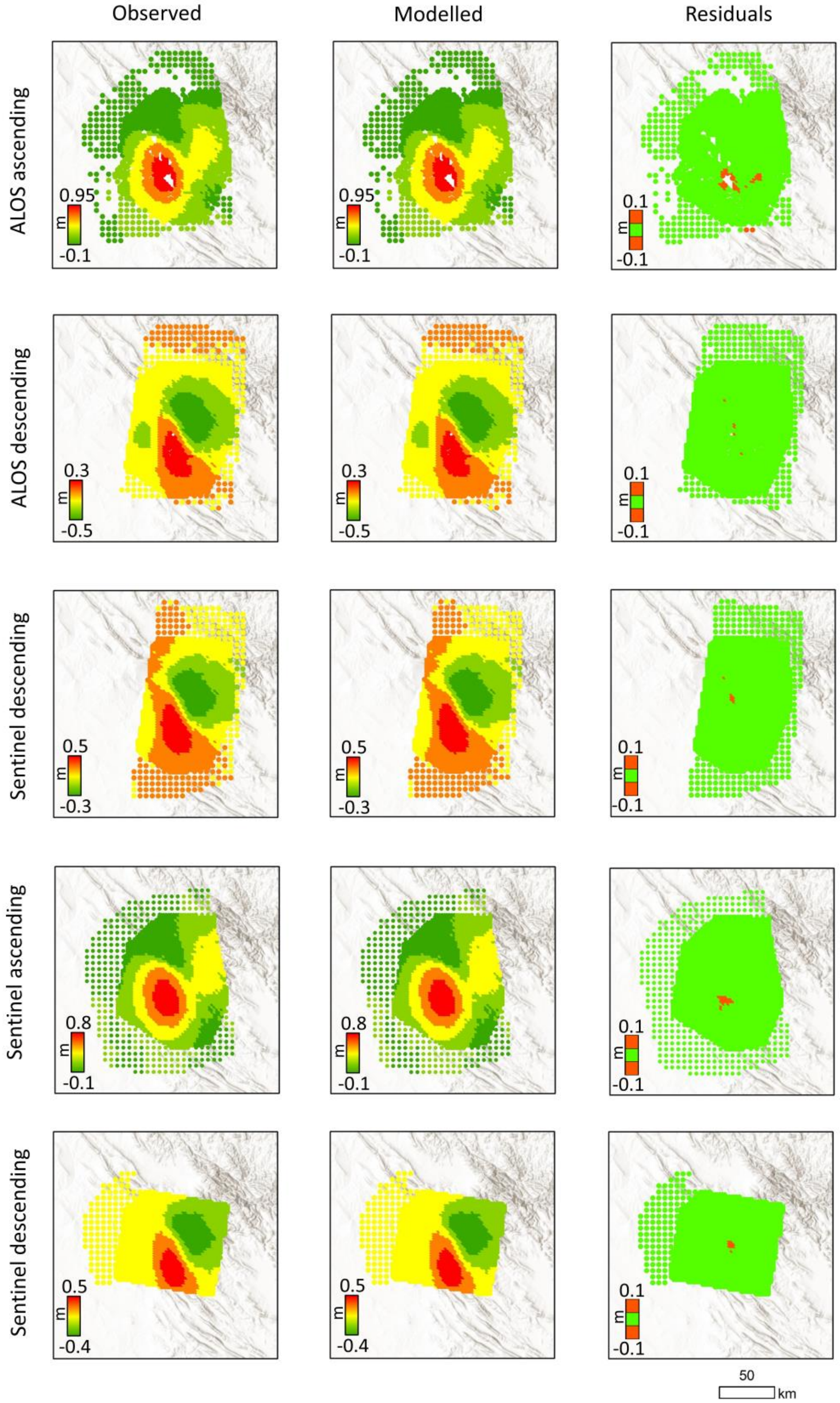

Figure 5.13 Comparison of observed interferograms and the modelled that derived from the linear inversion.

The main fault parameters are in accordance with other studies. The estimated dip 16.3° is in accordance with Vajedian et al. (2018) (17°), Barnhart et al. (2018)(15°), Feng et al. (2018)(14.5°) and in great accordance with Ding et al. (2018) (16.3°). The defined strike is similar to Vajedian et al. (2018) (354°) and Ding et al. (2018) (354.7°). Also, the defined rake value (137.5°) is close to the values proposed by Feng et al. (2018)(136°) and Ding et al. (2018)(137°). Overall, all the existing geometry InSAR results from the various studies could be considered that they are in a general accordance; in part this is due to the high quality of the displacement signal caused by the 2017 earthquake.

5.1.5 Conclusion

The surface deformation caused by the 2017 November Iran-Iraq was studied here. Using Sentinel-1 and ALOS-2 satellites from both ascending and descending passes it was estimated that the event caused a displacement pattern covering an area with a size of more than 140 × 150 km. Source results indicate a structure with a strike of 354° that generated a thrust event together with a horizontal component. The event was a result of the collision between the Arabian and Eurasian plate. The dip angle was significantly shallow expressing, the tectonics of the Zagros Fold-Thrust Belt. Connections of this geometry could be potentially found with the 2015 Gorkha earthquake that occurred in in Nepal (dip ~11°, e.g. Lindsey et al. 2015).

5.2 The Lefkada 2015 Sequence

5.2.1 Introduction

The Cephalonia-Lefkada Transform Fault Zone (CTF) in western Greece (Fig. 5.14), connects two different tectonic regimes: continental collision to the north, with subduction of oceanic lithosphere to the south. CTF is known for its frequent seismic activity with a well-known historical record (e.g. Papazachos et al. 1997; Karakostas et al. 2004; 2010) and is related to dextral-strike slip motions, which sometimes are connected with thrust components (Kiratzi et al. 1991; Louvari et al. 1999; Sachpazi et al. 2000; Scordilis et al. 1985). CTF consists of two active segments: the Cephalonia segment and the Lefkada segment, which run parallel and very close to the western coastline of these islands (Louvari et al. 1999). The exact mapping of the fault trace is still not known, and its position is inferred, mainly, from the bathymetry.

On 17 November 2015, an earthquake (Mw 6.4) (Fig. 5.14b) struck the western coast of Lefkada island. It stimulated a wealth of publications (Avallone et al. 2017; Bie et al. 2017; Chousianitis et al. 2016; Ganas et al. 2016a; Melgar et al. 2017; Saltogianni et al. 2017; Sokos et al. 2016; Papathanasiou et al. 2015; Lekkas et al. 2018; Lekkas et al. 2016; Kassaras et al. 2018; Ganas et al. 2016b). Sokos et al. (2015) were the first to identify that the mainshock broke a strong asperity, left unbroken, in-between two large subevents of the previous 2003-doublet earthquake of Mw 6.2. Similarly, the same authors, using seismic waveforms modelled the 2015 event as a multiple point source event, with two well-resolved sources close to Lefkada and a third southern one, less reliable, located at the latitude of the tip of Cephalonia island, offshore. It is noteworthy, that the recent (in 2003, 2014 and 2015) events that ruptured parts of CTF, were all modelled as multiple source events, which indicates faulting complexity (Sokos et al. 2016; Sokos et al. 2015; Kiratizi 2014). Papadimitriou et al. (2017), using high precision aftershocks of the 2015 sequence, proposed that the area has a network of fault segments, which in some cases are not clearly identified or easily distinguished.

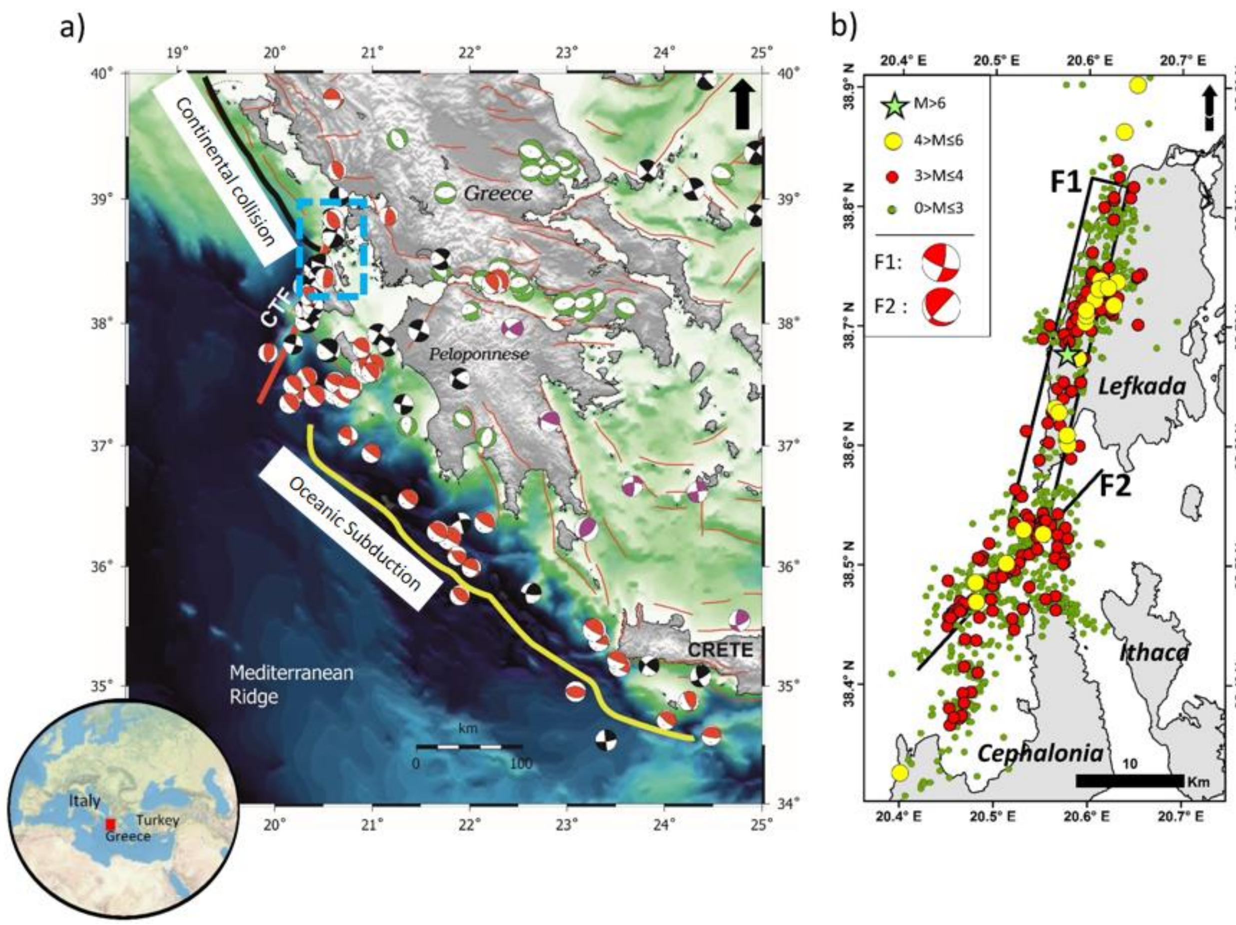

Figure 5.14 a) Tectonic setting in the western Hellenic Subduction Zone, depicting the two different tectonic regimes, which are offset (~100 km) by the operation of the Cephalonia Transform Fault Zone (CTF). Beach balls denote focal mechanisms of M>5.5 earthquakes and the magenta colors denote focal depths >50 km. Black beach balls = strike-slip faulting, Red=thrust/reverse faulting, Green=normal faulting. The dashed blue rectangle indicates the area of this study. The red rectangle in the lower left inset globe map is the locus of interest. b) Map showing the Lefkada 2015 relocated seismic sequence (location data are from Papadimitriou et al. (2017)) and our proposed fault segmentation (F1 and F2) for Cephalonia-Lefkada Transform Fault zone (from Svigkas et al. 2019c).

This complexity is also reflected in the modelling of geodetic data. For example, Ganas et al. (2016b) based on InSAR and GPS data, presented two uniform slip fault models: One with a unique fault and another one with two faults. Their preferred solution is the two-fault uniform slip model, which comprises of the main fault alongside a smaller fault, parallel to the main one, located partly onshore the island of Lefkada, close to the latitude of the mainshock. Bie et al. (2017) used Sentinel-1 imagery as input and performed a series of tests to identify the slip distribution. They show three slip patches in their preferred slip distribution. The southern patch, is related with the displacement detected at the tip of Cephalonia Island and according to the authors, this southern slip patch was constrained only by their Sentinel descending data. Moreover, this slip patch was defined to be at depths >10km, and Bie et al. (2017) claim that it was not well resolved by their dataset. It must be noted though, that monitoring tectonic phenomena in the Ionian Sea is a challenging task, and to elucidate the fault segmentation is difficult, as previously mentioned also by Bie et al. (2017), Chousianitis, et al. (2016), Saltogianni et al. (2017), Sokos et al. (2015).

The advent of remote sensing and more specifically, the radar satellite data have provided new means of research to the scientific community for earthquake studies (Polcari et al. 2016; Polcari et al. 2018; Barba-Sevilla et al. 2018; Albano et al. 2017; Vajedian et al. 2018; Boncori et al. 2015). The aim of this study is to examine the fault segmentation of CTF, taking advantage of new remote sensing radar data. The new SAR datasets used here (Radarsat-2 and ALOS-2) have not been previously exploited and they are consisted of imagery from different viewing geometries. These are utilized together with Sentinel-1 data and provide a clearer picture, regarding the displacement that occurred on both the Lefkada and Cephalonia islands.

The deformation induced by the 2015 earthquake sequence, detected by this new multi-sensor InSAR dataset, together with the exploitation of external data (relocated aftershocks), lead to a more complex fault setting, and to new insights in terms of the fault segmentation and the tectonic processes currently acting at CTF.

5.2.2 Data and Methods

SAR interferometry was used here to calculate displacement of the earth's surface caused by the Lefkada earthquake, based on a diverse dataset consisting of multi-band (C-, X- and L-) multi-resolution SAR imagery. Initially we considered 4 Sentinel-1 C-band (European Space Agency) images, 2 from ascending and 2 from descending orbits, 4 Radarsat C-band (Canadian Space Agency) images, from ascending orbits, 2 ALOS L-band (Japanese Aerospace Exploration Agency) wide-swath images from descending orbits and 8 ascending COSMO-SkyMed X-band images (Italian Space Agency). After calculating several differential interferograms, a number of them was discarded due to the excessive impact of low interferometric coherence. The analysis was therefore carried out with the datasets presented in Table 5.5.

Table 5-5 SAR dataset used.

Satellite	Master Date (m/d/y)	Slave Date (m/d/y)	Temporal Baseline (days)	Normal Baseline (m)	Pass	Linear inversion RMS (m)
Radarsat-2	2/21/2014	12/1/2015	648	165.4	Asc.	0.016
Sentinel-1	11/5/2015	11/17/2015	12	22.5	Asc.	0.018
ALOS-2	10/12/2015	11/23/2015	42	77.35	Desc.	0.025
Sentinel-1	11/11/2015	11/23/2015	12	66.2	Desc.	0.012

InSAR processing was carried out with the "repeat-pass" approach (Massonnet et al. 1995) using the SARscape software. After coregistering the pre-event and the post-event images, the phase difference was calculated and the topographic phase contribution removal was achieved using the Shuttle Radar Topography Mission (SRTM) Digital Elevation Model (Farr et al. 2000). Spatially correlated noise, was filtered with the approach of Goldstein et al. (1988), and the wrapped interferometric phase was then unwrapped with a Minimum Cost Flow algorithm (Costantini et al. 1998). We then proceeded to the phase (radians) to displacement (meter) conversion and geocoding and finally we obtained deformation maps, in the satellite Line-of-Sight (LoS). We considered the existence of atmospheric artefacts by using the Generic Atmospheric Correction Online Service (GACOS, http://ceg-research.ncl.ac.uk/v2/gacos/) for InSAR (Yu et al. 2017; 2018a; 2018b).

To avoid excessive and unnecessary computational load, all displacement maps were downsampled at regular intervals of 200 m in the epicentral area and of 500 m outside it. We identified the seismic sources by means of equations describing the surface displacement induced by a dislocation in an elastic, homogeneous and isotropic half-space (Okada et al. 1985). The source retrieval is carried out in two steps: initially, the fault geometry and mechanism are modelled through a nonlinear optimization scheme based on the Levenberg-Marquardt algorithm (Levenberg, 1944; Marquardt, 1963). The next stage of the modelling, follows the retrieval of the fault plane, and includes modelling the dislocation distribution adopting a linear inversion algorithm (Atzori et al. 2009). In this inversion approach, we extended the size of the retrieved uniform slip fault planes in order to let the slip vanish at the edges; we then subdivided the faults in 1 km ×1 km sized patches. Imposing constraint of a damped and non-negative solution (Menke et al. 1989), we solve the system:

$$\begin{bmatrix} \boldsymbol{d} \\ 0 \end{bmatrix} = \begin{bmatrix} \mathrm{G} \\ \varepsilon \nabla^2 \end{bmatrix} \cdot \mathbf{m} \tag{5.1}$$

where $\boldsymbol{d}$ is the InSAR data, G is the Green's functions matrix, ∇^2 is the Laplacian operator, ε is the damping factor obtained by trial-and-error (Menke et al. 1989). To adopt a value for the latter, we selected the best compromise between best data fit and fault reliability according to the resulting slip distribution and peak slip values. Finally **m** is the vector of parameters.

5.2.3 Consideration for Atmospheric artefacts

In our analysis, we used the GPS displacement values as an external factor, to decide whether there could be atmospheric artefacts. After projecting the GPS to LoS Sentinel descending interferogram, we compared the derived GPS values: at first with the corresponding InSAR pixels of the original InSAR results (right graph Figure 5.15) and then with the GACOS-modified InSAR results (right graph Figure 5.15). Retrieved results indicate that the correlation coefficient between InSAR and GPS is in essence the same in both cases, indicating that no significant atmospheric artefacts are present in the interferograms and the detected signal can be used for tectonic modelling.

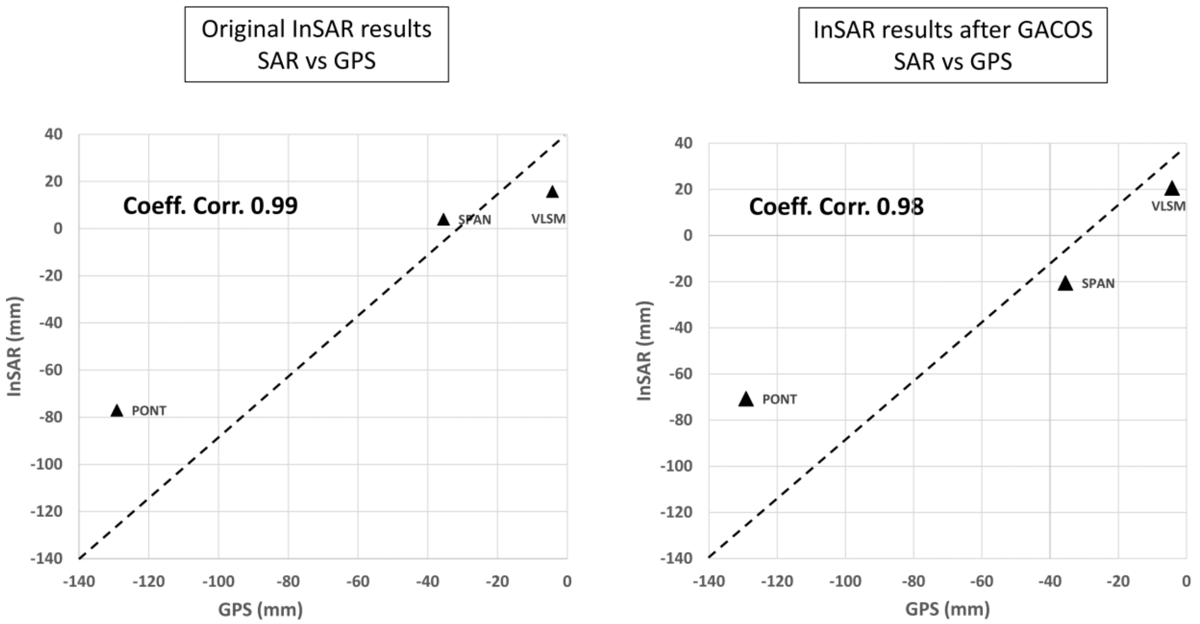

Figure 5.15 Comparison of correlation between InSAR vs GPS (left) and GACOS-corrected InSAR vs GPS (right). Correlation coefficient is the same indicating that atmospheric artefacts are not covering the tectonic signal.

5.2.4 Surface displacement results

The 2015 sequence affected the surface of both Lefkada and Cephalonia islands. The differences in patterns of the displacement results is expected, due to the different viewing angles of the satellites. When looking at all the displacement results, the differences between the ascending and the descending acquisitions indicate a horizontal movement (Fig. 5.16). The Sentinel and Radarsat ascending interferograms indicate that both islands (Lefkada and Cephalonia) approached the satellite sensors. As also stated by Bie et al. (2017), the Sentinel descending displacement result is more complicated:

looking from north to south, on Lefkada at first there is a small signal of negative displacement and then a lobe of positive displacement. Then at the tip of Cephalonia, there is also a displacement signal. The ALOS descending result confirms the pattern of the Sentinel descending and offers additional input on the descending viewing geometry. The two lobes on Lefkada as seen in the descending unwrapped pairs are part of the classic strike-slip deformation pattern (the rest is covered by the sea body). Previous studies have noted the existence of displacement at the tip of Cephalonia (Avallone et al. 2017; Bie et al. 2017; Ganas et al. 2016b). The geodetic InSAR results, presented here provide additional evidence on the displacement at the northern tip of Cephalonia. This, in turn, offers additional constraints regarding the fault segmentation, as shown in the next section. As it can be seen in Figure 5.17, the northern edge of Cephalonia has a positive displacement pattern, which is evident in all the InSAR results.

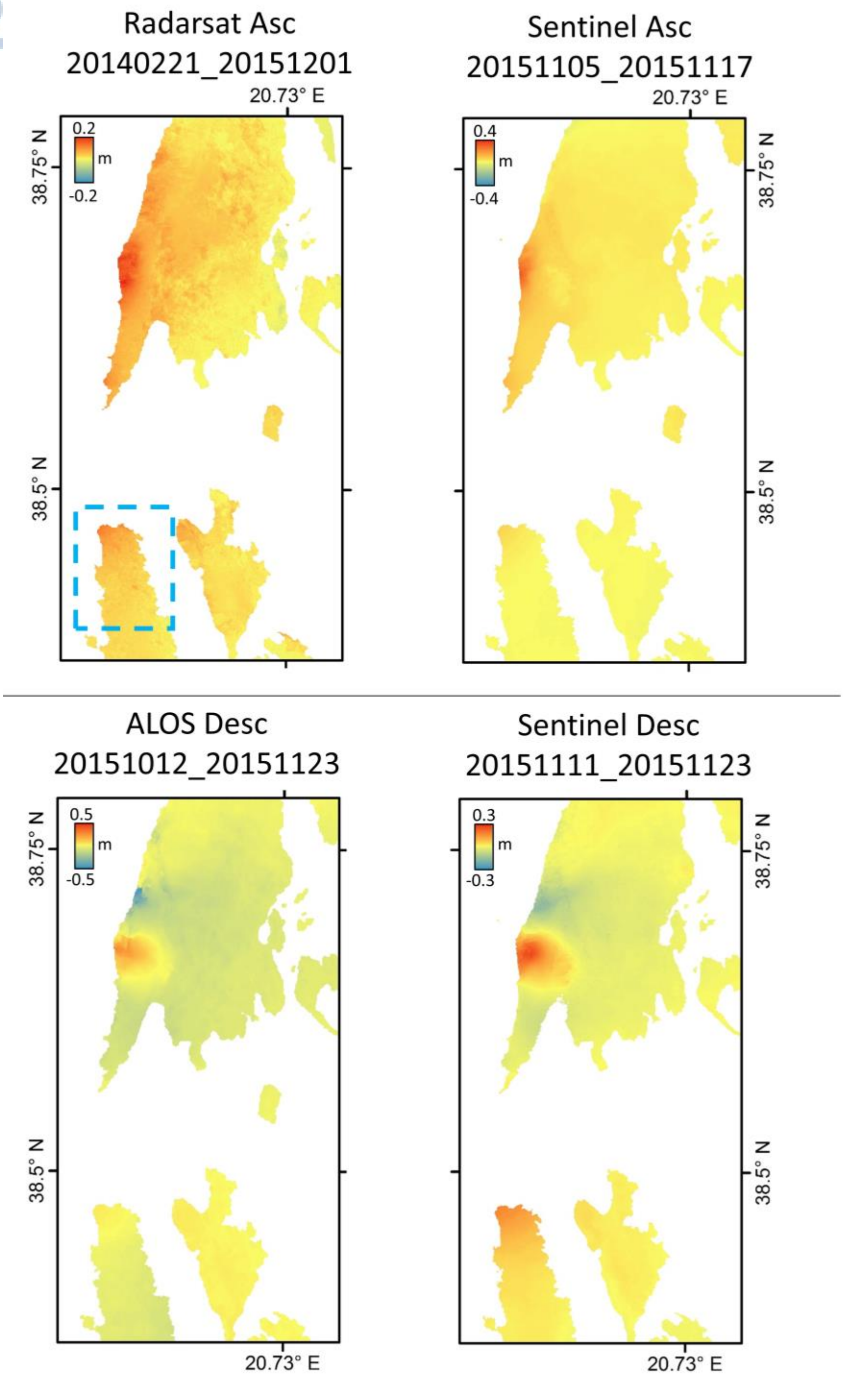

Figure 5.16 Displacement pattern from the different SAR sensors. The blue dashed rectangle is the area shown in Figure 5.17 (Svigkas et al. 2019c).

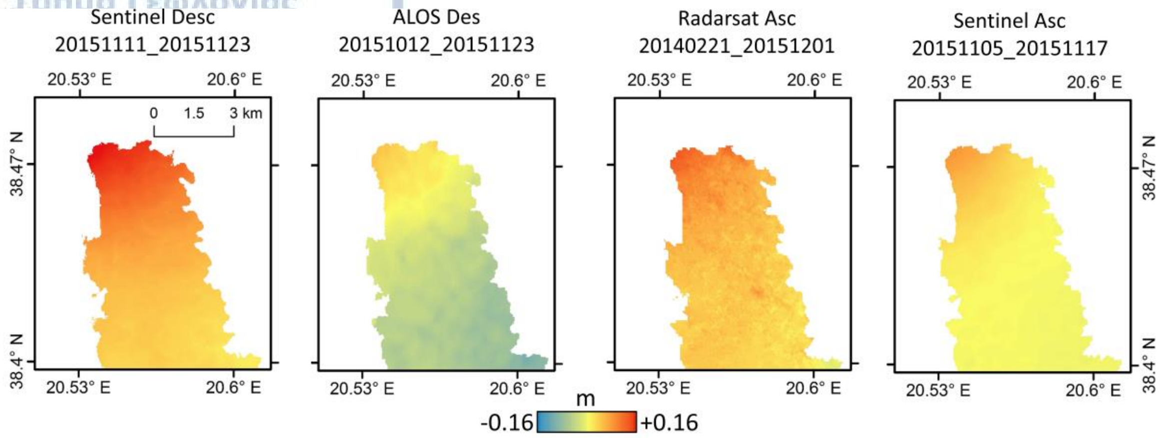

Figure 5.17 Detail of the unwrapped interferograms used in this study, showing the deformation at the northern tip of Cephalonia (blue dashed rectangle in Fig. 5.16). The displacement at the tip of Cephalonia is apparent in all interferograms and it is this which offers new constraints on the fault segmentation of the area (Svigkas et al. 2019c).

5.2.5 Single Fault model

Initial attempts were made to model our InSAR results jointly with GPS data (Chousianitis et al. 2016; Ganas et al. 2016b; Saltogianni et al. 2017). However, the joint geodetic inversion led to large residuals in both datasets. The projection of the three components of GPS measurements into the LOS of every InSAR dataset, confirmed a disagreement between the GPS projected values and InSAR results. In fact, the GPS and InSAR inconsistency is not surprising and it was already observed (Melgar et al. 2017). While potential sources of error cannot be excluded, this divergence could be attributed, as also stated by Melgar et al. (2017), to early afterslip signal contained in InSAR maps, taking into account that the InSAR data include few days of possible slow deformations after the mainshock (Avallone et al. 2017; Bie et al. 2017; Melgar et al. 2017). It is thus possible that the dataset used here, contains postseismic signal; the InSAR input is of course still essential, since our goal is to define the fault segmentation of the area. Given the unavailability of published GPS measurements capturing the displacement at the northern tip of Cephalonia, only the InSAR results were used in the inversion. Moreover, InSAR offers spatially well-constrained slip patterns especially for the shallow earthquake events and is able to identify complex fault segmentations (Elliot et al. 2016).

Firstly a nonlinear inversion was performed, to identify the faulting geometry and mechanism assuming that rupture occurred on a single fault. For setting an initial range of allowed values for the fault parameters, we took into consideration the already published ones for the Lefkada 2015 event. In this inversion, every parameter was left free, except the dip value that could not be constrained, thus we adopted a dip of 70° in accordance with (Avallone et al. 2017). However, a single fault solution was able to model only the displacement of the Lefkada Island. A successful reproduction of the displacement at the northern tip of Cephalonia could not be attained (Fig. 5.19a). Therefore, the single fault solution was considered insufficient for modelling our dataset.

5.2.6 Two-Fault model

Subsequently, a two-fault model scenario was attempted, by adding also a southern fault segment (F2) and repeating the previous procedure. The deformation signal demanded to lower the number of free parameters. Thus, the parameters of one of the faults was kept fixed, adopting the values previously found with the one-fault solution, which had successfully modelled the displacement of Lefkada. The location and the strike of the second fault segment (F2 in Fig. 5.14b) was based on the relocated seismicity of Papadimitriou et al. (2017). Moreover, topographic profiles along part of the F2 segment show that the fault passes by a bathymetric feature that could be related with tectonic activity. More specifically, the fault is located at the peaks of the bathymetric curvature (Fig. 5.18). The dip angle was grid searched in terms of the lowest rms, which were obtained for dips in the range 80° to 90°, with the lowest values indicating a vertical fault. This is in accordance with Papadimitriou et al. (2017) which state that the aftershock locations possibly indicate a vertical structure at that specific area. Results of the nonlinear inversion are summarized in Table 5.6 and uncertainties are shown in Figures 5.20 and 5.21. The rms values are included in Table 5.7.

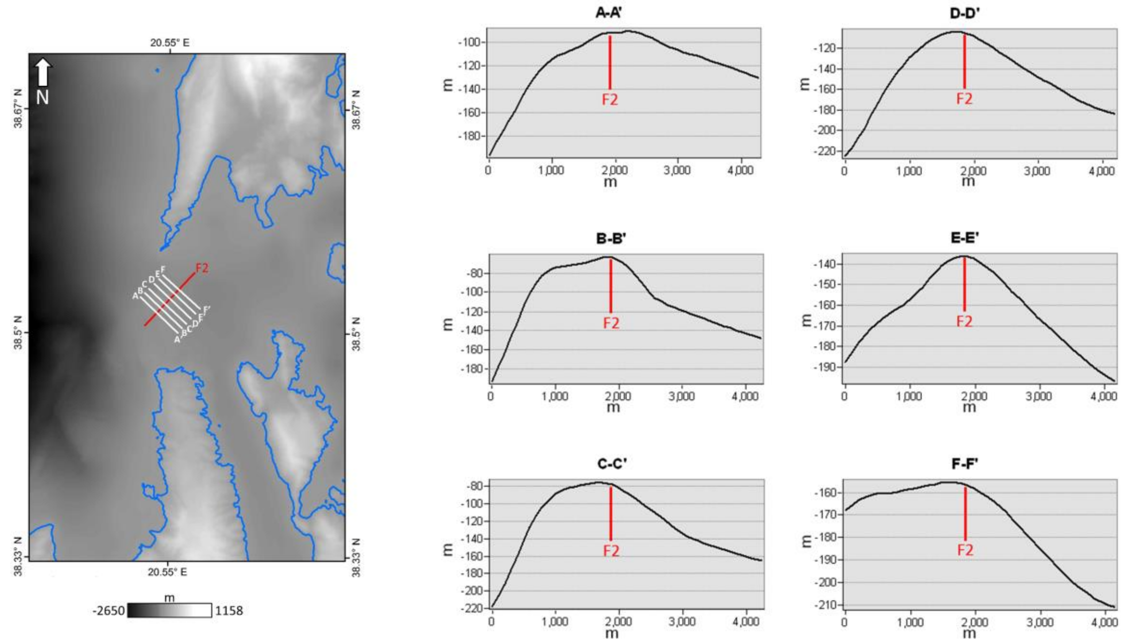

Figure 5.18 Topography (from http://www.emodnet-bathymetry.eu) of the study area. A profile screening along the segment F2, indicates the existence of a seafloor feature. Red line: Southern fault segment F2. Green lines A-A', B-B', C-C', D-D', E-E', F-F' are the bathymetric profiles. In each profile graph, the location of F2 along the profile is noted with a red line (Svigkas et al. 2019c).

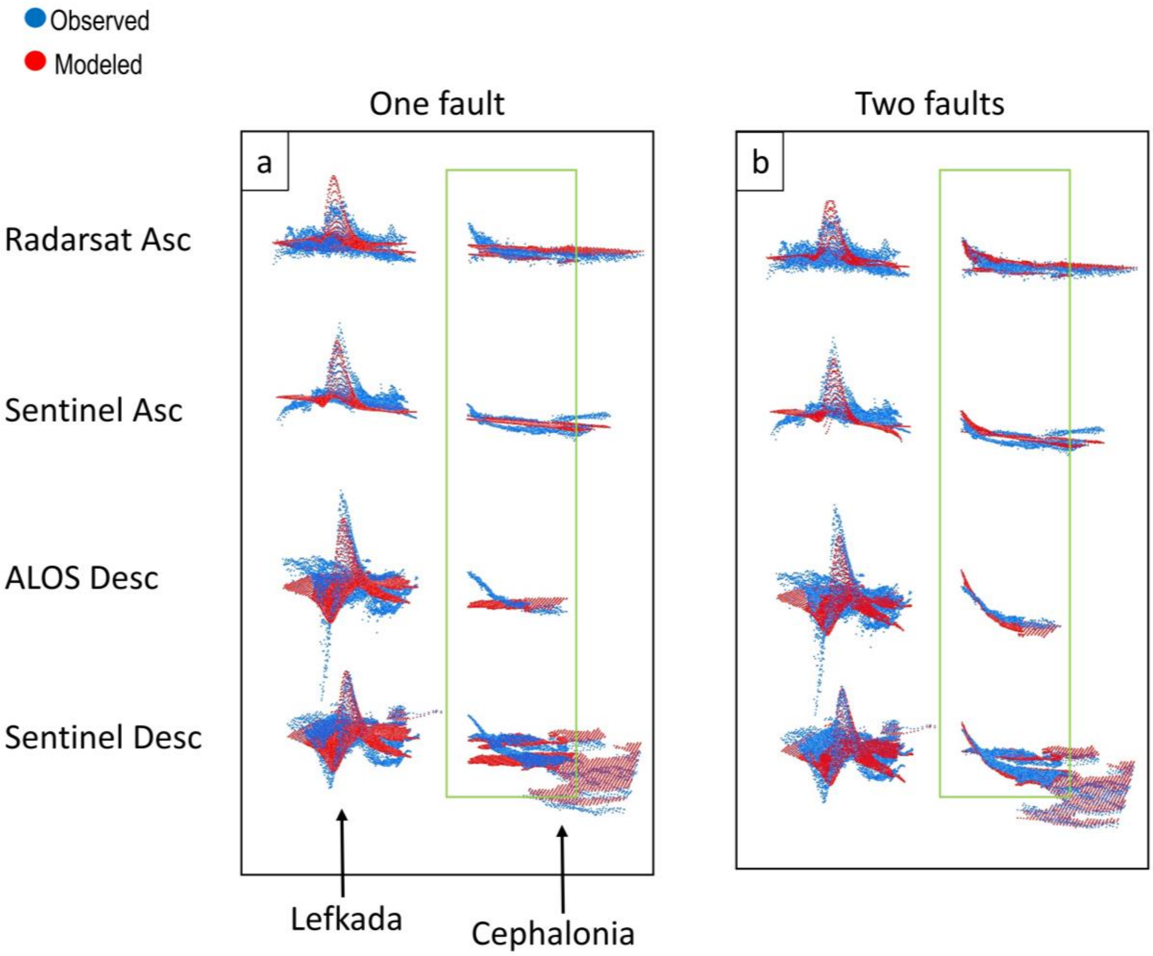

Figure 5.19 3D comparison of the Observed and Modeled (non-linear inversion) interferograms between the 1- and the 2-Fault configurations. a) 1-Fault configuration is not able to reproduce the displacement at the tip of Cephalonia (green rectangle). b) 2-Fault configuration reproduces well the displacement in both islands.

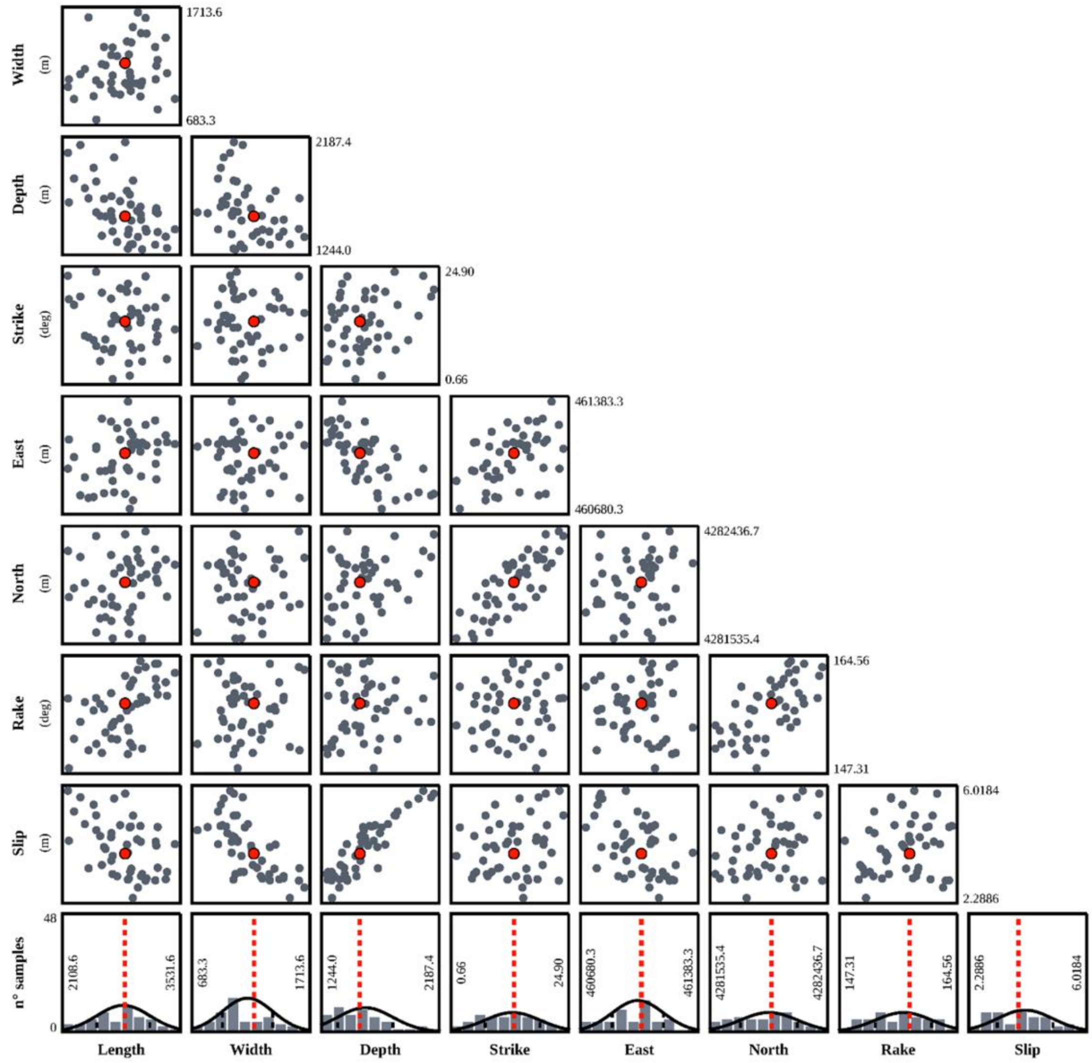

Figure 5.20 Scattered plots and histograms showing the trade-offs and uncertainties of source parameters of the nonlinear inversion for the northern segment (F1).

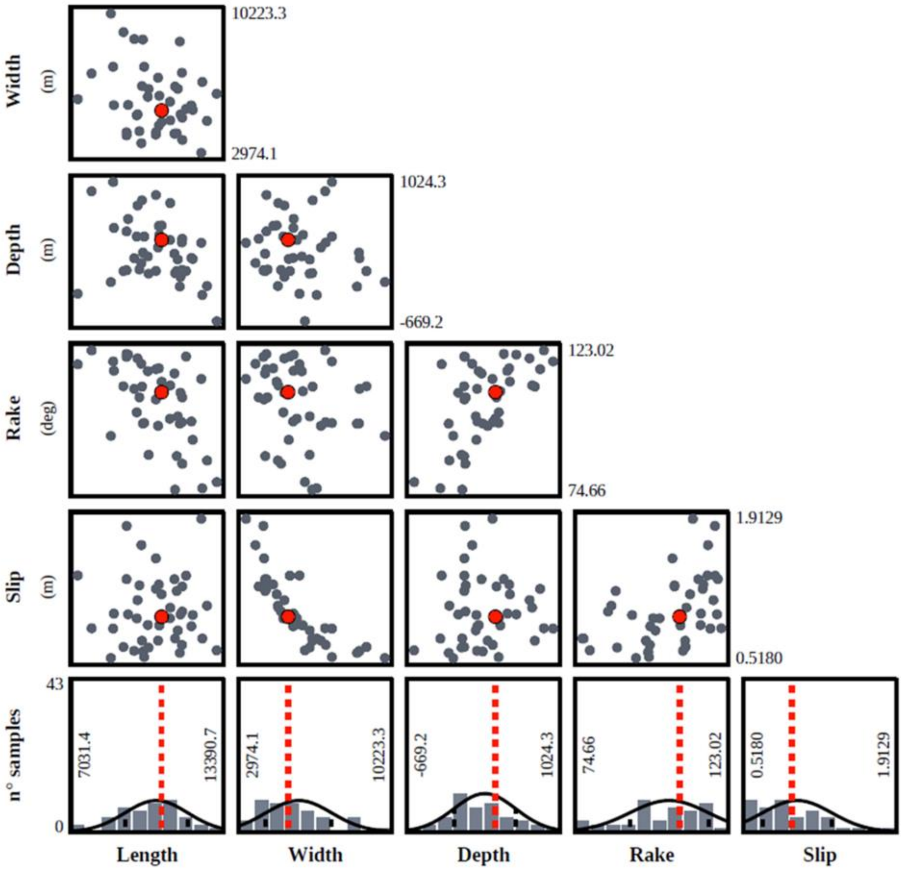

Figure 5.21 Scattered plots and histograms showing the trade-offs and uncertainties of source parameters of the nonlinear inversion for F2.

After defining a geometry assuming a uniform slip, we estimated the slip distribution on the two fault planes. It can be seen in Figure 5.22 that the northern fault segment (F1), which projects underneath the Lefkada Island, hosted three separated slip patches. The middle patch, which was the one located at the locus of the mainshock (green asterisk in Figure 5.22a), had a length of about 8 km and a width of 6 km; the peak slip is 2.9 m and this was the highest slip value overall. The southernmost slip patch of F1 expressed a peak slip of 1.7 m. The northern part of F1 hosted a smaller-sized slip patch with peak slip of 0.6 m that did not reach the surface. The locus of the major slip patch and its peak values at shallow depths can explain the damage pattern (rockfalls, landslide phenomena, building failures) observed in-situ (Ganas et al. 2016b; Papathanassiou et al. 2015; Lekkas et al. 2016; Kassaras et al. 2018; Kazantzidou-Firtinidou et al. 2016). The main amount of slip on F1 is expressed above 7 km and there is no slip below 10 km. The southern fault segment (F2), hosted a single slip patch with a peak slip of 1.6 m that did reach the seafloor surface. This slip patch predicts the deformation signal of northern Cephalonia (Fig. 5.17). Results indicate that on F2, there was no on-fault dislocation below 6 km. The Root-Mean-Square (RMS) values of linear inversion for each SAR dataset are shown in Table 5.5, the source results of this study are in Table 5.8, while the fits to the data are included in the central and right panels of Figure 5.23.

Table 5-6 Parameters of the Nonlinear Inversions.

Segment F1		
Length:	2863.2 m	(sigma 320 m)
Width:	1224.2 m	(sigma 219 m)
Depth:	1551.5 m	(sigma 220.6 m)
Dip:	70.00 deg.	fixed
Strike:	13.60 deg.	(sigma 5.64 deg.)
East:	461043.9 m	(sigma 152 m)
North:	4282005.9 m	(sigma 218.2 m)
Rake:	157.58 deg.	(sigma 4.12 deg.)
Slip:	3.8582 m	(sigma 0.87 m)

Segment F2		
Length:	10807.1 m	(sigma 1300m)
Width:	5303.6 m	(sigma 1553.9m)
Depth:	307.7 m	(sigma 339.3m)
Dip:	90.00 deg.	fixed
Strike:	43.00 deg.	fixed
East:	457974.2 m	fixed
North:	4261074.4 m	fixed
Rake:	107.64 deg.	(sigma 12.44 deg.)
Slip:	0.9579 m	(sigma 0.315 m)

**East and North are in UTM-WGS84 zone 34 north coordinates*

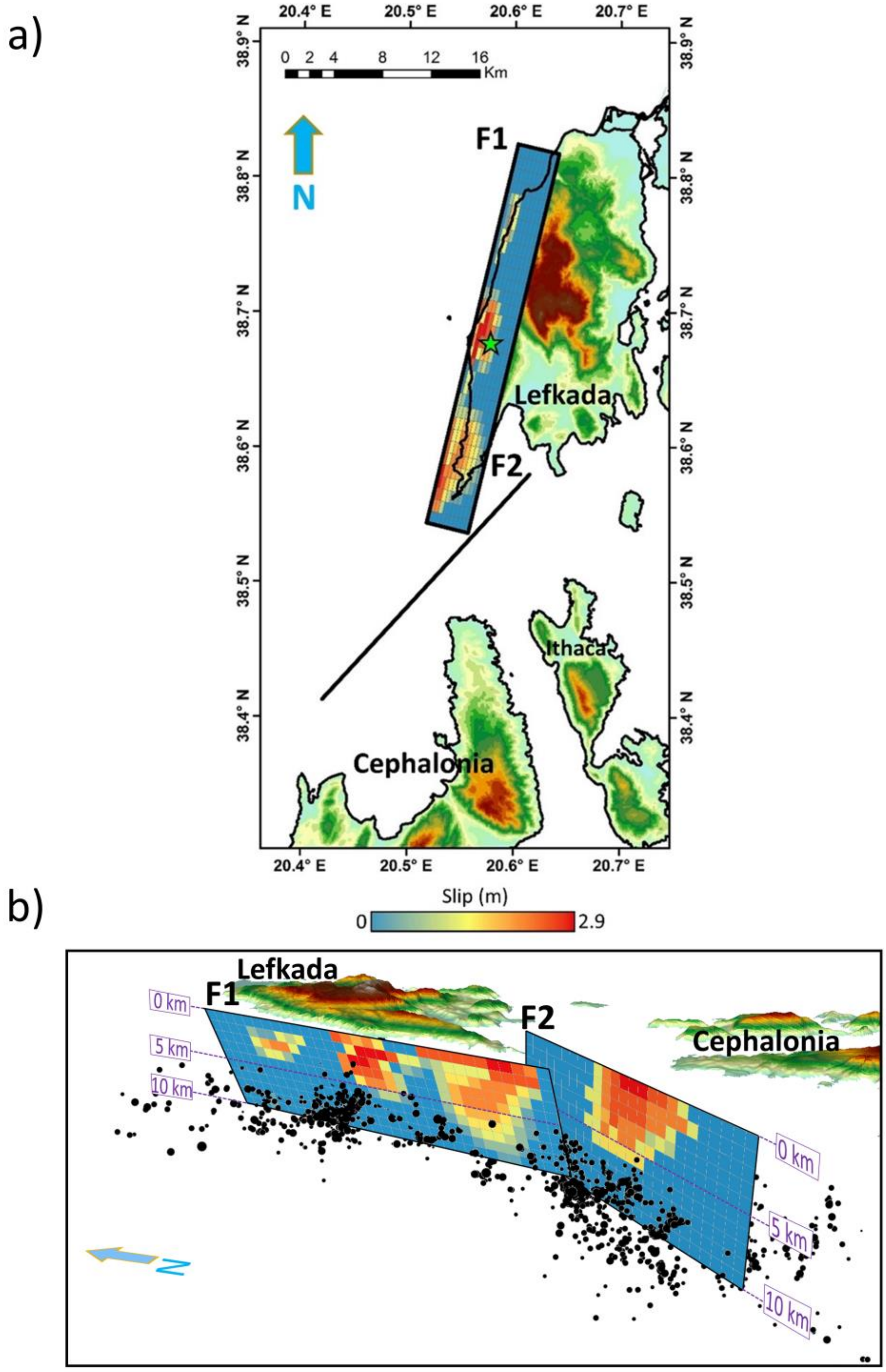

Figure 5.22 Map showing the two fault segments and the slip distribution. a) Plane view (green asterisk denotes the mainschock). b) 3D view (Svigkas et al. 2019c).

Table 5-7 RMS of Nonlinear Inversions.

One Fault (F1)	
ALOS Desc.	0.039 m
Radarsat Asc.	0.020 m
Sentinel Asc.	0.025 m
Sentinel Desc.	0.029 m

Two faults (F1 & F2)	
ALOS Desc.	0.036 m
Radarsat Asc.	0.018 m
Sentinel Asc.	0.023 m
Sentinel Desc.	0.020 m

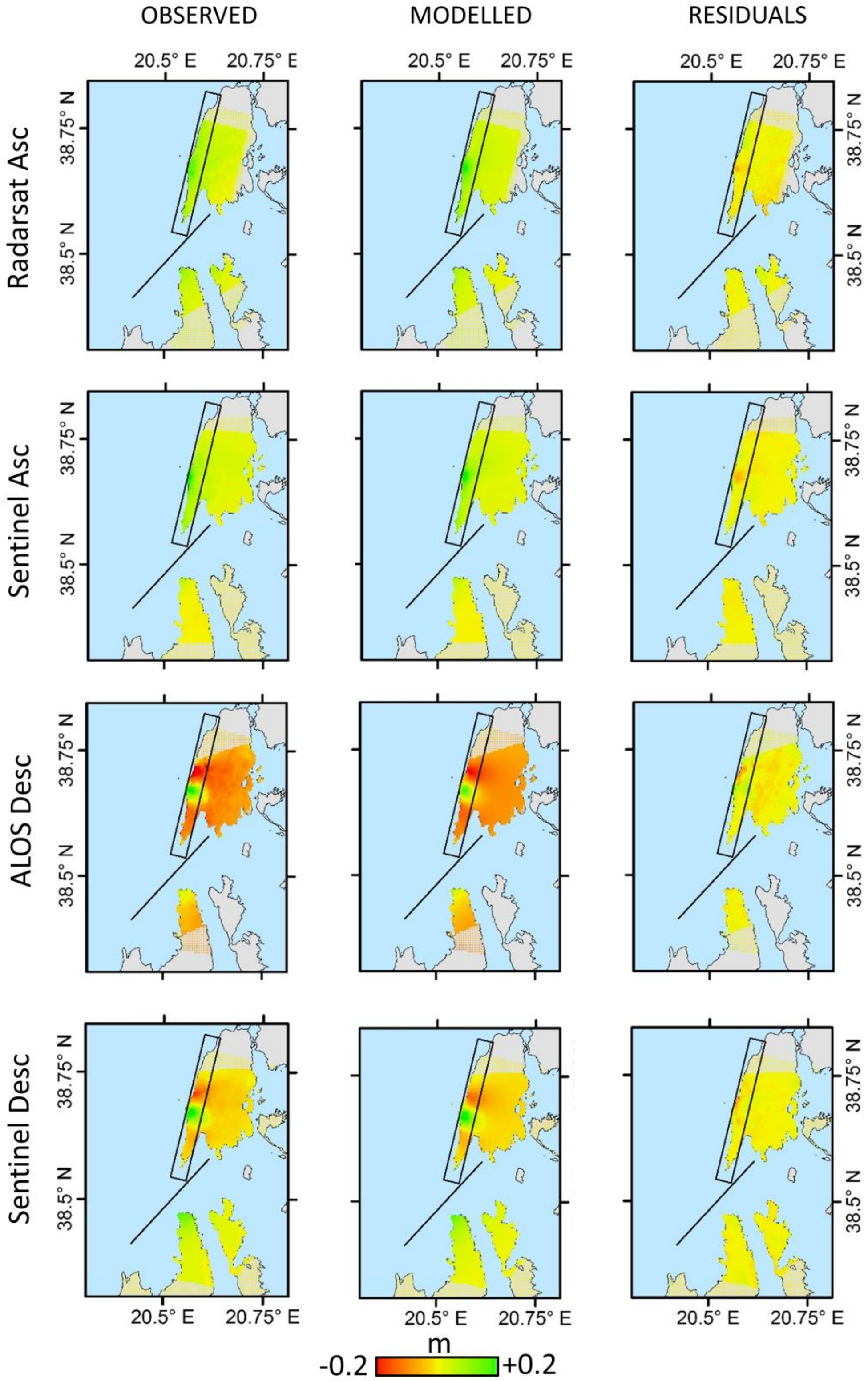

Figure 5.23 Observed, modelled and residuals of the linear inversion (Svigkas et al. 2019c).

Since here a new fault segmentation is presented (2 segments, striking obliquely to each other), a straight comparison of our slip distribution with previous studies is not feasible. The F1 segment is the only one that could be compared to other slip models, at a first approximation, as published slip distributions are only provided for a single fault segment. Our estimated peak slip of 2.9 m is comparable to the 2.3 m calculated by Chousianitis et al. (2016). Additionally, our model predicts a small slip pattern to the northeast of the Lefkada Island. This patch, with slightly different characteristics, also seem to appear in the models of Avallone et al. (2017) and Chousianitis et al. (2016).

Table 5-8 Source parameters of the two-fault segments.

Segment F1					
Strike °	Dip°	Rake°	Length (km)	Width (km)	Max Slip (m)
13	70	158	32	10	2.9
Segment F2					
Strike °	Dip °	Rake°	Length (km)	Width (km)	Max Slip (m)
43	90	108	25	10	1.6

5.2.7 Variable slip patch size solution

To evaluate the resolution power of the data, we also performed the source modelling using the variable patch size, "full resolution" method introduced by Atzori and Antoniolli (2011). The full-resolution algorithm is based on the model resolution matrix R, defined as:

$$R = G^{-g} \times G \tag{5.2}$$

where G is the Green's function matrix used to calculate the slip distribution, i.e. including the Laplacian operator, and G^{-g} is its generalized inverse.

Diagonal values in the R matrix describe the resolution for every parameter, ranging from 1 (perfectly resolved) to 0 (completely undefined). In InSAR modelling, the latter is only a theoretical limit, since every fault element contributes to every point on the surface.

What generally happens after a subdivision with equally sized patches is that shallower patches are perfectly resolved, implying that they could be further subdivided; and then the resolution rapidly drops down with depth to very low values. However, the depth is not the only parameter driving the resolution. For example, in subduction zones, shallower patches are those less resolved because of their distance from the coastline, where the closest InSAR observations are available.

The full-resolution algorithm iteratively splits the fault into patches such that the resulting R matrix is as close as possible to the identity matrix, i.e. such that every fault element can be nearly fully constrained by data. Details about the algorithm can be found in Atzori and Antonioli (2011).

In the case of Lefkada, the fault parameters adopted to perform the linear inversion with the variable patch size were those derived from the nonlinear inversion: Strike/Dip/Rake = 13°/70°/158° for the northern fault segment and Strike/Dip/Rake= 43°/90°/108° for the southern segment. After the full resolution algorithm application, we obtained the northern fault subdivided into 169 elements, with length ranging from 250m to 4km and width from 312m to 2.5km. The southern fault was subdivided to 34 patches and the patches' length values vary from 1km to 3km and the width from 1km to 5km. We assume that our subdivision in the main text of fixed patches is a good compromise with the resolution power of observed data. Slip distribution results from the variable patch size method (Figure 5.24) are in accordance with those from the equal patch size solution (Figure 5.22) both spatially and also in terms of magnitude. The rms values of the variable patch size method are: 0.024 m, 0.015 m, 0.017 m and 0.012 m for ALOS Descending, Radarsat Ascending, Sentinel Ascending and Sentinel Descending respectively. Observed and modelled displacements, together with their residuals are shown in Figure 5.25.

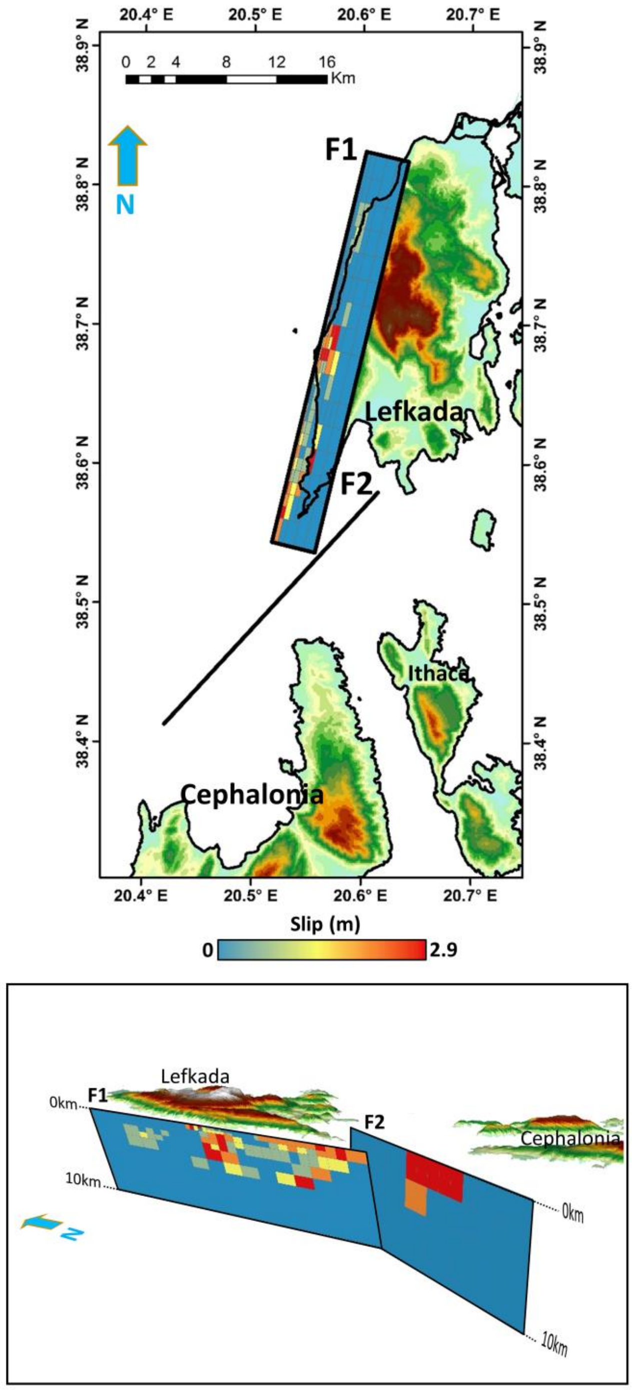

Figure 5.24 InSAR slip distribution with a variable patch size. Upper panel: map view, Lower panel: 3D View.

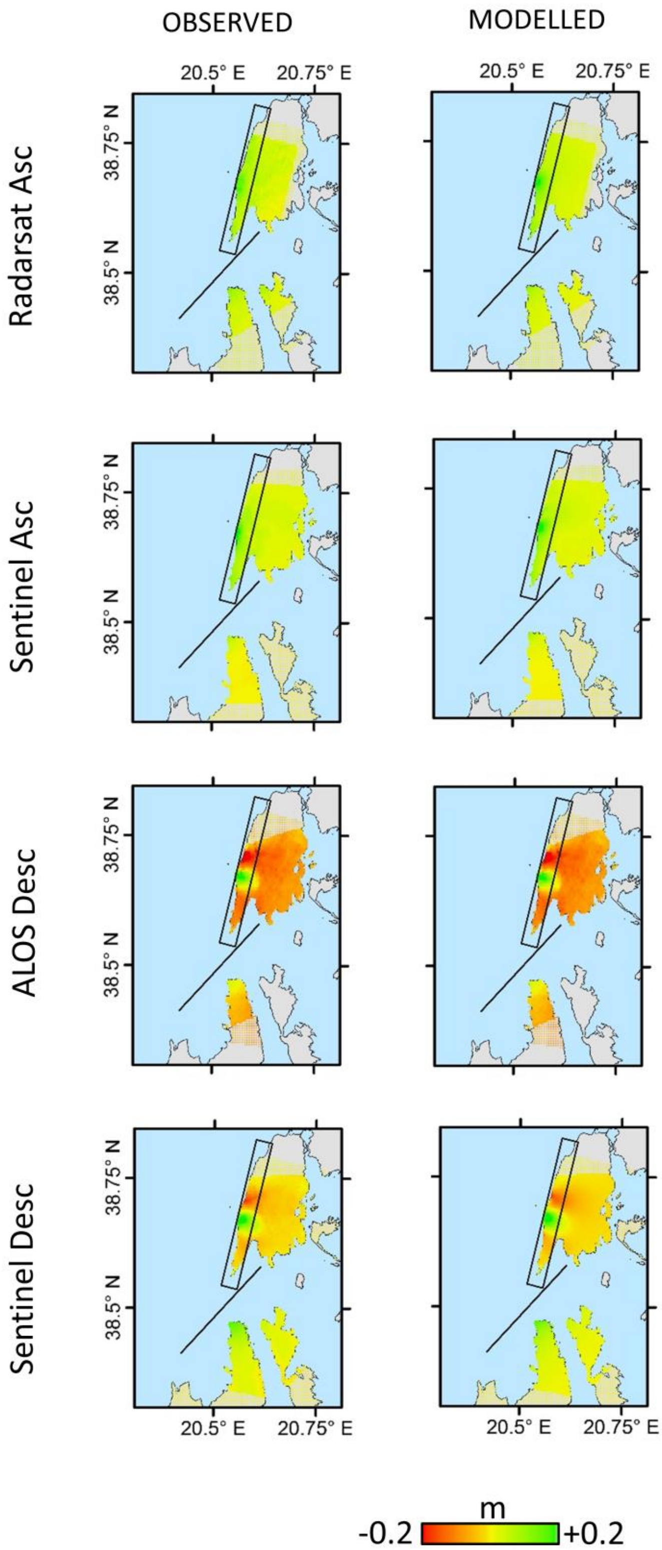

Figure 5.25 Observed, modelled and residuals for the variable patch size model of Figure 5.24.

5.2.8 Insights in the evolution of the deformation pattern

InSAR cannot offer information on the deformation at the areas that are covered by water bodies. The same is for the limited in number, on-land GPS stations that are installed at the area. Based on all the previous results of this study, the reconstruction of the three dimensional displacement that took place during the 2015 Lefkada sequence is presented and how it evolved. Figure 5.26 shows the forward models. We separate the sequence into two phases: Phase 1 is the one during which F1 had acted and Phase 2 is the full displacement pattern caused by both the two fault segments (F1 & F2) that ruptured according to our results. The upper three panels reconstruct the three dimensional movement of Phase 1, while the lower panels depict displacement during Phase 2. It can be derived that in both the Phases 1 and 2, to the most part, the island of Lefkada moved towards the west. During Phase 1, Ithaca and the tip of Cephalonia are subsiding due to the activity of the northern fault segment; the opposite occurs at the time when F2 is activated in Phase 2 where all three islands were uplifted, to the most part. The north-south component in both phases is dominated by the strike-slip character of the activity. Overall, the mainshock segment F1 that had moved as a combination of a strike-slip and a reverse component, appeared to have affected a more southern, possibly pre-existing, vertical structure (F2), which in turn expressed a movement with a reverse and strike-slip character.

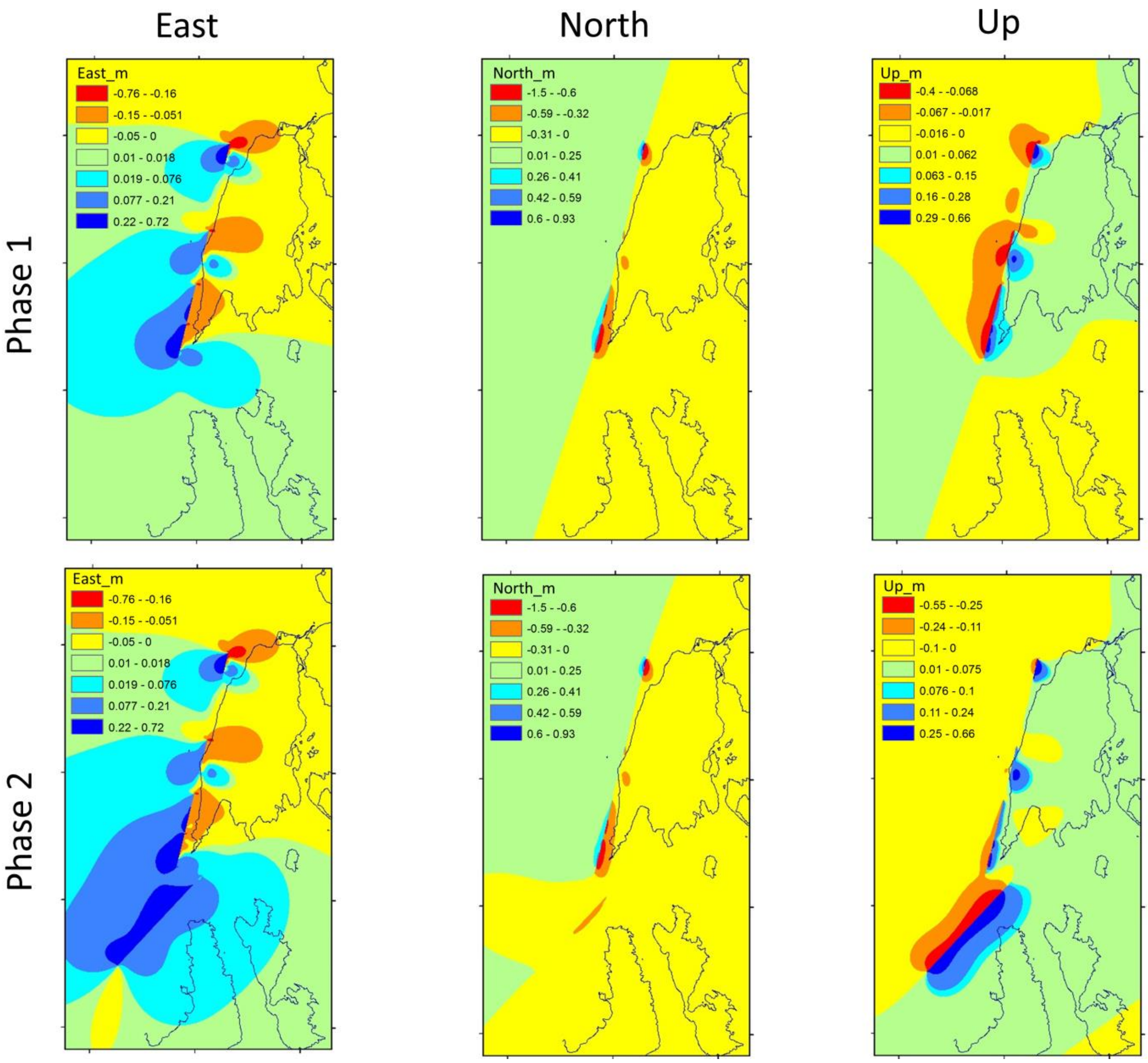

Figure 5.26 Reconstruction in the three dimensions, of the evolution of the displacement pattern during the Lefkada 2015 sequence. Phase 1 is the model of the displacement caused by fault F1 (Figure 5.24); Phase 2 is the displacement of the movements caused by both F1 and F2.

5.2.9 Stress transfer

The obtained source mechanisms were used to investigate a potential stress interaction between F1 and F2 (with F2 as receiver fault). A similar scenario was previously examined (Papadimitriou et al. 2017), however with a different fault configuration for the receiver fault, than the one we adopt. Based on the slip distributions, the static Coulomb stress changes ΔCFF, taking into account the pore pressure contribution, were estimated as (Harris et al. 1998):

$$\Delta CFF = \Delta\tau + \mu'\Delta\sigma_n \tag{5.3}$$

where $\Delta\tau$ is the shear stress, $\Delta\sigma n$ is the normal stress change (unclamping is positive) and μ' is the apparent friction coefficient where $\mu'=\mu(1-B)$ and B is the Skempton coefficient. Here, μ' was adopted to be 0.4 (Papadimitriou, 2002). Positive ΔCFF indicates that failure is promoted, in the opposite case (negative ΔCFF value), that failure is suppressed.

Figure 5.27 summarizes the results which indicate that the slip distribution of F2 occurred at an area of a positive stress loading (max 0.35 MPa) caused by F1.

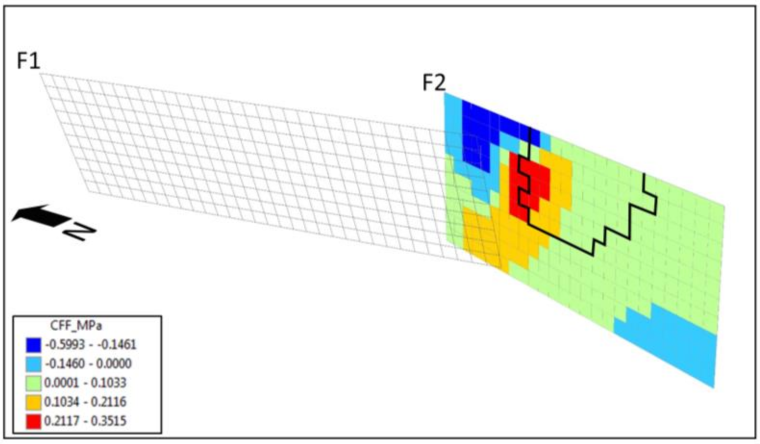

Figure 5.27 Coulomb stress changes caused from F1 onto the receiver fault F2. The black-noted polygon on F2 denotes the extent of the source's slip distribution (Svigkas et al. 2019c).

5.2.10 Discussion and Conclusions

A new InSAR multi-modal dataset was exploited to revisit the displacement pattern of Lefkada and Cephalonia islands (Ionian Sea) caused by the occurrence of the 2015 Lefkada earthquake sequence. The displacement fields retrieved here support the operation of a more complex set of structures for the 2015 case study. The InSAR input indicates that a rupture of a single fault, parallel to the western coastline of Lefkada Island, is not able to account for the entire observed displacement pattern. It is the observed displacement at the northern tip of the Cephalonia Island, which requires a second fault segment, to be sufficiently modelled.

This study is in agreement with Ganas et al. (2016b) about the general concept of a second fault segment and with Bie et al. (2017) about the fact that the signal at the tip of Cephalonia is an important feature to be considered in the modelling procedure. The importance of the signal at the tip of Cephalonia was furtherly highlighted here and additional information on it was obtained by the specific InSAR dataset used. The exploited radar signal provided more insights on the on-land deformation pattern of both islands and in consequence, it offered better constraints regarding the fault segmentation. The multi-segment hypothesis was further investigated and building upon the study of Papadimitriou et al. (2017), it was possible to present a new fault segmentation that predicts well all the InSAR displacement data (both ascending and descending) which is at the same time justified by the relocated seismicity, the seafloor bathymetry and the stress transfer computation.

The preferred model identifies two distinct fault segments, which are both required to interpret the geodetic data: a northern fault, bordering the western coastline of Lefkada, associated with the mainshock, encompassing three discrete slip patches, and a secondary southern fault segment, oblique to the northern segment, hosting a single slip patch, at a shallow depth. For this southern segment, no slip is evident below 6 km. The detected dip-slip of the movement of F2 is unfavourably oriented, being a pseudo-vertical fault, not encouraging a dip-slip mechanism; a possible explanation is proposed here, involving block rotation bounded with pre-existing structure, shown in Figure 5.28. Regardless of the real block length, by assuming L equal to 1 km, a dislocation of 1.6 m at the surface can be obtained with a negligible rotation α of 0.09°. This movement could have been further facilitated by the existence of evaporites at the broader area (Stiros et al. 1994; Karakitsios et al. 2007; Saltogianni et al. 2018; Brooks et al. 1984; Velaj et al. 1999) that can promote frictional instabilities, under specific conditions (Scuderi et al. 2013).

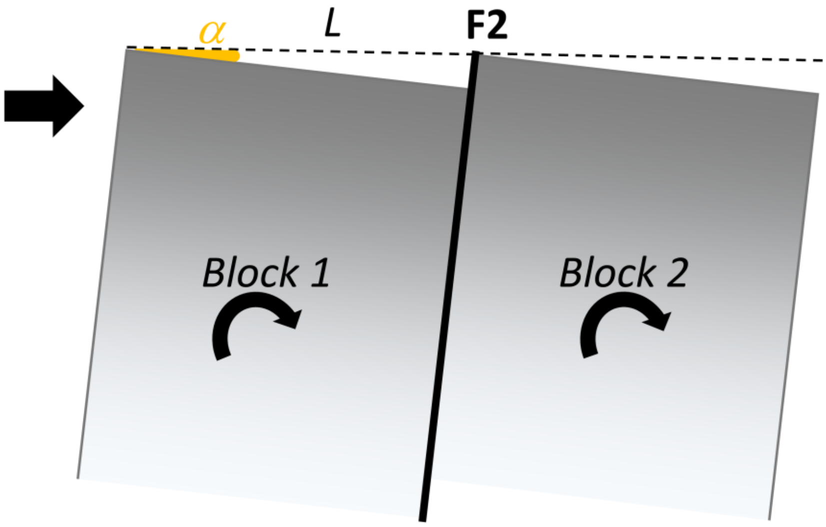

Figure 5.28 Schematic interpretation of the movement of F2 (Svigkas et al. 2019c).

To summarize, the Cephalonia Transform Fault (CTF) zone is better viewed as a wide zone where the deformation is taken up by multiple strike-slip fault segments (Fig. 5.29), whereas the thrust components are not negligible at all, possibly related to the Ionian Thrust zone. The existence of an oblique fault segment (F2) is proposed, in the intersection of the Cephalonia branch with the Lefkada branch and it is probable that other similar structures co-exist in the broader region, as Papadimitriou et al. (2017) and Karakostas et al. (2014) proposed. This oblique fault to the main CTF zone highlights the importance of pre-existing structures in the rupture processes occurring on CTF.

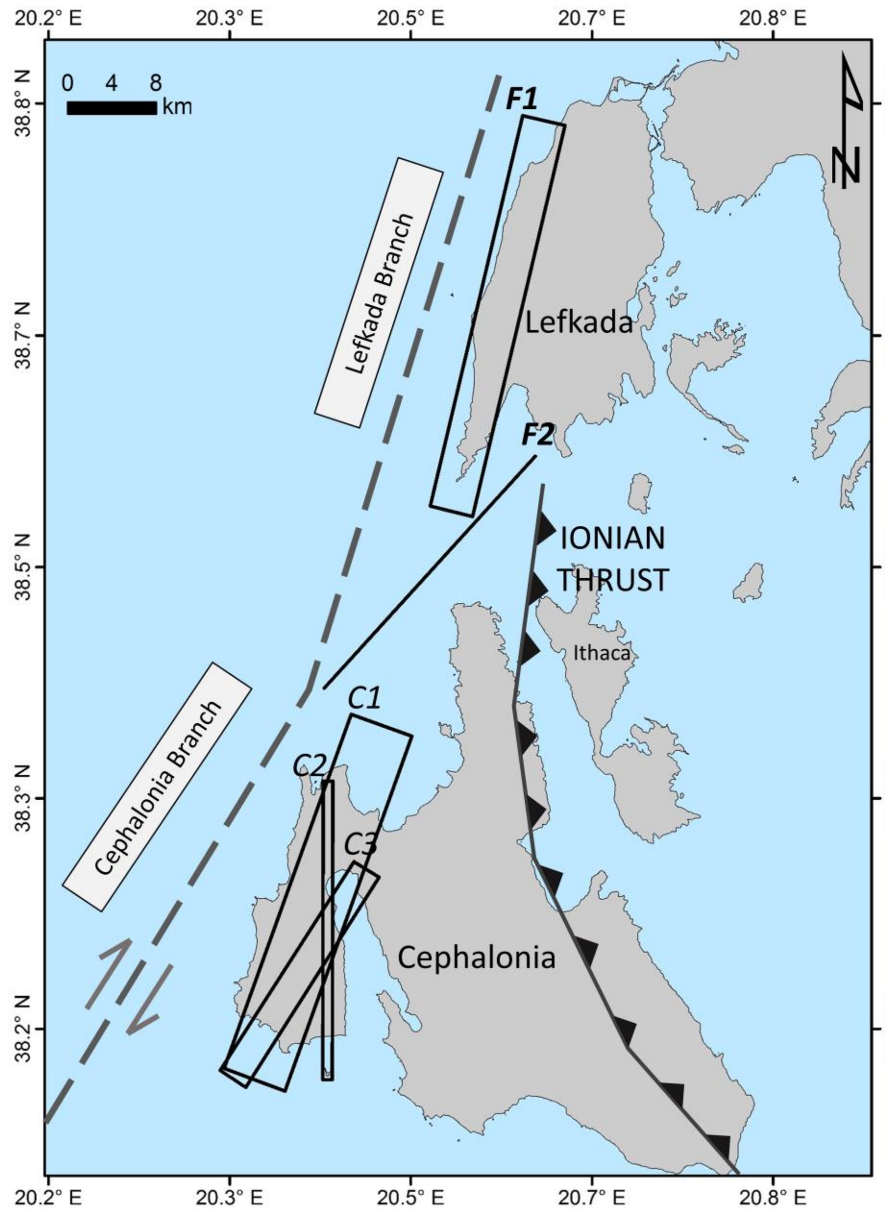

Figure 5.29 The configuration of the Cephalonia Transform Fault (CFT) zone with the two branches: Cephalonia and Lefkada. The black rectangles outline the faults. F1 and F2 are the sources of the November 2015 earthquake sequence. C1 to C3 are the faults that ruptured during the January-February 2014 earthquakes (Sokos et al. 2015; Boncori et al. 2015). CTF is a wide off- and on-shore multi-segmented fault zone; F2 is a structure that separates CTF to the so-called "Lefkada" and "Cephalonia" branches (Svigkas et al. 2019c).

5.3 STUDYING EARTHQUAKE SWARMS WITH INSAR

5.3.1 Introduction

InSAR investigations of strong seismic events have relatively recently started to be a systematic tool for the study of their displacement pattern. There are very few studies in the bibliography that have implemented it as a tool for studying seismic swarms; for the swarms occurring globally, in most of the cases, there is a complete absence of InSAR studies. During the first three months of 2017, a shallow earthquake swarm of moderate magnitude M5+, occurred at the tip of the Biga peninsula (Fig. 5.30), in western Anatolia (Turkey). The sequence, also called the Ayvacik (Çanakkale) swarm, was characterized by the occurrence of more than 1,500 events by the end of March 2017.

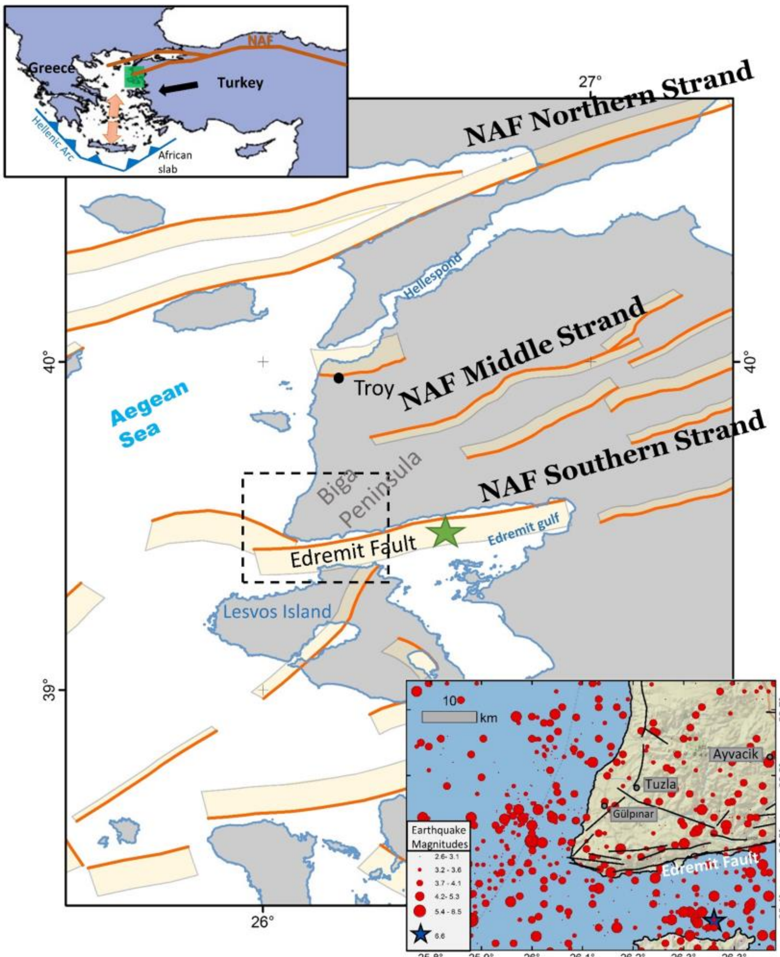

Figure 5.30 Location of the study area (dashed rectangle) in the broader tectonic framework of the North Anatolian Fault Zone (NAFZ). The orange polygons depict seismogenic sources (Caputo and Pavlides, 2013): lines denote the fault-top trace, whereas the transparent polygons show the fault-dipping plane. The green star on Edremit fault marks the location of the 1944 earthquake. Upper left inset: location of the study area (green square) in a regional framework. Lower right inset: close-up on the area of study, with the local fault network (black lines, after Yılmaz & Karacık, 2001). The geothermal power plant is located in Tuzla (coordinates 39.566066°N, 26.173216°E). The seismicity (red dots) is sparse on the Biga peninsula, but strong M≥6.0 events are mainly observed offshore (the data span the period 1300 – 2016) (Svigkas et al. 2019b).

The swarm seismic activity at Biga peninsula is shown in Figure 5.31. The focal mechanisms of three of the main events (no 1-3, Table 5.9), are numbered and denoted with the green beach-balls. Other available focal mechanisms (Table 5.10) of smaller-size events are indicated in black colour.

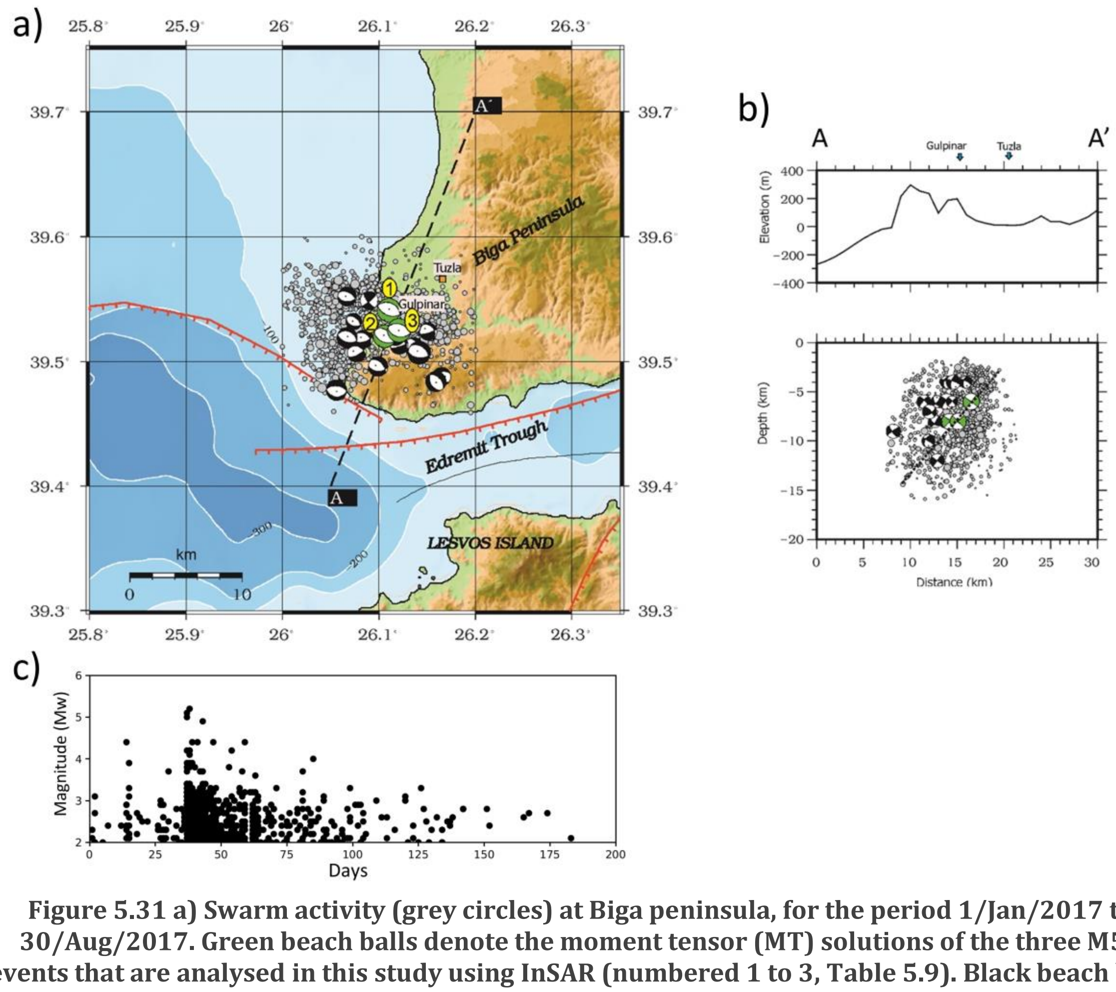

Figure 5.31 a) Swarm activity (grey circles) at Biga peninsula, for the period 1/Jan/2017 to 30/Aug/2017. Green beach balls denote the moment tensor (MT) solutions of the three M5+ events that are analysed in this study using InSAR (numbered 1 to 3, Table 5.9). Black beach balls depict other published MT solutions of the swarm (listed in Table 5.10). Normal faulting along WNW-ESE striking planes is well depicted. The red lines denote faults (Caputo and Pavlides, 2013). b) Cross-section along dip, profile A-A' depicted in (a). The approximate location of the

Gülpınar and Tuzla villages is marked. The dashed line passing through the projection of the three major events (green beach-balls) supports the assumption that the swarm is due to the activation of a SW dipping normal fault, located below these villages. c) Magnitude-Time graph showing the evolution of the sequence (Svigkas et al. 2019b).

The focal mechanisms (Fig. 5.31) indicate the prevalence of WNW-ESE almost pure normal faulting, in accordance with the regional stress field (Chatzipetros et al. 2013; Kiratzi 2014; 2018 and references therein). Seismicity is confined to the tip of Biga peninsula, almost beneath the village of Gülpinar, and extends offshore to the west. The along dip A-A' cross-section (Fig. 5.31b) shows that the swarm operated in the upper crust, at shallow depths (3-12 km). In conclusion, the sequence is attributed to the rupture of a normal fault dipping to the SW, in accordance with the most prominent faults in the region, as concluded by others as well (Ganas et al. 2018; Mesimeri et al. 2018).

Although the number of reported injuries was small, some locals were placed in tents to reduce the risk of injury from collapsing buildings in consequent events. The strongest M5+ events caused damage to ~2,600 poorly constructed structures in 30 nearby villages, as reported by the field survey carried out after their occurrence (Livaoğlu et al. 2018).

Table 5-9 Focal depths, seismic moments, Mo, and focal mechanisms of Events 1, 2 and 3 (Svigkas et al. 2019b).

Event	Date YR/MM/DD	Origin Time UTC	Lat. °N	Long. °E	Depth (km)	Mo ×10e24 dyn-cm	Mw	Nodal Plane 1 strike/dip/rake			Nodal Plane 2 strike/dip/rake		
1	2/6/2017	3:51:40	39.541	26.1102	6 (-2, +1)	1.1	5.3	112	53	-91	294	37	-88
2	2/6/2017	10:58:02	39.520	26.1058	8 (-2, +0)	0.52	5.1	115	48	-99	308	43	-80
3	2/7/2017	2:24:04	39.525	26.1208	8 (-1, +0)	1.2	5.3	103	43	-93	288	47	-87

Table 5-10 Available focal mechanisms for other earthquakes of the swarm, determined by moment tensor inversion retrieved from the database of the Geodynamic Institute of Athens (http://bbnet.gein.noa.gr).

Date	Origin	Lat.	Long.	h	Mw	Nodal Plane 1			Nodal Plane 2			P axis		T axis	
YR/M/D	Time	°N	°E	km		strike°	dip°	rake°	strike°	dip°	rake°	az°	pl°	az°	pl°
20170114	22:39:01	39.496	26.099	6	4.4	315	48	-59	93	50	-120	296	68	204	1
20170115	4:03:21	39.518	26.084	6	4	307	38	-45	75	64	-119	302	60	186	14
20170206	11:45:02	39.507	26.077	10	4.2	294	32	-43	62	69	-115	297	59	170	20
20170207	5:15:51	39.488	26.165	8	4.1	252	48	-133	126	57	-53	92	59	191	5
20170207	5:17:09	39.506	26.14	8	4.2	329	38	-29	83	73	-124	314	50	198	20
20170207	21:00:55	39.512	26.136	6	4.1	328	44	-52	101	57	-121	317	64	212	7
20170207	21:35:01	39.513	26.121	4	4	316	28	-30	73	76	-115	314	52	182	27
20170208	1:38:04	39.521	26.117	4	4.5	319	23	-38	85	76	-108	332	55	190	29
20170208	2:16:15	39.524	26.151	4	3.9	321	31	-26	74	77	-118	312	50	186	27
20170209	10:13:11	39.519	26.066	6	3.8	252	58	-122	122	44	-49	109	62	4	8
20170210	8:55:26	39.484	26.159	7	4.5	313	49	-103	152	43	-76	159	80	52	3
20170212	13:48:17	39.507	26.142	6	5.1	308	42	-64	95	53	-111	308	72	200	6
20170216	0:19:00	39.519	26.067	12	4.5	108	55	-92	291	35	-88	11	80	199	10
20170222	1:24:22	39.532	26.074	6	3.6	309	47	-75	108	45	-105	293	79	29	1
20170223	1:55:14	39.552	26.067	6	4.2	298	49	-73	93	44	-109	275	77	16	3
20170228	23:27:35	39.477	26.056	9	4.6	97	35	-89	276	55	-91	184	80	6	10
20170324	15:19:06	39.549	26.09	6	4	50	83	161	142	71	7	97	8	5	18

The stress field in the broader region combines shearing and extension, placing the tip of the Biga peninsula in an active transtentional tectonic regime (e.g. Chatzipetros et al. 2013; Bulut et al. 2018). Shearing is imposed by the activity of the dextral strike-slip North Anatolian Fault (NAF) and its middle and southern strands (Fig. 5.30) (e.g. Özalp et al 2013; Şengör, 1979, Şengör et al. 2005). The southern shore of the peninsula is controlled by the southern strand, where the dominant structure is the Edremit Fault Zone (EFZ) (Sözbilir et al. 2016 and references therein). The strongest seismic event recorded at EFZ, within the instrumental period, is the 6 October 1944, Mw 6.8 Edremit-Ayvacik earthquake (Ambraseys, 1988; Fig. 5.30), with a normal south-dipping source (dip ~46°, e.g. Paradisopoulou et al. 2010) which caused 73 fatalities, 275 injuries and over 2,000 building failures (Altinok et al. 2012).

The tip of Biga peninsula exhibits generally moderate-size seismicity; no M>5 earthquakes occurred during instrumental period and no strong M>6-7 during historical times. The site hosts important geothermal fields (e.g. Şamilgil, 1966; Mützenberg, 1997; Şanlıyüksel & Baba, 2007; Baba and Ertekin, 2007) which have been exploited since the ancient times. The seismic sequence occurred near to the Tuzla Geothermal Field (Baba et al. 2008, 2015), where a geothermal power plant, has been operating since 2010. It is well accepted that in the presence of migrating fluids, fluid pore-pressure variations might be the driving mechanism or at least facilitate the occurrence of swarm-type activity. The connection between the swarm occurrence and geothermal activity is not clear, and this investigation is outside the scope of the present work.

Studies on swarm surface displacements are very limited and only recently, after the advent of space geodetic techniques, have been made available (Kyriakopoulos et al. 2013; Bell et al. 2012; Lohman and McGuire 2007, among others). Swarms often leave a weak surface signal that in many cases cannot be detected by radar satellites. This difficulty is the main reason for the lack of InSAR swarm studies in the existing bibliography. Even though the shorter satellite revisit times of Sentinel-1 have created more opportunities in terms of the ability to isolate specific seismic events, in many cases, it is still difficult to isolate all earthquakes. In most cases there will usually be a signal related to rapid afterslip (Elliott et al. 2016) and in some cases even strong post-seismic components. This a basic disadvantage of InSAR compared to the high temporal resolution that seismic data can offer.

In this study, the displacement patterns associated with three main events of the 2017 Biga swarm was detected. Using Differential InSAR (e.g. Dixon, 1994; Massonnet and Feigl 1998; Massonnet, 1997; Zebker and Goldstein, 1986) three M5+ events, hereinafter referred to as Event 1, 2 and 3 (Table 5.9), were analysed. The revisit time of the Sentinel-1 A & B radar sensors were exploited and by applying an ad hoc modelling strategy, the distribution of all three M5+ events separately were estimated, while proposing fault segmentation for the swarm activity. Additionally, using Sentinel-1 and ALOS-2 data, the detected cumulative displacement was modelled to find the cumulative slip distribution. The results of geodetic modelling, are also compared with the sources and slip distributions, obtained from the inversion of regional waveform data. Eventually, InSAR results are exploited to investigate the on-fault Coulomb Stress Changes and the possible interaction between the source of the 2017 swarm and the Edremit Fault.

5.3.2 Data and Methods

Throughout this study, each acquisition date follows the naming convention of yyyymmdd, as shown in Table 5.11, which lists the radar acquisitions used. The data exploited are from Sentinel-1A & 1B and ALOS-2 satellites, which were launched relatively recently (2014, 2016 and 2014 respectively) and are a courtesy of European Space Agency (ESA) and Japan Aerospace Exploration Agency (JAXA). Atmospheric corrections were applied using the Generic Atmospheric Correction Online Service for InSAR (GACOS) (Yu et al. 2017, 2018). The InSAR topographic contribution was removed using the Shuttle Radar Topography Mission SRTM –1 (resolution ~30m) Digital Elevation Model (e.g. Farr and Kobrick, 2000).

The image processing was carried out with the SARscape software. For each pair of images, the master (pre-event) and slave (post-event) images were co-registered. Then, each master image was multiplied by the complex conjugate of the corresponding slave image, creating an interferogram. The latter was corrected in terms of orbits, atmosphere and topography. All interferograms were filtered using Goldstein filtering (Goldstein and Werner, 1998). Interferometric fringes were then unwrapped with the minimum cost flow algorithm (Costantini, 1998) and geocoded to get the Line of sight (LoS) displacement maps used in modelling.

First, the optimum SAR pairs to isolate the main seismic events were identified (Table 5.11). Earthquake isolation, through the choice of specific radar images, depends mainly on the time and date of satellite acquisition and is not always guaranteed. For this reason, as will be shown below, a specific strategy was adopted for the source study of the events. In all the selected interferograms for inversion, there is at least one M ≥ 4.9 event.

Table 5-11 Combination of SLC images used in the study and the seismic events they contain (Svigkas et al. 2019b).

Interferogram No.	Master Image Date	Master Image Time	Satellite of Master Image	Slave Image Date	Slave Image Time	Satellite of Slave Image	Satellite Pass	Incidence Angle (°)	Satellite Look direction	Seismic Events Contained
1	20170125	04:14:47	Sentinel-1A (TOPS)	20170206	04:14:47	Sentinel-1A (TOPS)	Descending	43.88	*Right*	*Event 1:* 06 FEB 2017 03:51:40.7 Depth: 6km Mw5.3
2	20170131	04:14:04	Sentinel-1B (TOPS)	20170206	04:14:47	Sentinel-1A (TOPS)	Descending	43.84	*Right*	
3	20170206	16:06:23	Sentinel-1B (TOPS)	20170212	16:07:09	Sentinel-1A (TOPS)	Ascending	37.77	*Right*	*Event 3:* 07 FEB 2017 02:24:04.0 Depth: 8km Mw5.3
4	20170125	16:06:23	Sentinel-1B (TOPS)	20170206	16:06:23	Sentinel-1B (TOPS)	Ascending	37.77	*Right*	*Event 1:* 06 FEB 2017 03:51:40.7 Depth: 6km Mw5.3 *Event 2:* 06 FEB 2017 10:58:02.2 Depth: 8km Mw5.1
5	20170131	16:07:09	Sentinel-1A (TOPS)	20170212	16:07:09	Sentinel-1A (TOPS)	Ascending	33.94	*Right*	*Event 1:* 06 FEB 2017 03:51:40.7 Depth: 6km Mw5.3 *Event 2:* 06 FEB 2017 10:58:02.2 Depth: 8km Mw5.1 *Event 3:* 07 FEB 2017 02:24:04.0 Depth: 8km Mw5.3
6	20170106	04:22:48	Sentinel-1A (TOPS)	20170223	04:22:48	Sentinel-1A (TOPS)	Descending	33.85	*Right*	
7	20161202	22:04:00	ALOS-2 (StripMap)	20170210	22:03:59	ALOS-2 (StripMap)	Ascending	31.41	*Right*	
8	20170106	10:20:48	ALOS-2 (WideSwath)	20170217	10:20:48	ALOS-2 (WideSwath)	Descending	39.04	*Right*	

Within the modelling procedure, we also assessed the parameters of possible orbital ramps affecting input datasets. Given the large amount of coherent pixels in the InSAR output and to avoid a computational overload, the displacement maps were down-sampled with a two-level density sampling grid: denser in the event proximity and coarser elsewhere.

The initial modelling is carried out by adopting the uniform slip in a homogenous and isotropic elastic half-space equation from Okada (1985); at first a non-linear inversion scheme (Levenberg, 1944; Marquardt, 1963) is adopted, to identify the fault parameters and mechanism (strike, dip, rake, slip, fault location, length, depth, width), possibly introducing seismological constraints from the focal mechanisms derived from the seismic waveform analysis. The optimisation starts from a random fault configuration within given parameter ranges and it keeps minimizing the cost function Φ, based on the weighted squares of the residuals between the observed and the predicted data:

$$\Phi = \frac{1}{N}\sum_{i}^{N}\frac{(\mathrm{d}_{i,obs} - \mathrm{d}_{i,mod})^2}{\sigma_i} \tag{5.4}$$

where $\mathrm{d}_{i,obs}$ and $\mathrm{d}_{i,mod}$ are the observed and modelled displacements of the i-th data point and σ_i is the standard deviation of the Nth points (we assume σ_i to be the same for all points). The downhill algorithm is implemented with multiple restarts to guarantee the convergence to the global cost function minimum. After defining the fault geometry, a linear inversion was applied to obtain the slip distribution, extending the fault length and width to let the slip vanish to zero and subdividing the fault plane into subfaults of 1 km × 1 km. The linear inversion scheme adopted (Atzori et al. 2009, 2012) is described by the equation:

$$\begin{bmatrix}\boldsymbol{d}\\0\end{bmatrix} = \begin{bmatrix}\mathrm{G}\\ \varepsilon\nabla^2\end{bmatrix}\cdot\mathbf{m} \tag{5.5}$$

where ***d*** is the InSAR data, G is the Green's functions matrix with the Laplacian operator ∇^2 tuned with the damping factor ε, obtained by trial-and-error (Menke, 1989), and **m** is the vector of parameters. A further constrain of parameters positivity is adopted to prevent back-slip.

5.3.3 Crustal deformation results

With the pairs of 20170125_20170206 and 20170131_20170206, both from Sentinel-1, isolation of Event 1 (Table 5.11, Fig. 5.32a) was achieved. Deformation at Biga peninsula for the period 20170206_20170212 during which Event 3 occurred (Table 5.11) is shown in Figure 5.32b and finally the interferogram 20170125_20170206 of Figure 5.32c contains Events 1 and 2 together. The interferograms showing the cumulative deformation of all the events analysed in this study, are presented in Figure 5.33, where both ascending and descending imagery was analysed from both Sentinel-1 and ALOS-2 satellites. Detected cumulative in the Line-of-Sight (LoS) deformation is more than 7 cm.

5.3.4 InSAR Source modelling

To initialize the InSAR non-linear inversion, where the range of possible values must be set for each fault parameter, the results of the seismic moment tensor inversion were taken into account and in some cases a number of the parameters were fixed (Table 5.12) by adopting the solutions as derived from the seismic data (Table 5.9). The pairs 20170125_20170206 and 20170131_20170206 were used to derive the source parameters for Event 1. After defining Event 1, the 20170206_20170212 interferogram was modelled to get Event 3 parameters; it should be noted that this InSAR pair contains also a fourth earthquake (12 February 2017, 13:48 Mw 5.1). However, it was found that this particular event did not cause any detectable surface deformation signal (Fig. 5.34).

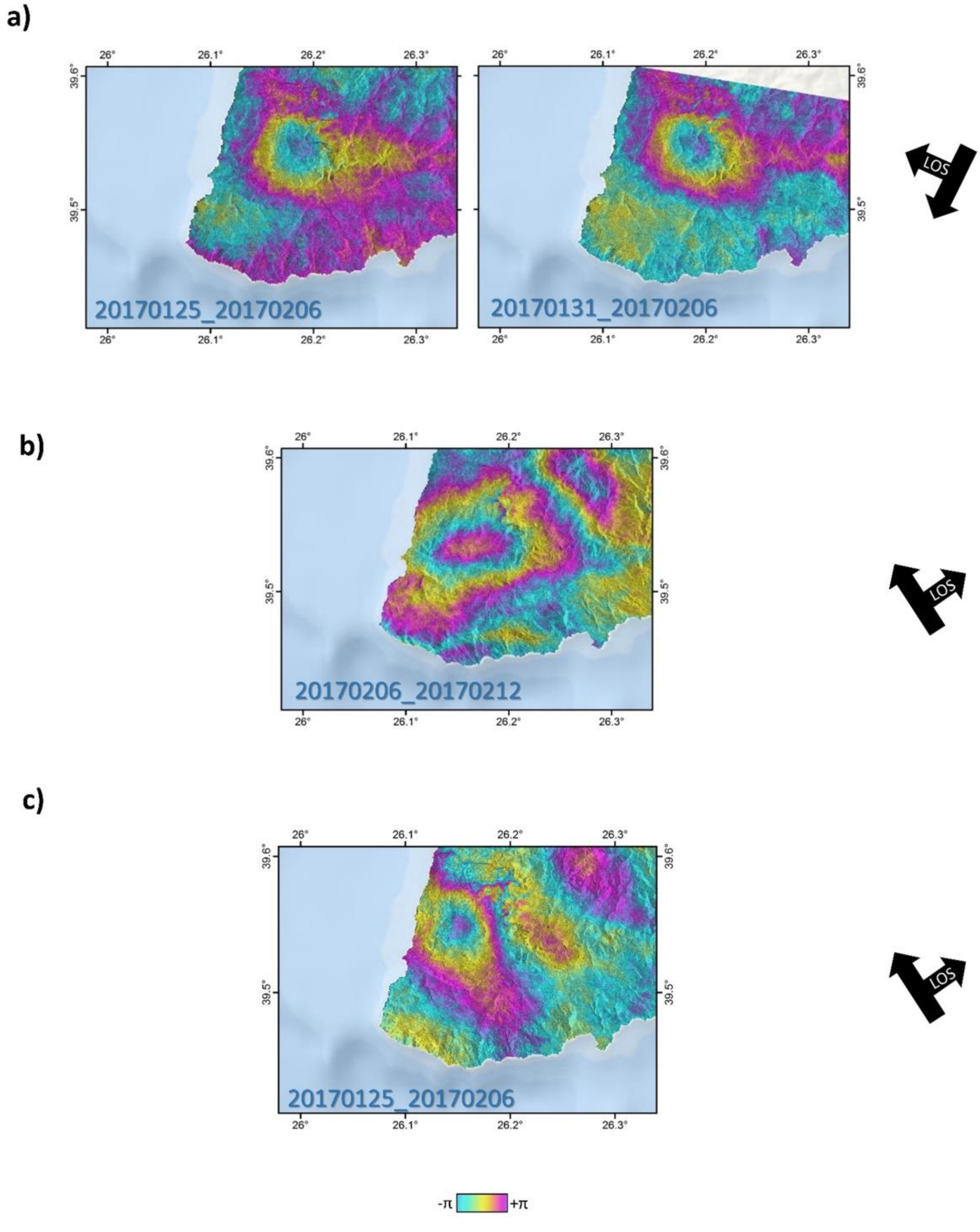

Figure 5.32 a) Sentinel-1 Interferograms from the Descending pass showing the displacement caused by Event 1 (Table 5.11). b) Sentinel-1 Ascending Interferogram showing the displacement caused by Event 3. c) Sentinel-1 Ascending Interferogram of Events 1 and 2 (Table 5.11) (Svigkas et al. 2019b).

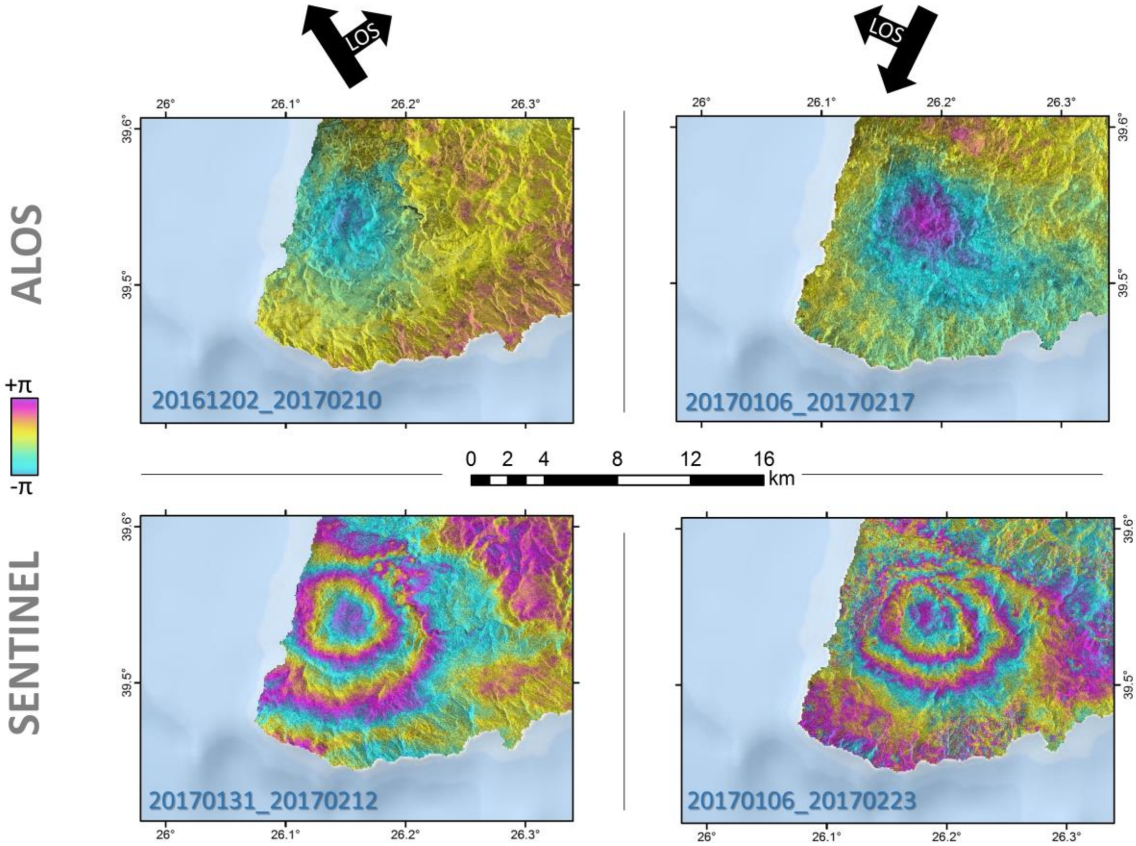

Figure 5.33 Fringe patterns from different satellites (Sentinel-1 and ALOS-2) and different viewing geometries (Left panels: Ascending, Right panels: Descending) that express the cumulative displacement caused by Events 1, 2 and 3 (Table 5.11) (Svigkas et al. 2019b).

Table 5-12 InSAR results of non-linear inversions of Events 1, 2 and 3.

	Strike°	Dip°	Rake°	Slip (m)	Top Depth along dip(km)	UTM Easting (m)	UTM Northing(m)	Width (m)	Length(m)
Event 1	112 (fixed)	24±19	-99±47	1.3±1.1	10.6±4	429745.2±2318	4385288.4 ±4408	1000 (fixed)	3467 ±3402
Event 2	115 (fixed)	48 (fixed)	-99 (fixed)	0.3±0.6	7.3±4	426703±3507	4378542.5±4350	2000 (fixed)	7000 (fixed)
Event 3	103 (fixed)	43 (fixed)	-93 (fixed)	0.5±0.3	7.6±2.6	428159±1914	4381658.3±2370	4000 (fixed)	3351.8±2723

Regarding event 2, it was not possible to isolate its surface displacement just by choosing images with specific acquisition times; therefore, we used the interferometric pair 20170125_20170206, containing the contribution of both Event 1 and Event 2 (Table 5.11), and by keeping fixed the previously defined source of Event 1, the residual signal inverted the get the source parameters of Event 2.

Results of the non-linear inversions of all events and uncertainties are presented in Table 5.12 and Figures 5.35-5.37. The Root mean Square (rms) values of each inversion can be found in Table 5.13, while observed and modelled interferograms are presented in Figures 5.38-5.40.

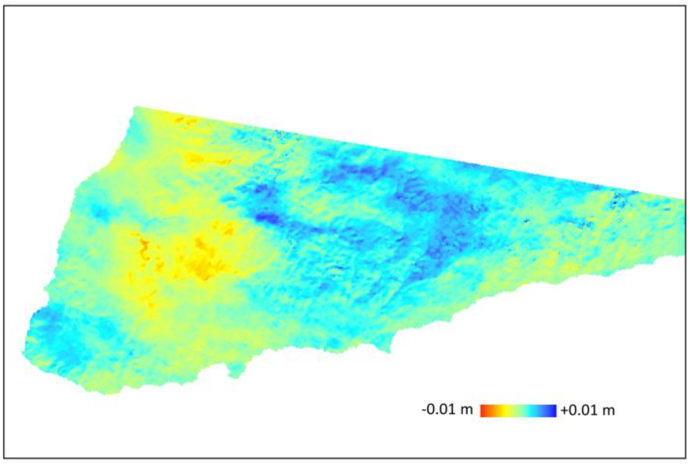

Figure 5.34 DInSAR result of the 4th seismic event, which indicates a lack of a significant deformation signal.

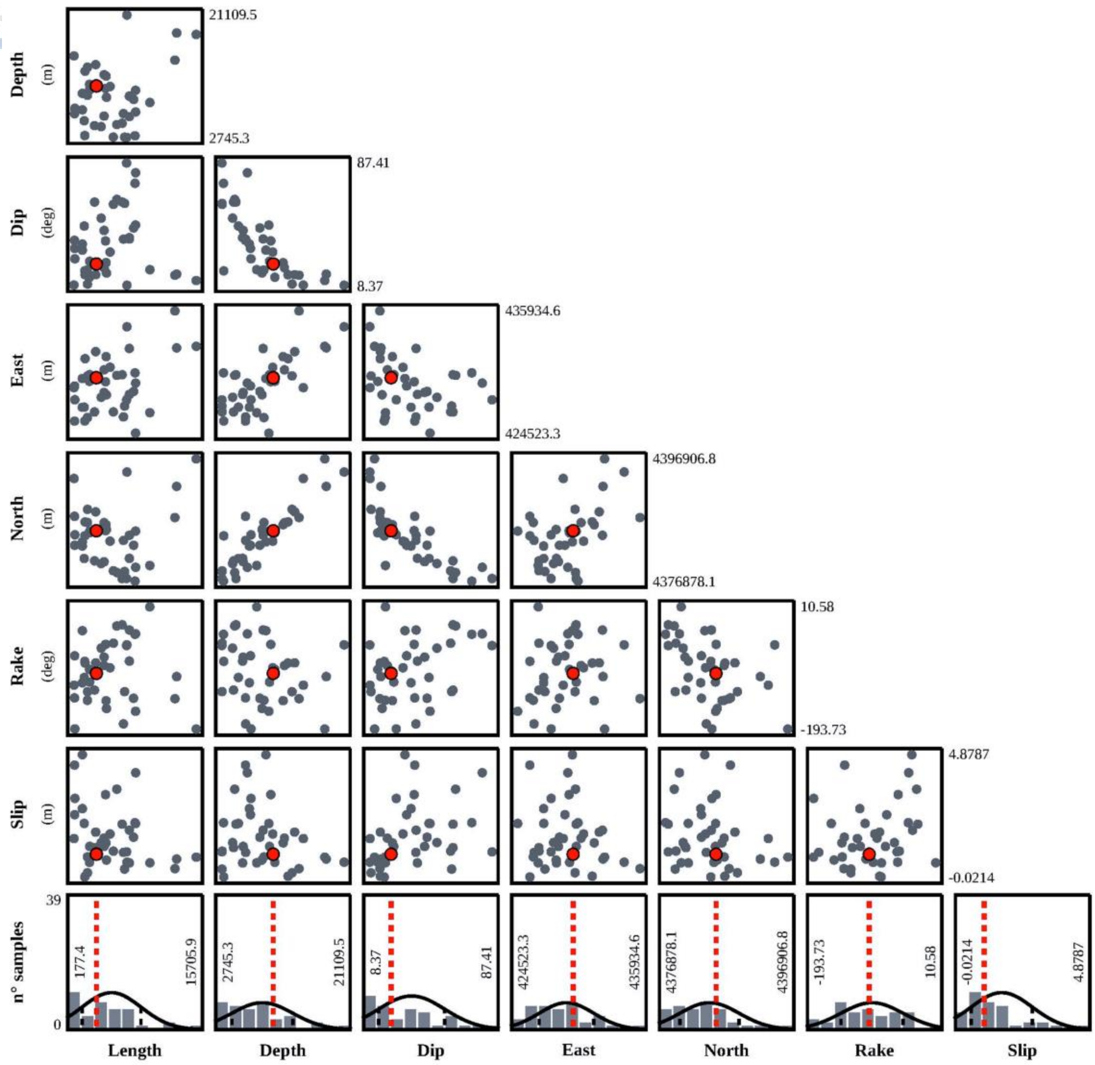

Figure 5.35 Trade-offs and uncertainties of source parameters for Event 1. For the estimation of uncertainties, interferograms with realistic noise were simulated and were subsequently inverted for the source parameters. The results were compared with the optimal values found by our preferred solution. Scattered plots show the trade-offs between the parameters. Red points indicate the optimal values. The bottom histograms are the a-posteriori probability distributions of the parameters. Black curves are showing the Gaussian fit.

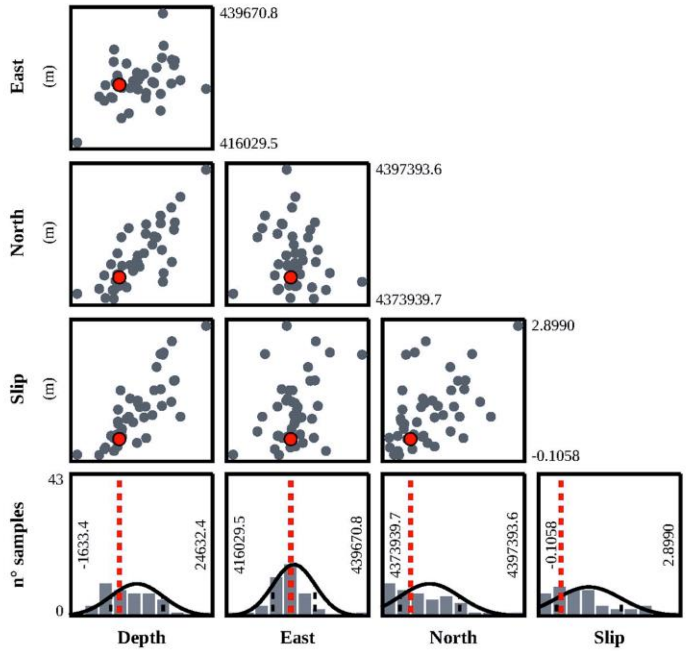

Figure 5.36 Trade-offs and uncertainties of source parameters of Event 2.

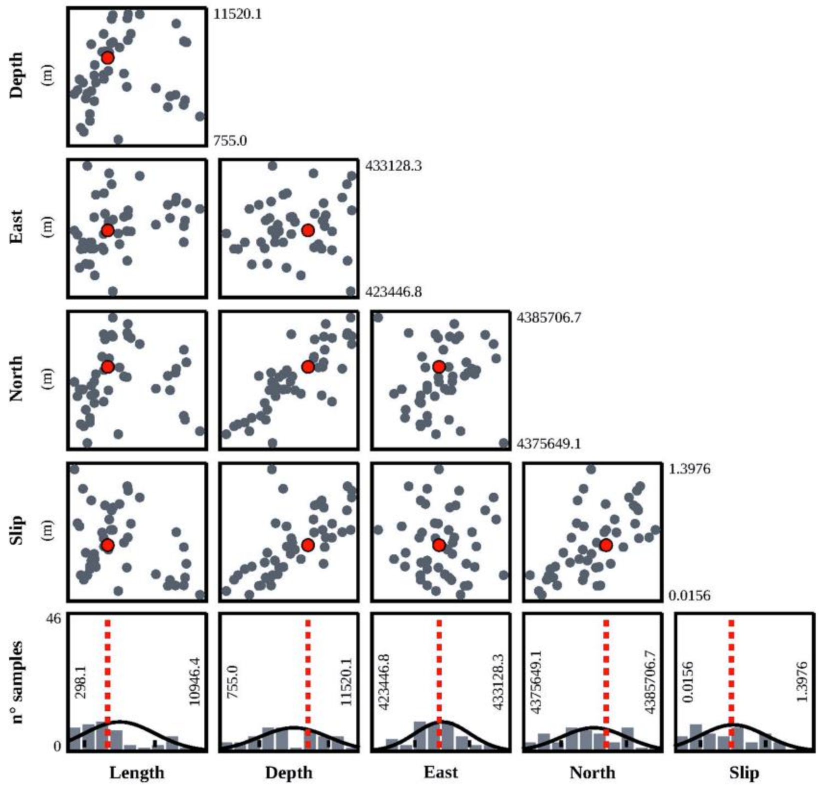

Figure 5.37 Trade-offs and uncertainties of source parameters of Event 3.

Table 5-13 Root mean square (rms) values of the non-linear and linear Inversions for Events 1, 2 and 3.

Event 1	Event 2	Event 3
Non-Linear inversion		
Int.: 20170125_20170206 rms: *0.004*	Int.: 20170125_20170206 *rms: 0.006*	Int.: 20170206_20170212 *rms: 0.005*
Int.: 20170131_20170206 rms: *0.003*		
Linear Inversion		
Int.: 20170125_20170206 *rms: 0.003*	Int.: 20170125_20170206 *rms: 0.004*	Int.: 20170206_20170212 *rms: 0.003*
Int.: 20170131_20170206 *rms: 0.003*		

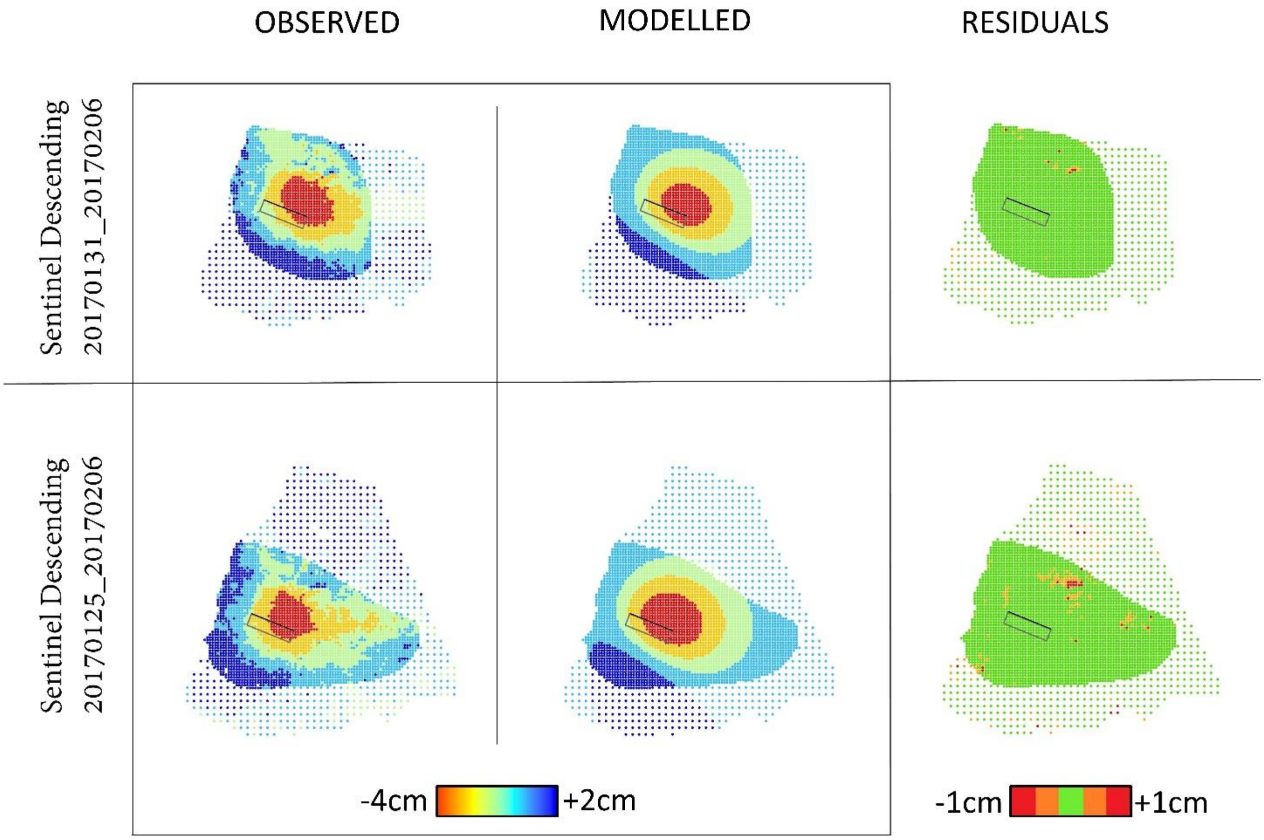

Figure 5.38 Observed, Modelled and Residuals of the InSAR non-linear inversion of 20170125_20170206 and 20170131_20170206 for the source of Event 1. Positive and negative signs mean, LoS shortening and lengthening respectively

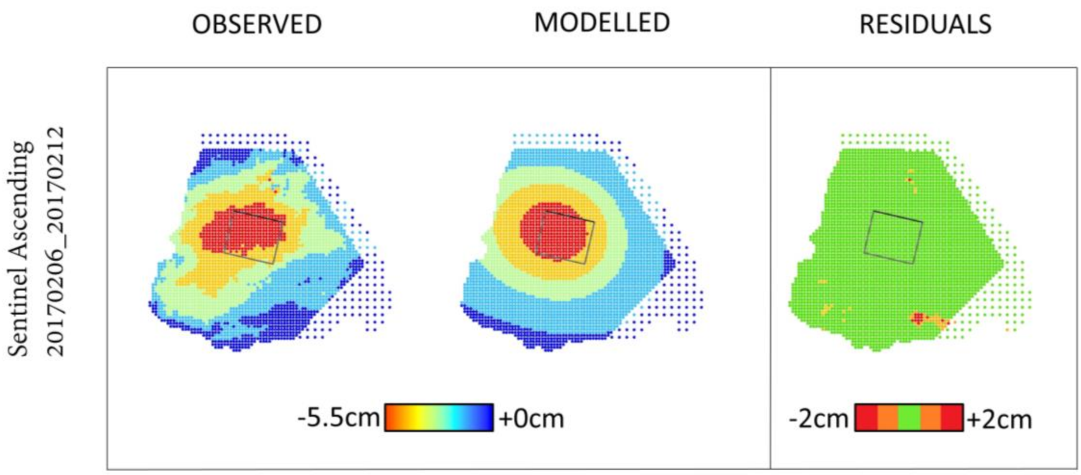

Figure 5.39 Observed, Modelled and Residuals of the InSAR non-linear Inversion for the source of Event 2. Positive and negative signs mean, LoS shortening and lengthening respectively.

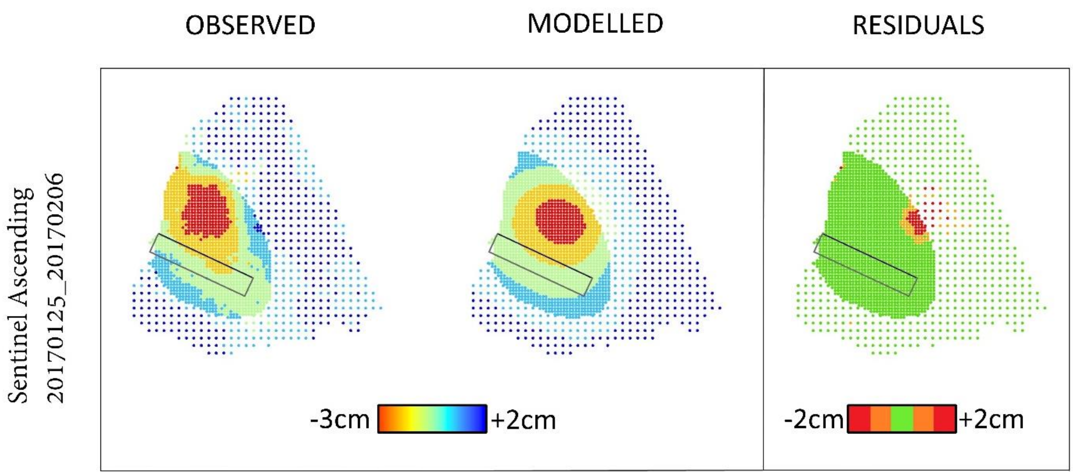

Figure 5.40 Observed, Modelled and Residuals of the InSAR non-linear inversion of 20170206_20170212 for the source of Event 3. Positive and negative signs mean, LoS shortening and lengthening respectively.

5.3.5 Comparison of the InSAR sources with hypocentres

Below a comparison between the uniform slip sources and the hypocentres is presented. The centroid is an expression with regard to the energy released; the hypocentre is where the rupture initiated. These two might or might not coincide. The InSAR results can be compared with the centroids, but they are not directly comparable with the hypocentres. However, as shown later a comparison between the InSAR sources and the hypocentres might possibly indicate interesting facts on the rupture process.

Figure 5.41 shows the catalogue epicentres and hypocentres of different agencies (blue circles with black dot in centre) together with the InSAR results (red circles). Results from KOERI, AUTH, NOA and additionally from the International Seismological Centre (ISC) are shown. Variability is present in the event's locations (Fig. 5.41a) and regarding the hypocentral depths (Fig. 5.41b) we see that, with the exception of the AUTH hypocentre in Events 2 and 3, the rest hypocentre solutions from all seismic catalogues are located at larger depths than InSAR.

Earthquake locations from seismic waveforms often have a variability in the position of the location. That is why earthquake relocation techniques had been developed in order to have a better definition of the earthquake's initiation point. This variability in the location of the events can be seen also in the case of Biga swarm. In general, differences between the InSAR and seismic catalogues themselves could derive from inaccurate seismic velocity models. The comparison of the seismic locations with InSAR locations is an additional way to have an independent look of the earthquake locations that derived from waveforms. In case the earthquake event takes place on-land at shallow depths, like in the case of Biga, InSAR can provide strong constrains because its result are considered as a "ground truth" measurement, as mentioned by Weston et al. (2012).

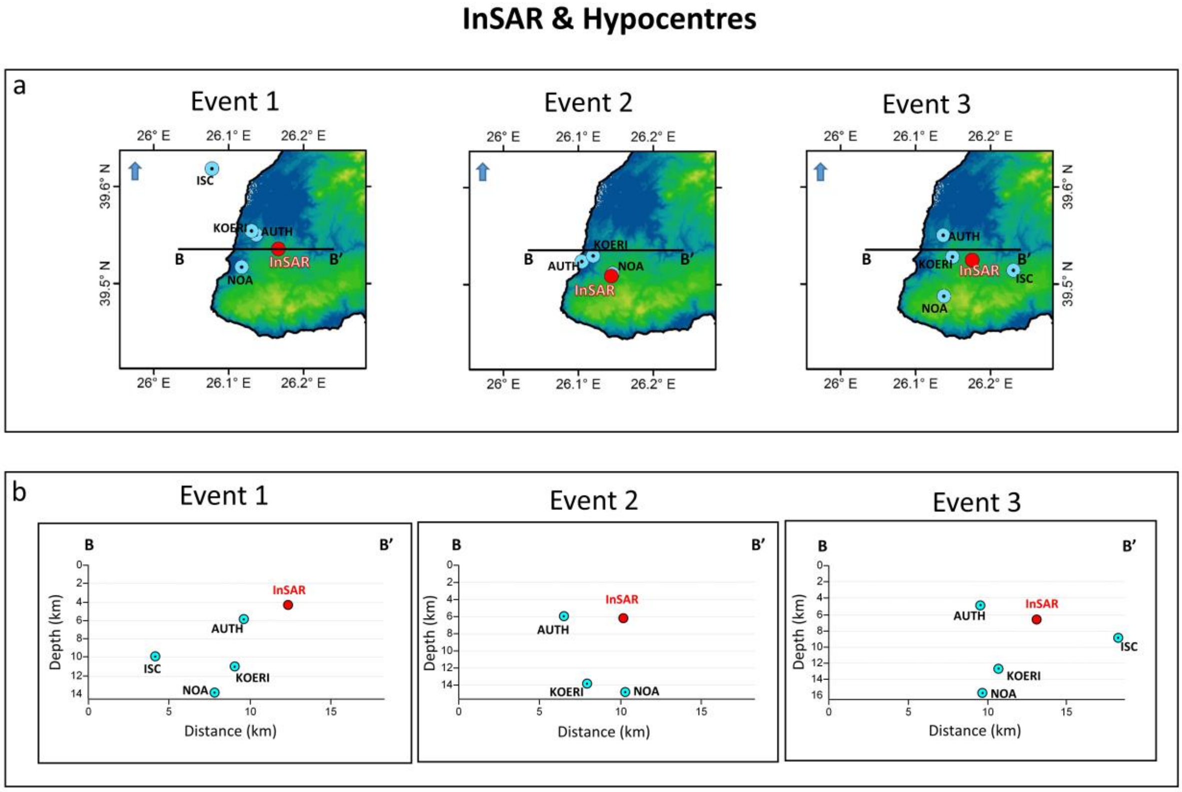

Figure 5.41 Comparison between the InSAR derived uniform slip sources and the hypocenters a) Map view b) cross-sections indicating depicting the depth differences. Blue dots are from seismic catalogues, red dot is the location of the uniform-slip source of this study.

Regarding the depth differences, except the potentially inaccurate velocity models, another issue for the seismic stations is that they are located at the top of the crust and the arrival times are sensed on the surface which makes depth estimation difficult (Bai et al. 2006). On the other hand, systematically shallow depths from InSAR had been previously reported in literature (e.g. Lohman and Simons, 2005a; Feigl, 2002) and this difference in depth values might be due to the fact that the InSAR source analysis is using an elastic homogeneous half-space that is not taking into account the variations of the upper crust (e.g. Wald and Graves, 2001).

As previously stated, the InSAR depth is representing the centroid solution, whereas the hypocentre indicates the nucleation point of the rupture. Based on this, differences between the hypocentre and the shallower InSAR depths could give an insight in the rupture directivity. If stress is increased with depth (Das and Scholz, 1983) the earthquakes that are generated at depths of low stress might not propagate to higher depths. Thus, in case the shallow InSAR depth is valid for the Biga case, it could potentially be an indicator of an upward rupture propagation.

5.3.6 Slip distribution onto the causative fault plane

Since an advantage of InSAR is its ability to constrain fault segmentation (Elliott et al. 2016), as a first step, the InSAR uniform-slip modelling results are exploited from models for Events 1-3 (Fig. 5.42), to investigate the segmentation. Although the three fault planes retrieved for Events 1-3 are not exactly coincided, the different positions and mechanisms can be attributed to the uncertainty, necessarily present in InSAR data that propagated to the fault parameters. Considering also that the Okada solution is a simplified description of a fault system, it can be assumed that the three events occurred on the same fault (or fault system).

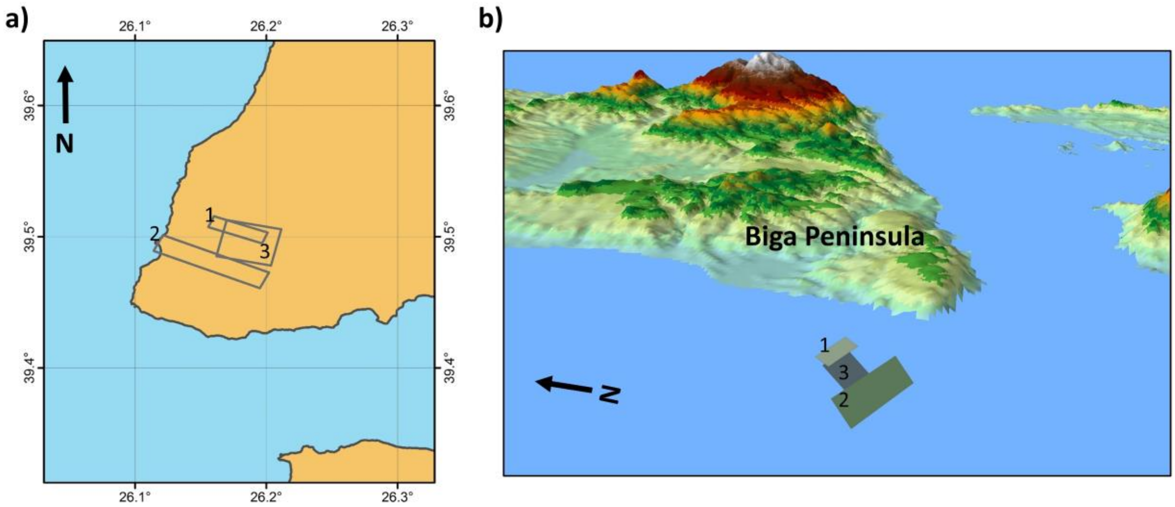

Figure 5.42 The non-linear solutions of Events 1, 2 and 3 a) planar view, b) 3D view.

Next step, was the slip distribution calculation, for InSAR and seismic waveforms inversion, adopting a strike 110°, dip 39° and rake -97° fault plane, which are the mean values of those derived for Events 1-3. To linearly model geodetic data, a stepwise procedure was followed: first was the estimation of the slip distribution for Event 1, using interferograms No. 1 and No. 2 (Table 5.11); then the calculation of the slip distribution of Event 3 using interferogram No. 3. For the linear inversion of Event 2, the same strategy was followed as the one adopted in the non-linear inversion, exploiting interferogram No. 4, setting as fixed the source of Event 1, which had already been assessed.

Figure 5.43 depicts the slip models. For the geodetic modelling, the rms values are listed in Table 5.14, while the observed, modelled and the residuals are summarized in Figure 5.44. Figure 5.45 show the uncertainties of the slip distributions.

The following observations can be deduced from the slip distribution models (Fig. 5.43):

- In all cases the slip is mainly confined to the mainland of Biga peninsula.

- The largest slip value is 25 cm, that of Event 3.

- In all cases, the town of Gülpınar is above the locus of peak slip and the town of Tuzla in close proximity.

- For Event 1, the slip extents to very shallow depths updip, almost reaching the surface.

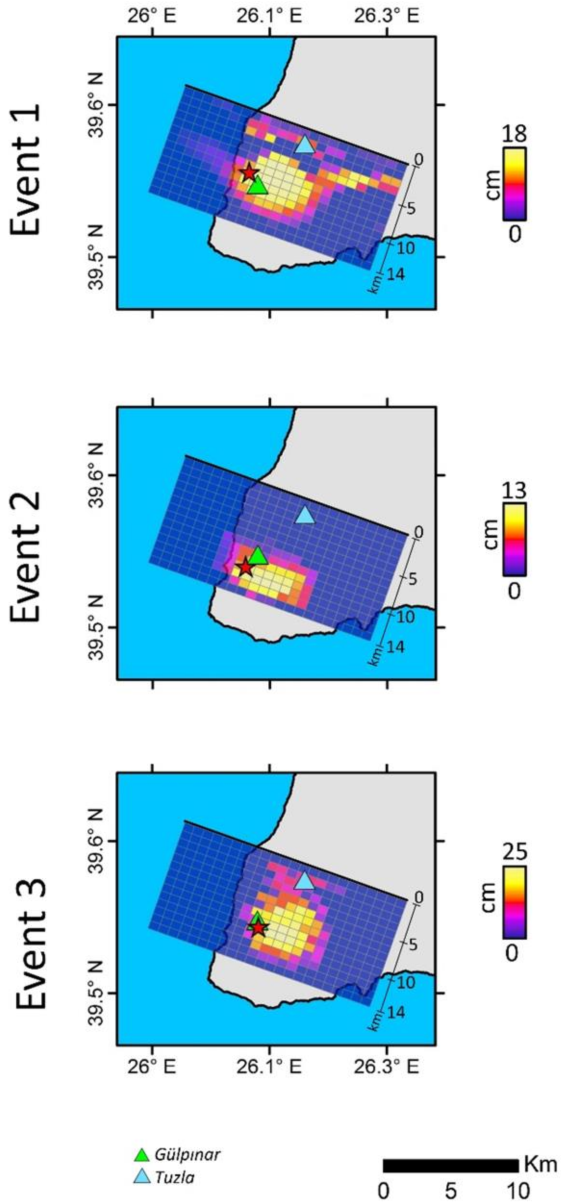

Figure 5.43 InSAR slip distributions of Events 1, 2 and 3.

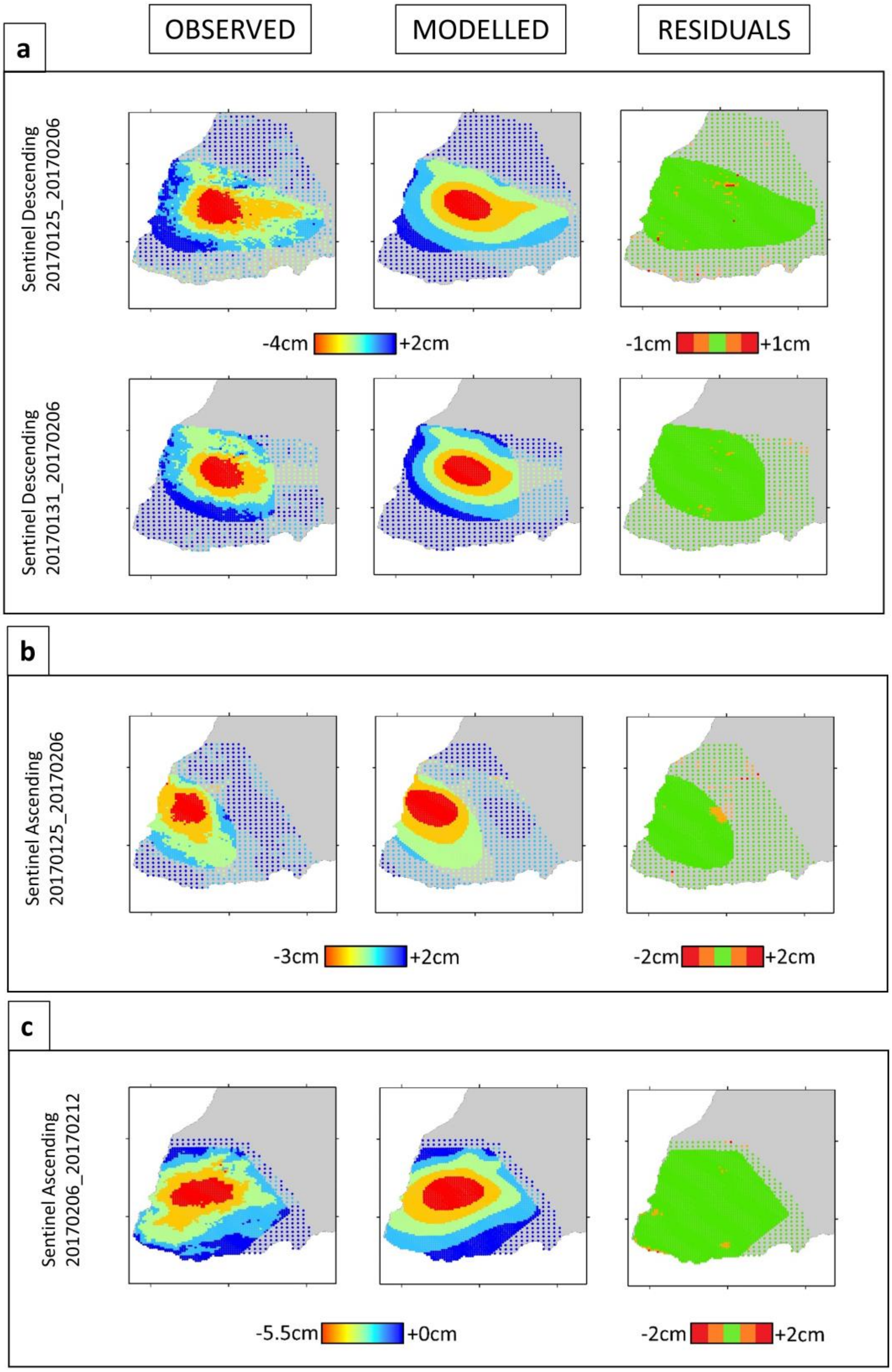

Figure 5.44 Observed, modelled and residuals of the slip distribution model of a) Event 1, b) Event 2 and c) Event 3. Positive and negative signs mean, LoS shortening and lengthening respectively.

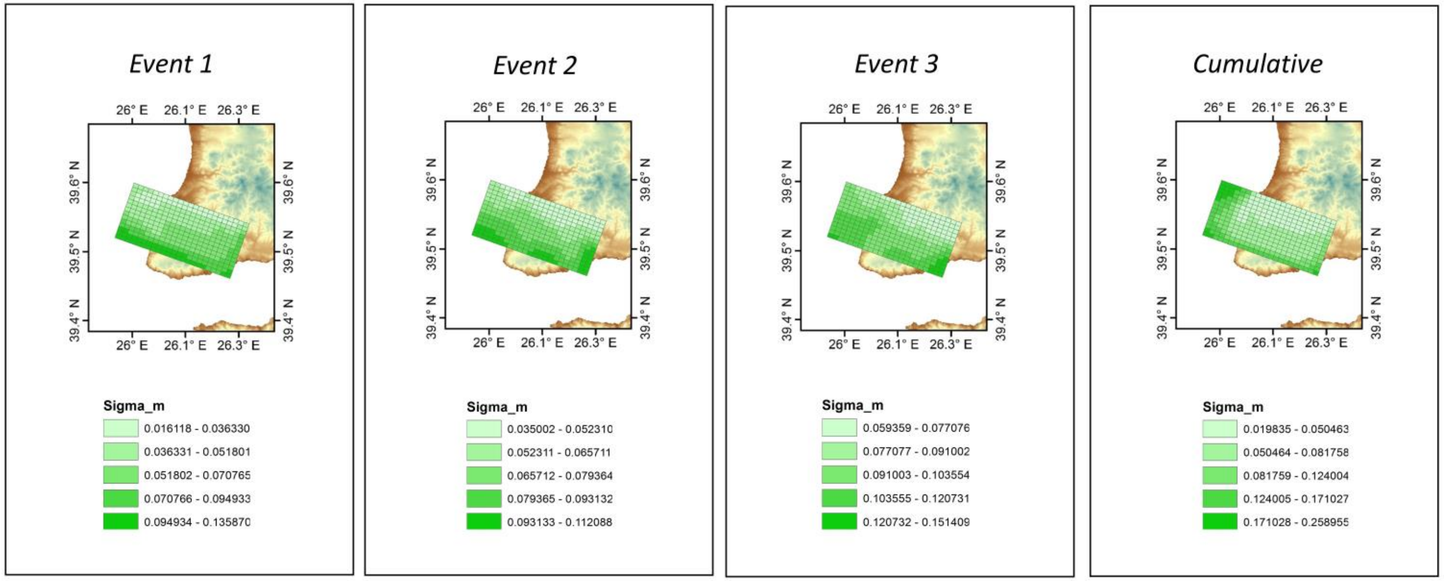

Figure 5.45 Slip distribution uncertainties. For practical reasons, we only show the diagonal values of the full variance-covariance matrix of the model parameters. The distributed uncertainty gives a qualitative idea of the parameter uncertainty, since off-diagonal values (not shown) do not allow them to vary independently (i.e. for the i^{th} patch, the slip value s_i is not strictly $s_i \pm \sigma_i$).

5.3.7 Slip modelling validation and cumulative slip distribution

To further validate the adopted InSAR modelling strategy and to demonstrate that it was possible to separate correctly the contributions of the three events, an independent modelling was carried out having as input an InSAR dataset encompassing all the three events (Interferograms No 5-8, Table 5.11). The retrieved slip distribution, was compared with the total amount of the separate slip distributions of the three events (Slip distributions of: Event1+Event2+Event3) described in the previous section.

The addition of the separate slip distributions indicates a peak slip value of 44 cm at a depth of 5.6 km (Fig. 5.46a). The cumulative slip distribution of the three events (estimated onto the same mean fault surface), this time found from the inversion of the interferograms No. 5-8 in Table 1, indicates a peak slip value of 47cm, located at a depth of 7.5 km (Fig. 5.46b). The high similarity of the two results, indicate that the sources' isolation strategy adopted in this study, has been successful. Observed modelled and residuals of the inversion of the cumulative interferograms are shown in Figure 5.47. Results and the rms values are found in Table 5.14.

Table 5-14 InSAR Linear Inversion Results of the cumulative slip.

Fault Plane			**Cumulative Slip Distribution from the cumulative interferograms (No 5-8, Table 5.11)**	
Strike°	Dip°	Rake°	Peak Slip (cm)	Depth of peak slip (km)
110	39	-97	47	7.5
			RMS values (m) Int. 20161202_20170210: 0.007 Int. 20170106_20170223: 0.007 Int. 20170106_20170217: 0.006 Int. 20170131_20170212: 0.005	

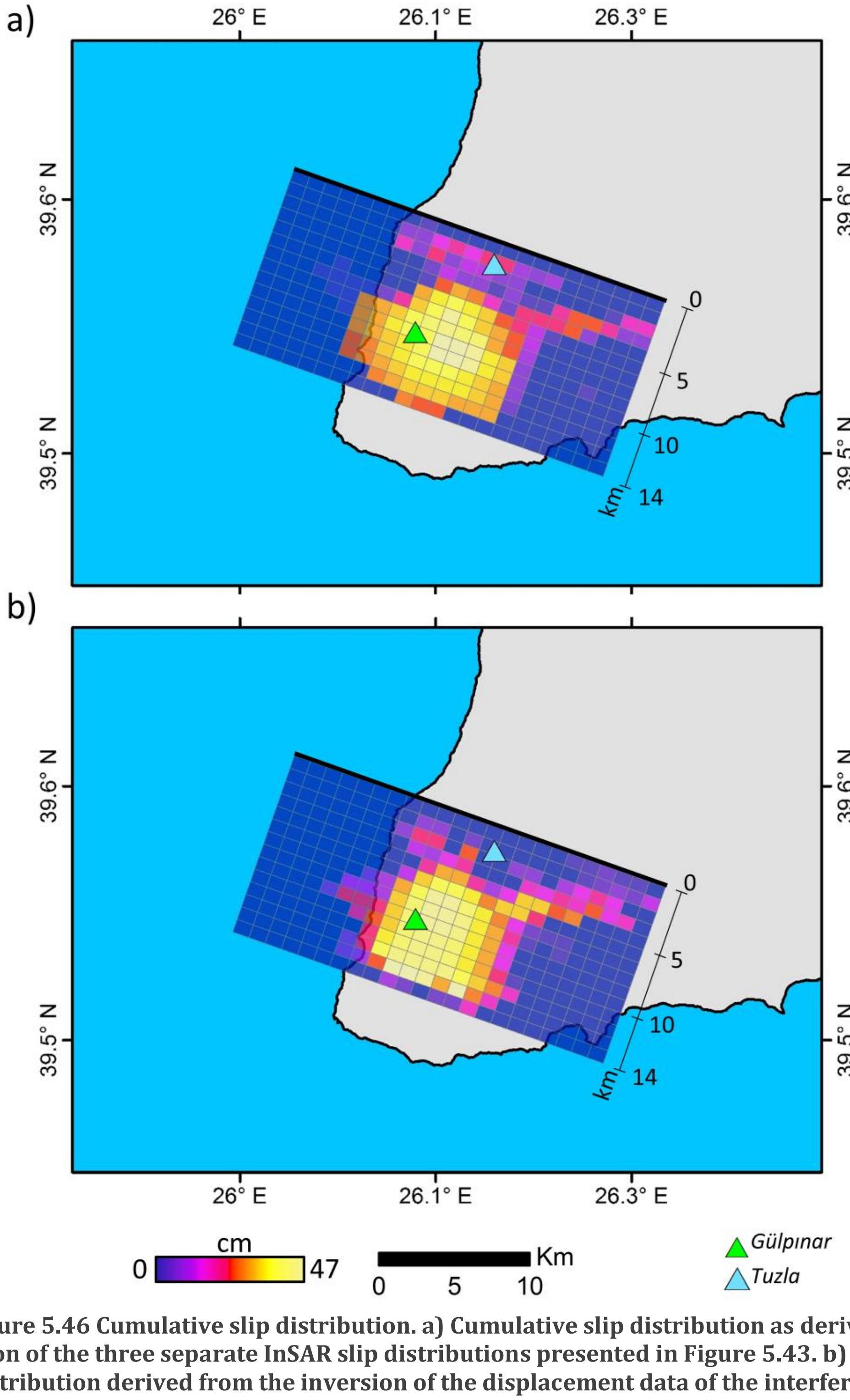

Figure 5.46 Cumulative slip distribution. a) Cumulative slip distribution as derived from the addition of the three separate InSAR slip distributions presented in Figure 5.43. b) Cumulative slip distribution derived from the inversion of the displacement data of the interferograms that contain all the three events. The two results are in agreement, both in terms of slip amplitude and slip distribution (Svigkas et al 2019b).

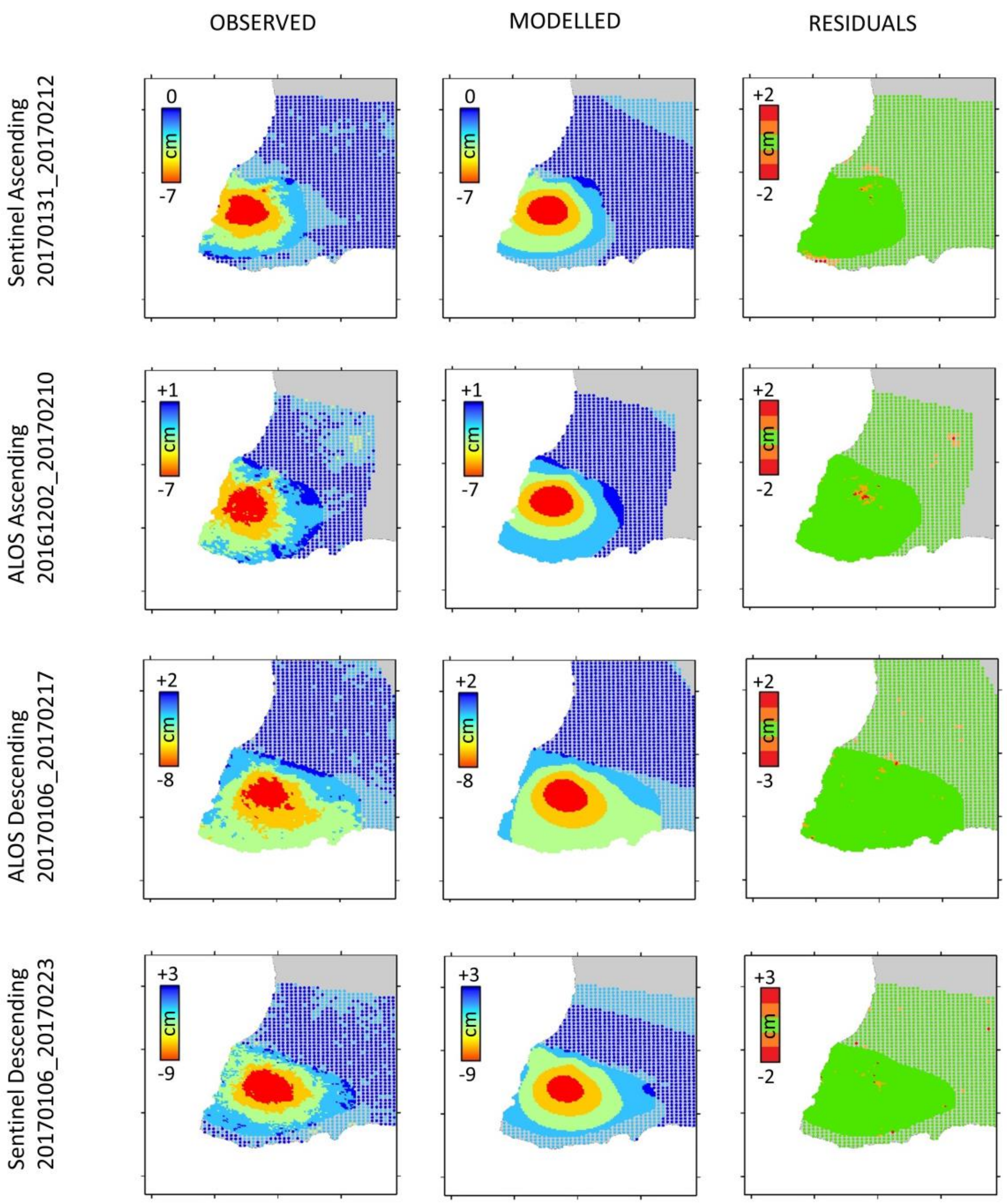

Figure 5.47 Comparison between Observed and Modelled cumulative displacement according to the InSAR slip distribution model. Positive and negative signs mean, LoS shortening and lengthening respectively.

5.3.8 On-fault CFF changes

A further objective is to investigate the possible interaction between the three major events, from the redistribution of stress that occurred on the causative fault. Failure is expected when there is an exceeding of cohesion of the combination of normal and shear stresses. Change in the Coulomb Failure Function (ΔCFF) is defined as:

$$\Delta CFF = \Delta\tau + \mu' \,\Delta\sigma \qquad (5.6)$$

where $\Delta\tau$ is the change in the shear stress, $\Delta\sigma$ is the change in the normal stress and μ' is the apparent coefficient friction (e.g. Reasenbeg and Simpson, 1992; Harris, 1998). Positive values of the results of equation (5.6), favour failure of the faults, while the negative values suppress it. Poisson's ratio was 0.25 and the coefficient of friction was set to 0.4.

To carry out this analysis, the geodetic-based slip distribution models were adopted for each event and the stress change was calculated using the formulation presented by Okada, (1992). Figure 5.51 shows the results of the Coulomb stress changes modelling, having as input, for the CFF calculation, first the source of Event 1 and then the sum of Event 1 and 2 slip distributions. In every estimate, we calculate the CFF adopting the rupture mechanism of the upcoming event, i.e. Event 2 for the first calculation and Event 3 for the second. In the figure, orange to red colors represent stress increase.

In Figure 5.48, in the upper panel, it is shown that within the extent of the slip distribution of Event 2, positive values of ΔCFF (caused by Event 1) are estimated to exist. This implies that Event 2 could have been triggered from the stress changes of Event 1. The same criterion applies to the case of Event 3 (Fig. 5.48 lower panel); it is indicated that its failure could have been promoted from the areas of higher ΔCFF values, caused by both Events 1 and 2.

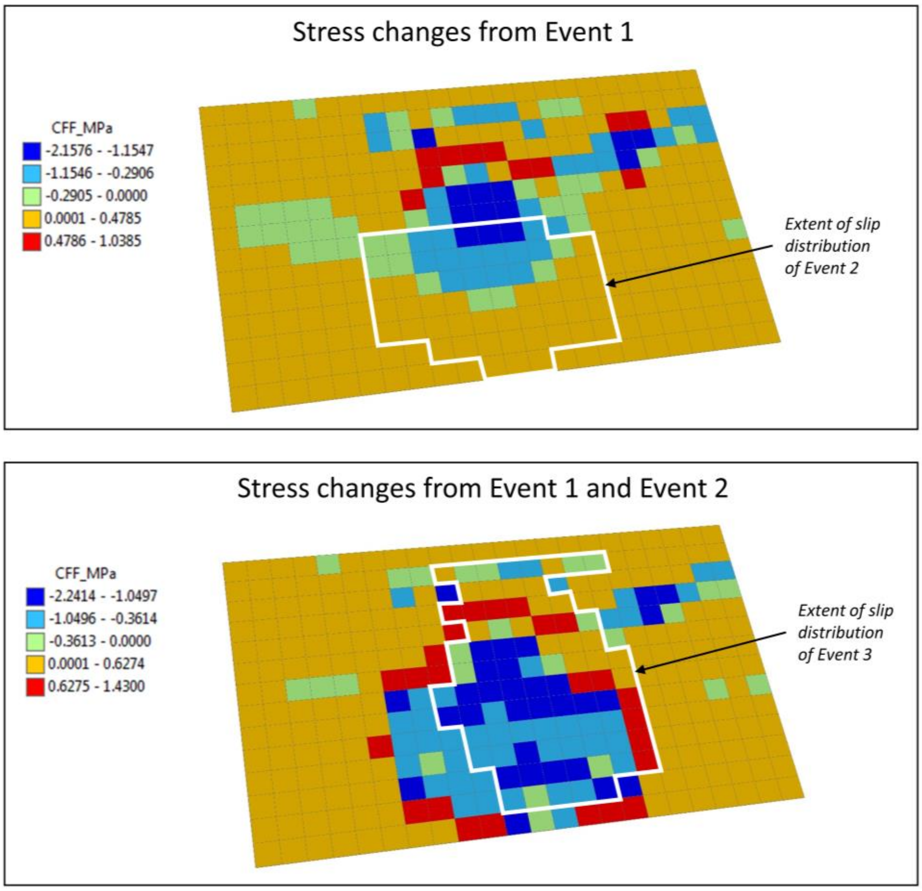

Figure 5.48 On-fault CFF changes based on the slip distribution models of each event. In the upper panel, receiver source is Event 2 and in the lower panel receiver source is Event 3. White polylines show in each case the slip distribution of the upcoming event (Svigkas et al 2019b).

5.3.9 Cumulative and seismic geodetic moment

An important implication for the seismic hazard of an area is the evaluation of seismic and geodetic release (e.g. Cheloni et al. 2017). Only recently, with the use of geodetic measurements, have we been able to have an insight into slow or aseismic processes. These type of activities can exist for example in active transform plate boundaries, where it has been found that they express aseismic slip (e.g. Lohman and McGuire, 2007) and also volcanic regions (Segall et al. 2006). Among the most known “silent” phenomena is the aseismic slow slip detected to occur at subduction zones around the globe (e.g. Wallace et al. 2013; Pritchard and Simons 2006). While usually swarms are associated with high pore fluid pressure in the crust (Hainzl, 2004), other studies (Vidale and Shearer 2006) have suggested that aseismic processes may be one of their common features.

Motivated by the above, this study's moment tensor solution results were used together with those of Özden et al. (2018) and the cumulative moment release of the earthquakes (during the time-span covered by the cumulative interferograms) was found to be equivalent to Mw 5.7. The cumulative slip distribution derived from the ALOS-2 and Sentinel-1 interferograms indicates a moment release (assuming rigidity μ=30 GPa) of Mw 5.8. The two values agree, which reveals that almost all of the deformation of the 2017 Biga swarm was seismic. However, from this swarm alone there cannot be any conclusions on whether the absence of aseismic transients characterizes the way of strain accumulation in this region. Future geodetic analyses and future seismic activity evaluation could potentially reveal whether this behaviour is typical of the area or whether there could be periods when strain is expressed aseismically

5.3.10 Conclusions

The 2017 Biga swarm created a signal strong enough to be detectable by the radar satellites and here we demonstrate a case in which InSAR is used to study swarm activity. Because of its high spatial resolution, InSAR is able to offer better constraints to epicentral positions with regard to waveform inversion. It can also clarify issues related to fault segmentation. Moreover, it offers insights into aseismic processes that cannot be observed solely by seismic measurements. The contribution from GPS campaigns is also valuable in such studies, but are more expensive and not always publically available, like in the case of free SAR data available to the scientific community.

The studied swarm in Biga peninsula was caused by the rupture of a normal fault, striking ~E-W and dipping (~40°) to SW, compatible with regional tectonics (Kiratzi, 2018 and references therein). The entire sequence occurred at shallow focal depths in the upper crust. The slip distribution models obtained from geodetic and seismic data converge to show that the slip was confined mainly to a single compound patch, located underneath the town of Gülpınar and close to the town of Tuzla. Event 1 shows greater complexity in its geodetic slip model, while Event 3 was more energetic in terms of peak slip values. The accumulated strain was released seismically with no aseismic transient.

Sentinel-1 family, together with the other available radar satellite installations, could potentially provide more opportunities to study these phenomena and even face the low temporal resolution of InSAR and define separate slip distributions of a swarm's events by applying specific strategies. This additional input could improve the knowledge of each specific tectonic environment studied, but even on a larger scale, it can shed light on phenomena that occur during swarm activity and are not detectable with traditional instrumentation.

Chapter.6 SUMMARY AND CONCLUSIONS

The first goal of the thesis was to study the earth's surface displacement based on geodetic measurements. To do so, the techniques of conventional and multi-temporal SAR interferometry were employed. The second goal was to interpret the surface deformation and define its cause for each specific case. The thesis has two components based on the type of deformation under study: a) anthropogenic driven deformation and b) tectonic driven deformation. More specifically the cases studied are the following:

- The displacement at the area of Kalochori
- The displacement of Anthemountas graben
- The deforming trends at Oreokastro
- Iran-Iraq 2017 earthquake source study
- The Cephalonia-Lefkada transform fault based on the Lefkada 2015 sequence
- The Biga 2017 seismic swarm

In the following, the main points of each study are reported in brief.

6.1 THE DISPLACEMENT AT THE AREA OF KALOCHORI

Ground truth techniques had indicated the existence of surface deformation in the 1960s, at the area of Kalochori. At the same time, seawater invasion started to be an issue at the area, threatening houses nomatter the counter-measures taken by the government over the years. ERS 1, 2 data from the '90s had successfully verified the subsidence phenomena adding new information on their distribution and deformation rate. Among the different proposed mechanisms causing the displacement, was the excessive ground water pumping. Here, all the available ERS 1, 2 and ENVISAT archive was processed to measure the displacement occurring during about 2 decades. The previously detected subsidence was further validated, whereas an uplifting trend was highlighted for the first time taking place during the period of 2003 to 2010. The detected deformation rebound of 2003 to 2010, occurring in agreement to the recharge of the aquifers, proves that the ground water overexploitation was the driving mechanism of the subsidence phenomena. An intriguing result was the detected 1.3 to 2 years long time-lag between the recharge initiation and the responding uplift of the ground surface, indicating that the surface displacement at the area is sensitive to the trends of the aquifers.

6.2 THE DISPLACEMENT OF ANTHEMOUNTAS GRABEN

Anthemountas graben lies in the immediate proximity of the city of Thessaloniki. The development trends in Anthemountas had already started before the beginning of the '90s, and caused a drop of the underground water level. In this thesis, the already studied deformation period '90s is extended to present new surface displacement results for the graben during the '00s based on SAR time-series. The detected deforming points indicate that the whole graben was subsiding (and not only the area close to the coast) for at least two decades with an increasing rate. Different areas of interest were focused on like the NOESIS Science and Technology center, the Town of Perea and the international airport of Thessaloniki. For the latter, deformation findings indicate the existence of subsidence during the monitoring period at areas where a future extension (new Terminal) is planned to be established. The detected subsidence in Anthemountas has mainly an anthropogenic cause that lasted continuously at least for 20 years. Nevertheless, the existence of faults are found to directly affect the velocity tendencies. This is reasonable as the footwall consists of stiff Neogene deposits while at the hanging wall the Neogene deposits are covered by a thick layer of compressible quaternary formations, presenting stronger deformation values.

6.3 THE DEFORMING TRENDS AT OREOKASTRO

The industrial area of Oreokastro was studied in terms of surface deformation. Previous important contribution was at first the existence of a deforming signal that was achieved for the first time with the InSAR techniques. Among the various interpretations proposed in the literature regarding the specific displacement signal was: aquifer overpumping, tectonic activity, microseismicity, aseismic slip. However, no clear answer and in-depth investigation had been provided about the surface deformation in detail and the cause of it. Results from MT-InSAR presented here, indicated a subsidence signal during the '90s in accordance to previous studies. On the contrary, after 2000 the deforming trend has changed to uplift, a fact that made the area an intriguing case study. The fact that the subsiding deformation has been confined within the limits of the industrial area with the overexploited aquifers, as well as the fact that the deformation trend changed radically to uplift when the consumption of the underground water level was decreased, indicates also in this case the anthropogenic factor as the main driving mechanism. There is a strong relation of shape of the deformation the local fault network. The latter indicates that the faults acts as a boundary of the aquifer, rendering the detected signal as a fault-controlled deformation. Moreover, this fault-controlled deformation revealed a new, previously unknown tectonic structure.

6.4 IRAN-IRAQ 2017 EARTHQUAKE SOURCE STUDY

The 2017 earthquake (known also as Sarpol-e Zahab event) Mw 7.3 is studied in terms of surface deformation exploiting C- and L- band satellite data. The event was the strongest earthquake reported at the area caused a lot of building failures and loss of lives. It occurred at the area where the collision between the Arabian and the Eurasian plate takes place at the Zagros Mountains. The dielectric characteristics and also the large magnitude of the event allowed to have a great special coverage InSAR signal. Source results indicate a structure with a strike of 354°, that generated a thrust event with a horizontal component. The dip angle was significantly shallow expressing, the tectonics of the Zagros Fold-Thrust Belt.

6.5 THE CEPHALONIA-LEFKADA TRANSFORM FAULT BASED ON THE LEFKADA 2015 SEQUENCE

Cephalonia-Lefkada Transform fault Zone (CTF) is located in the Ionian Sea and is known for its frequent seismicity. Its geometry is still an open scientific issue. Being close to the densely populated islands of Lefkada and Cephalonia, especially during summer times, there is also a strong societal motivation for studying the tectonics of this area. An opportunity to study this area was the 2015 earthquake sequence that occurred in November and exhibited a Mw 6.4 mainshock. Previous studies of the sequence have highlighted the difficulties of conducting tectonic studies in the Ionian Sea and the potential limitations. A new dataset of radar satellite data was exploited to look into the sequence and model the rupture process. In this case, InSAR offered a high coverage of geodetic data that contributed to better constrain the tectonic sources. By building upon previous studies, a new fault segmentation was presented for the area of the Ionian Sea.

6.6 BIGA 2017 SEISMIC SWARM

Seismic swarms are sequences without any distinct mainsock. This fact, together with the weak deformation signal, consists them an understudied phenomenon from a geodetic point of view and especially regarding the InSAR approach. There is a complete absence of InSAR studies for most seismic swarms occurring globally. After the new advancements regarding the satellite constellations here the ability to study these phenome is tested, focusing on a swarm occurred at Biga peninsula in western Anatolia. At first the InSAR data were selected based on the acquisition times in an attempt to isolate temporally three moderate seismic events. Since this was not possible for all the events, a specific modelling strategy was adopted and indeed it was possible to define separate slip distributions for each one of the three events. The validation of the results from an independent procedure indicated that currently, there are new capabilities to start studying these phenomena more frequently using InSAR and in consequence have additional information together with the traditional instrumentations.

6.7 CONSIDERATIONS

The results derived from the deformation analysis in northern Greece shows that Thessaloniki is actually surrounded by areas that are subject to surface deformation. A detailed measurement and analysis for the broader area of Thessaloniki was performed and it was shown that all the deforming sites, share similarities. In all cases the deformation was not mainly due to a natural procedure. These surface movements are able to cause failures to buildings, houses and important infrastructure like the international airport of Thessaloniki. About the latter, results presented here and in general InSAR displacement results, could potentially be taken into account from the airport's construction management regarding any restoration or any future construction activity. In any case, a continuous monitoring for this kind of critical infrastructure would be essential, taking also into account the proximity to tectonic structures of Anthemountas that have an optimum orientation to the current stress regime. Overall, the deforming trends were proved to be a surface response to the anthropic activities and more specifically they appear to be following the financial status since they are related with the industrial activity and the water demands in each area, in each epoch. This means that if the same situation continues, the existence of deformation will continue (maybe even increased) every time that there is development. Since in this thesis it has been proved that at the study areas, the impact of these activities to the earth's surface can be reversible even naturally, a water management plan is of high priority for Thessaloniki and its surroundings, to diminish the anthropogenic hazard in the years to come.

Regarding the tectonic studies, for the case of Iran the 2017 event expressed the local tectonics of the collision zone between the Arabian and Eurasian plate. The thrust character of the movement was devastating for the area of the Zagros, considering also the high population density existing at the site. About the Cephalonia–Lefkada Transform Fault (CTF) zone, a new fault segmentation was presented and it was proposed that CTF could be better viewed as a wide zone where the deformation is taken up by multiple strike-slip fault segments, whereas the thrust components are not negligible at all. The proposed oblique segment in the intersection of the Cephalonia branch with the Lefkada branch could partially explain why the Cephalonia Fault Zone tends to rupture in segments with characteristic doublets. The fault segmentation in the Ionian Sea, is still an open issue and further studies are needed to have a clearer picture on the local tectonics. In the future, new seismic sequences might reveal more information on the processes that take place. However, monitoring should not be focused only on the cases of the major seismic events such as the 2015 one. A continuous monitoring of microseismicity could provide insights about the potential pre-existing structures. These appear to play an important role in the evolution of the seismic sequences. The study of the specific fault network is crucial, since it is a threat to the Ionian Islands, which are densely populated, especially during the summer. The study of the Biga 2017 sequence proved that the temporal sampling limitations of InSAR can be overcome up to a specific point and nowadays InSAR can be used to perform research for the phenomena of swarms offering an additional aspect, together with the traditional instrumentation.

Earthquake studies can give us a lot insights on the natural procedures. At the same time, when thinking of the tectonic phenomena as a whole, earthquake is only a small part of the full seismic cycle. Geodetic tools now offer us improved opportunities to look into these less understood procedures. For InSAR this means that the imagery archives become richer and richer as time goes by. Even though a large number of images are technically important to perform SAR time-series to monitor a fault, what is also very important for the geophysical interpretation, is to have also datasets spanning long time enough to be able to characterize the faults' behaviour. Thus, in the future, long-lasting and new radar satellite missions (together with the establishment of new GPS sites and maintenance of the old ones) might enable us to record a lot of completed seismic cycles for different faults in the globe, a fact that could potentially offer important findings.

On a more practical aspect regarding InSAR, in the future we will have more radar missions (currently expecting the upcoming NISAR mission). A more frequent image acquisitions rate would of course decrease in part the issue of low temporal resolution. One of the main priorities would be to plan new missions that would solve the limited north-south sensitivity of InSAR.

ΠΕΡΙΛΗΨΗ

Οι γεωδαιτικές μετρήσεις μπορούν να συνεισφέρουν στη μελέτη πολλαπλών φαινομένων. Η τεχνολογική εξέλιξη και οι δορυφορικές αποστολές ραντάρ, προσέφεραν καινούργιους τρόπους μελέτης της επιφανειακής παραμόρφωσης. Στην παρούσα διατριβή, γίνεται χρήση αυτών των δεδομένων ραντάρ, για την παρακολούθηση της γήινης επιφανειακής παραμόρφωσης, μέσω της ανάλυσης τους με τη χρήση των τεχνικών συμβολομετρίας ραντάρ συνθετικού ανοίγματος (InSAR). Μελετώνται δυο τύποι επιφανειακής παραμόρφωσης: ανθρωπογενής και τεκτονική. Όσον αφορά την πρώτη κατηγορία η εστίαση τίθεται στη βόρεια Ελλάδα και ειδικότερα στη Θεσσαλονίκη (τη δεύτερη μεγαλύτερη πόλη της Ελλάδας) και τα περίχωρά της. Η περιοχή ήταν γνωστό ότι ήταν υπό καθεστώς παραμόρφωσης, και σε αυτή τη διατριβή παρουσιάζονται νέα, πιο πρόσφατα αποτελέσματα των οποίων τα χαρακτηριστικά αναλύονται λεπτομερώς. Επιπρόσθετα, οι κύριοι μηχανισμοί που προκαλούν το φαινόμενο προτείνονται με βάση και την αξιοποίηση εξωτερικών δεδομένων. Οι περιοχές ενδιαφέροντος είναι το Καλοχώρι, η λεκάνη του Ανθεμούντα και η ευρύτερη περιοχή του Ωραιοκάστρου. Τα αποτελέσματα δείχνουν ότι υπάρχουν σημαντικά σήματα παραμόρφωσης, τα οποία κατά περιπτώσεις μπορεί να προκαλέσουν σοβαρές αστοχίες σε σπίτια, κτίρια και υποδομές υψηλής σημασίας. Αξιολόγηση των in-situ δεδομένων, μαζί με τα Τηλεπισκοπικά, δείχνουν ότι η δραστηριότητα των υδροφορέων είναι η κύρια αιτία της επιφανειακής παραμόρφωσης και ότι η δραστηριότητα του υπόγειου νερού καθορίζει τις επιφανειακές ανυψωτικές και καθιζηματικές τάσεις, των υπό μελέτη περιοχών. Ως γενική πρόταση, η ανάγκη για διαχείριση των υπόγειων υδάτων, θεωρείται κρίσιμη προτεραιότητα για την ευρύτερη περιοχή της Θεσσαλονίκης, για την αποφυγή μελλοντικών κινδύνων.

Στη δεύτερη ενότητα της παρούσας διατριβής, γίνεται μελέτη σήματος τεκτονικής παραμόρφωσης αρχικά για την περίπτωση του σεισμού Ιράν-Ιράκ 2017 με σκοπό τον προσδιορισμό της πηγής του συμβάντος. Οι άγονες περιβαλλοντικές συνθήκες της περιοχής μελέτης, συνέβαλαν σε ένα σήμα παραμόρφωσης υψηλής

ποιότητας, το οποίο χρησιμοποιήθηκε για την αντιστροφή των γεωδαιτικών δεδομένων, με σκοπό τον υπολογισμό των παραμέτρων του ρήγματος, που σχετίζεται με την παραμόρφωση της ενεργού τεκτονικής των πλακών που παρατηρείται στην περιοχή. Μια άλλη μελέτη που παρουσιάζεται εδώ, επικεντρώθηκε στην περιοχή του Ιονίου, το πιο ενεργό τεκτονικό τμήμα της ανατολικής Μεσογείου. Με την αξιοποίηση δεδομένων ραντάρ πολλαπλών ζωνών συχνοτήτων από διαφορετικές γεωμετρίες λήψης και με βάση τα αποτελέσματα των προηγούμενων μελετών της ακολουθίας της Λευκάδας του 2015, προτείνεται μια νέα γεωμετρία ρηξιγενών τεμαχών για τη ζώνη Κεφαλονιάς-Λευκάδας (Cephalonia-Lefkada Transform fault Zone -CTF). Στην παρούσα διατριβή, γίνεται επίσης εστίαση στις νέες δυνατότητες που προσφέρουν οι τελευταίες τεχνολογικές εξελίξεις των δορυφόρων ραντάρ και στη συμβολή που θα μπορούσαν να προσφέρουν στην κοινότητα των επιστημών της γης. Μελετώντας τη ακολουθία σμηνοσεισμών της χερσονήσου της Μπίγκα του 2017 και χρησιμοποιώντας μια συγκεκριμένη στρατηγική μοντελοποίησης, αποδεικνύεται ότι υπάρχουν νέες δυνατότητες σήμερα για να εξετάσουμε τις ακολουθίες σμηνοσεισμών. Οι τελευταίες είναι ελάχιστά μελετημένες απο τη σκοπιά της δορυφορικής συμβολομετρίας ραντάρ, σε σύγκριση με τις ακολουθίες που συνδέονται με σεισμούς μεγάλου μεγέθους.

ABSTRACT

Geodetic measurements can be used to study different phenomena. Technological advancements and the radar satellite constellations offered new ways of measuring surface deformation. These data are exploited in this thesis, to monitor surface deformation, by applying interferometric synthetic aperture radar (InSAR) techniques, conventional and multi-temporal. Two types of surface deformation are studied: anthropogenic and tectonic. Regarding the former, focus is set on northern Greece and especially Thessaloniki (the second largest city in Greece) and its surroundings. The area was known to be under a deforming trend. In this thesis, new recent deformation results are presented, whose characteristics are analysed in detail. Interpretations of the main driving mechanisms, are proposed by exploiting also external data. Areas of interest are Kalochori, Anthemountas basin and the broader area of Oreokastro. Results show that there are significant deformation signals, which in some cases, can cause severe failures to houses, buildings and critical infrastructure. In-situ data, together with the remote sensing results, indicate that aquifer activity is the main cause of surface displacement and that the underground water trends, directly affect the detected uplift and subsidence of the areas under study. A need for groundwater management, is considered as a crucial priority for the broader area of Thessaloniki, to avoid future hazard.

In the second part of this thesis, tectonic deformation signal is analysed at first for the case of the Iran-Iraq 2017 earthquake, to estimate the source properties of the event. Due to the arid conditions of the area, a high quality deformation signal was used as input to perform geodetic inversion, to estimate a fault which is related with the active plate boundary deformation, occurring at the area. Another study, exploiting radar data was focused in the territory of the Ionian Sea, the most active tectonic region of the eastern Mediterranean. By exploiting multi-band radar data from different acquisition geometries and based on results of the latest studies of the Lefkada 2015 sequence, a new fault segmentation is proposed for the Cephalonia-Lefkada Transform fault Zone (CTF).

Focus is also set on the new capabilities, offered by the latest radar satellite advancements and the contribution they could offer to the earth science community. By studying the 2017 Biga seismic swarm, using a specific modelling strategy, it is demonstrated that new possibilities are currently existing to look into the seismic swarm sequences. The latter are understudied from an InSAR point of view, in comparison to the sequences characterized by major seismic events.

REFERENCES

Agram, P., 2010. Persistent scatterer interferometry in natural terrain. *PhD thesis,* Stanford University.

Albano, M., Polcari, M., Bignami, C., Moro, M., Saroli, M. and Stramondo, S. 2017. Did anthropogenic activities trigger the 3 April 2017, Mw 6.5 Botswana earthquake?, *Remote Sens*., 9, 1028.

Altınok, Y., Alpar, B., Yaltırak, C., Pınar, A. and Özer, N., 2012. The earthquakes and related tsunamis of October 6, 1944 and March 7, 1867; NE Aegean Sea. *Natural Hazards*, 60, 3–25.

Ambraseys, N.N., 1988. Engineering seismology: Part I. *Earthquake Engineering & Structural Dynamics*, 17, 1–105.

Amelung, F., Jónsson, S., Zebker, H. and Segall, P. 2000. Widespread uplift and 'trapdoor' faulting on Galápagos volcanoes observed with radar interferometry. *Nature,* 407, 993–996.

Amelung, F., Galloway, D.L., Bell, J.W., Zbeker, H.A. and Laczniak, R.J., 1999. Sensing the ups and downs of Las Vegas: InSAR reveals structural control of land subsidence and aquifer-system deformation. *Geology,* 27 (6), 483–486.

Anastasiadis, A., Raptakis, D. and Pitilakis, K. 2001. Thessaloniki's Detailed Microzoning: Subsurface Structure as Basis for Site Response Analysis. *Pure Appl. Geophys*., 158, 2597–2633.

Andronopoulos, V., Rozos, D., and Hadzinakos, J., 1990. Geotechnical study of ground settlement in the Kalochori area, Thessaloniki District. *Unpublished Report IGME.*, E6319, p. 45.

Arnaud, A., Adam, N., Hanssen, R., Inglada, J., Duro, J., Closa, J. and Eineder, M. 2003. ASAR ERS interferometric phase continuity. In: *Proceedings of IGARSS 2003*, France, Toulouse.

Atzori, S. and Salvi, S. 2014. SAR Data Analysis in Solid Earth Geophysics: From Science to Risk Management. *IntechOpen*. http://dx.doi.org/10.5772/57479.

Atzori, S., and Antonioli A. 2011. Optimal fault resolution in geodetic inversion of coseismic data. *Geophys. J. Int.*, 185, 529–538, doi:10.1111/j.1365-246X.2011.04955.x.

Atzori, S., Hunstad, I., Chini, M., Salvi, S., Tolomei, C., Bignami, C., Stramondo, S., Trasatti, E. and Antonioli A. 2000. Finite fault inversion of DInSAR coseismic displacement of the 2009 L'Aquila earthquake (Central Italy). *Geophys. Res. Lett.*, 36, l15305, doi:10.1029/2009GL039293.

Avallone, A., Cirella, A., Cheloni, D., Tolomei, C., Theodoulidis, N., Piatanesi, A., Briole, P. and Ganas A. 2017. Near-source high-rate GPS, strong motion and InSAR observations to image the 2015 Lefkada (Greece) Earthquake rupture history. *Sci. Rep.*, Sep 4;7(1):10358. doi: 10.1038/s41598-017-10431-w.

Baba, A., Demir, M.M., Koç, A. G., and Tuğcu, C. 2015. Hydrogeological properties of hyper-saline geothermal brine andapplication of inhibiting siliceous scale via pH modification. *Geothermics,* 53, 406–412.

Baba, A., Ateş Ö. and Deniz, O. 2008. The environmental and hydrogeochemical properties of the tuzla-kestanbol-hidirlar geothermal sources. *Turkey engineering and* *architectural geothermal training programme 30th Anniversary Workshop,* Orkustofnun, Grensásvegur 9.

Baba, A. and Ertekin, C. 2007. Determination of the source and age of the geothermal fluid and its effects on groundwater resources in Kestanbol (Çanakkale-Turkey), GQ07: Securing Groundwater Quality in Urban and Industrial Environments. *7th International Groundwater Quality Conference*, Fremantle, Western Australia, 1-8.

Bai, L., Wu, Z., Zhang, T. and Kawasaki, I. 2006. The effect of distribution of stations upon location error: Statistical tests based on the double-difference earthquake location algorithm and the bootstrap method. *Earth Planets Space*, 58, 9–12, doi:10.1186/bf03353364.

Barba-Sevilla M., Baird, B.W., Liel A.B. and Tiampo, K.F. 2018. Hazard Implications of the 2016 Mw 5.0 Cushing, OK Earthquake from a Joint Analysis of Damage and InSAR Data. *Remote Sens., 10* (11), 1715; https://doi.org/10.3390/rs10111715.

Barnhart, W.D., Brengman, C.M.J., Li, S. and Peterson, K.E. 2018. Ramp-flat basement structures of the Zagros Mountains inferred from co-seismic slip and afterslip of the 2017 Mw7.3 Darbandikhan, Iran/Iraq earthquake. *Earth Planet. Sci. Lett*., 496, 96–107, https://doi.org/10.1016/j.epsl.2018.05.036.

Battazza, F., Ciappa, A., Coletta, A., Covello, F., Manoni, G., Pietranera, L. and Valentini, G. 2009 COSMO-SkyMed Mission: a set of X-band SAR Applications conducted during 2008. *Ital. J. Remote Sens*., 41(3):7–21. doi:10.5721/ItJRS20094131.

Bawden, G.W., Thatcher, W., Stein, R.S., Hudnut, K.W. and Peltzer, G. 2001. Tectonic contraction across Los Angeles after removal of groundwater pumping effects. *Nature,* 412:812–815.

Bell, J., Amelung, F. and Christopher, H. 2012. InSAR analysis of the 2008 Reno-Mogul earthquake swarm: Evidence for westward migration of Walker Lane style dextral faulting. *Geoph. Res. Lett.*, vol. 39, L18306, doi:10.1029/2012GL052795.

Bell, J.W., Amelung, F.A., Ferretti, A., Bianchi, M. and Novali, F. 2008. Permanent scatterer InSAR reveals seasonal and long-term aquifer-system response to groundwater pumping and artificial recharge. *Water Resour. Res*., 44 (2), 2407–2425.

Berardino, P., Fornaro, G., Lanari, R. and Sansosti, E. 2002. A new algorithm for surface deformation monitoring based on small baseline differential SAR interferograms. I*EEE Trans. Geosci. Remote Sens*., 40, 2375–2383.

Bie, L., González, P.J. and Rietbrock, A. 2017. Slip distribution of the 2015 Lefkada earthquake and its implications for fault segmentation. *Geoph. Jour. Int*., 210, 1, 420–427, https://doi.org/10.1093/gji/ggx171.

Björk, A., 1996. Numerical methods for least squares problems. *SIAM*, Philadelphia. Bonafede, M., J. Strehlau and Ritsema A.R. 1992. Geophysical and structural aspects of fault mechanics – a breef historical review. *Terra Nova*, 4, 458-463.

Boncori, J.P.M., Papoutsis, I., Pezzo, G., Tolomei, C., Atzori, S., Ganas, A., Karastathis, V., Salvi, S., Kontoes C. and Antonioli, A. 2015. The February 2014 Cephalonia earthquake (Greece): 3D deformation field and source modeling from multiple SAR techniques. *Seismol. Res. Lett.* 86-1, 124–137. http://dx.doi.org/10.1785/0220140126.

Brooks, M., and Ferentinos, G. 1984. Tectonics and sedimentation in the Gulf of Corinth and the Zakynthos and Kefallinia channels, Western Greece. *Tectonophysics*, 101(1–2), 25–54. https://doi.org/10.1016/0040-1951(84)90040-4.

Bulut, F., Havazlı, E., Yaltırak, C., Doğru, A., Sabuncu, A. & Özener, H., 2018. The 2017 Ayvacık Earthquake Sequence: A Listric Fault Activated Beneath Tuzla/Çanakkale Geothermal Reservoir (Western Turkey). *Proceedings, 43rd Workshop on Geothermal Reservoir Engineering Stanford University*, Stanford, California, February 12-14, 2018 SGP-TR-213.

Caputo, R. and Pavlides, S. 2013. The Greek Database of Seismogenic Sources (GreDaSS), Version 2.0.0: A compilation of potential seismogenic sources (Mw>5.5) in the Aegean region. doi:10.15160/unife/gredass/0200. [http://gredass.unife.it/].

Chan, Y.K. and Koo, V.C. 2008. An introduction to Synthetic Aperture Radar (SAR), P*rogress in Electromagnetics Research B,* 2.

Chatzipetros, A., Kiratzi, A., Sboras, S., Zouros, N., and Pavlides, S. 2013. Active faulting in the north-eastern Aegean Sea Islands. *Tectonophysics,* 597-598:106-122.

Chen, C., Hu, J., Lu, C., Lee, J. and Chan, Y. 2007. Thirty-year land elevation change from subsidence to uplift following the termination of groundwater pumping and its geological implications in the Metropolitan Taipei Basin, Northern Taiwan. *Eng. Geol*., 95, 30–47.

Chousianitis, K., Konca, A. O., Tselentis, G.A., Papadopoulos, G.A. and Gianniou, M. 2016. Slip model of the 17 November 2015 Mw = 6.5 Lefkada earthquake from the joint inversion of geodetic and seismic data. *Geophys. Res. Lett.*, 2016, 43, 7973–7981, doi:10.1002/2016GL069764.

Cheloni, D., D'Agostino, N., Selvaggi, G., Avallone, A., Fornaro, G., Giuliani, R., Reale, D., Sansosti, E. Tizzani, P., 2017. Aseismic transient during the 2010–2014 seismic swarm: evidence for longer recurrence of M≥6.5 earthquakes in the Pollino gap

(Southern Italy)?. *Scientific Reports*, 57671, https://doi.org/10.1038/s41598-017-00649-z

Corine (coordination of information on the environment) LandCover: http://land.copernicus.eu/pan-european/corine-land-cover. Accessed: 02-02-2017

Costantini, F., Mouratidis, A., Schiavon, G., Sarti F. 2016. Advanced InSAR techniques for deformation studies and for simulating the PS-assisted calibration procedure of Sentinel-1 data: Case study from Thessaloniki (Greece), based on the Envisat\ASAR archive. *Int. J. Remote Sens*. doi:10.1080/01431161.2015.1134846.

Costantini, M., Falco, S., Malvarosa, F., and Minati, FA 2008. New method for identification and analysis of persistent scatterers in series of SAR images. In: *Proceedings of IEEE international geoscience and remote sensing symposium*, Boston, MA, USA, pp 449–452.

Costantini, M. 1998. A novel phase unwrapping method based on network programming, *IEEE Trans. Geosci. Remote Sens*. 36 (3), 813–821 1998.

Crosetto, M., Crippa, B., Biescas, E., Monserrat, O., Agudo, M. and Fernández, P. 2005. Land deformation monitoring using SAR interferometry: state-of-the-art Photogrammetrie. *Fernerkundung und Geoinf*., 6, pp. 497-510.

Curlander, J.C. and Mcdonough, R.N 1991. Synthetic aperture radar: systems and signal processing. *Wiley*, New York.

Das, S. and Scholzm C. H. 1983. Why large earthquakes do not nucleate at shallow depths. *Nature*, 305.

David, M. 1977. Geostatistical ore reserve estimation. *Elsevier*, Amsterdam

Demiris, K., 1988. Geological settings and their influence on the development of the areas on the west of Thessaloniki. Proceedings of the Symposium on the Technical Problems Affecting the Areas on the West of Thessaloniki. *Tech. Cham. of Gr.*, Thessaloniki.

Ding, K., He, P., Wen, Y., Chen, Y., Wang, D., Li, S. and Wang, Q. 2018. The 2017 M w 7.3 Ezgeleh, Iran earthquake *Geoph. Jour. Int.*, Volume 215, Issue 3, Pages 1728–1738, https://doi.org/10.1093/gji/ggy371.

Doukakis, E., 2005. Coastal red spots along the western Thermaikos gulf. *Proceedings of the 9th International Conference on Environmental Science and Technology*, University of Aegean, Rhodes, Greece, pp. A334–A339.

Dimopoulos, G., 2005. Investigation of the conditions generating soil settlements in Sindos–Kalochori area of Thessaloniki. *Proceedings of the 7th Hellenic Hydrogeological Conference and 2nd MEM Workshop on Fissured Rocks Hydrogeology*, Athens. Hellenic Committee of Hydrogeology, pp. 135–146.

Dixon, T.H., 1994. SAR interferometry and surface change detection. *Report of a Workshop*, Boulder, Colorado, USA.

Doukas, I.D., Ifadis, I.M., and Savvaidis, P. 2004. Monitoring and analysis of ground subsidence due to water pumping. *FIG Working Week*, Athens, Greece, May 22–27.

Duro, J, Closa, J, Biescas, E., Crosetto, M. and Arnaud A. 2005. High resolution differential interferometry using time series of ERS and ENVISAT SAR data. In: *Proceedings of the 6th geomatic week conference*, Barcelona, Spain, 8–11 February.

EPPO 1996. Neotectonic Map of Greece, Thessaloniki sheet, scale: 1:100000.

Elliott, J.R., Walters, R.J., and Wright, T.J. 2016. The role of space-based observation in understanding and responding to active tectonics and earthquakes. *Nature Communications*, http://dx.doi.org/10.1038/ncomms13844.

Farr, T., Rosen, P., Caro, E., Crippen, R., Duren, R., Hensley, S., Kobrick, M., Paller, M., Rodriguez, E., Roth, L., Seal, D., Shaffer, S., Shimada, J., Umland, J., Werner, M., Oskin M, Burbank D and Alsdorf, D. 2007. The shuttle radar topography mission. *Reviews of Geophysics*, 45, RG2004 doi:10.1029/2005RG000183.

Farr, T.G. and Kobrick M. 2000. Shuttle radar topography mission produces a wealth of data, *Eos Trans*, 2000, AGU 2000, 81, 583–585.

Feng, W., Samsonov, S., Almeida, R., Yassaghi, A., Li, J., Qiu, Q., Li, P. and Zheng, W. 2018. Geodetic constraints of the 2017 Mw7.3 Sarpol Zahab, Iran earthquake, and its implications on the structure and mechanics of the northwest Zagros thrust-fold belt. *Geoph. Res. Lett.*, *45*, https://doi.org/10.1029/ 2018GL078577.

Feigl, K.L. 2002. Estimating earthquake source parameters from geodetic measurements, *International Handbook of Earthquake and Engineering Seismology*, 81A, 607– 620.

Ferretti, A., Savio, G., Barzaghi, R., Borghi, A., Musazzi, S., Novali. F., Prati, C. and Rocca, F. 2007. Submillimeter accuracy of InSAR time series: experimental validation, *IEEE TGRS*, 45 (5), pp. 1142-1153.

Ferretti, A., Prati, C. and Rocca, F. 2001. Permanent scatterers in SAR interferometry. *IEEE Trans. Geosci. Remote Sens.*, 39(1), 8 –20.

Ferretti, A., Prati, C. and Rocca, F. 2000. Nonlinear subsidence rate estimation using Permanent Scatterers in differential SAR interferometry. *IEEE Trans. Geosci. Remote Sens.*, 38 (5), 2202– 2212.

Fikos, I., Ziankas, G., Rizopoulou, A. and Famellos, S. 2005. Water balance estimation in Anthemountas river basin and correlation with underground water level. *Global NEST Journal*, Vol 7, No 3, pp 354-359.

Franceschetti, G. and Lanari, R. 1999. Synthetic Aperture Radar Processing. Boca Raton, FL: CRC Press.

Funning, G., Parsons, B., Wright, T., Jackson, J. and Fielding, E. 2005. Surface displacements and source parameters of the 2003 Bam (Iran) earthquake from Envisat advanced synthetic aperture radar imagery Journal of Geophysical Research https://doi.org/10.1029/2004JB003338.

Gabriel, A.K., Goldstein, R.M. and Zebker, H.A. 1989. Mapping small elevation changes over large areas: differential radar interferometry. *J. Geophys. Res*., 94(B7):83–91.

Ganas, A., Kourkouli, P., Briole, P., Moshou, A., Elias, P. and Parcharidis, I. 2018. Coseismic Displacements from Moderate-Size Earthquakes Mapped by Sentinel-1 Differential Interferometry: The Case of February 2017 Gulpinar Earthquake Sequence (Biga Peninsula, Turkey). *Remote Sens.*, *10*, 1089.

Ganas, A., Briole, P., Melgar, D., Bozionelos, G., Valkaniotis, S, Avallone, A., Papathanassiou, G., Mendonidis, E. and Elias, P. 2016a. Coseismic Deformation and Seismic fault of the 17 November 2015 M=6.5 earthquake, Lefkada island. *Bul. Geol. Soc. Gr., 50*(1), 491-498. doi:http://dx.doi.org/10.12681/bgsg.11750.

Ganas, A., Elias, P., Bozionelos, G., Papathanassiou, G., Avallone, A., Papastergios, A., Valkaniotis, S., Parcharidis I. and Briole, P. 2016b. Coseismic deformation, field observations and seismic fault of the 17 November 2015 M = 6.5, Lefkada Island, Greece earthquake, *Tectonophysics,* 687, 210–222 dx.doi.org/10.1016/j.tecto.2016.08.012.

Ganas, A, Oikonomou, A., and Tsimi, C. 2013. NOAFAULTS: a digital database for active faults in Greece. In: Bulletin of the Geological Society of Greece. *Proceedings of the 13th International Congress*, Chania, vol. XLVII 2013

Garlaouni, C., Papadimitriou, E., Karakostas, V, Kilias, A. and Lasocki, S. 2015 Fault population recognition through microsismicity in Migdonia region (northern Greece). *Bollettino di Geofisica Teorica ed Applicata,* 56(3):367–382.

GACOS, Generic Atmospheric Correction Online Service for InSAR (GACOS) http://ceg-research.ncl.ac.uk/v2/gacos/.

Gavin, H., 2011 The Levenberg-Marquardt method for nonlinear least squares curve-fitting problems, Department of Civil and Environmental Engineering, *Duke University Online notes on LM algorithm*: people.duke.edu/~hpgavin/ce281/lm.pdf.

Galloway, D.L. and Hoffmann, J., 2007. The application of satellite differential SAR interferometry-derived ground displacements in hydrogeology. *Hydrogeol. J.,* 15 (1), 133–154, http://dx.doi.org/10.1007/s10040-006-0121-5.

Galloway, DL, Jones DR and Ingebritsen, SE., (1999) Land subsidence in the United States: U.S. Geological Survey Circular 1182.

Galloway, D.L., Hudnut, K.W., Ingebritsen, S.E., Phillips, S.P., Peltzer, G., Rogez, F. and Rosen, P.A., 1998. Detection of aquifer system compaction and land subsidence using interferometric synthetic aperture radar, Antelope Valley, Mojave Desert, California. *Water Resour. Res*., 34, 2573–2585.

Gkarlaouni, C., Papadimitriou, E., Karakostas, V., Kilias, A. and Lasocki, S., 2015. Fault population recognition through microseismicity in Mygdonia region (northern

Greece). *Bollettino di Geofisica Teorica ed Applicata*, 56 (3) 367-382, doi: 10.4430/bgta0153.

Goldstein, RM, and Werner, C.L. 1998. Radar interferogram filtering for geophysical applications. *Geoph. Res. Lett.*, 25, 4035-4038.

Goldstein, R.M., and Werner, C.L., 1998. Radar interferogram filtering for geophysical applications. *Geoph. Res. Lett*, 25, 4035-4038.

Goldstein, R. 1995. Atmospheric limitations to repeat-track radar interferometry. *Geoph. Res. Lett.*, 22, 2517–2520.

Graham, L.C., 1974. Synthetic interferometer radar for topographic mapping. P*roc. of the IEEE*, 62, 763-768.

Hanssen, R.A. 2001. Radar Interferometry: Data Interpretation and Error Analysis. *Springer*, New York.

Harris, R. and Simpson, R.W. 1998. Suppression of large earthquakes by stress shadows: A comparison of Coulomb and rate-and-state failure. *J. Geophys. Res.*, *103*, 24,439 – 24,451.

Hatzinakos, I., Rozos, D. and Apostolidis, E. 1990. Engineering geological mapping and related geotechnical problems in the wider industrial area of Thessaloniki, Greece. In: *PRICE, D. (Ed.), Proceedings of Sixth International IAEG Congress*, Amsterdam, Balkema, 127–134.

Hainzl, S. 2004. Seismicity patterns of earthquake swarms due to fluid intrusion and stress triggering. *Geophys. J. Int*, 159, 1090–1096.

Hooper, A. 2009. A statistical-cost approach to unwrapping the phase of InSAR time series. In: *Proceedings of ESA FRINGE Workshop*, Frascati, Italy, November 30–December 4.

Hooper, A. 2008. A multi-temporal InSAR method incorporating both persistent scatterer and small baseline approaches. *Geoph. Res. Lett.*, 35, doi: 10.1029/2008GL034654.

Hooper, A., and H. Zebker 2007. Phase unwrapping in three dimensions with application to InSAR time series. *J. Opt. Soc. Am. A,* Opt. Image Sci., 24, 2737– 2747.

Hooper, A., Segall, P. and Zebker, H. 2007. Persistent scatterer interferometric synthetic aperture radar for crustal deformation analysis, with application to Volcán Alcedo, Galápagos. *J. Geophys. Res.*, 112, B07407, doi: 10.1029/2006JB004763.

Hooper, 2006 . Persistent Scatterer Radar Interferometry for Crustal Deformation Studies and Modeling of Volcanic Deformation. *PhD thesis*, Stanford University.

Hooper, A., Zebker, H., Segall, P. and Kampes, B. 2004. A new method for measuring deformation on volcanoes and other natural terrains using InSAR persistent scatterers. *Geoph. Res. Lett.*, 31, L23611, doi:10.1029/2004GL021737.

Ikehara, M.E. and Phillips, S.P. 1994. Determination of land subsidence related to groundwater-level declines using Global Positioning System and leveling surveys in Antelope Valley, Los Angeles and Kern counties, California, 1992. *U.S. Geol. Surv. Water Resour. Invest.*, Rep. 94–4184.

Institute of Geological and Mineral Exploration (IGME). *Geological map sheets*, Scale 1:50.000: Epanomi (1969), Thessaloniki (1978), Thermi (1978) and Vasilika (1978).

Ishitsuka, K., Fukushima, Y., Tsuji, T., Yamada, Y., Matsuoka, T. and Giao, P.H. 2014. Natural surface rebound of the Bangkok plain and aquifer characterization by persistent scatterer interferometry. *Geochem. Geophys. Geosyst.* 15:965–974. doi:10.1002/2013GC005154.

Jónsson, S., Zebker, H., Segall, P., and Amelung, F. 2002. Fault slip distribution of the 1999 Mw 7.1 Hector Mine, California, earthquake, estimated from satellite radar and GPS measurements*. Bull. Seis. Soc. Am.,* 92, 1377– 1389.

Kampes, B., Hanssen, R. ans Perski, Z. 2003. Radar Interferometry with Public Domain Tools. In: *Proceedings of FRINGE 2003*, Frascati, Italy, December 1-5.

Kampes, B. and Usai, S. 1999. Doris: the delft object-oriented radar interferometric software. In: *Proceedings of the 2nd international symposium on operationalization of remote sensing*. Enschede, The Netherlands.

Kapsimalis, V., Poulos, S.E., Karageorgis, A.P., Pavlakis, P. and Collins, M.B., 2005. Recent evolution of a Mediterranean deltaic coastal zone: human impacts on the Inner Thermaikos Gulf, NW Aegean Sea. *J. Geol. Soc. Lond*., 162, 1–12.

Karakitsios, V. and Rigakis, N. 2007. Evolution and Petroleum potential of western Greece, *Journal of Petroleum Geology*, 30(3), 197-218.

Karakostas, V. G., Papadimitriou, E.. and Papazachos, C. B. 2004. Properties of the 2003 Lefkada, Ionian Islands, Greece, earthquake seismic sequence and seismicity triggering. *Bull. Seis. Soc. Am.*, 94, 1976–1981.

Karakostas V, and Papadimitriou E., 2010. Fault Complexity Associated with the 14 August 2003 Mw6.2 Lefkada, Greece, Aftershock Sequence. *Acta Geophysica* DOI: 10.2478/s11600-010-0009-6.

Karakostas V., Papadimitriou E., Mesimeri M., Gkarlaouni Ch., and Paradisopoulou P. 2014. The 2014 Kefalonia Doublet (*Mw*6.1 and *Mw*6.0), Central Ionian Islands, Greece: Seismotectonic Implications along the Kefalonia Transform Fault Zone. *Acta Geophysica* DOI: 10.2478/s11600-014-0227-4

Kassaras, I., Kazantzidou-Firtinidou, D., Ganas, A., Tonna, S., Pomonis, A., Karakostas, C., Papadatou-Giannopoulou, C., Psarris, D., Lekkas, E., Makropoulos, K. 2018. On the Lefkas (Ionian Sea) November 17, 2015 Mw=6.5 Earthquake Macroseismic Effects, *Journal of Earthquake Engineering*, doi: 10.1080/13632469.2018.1488776.

Kazakis, N., Voudouris, K., Vargemezis, G. and Pavlou, A. 2013. Hydrogeological regime and groundwater occurrence in the Anthemountas River basin, northern Greece. *Bull. Geol. Soc. Gr,* 47 (2), 711-720.

Kazantzidou-Firtinidou, D., Kassaras, I., Tonna, S., Ganas, A., Vintzileou E. and Chesi, C. 2016. The November 2015 Mw6.4 earthquake effects in Lefkas Island. *1st International Conference on Natural Hazards & Infrastructure*, Chania, Greece.

Ketelaar, V.B.H.G. 2009. Satellite radar interferometry: subsidence monitoring techniques. *Springer*, New York (Chapter 3).

Kiratzi, A., 2018. The 12 June 2017 Mw 6.3 Lesvos Island (Aegean Sea) earthquake: Slip model and directivity estimated with finite-fault inversion, Tectonophysics, 724-725, 1-10.

Kiratzi, A., 2014. Mechanisms of Earthquakes in Aegean, in: Beer, M., Kougioumtzoglou, I.A., Patelli, E., Siu-Kui Au, I. (Eds.), *Encyclopedia of Earthquake Engineering*, Springer Berlin Heidelberg, pp. 1–22. doi:10.1007/978-3-642-36197-5_299-1.

Kiratzi, A. and Langston, C. 1991. Moment tensor inversion of the January 17, 1983 Kefallinia event of Ionian Islands (Greece), *Geoph. Jour. Int.*, 105, 529-535.

Kobayashi, T., Morishita, Y., Yarai, H. and Fujiwara, S. 2018. InSAR-derived crustal deformation and reverse fault motion of the 2017 Iran-Iraq Earthquake in the Northwest of the Zagros Orogenic Belt. *Bull. Geospatial Info. Auth.,* 66, http://www.gsi.go.jp/ENGLISH/Bulletin66.html.

Kumar, V. 2007. Optimal contour mapping of groundwater levels using universal kriging—a case study. *Hydrol. Sci. J.,* 52(5):1038–1050.

Kyriakopoulos, C., Chini, M., Bignami, C., Stramondo, S., Ganas, A., Kolligri, M. and Moshou, A. 2013. Monthly migration of a tectonic seismic swarm detected by DInSAR: southwest Peloponnese, Greece. *Geophys. J. Int*., 194, 1302–1309, doi: 10.1093/gji/ggt196.

Lanari, R., Mora, O., Manunta, M., Mallorquı J.J., Berardino, P. and Sansosti, E. 2004. A small baseline approach for investigating deformation on full resolution differential SAR interferograms. *IEEE Trans. Geosci. Remote Sens* 42(7):1377–1386.

Levenberg, K., 1944. A method for the solution of certain problems in least squares, *Quarterly of applied mathematics*, 2, 164-168.

Lekkas, E., Mavroulis, S., Carydis, P. and Alexoudi, V. 2018. The 17 November 2015 Mw 6.4 Lefkas (Ionian Sea, Western Greece) Earthquake: impact on Environment and Buildings, *Geotech. Geol. Eng.,* 2018 36:2109–2142 https://doi.org/10.1007/s10706-018-0452-8.

Lekkas, E., Mavroulis, S. and Alexoudi, V. 2016. Field observations of the 2015 (November 17, Mw 6.4) Lefkas (Ionian sea, western Greece) earthquake impact on natural environment and building stock of Lefkas island. *Bull. Geol. Soc. Gr.*, 2016, 499-510.

Lindsey, E.O., Natsuaki,R., Xu, X., Shimada, M.,Hashimoto ,M., Melgar, D. and Sandwell, D.T. 2015. Line-of-sight displacement from LOS-2 interferometry: Mw 7.8 Gorkha Earthquake and Mw 7.3 aftershock. *Geophys. Res. Lett.,* 42**,** 6655–6661.

Livaoğlu, R., Timurağaoğlu, M.Ö, Serhatoğlu, C.S. and Döven, S. 2018. Damage during the 6-14 February 2017 Ayvacik (Çanakkale) earthquake swarm. *Nat. Hazards Earth Syst. Sci.,* 18, 921–934.

Lohman, R.B., and McGuire, J.J. 2007. Earthquake swarms driven by aseismic creep in the Salton Trough, California. *J. Geophys. Res.*, 112, B04405, doi:10.1029/2006JB004596.

Lohman, R.B. and Simons M. 2005. Locations of selected small earthquakes in the Zagros mountains. *Geoch. Geoph. Geos.*, 6(3) , doi: 10.1029/2004GC00849

Lohman, R.B. and Simons M. 2005. Some thoughts on the use of InSAR data to constrain models of surface deformation: noise structure and data downsampling. *Geoch. Geoph. Geos*, 6, Q01007.

Loupasakis, C. and Rozos, D. 2010. Land subsidence induced by the overexploitation of the aquifers in Kalochori village – new approach by means of the computational geotechnical engineering. Proceedings of the 12th International Congress of the Geological Society of Greece. *Bull. Geol. Soc. Gr.,* XLIII, pp. 1219–1229 No 3.

Loupasakis, C. and Rozos, D. 2009. Land subsidence induced by water pumping in Kalochori village (North Greece) - simulation of the phenomenon by means of the finite element method. *Q. J. Eng. Geol. Hydrogeol.*, Geol. Soc. Lond. 42 (3), 369–382.

Lourakis. M.I.A. 2005. A brief description of the Levenberg-Marquardt algorithm implemented by levmar. *Technical Report*. Institute of Computer Science, Foundation for Research and Technology – Hellas.

Louvari, E., Kiratzi, A. and Papazachos, B.C. 1999. The Cephalonia Transform Fault and its continuation to western Lefkada Island. *Tectonophysics*, 308, 223-236.

Lu Z. and Danskin, W.R. 2001. InSAR analysis of natural recharge to define structure of a ground-water basin, San Bernardino, California. *Geoph. Res. Lett.*, 28:2661–2664.

Ly, S., Charles, C. and Degré, A. 2013. Different methods for spatial interpolation of rainfall data for operational hydrology and hydrological modeling at watershed scale. A review. *Biotechnol. Agron. Soc. Environ.*, 17(2):392–406

Madsen, K., Nielsen N.B. and Tingleff, O. 2004. Methods for nonlinear least squares problems. *Technical Report. Informatics and Mathematical Modeling*, Technical University of Denmark.

Maerten, F., Resor, P., Pollard, D., and Maerten, L. 2005. Inverting for Slip on Three-Dimensional Fault Surfaces Using Angular Dislocations. *Bull. Seism. Soc. Am.*, 95, 5, 1654–1665, doi: 10.1785/0120030181.

Marquardt, D. 1963. An Algorithm for Least-Squares Estimation of Nonlinear parameter. *SIAM Journal on Applied Mathematics*, 11 (2): 431–441, doi:10.1137/0111030.

Massonnet, D. and Feigl, K.L. 1995a. Satellite radar interferometric map of the coseismic deformation field of the M = 6.1 Eureka Valley, California earthquake of May 17, 1993. *Geophys. Res. Lett.*, 22(12), 1541-1544.

Massonnet, D. and Feigl, K. 1998. Radar interferometry and its application to changes in the Earth's surface. *Rev. Geophys.* 36, 441–500.

Massonnet, D. 1997. Satellite radar interferometry. *Sci. Am.* 276 (2), 46–53.

Massonnet, D., Rossi, M., Carmona, C., Adragna, F., Peltzer, G., Feigl, K. and Rabaute, T. 1993. The displacement field of the Landers earthquake mapped by radar interferometry. *Nature*, 364:138-142.

Melgar, D., Ganas, A., Geng, J., Liang, C., Fielding, E. J. and Kassaras I. 2017. Source characteristics of the 2015 Mw 6.5 Lefkada, Greece, strike-slip earthquake. *J. Geophys. Res. Solid Earth*, 122, 2260–2273, doi:10.1002/2016JB013452.

Menke, W. 1989. Geophysical Data Analysis: Discrete Inverse Theory *Academic Press*, , San Diego, California.

Mesimeri, M., Kourouklas, C., Papadimitriou E., Karakostas, V. and Kementzetzidou D. 2018. Analysis of microseismicity associated with the 2017 seismic swarm near the Aegean coast of NW Turkey. *Acta Geophysica*, 1–17.

Mora, O, Mallorquı J.J. and Broquetas, A. 2003. Linear and nonlinear terrain deformation maps from a reduced set of interferometric SAR images*. IEEE Trans Geosc. Remote Sens.* 41:2243–2253.

Moreira, A, Prats-Iraola, P., Younis, M., Krieger, G., Hajnsek, I. and Papathanassiou, K. 2013. A Tutorial on Synthetic Aperture Radar, Microwaves and Radar Institute of the German Aerospace Center (DLR). *IEEE Geoscience and Remote Sensing Magazine* 1(1):6-43 DOI: 10.1109/MGRS.2013.2248301.

Mouratidis, A., Costantini, F. and Votsis A. 2011. Correlation of DInSAR deformation results and active tectonics in the city of Thessaloniki (Greece), In: Stilla, U., Gamba, P., Juergens, C., Maktav, D. (eds) JURSE 2011—Joint urban remote sensing event—Munich, Germany, April 11–13, 2011, IEEE, pp 421–424.

Mouratidis, A. 2010. Contribution of -GPS and GIS-assisted spaceborne remote sensing in the morphotectonic research of Central Macedonia (N. Greece). *Ph.D. thesis*, Aristotle University of Thessaloniki.

Mouratidis, A., Briole, P., Ilieva, M., Astaras, T., Rolandone, F. and Baccouche, M., 2009. Subsidence and deformation phenomena in the vicinity of Thessaloniki (N. Greece) monitored by Envisat/ASAR interferometry. *Proceedings of Fringe 2009*, Frascati, Italy.

Mützenberg, S. 1997. Nature and origin of the thermal springs in the Tuzla area, Western Anatolia, Turkey, in Schindler, C. and Pfister, M. (Eds.): *The Marmara Poly-Project,* pp.301–317, Vdf Hochschulverlag AG an der ETH, Zurich.

Nagoulis, A. and Loupasakis, C. 2001. Hydrogeological conditions of the plain area of the Anthemounta basin (Macedonia, Greece). *Bul. Geol. Soc. Gr.,* 34, 1859–1868.

Okada, Y., 1992. Internal deformation due to shear and tensile faults in a half-space. *Bull. Seismol. Soc. Am*., 82, 1018-1040.

Okada, Y. 1985. Surface deformation due to shear and tensile faults in a half-space. *Bull. Seismol. Soc. Am*, 75, no. 4, 1135–1154.

Osmanoğlu, B., Filiz, S., Shimon, W. and Enrique, C. 2016. Time series analysis of InSAR data: Methods and trends. *ISPRS Journal of Photogrammetry and Remote Sensing,* 115 90-102 http://dx.doi.org/10.1016/j.isprsjprs.2015.10.003.

Özalp, S., Emre, Ö. and Doğan, A. 2013. The segment structure of southern branch of the North Anatolian Fault and paleoseismological behaviour of the Gemlik Fault, NW Anatolia, *General Directorate of Mineral Research and Exploration (MTA) Bulletin*, 147, 1–17.

Özden, S., Över, S., Poyraz, S. A., Güneş, Y., and Pınar, A. 2018. Tectonic implications of the 2017 Ayvacık (Çanakkale) earthquakes, Biga Peninsula, NW Turkey. *Journal of Asian Earth Sciences*, *154*, 125-141

Papadimitriou, E., Karakostas, V., Mesimeri, M., Chouliaras, G. and Kourouklas Ch. 2017. The Mw 6.5 17 November 2015 Lefkada (Greece) Earthquake: Structural Interpretation by Means of the Aftershock Analysis. *Pure Appl. Geophys*., 2017 174, 3869–3888, doi: 10.1007/s00024-017-1601-3.

Papathanassiou, G., Valkaniotis, S., Ganas, A., Grendas, N. and Kollia, E. 2015. The November 17th, 2015 Lefkada (Greece) strike-slip earthquake: Field mapping of generated failures and assessment of macroseismic intensity ESI-07. *Eng. Geol,* 220, 13–30.

Papazachos, C., Soupios, P., Savvaidis, A. and Roumelioti, Z. 2000. Identification of small-scale active faults near metropolitan areas: an example from the Asvestochori fault near Thessaloniki. In*: Proceedings of XXXII ESC General Assembly*, Lisbon, Portugal, 221–225.

Papazachos, B.C and Papazachou, C.B. 1997. The Earthquakes of Greece, Publisher: *Ziti*, Thessaloniki, Greece

Paradisopoulou P.M., Papadimitriou E.E. and Mirek J. 2016. Significant earthquakes near the city of Thessaloniki (northern Greece) and probability distribution on faults Bulletin of the Geological Society of Greece, vol. L, p. 1389-1398 Proceedings of the 14th International Congress, Thessaloniki

Paradisopoulou P. M., Papadimitriou E. E., Karakostas V. G, Taymaz T., Kilias A., and Yolsal S. 2010. Seismic Hazard Evaluation in Western Turkey as Revealed by Stress Transfer and Time-dependent Probability Calculations. *Pure Appl. Geophys*. 167, 1013–1048, 2010, doi:10.1007/s00024-010-0085-1.

Paradisopoulou, P.M., Karakostas, V.G., Papadimitriou, E.E., Tranos, M.D., Papazachos, C.B., Karakaisis, G.F. 2006. Microearthquake study of the broader Thessaloniki area (Northern Greece). *Ann. Geophys.* 49(4/5):1081–1093.

Parsons, B., Wright, T., Rowe, P., Andrews, J., Jackson, J., Walker, R., Khatib, M., Talebian. M., Bergman, E. and Engdahl, E.R. 2006. The 1994 Sefidabeh (eastern Iran) earthquakes revisited: new evidence from satellite radar interferometry and carbonate dating about the growth of an active fold above a blind thrust fault. *Geoph. Journ. Int.*, doi: 10.1111/j.1365-246X.2005.02655.

Petsas, P. 1978. Pella, Alexander the Great's Capital. *Institute for Balkan Studies*, Thessaloniki (164.).

Phien-wej, N., Giao, P.H. and Nutalaya, P. 2006. Land subsidence in Bangkok, Thailand. *Eng. Geol.*, 82 (4), 187–201.

Polcari, M., Palano, M., Fernández, J., Samsonov, S.V., Stramondo S. and Zerbini S. 2016. 3D displacement field retrieved by integrating Sentinel-1 InSAR and GPS data: the 2014 South Napa earthquake. *European Journal of Remote Sensing,* 2016, Volume 49, - Issue 1.

Polcari, M., Albano, M., Atzori, S., Bignami C. and Stramondo, S. 2018. The Causative Fault of the 2016 Mw 6.1 Petermann Ranges Intraplate Earthquake (Central Australia) Retrieved by C- and L-Band InSAR Data, *Remote Sens.,* 10(8), 1311, https://doi.org/10.3390/rs10081311.

Pritchard, M.E. and Simons, M. 2006. An aseismic slip pulse in northern Chile and along-strike variations in seismogenic behaviour. *J. Geophys. Res.*, 111, B08405, doi:10.1029/2006JB004258

Psimoulis, P., Ghilardi, M., Fouache, E. and Stiros, S. 2007. Subsidence and evolution of the Thessaloniki plain, Greece, based on historical leveling and GPS data. *Eng. Geol.*, 90, 55–70.

Raspini, F., Loupasakis, C., Rozos, D., Adam, N., and Moretti, S. 2014. Ground subsidence phenomena in the Delta municipality region (Northern Greece): Geotechnical modeling and validation with Persistent Scatterer Interferometry. *Int. J. Appl. Earth Obs. Geoinf*. 28, 78–89.

Raspini, F., Loupasakis, C., Rozos, D. and Moretti, S. 2013. Advanced interpretation of land subsidence by validating multi-interferometric SAR data: the case study of the Anthemountas basin (Northern Greece). *Nat. Hazards Earth Syst. Sci*., 13 (10), 2425–2440.

Raucoules, D., Parcharidis, I., Feurer, D., Novalli, F., Ferretti, A., Carnec, C., Lagios, E., Sakkas, V., Le Mouelic, S. and Cooksley, G. 2008. Ground deformation monitoring of the broader area of Thessaloniki (Northern Greece) using radar interferometry techniques. *Nat. Hazards Earth Syst Sci,* 8:779–788.

Reasenberg, P. and Simpson, R. 1992. Response of Regional Seismicity to the Static Stress Change Produced by the Loma Prieta Earthquake. *Science,* 255(5052):1687-90, doi:0.1126/science.255.5052.1687.

Reilinger, R., McClusky, S., Vernant, P., Lawrence, S., Ergintav, S., Cakmak, R., Ozener, H., Kadirov, F., Guliev, I., Stepanyan, R., Nadariya, M., Hahubia, G., Mahmoud, S.H., Sakr, K., ArRajehi, A., Paradissis, D., Al-Aydrus, A., Prilepin, M., Guseva, T., Evren, E., Dmitrotsa, A., Filikov, S.V., Gómez, F., Al-Ghazzi, R. and Karam G.N. 2006. GPS constraints on continental deformation in the Africa-Arabia-Eurasia continental collision zone and implications for the dynamics of plate interactions. *J. geophys. Res.,* 549(1), 43–55.

Rosen, P., Hensley, S., Peltzer, G. and Simons M. 2004. Updated repeat orbit interferometry package released. *Eos Trans.,* AGU,85 (5), 47.

Ross, Z., Idini, B., Jia, Z., Stephenson, O., Zhong, M., Wang, X., Zhan, Z., Simons, M., Fielding, E., Yun, S., Hauksson, E., Moore, A, Liu, Z. and Jung J. 2019. Hierarchical interlocked orthogonal faulting in the 2019 Ridgecrest earthquake sequence. *Science,* 366, 346–351.

Rozos, D., Apostolidis, E. and Christaras, B. 2000. Engineering – geological map of Thessaloniki wider area. *Proceedings of National meeting on protection of Thessaloniki from Natural Hazards,* 46–53.

Rozos, D., Hatzinakos, I. and Apostolidis E. 1998. *Engineering Geological Map of Thessaloniki wider area*, Scale 1 : 25.000, I.G.M.E., Athens.

Rozos, D. and Hatzinakos, I. 1993. Geological conditions and geomechanical behaviour of the neogene sediments in the area west of Thessaloniki (Greece). In: Anagnostopoulos, et al. (Eds.), *Proceedings of International Symposium on Geotechnical Engineering of Hard Soils – Soft Rocks*, Greece 1. Balkema, Rotterdam, 269–274.

Sachpazi, M., Hirn, A., Clément, C., Haslinger, F., Laigle, M., Kissling, E., Charvis, P., Hello, Y., Lépine, J.C., Sapin, M. and Ansorge, J. 2000. Western Hellenic subduction and Cephalonia Transform: local earthquakes and plate transport and strain, *Tectonophysics*, 319, 301-31.

Saltogianni, V., Moschas, F. and Stiros, S. 2018. The 2014 Cephalonia Earthquakes: Finite Fault Modeling, Fault Segmentation, Shear and Thrusting at the NW Aegean Arc (Greece), *Pure Appl. Geophys.* , 175: 4145. https://doi.org/10.1007/s00024-018-1938-2.

Saltogianni, V., Taymaz, T., Yolsal-Çevikbilen, S., Eken, T., Moschas F. and Stiros S. 2017. Fault Model for the 2015 Leucas (Aegean Arc) Earthquake: Analysis Based on Seismological and Geodetic Observations, *Bull. Seis. Soc. Am.*, 107, No. 1, doi: 10.1785/0120160080.

Şamilgil, E. 1966. Hydrogeological report of geothermal energy possibility survey of hot springs of Kestanbol and Tuzla village of Çanakkale. *MTA, Ankara, report* 4274.

Şanlıyüksel, D. and Baba A. 2007. Hydrogeochemical and isotopic study of Kırkgeçit (Biga - Çanakkale) geothermal area, *Proceedings of the 60th Geological Congress*, Ankara, 89-92.

Schmidt, D.A. and Burgman, R. 2003. Time-dependent land uplift and subsidence in the Santa Clara valley, California, from a large interferometric, synthetic aperture radar dataset. *J. Geophys. Res.,* 108**,** 8534–8543.

Scordilis, M., Karakaisis, F., Karacostas, G., Panagiotopoulos, G., Comninakis, E. and Papazachos, C. 1985. Evidence for transform faulting in the Ionian Sea: The Cephalonia Island earthquake sequence of 1983, *PAGEOPH*, 123, 388–397.

Scuderi, M.M., Niemeijer, A.R.., Collettini, C, and Marone, C. 2013. Frictional properties and slip stability of active faults within carbonate–evaporite sequences: The role of dolomite and anhydrite*, Earth and Planetary Science Letters*, http://dx.doi.org/10.1016/j.epsl.2013.03.024i.

Segall, P. 2010. Earthquake and Volcano Deformation, *Princeton university press*

Segall, P., Desmarais, E.K., Shelly, D., Miklius, A. and Cervelli, P. 2006. Earthquakes triggered by silent slip events on Kilauea volcano, Hawaii. *Nature,* 442**,** 71–74.

Şengör, A.M.C., 1979. The North Anatolian transform fault: Its age, offset and tectonic significance. *Journal of the Geological Society London*, 136, 269–282.

Şengör, A.M. C., Tüysüz, O., İmren, C., Sakınç, M.,Eyidoğan, H., Görür, G., and Le Pcihon, X. 2005. North Anatolian Fault: A new look, *Annual Review of Earth and Planetary Sciences*, 33, 37–112

Sivignon, M. 1987. La mise en valeur du delta de l'Axios, *in* J. Bethemont, C. Villain-Gandossi (éds), *Les Deltas méditerranéens*, Centre européen de coordination de recherche et de documentation en Sciences sociales, Vienne, 279‑296

Sokos, E., Zahradník, J., Gallovic, F., Serpetsidaki, A., Plicka, V. and Kiratzi, A. 2016. Asperity break after 12 years: The Mw6.4 2015 Lefkada (Greece) earthquake. *Geoph. Res. Lett.*, 43, doi:10.1002/2016GL069427.

Sokos, E, Kiratzi, A., Gallovič, F., Zahradník, J., Serpetsidaki, A., Plicka, V., Janský, J., Kostelecký J. and Tselentis G.A. 2015. Rupture process of the 2014 Cephalonia, Greece, earthquake doublet (Mw6) as inferred from regional and local seismic data, *Tectonophysics*, 656, 131–141.

Sonobe, R., Tani, H., Wang. X., Kobayashi, N., Kimura, A. and Shimamura, H. 2014. Application of Multi-temporal TerraSAR-X Data to Map Winter Wheat Planted Areas in Hokkaido, Japan. *JARQ 48*(4):465–470.

Soulios, G. 1999. Research for the development of the aquifers in the low lands on the west of Thessaloniki for the interests of the Water Company of Thessaloniki. *Research Committee Technical Report*. Aristotle University of Thessaloniki, 99.

Sözbilir, H., Sümer, O., Özkaymak, C., Uzel, B., Tayfun, G. and Semih, E. 2016. Kinematic analysis and palaeoseismology of the Edremit Fault Zone: evidence for past earthquakes in the southern branch of the North Anatolian Fault Zone, Biga Peninsula, NW Turkey. *Geodinamica Acta*, 28:4, 273-294, doi: 10.1080/09853111.2016.1175294.

Steketee, J. A. 1958a. On Volterra's Dislocations in a Semi-infinite Medium. *Can. Jour. Phys.*, 36: 192-205.

Stiros, S., 2001. Subsidence of the Thessaloniki (northern Greece) coastal plain, 1960–1999. *Eng. Geol.*, 61 (4), 243–256.

Stiros, S., Pirazzoli, P., Labore, J. and Laborel-Deguen, F. 1994. The 1953 earthquake in Cephalonia (Western Hellenic Arc): coastal uplift and halotectonic faulting. *Geophys. J. Int.* , 117, 834-849

Sudhaus, H. and Jónsson, S. 2009. Improved source modelling through combined use of InSAR and GPS under consideration of correlated data errors: application to the June 2000 Kleifarvatn earthquake, Iceland. *Geoph. Journ. Int.*, Volume 176, Issue 2, February, 389–404, https://doi.org/10.1111/j.1365-246X.2008.03989.x

Svigkas, N., Atzori S., Kiratzi, A., Tolomei, C., Antonioli, A., Papoutsis, I., Salvi, S. and Kontoes Ch. 2019c. On the Segmentation of the Cephalonia–Lefkada Transform Fault Zone (Greece) from an InSAR Multi-Mode Dataset of the Lefkada 2015 Sequence. *Remote Sensing*, 11(16), 1848; https://doi.org/10.3390/rs11161848

Svigkas, N., Atzori, S., Kiratzi, A., Tolomei, C. and Salvi, S. 2019b. Isolating swarm sources using InSAR: the case of the February 2017 seismic swarm in Western Anatolia (Turkey). *Geoph. Jour. Int.*, https://doi.org/10.1093/gji/ggz093

Svigkas, N., Papoutsis, I., Loupasakis, C., Tsangaratos, P., Kiratzi, A. and Kontoes, Ch. 2019a. Radar space measurements of the deforming trends at northern Greece resulting from underground water activity. *Adv. Remote Sensing Geo Inform. Appl.*, 309-313.

Svigkas, N., Papoutsis, I., Loupasakis, C., Tsangaratos, P., Kiratzi, A., Kontoes, Ch. 2017. InSAR time-series monitoring of ground displacement trends in an industrial area (Oreokastro—Thessaloniki, Greece): detection of natural surface rebound and new tectonic insights. *Environ. Earth Sci.*, 76:195, doi: 10.1007/s12665-017-6517-9.

Svigkas, N., Papoutsis, I., Loupasakis, C., Tsangaratos, P., Kiratzi, A. and Kontoes, Ch. 2016. Land subsidence rebound detected via multi-temporal InSAR and ground truth data in Kalochori and Sindos regions, Northern Greece. *Engin. Geol.,* 209, 175-186, doi.org/10.1016/j.enggeo.2016.05.017.

Svigkas, N., Papoutsis, I., Loupasakis, K., Kontoes, H. and Kiratzi, A. 2015. Geo-hazard monitoring in northern Greece using InSAR techniques: the case Study of Thessaloniki, (Abstract ID33). In: *9thInternational Workshop Fringe 2015 ''Advances in the Science and Applications of SAR Interferometry and Sentinel-1 InSAR''*,ESA-ESRIN, Frascati, Italy, 23–27 March

Syrides, G.E. 1990. Lithostratigraphic, biostratigraphic and palaeogeographic study of the Neogene–Quaternary sedimentary deposits of Chalkidiki Peninsula, Macedonia, Greece *Ph.D. thesis,* Aristotle University of Thessaloniki 243 (in Greek).

Taniguchi, M., Shimada, J., Fukuda, Y., Yamano, M., Onodera, S., Kaneko, S. and Yoshikoshi, A. 2009. Anthropogenic effects on the subsurface thermal and ground water environments in Osaka, Japan and Bangkok, Thailand. *Sci. Total Environ.,* 407(9):3153–3164. doi:10.1016/j.scitotenv.2008.06.064.

Terzaghi, K. 1943. Theoretical Soil Mechanics. *John Wiley & Sons*, Inc., p. 265.

Thanasoulas, K. 1983 Geophysical study of Anthemountas area. *Unpublished technical report, I.G.M.E.*, Athens (in Greek).

Tomiyasu, K. 1978. Tutorial review of synthetic-aperture radar (SAR) with applications to imaging of the ocean surface. *Proc. IEEE*, vol. 66, no. 5, May.

Tranos, M.D., Papadimitriou, E.E. and Kilias, A. 2003. Thessaloniki–Gerakarou Fault Zone (TGFZ): the western extension of the 1978 Thessaloniki earthquake fault (Northern Greece) and seismic hazard assessment. *J. Struct. Geol.,* 25, 2109–2123.

Yilmaz, Y. and Karacik, Z. 2001. Geology of the northern side of the Gulf of Edremit and its tectonic significance for the development of the Aegean grabens. *Geodinamica Acta*, 14, 31–43.

Yu, C., Li, Z. and Penna, N.T. 2018a. Interferometric synthetic aperture radar atmospheric correction using a GPS-based iterative tropospheric decomposition model. *Remote Sens. Environ.*, doi:10.1016/j.rse.2017.10.038.

Yu, C., Li, Z., Penna, N. T. and Crippa, P. 2018b. Generic atmospheric correction model for Interferometric Synthetic Aperture Radar observations. Journ. of Geoph. Res.: Solid Earth, 123. https://doi.org/10.1029/2017JB015305.

Yu, C., Penna, N. T. and Li, Z. 2017. Generation of real-time mode high-resolution water vapor fields from GPS observations. *J. Geophys. Res. Atmos*., 2017 122, 2008–2025, doi:10.1002/2016JD025753.

Vajedian, S., Motagh, M., Mousavi, Z., Motaghi, K., Fielding, E.J., Akbari, B., Wetzel H.U. and Darabi, A. 2018. Coseismic Deformation Field of the Mw 7.3 12 November 2017 Sarpol-e Zahab (Iran) Earthquake: A Decoupling Horizon in the Northern Zagros Mountains Inferred from InSAR Observations, *Remote Sens.,* 10(10), 1589; https://doi.org/10.3390/rs10101589.

van der Kooij M., Hughes, W., Sato, S. and Poncos, V. 2006. Coherent target monitoring at high spatial density: examples of validation results. In: *European Space Agency Special Publications*, SP-610.

Velaj, T., Davison, I., Serjani, A. and Alsop, I. 1999. Thrust tectonics and the role of evaporites in the Ionian Zone of the Albanides. *AAPG Bulletin,* 83(9), 1408–1425.

Vidale, J.E. ans Shearer, P.M. 2006. A survey of 71 earthquakes bursts across southern California: Exploring the role of pore fluid pressure fluctuations and aseismic slip as drives. *J. Geophys. Res.,* 111, B05312, doi:10.1029/2005JB004034.

Wald, D. and Graves, R. 2001. Resolution analysis of finite fault source inversion using one- and three-dimensional Green's functions: 2. Combining seismic and geodetic data. *J. geophys. Res.*, 106, 8767–8788.

Wallace, L. M. and Eberhart-Phillips, D. 2013. Newly observed, deep slow slip events at the central Hikurangi margin, New Zealand: implications for downdip variability of slow slip and tremor, and relationship to seismic structure. *Geophys. Res. Lett.*, 40, (5393–5398).

Wang, Z., Zhang, R., Wang, X. and Liu, G. 2018 Retrieving three-dimensional co-seismic deformation of the 2017 MW7.3 Iraq earthquake by multi-sensor SAR images. *Remote Sens.,* 10, 857.

WaterinCore project 1G-MED-515 Water Management Analysis in "water district 10" of Region of Central Macedonia, Greece (2009) "*Sustainable Water Management through Common Responsibility enhancement in Mediterranean River Basins*", www.waterincore.eu.

Weston, J., Ferreira, A.M.G. and Funning G.J. 2012. Systematic comparisons of earthquake source models determined using InSAR and seismic data. *Tectonophys.*, 532, 61{81, doi:10.1016/j.tecto.2012.02.001.

Woodhouse, I., 2006. Introduction to Microwave Remote Sensing. *Boca Raton*, FL: CRC Press.

Wright, T.J., Lu, Z. and Wicks, C. 2003. Source model for the Mw 6.7, 23 October 2002, Nenana Mountain Earthquake (Alaska) from InSAR. *Geophys. Res. Lett.*, 30(18), doi:10.1029/2003GL018014.

Wright, P. and Stow, R. 1999. Detecting mining subsidence from space. *Int. J. Remote Sens.* 20 (6), 1183–1188.

Zare M., Kamranzad F., Parcharidis I. and Tsironi, V. 2017. Preliminary report of Mw7.3 Sarpol-e Zahab,Iran earthquake on November 12, 2017 (Updated on Nov. 22) https://www.emsc-csem.org/Doc/Additional_Earthquake_Report/629693/Preliminary_report_M7.3_20171112_v3.pdf.

Zebker, H.A. and Goldstein, R.M. 1986. Topographic Mapping from interferometric synthetic aperture radar observations. *J. Geophys. Res.*, 91, 4993–4999.

Zebker, H.A. and Villasenor, J. 1992. Decorrelation in Interferometric Radar Echoes. *IEEE Transactions on Geoscience and Remote Sensing,* 30, 950-959. http://dx.doi.org/10.1109/36.175330.

Zervopoulou, A. 2010. Neotectonic Faults of the Wide Area of Thessaloniki in association with foundation Soils. *Ph.D. Thesis*, University of Thessaloniki (in Greek).

Zervopoulou A. and Pavlides, S. 2005. Morphotectonic study of the broader area of Thessaloniki for the chartography of neotectonic faults. *Bull. Greek Geol. Soc*. 38:30–41 (in Greek).

Zhong, L. and Danskin, W.R. 2001. InSAR analysis of natural recharge to define structure of a ground-water basin, San Bernardino. *Geophys. Res. Lett*. 28 (13), 2661–2664.

Online sources

UNAVCO [accessed 12-1-2019]:

https://www.unavco.org/instrumentation/geophysical/imaging/sar-satellites/sar-satellites.html

European Space Agency [accessed 12-1-2019]:

http://www.esa.int/spaceinimages/Images/2000/10/ERS_satellite

https://earth.esa.int/web/eoportal/satellite-missions/e/envisat

https://sentinel.esa.int/web/sentinel/missions/sentinel-1/overview

https://directory.eoportal.org/web/eoportal/satellite-missions/a/alos-2

Canadian Space Agency [accessed 12-1-2019]:

http://www.asc-csa.gc.ca/eng/satellites/radarsat2/Default.asp

USGS [accessed 12-1-2019]:

https://earthquake.usgs.gov/earthquakes/eventpage/us2000bmcg/moment-tensor

EMSC [accessed 12-1-2019]:

https://www.emsc-csem.org/Earthquake/260/M7-3-IRAN-IRAQ-BORDER-REGION-on-November-12th-2017-at-18-18-UTC

EMODnet [accessed 5-4- 2019]:

Topographic Data. Available online: *http://www.emodnet-bathymetry.eu*

Geodynamic Institute of Athens [accessed 12-1-2019]:

http://bbnet.gein.noa.gr